Donor Doped $BaSnO_3$, SnO_2 Metal Oxide Photoanodes and Prickly Pear Fruit Extract Photosensitizer Alternatives for Dye Sensitized Solar Cells

THESIS

Submitted in partial fulfilment of the requirements

for the award of the degree of

DOCTOR OF PHILOSOPHY

In

PHYSICS

BY

N. PURUSHOTHAM REDDY

(Roll No: 717052)

Under the supervision of

Dr. D. Paul Joseph

DEPARTMENT OF PHYSICS
NATIONAL INSTITUTE OF TECHNOLOGY WARANGAL
WARANGAL - 506004, TELANGANA STATE, INDIA.

November – 2021

Work supported by DST-SERB, Govt. of India

NATIONAL INSTITUTE OF TECHNOLOGY
WARANGAL (T.S.) INDIA 506 004

APPROVAL SHEET

This thesis entitled **"Donor Doped $BaSnO_3$, SnO_2 Metal Oxide Photoanodes and Prickly Pear Fruit Extract Photosensitizer Alternatives for Dye Sensitized Solar Cells"** by **Mr. N. PURUSHOTHAM REDDY** (Roll No: **717052**) is approved for award of the degree of **Doctor of Philosophy.**

(External Examiner)
Institute designation
Address

Dr. D. Paul Joseph
(Research Supervisor)
Assistant Professor
Department of Physics
NIT Warangal, India

Prof. D. Dinakar
(Head and Chairman)
Department of Physics
NIT Warangal, India

Date:

Declaration

This is to declare that the work presented in the thesis entitled "**Donor Doped $BaSnO_3$, SnO_2 Metal Oxide Photoanodes and Prickly Pear Fruit Extract Photosensitizer Alternatives for Dye Sensitized Solar Cells"** is a bonafide work done by me under the supervision of Dr. D. Paul Joseph, Assistant professor, Department of Physics, and was not submitted elsewhere for the award of any degree.

I declare that this written submission represents my ideas in my own words and where other's ideas or words have been included, I have adequately cited and referenced the original sources. I also declare that I have adhered to all principles of academic honesty and integrity and have not misrepresented or fabricated or falsified any idea/data/fact/source in my submission. I understand that any violation of the above will be a cause for disciplinary action by the institute and can also evoke penal action from the sources which have thus not been properly cited or from whom proper permission has not been taken when needed.

Date: 26-11-2021 **N. PURUSHOTHAM REDDY**

Place: NIT Warangal **(Roll. No: 717052)**

NATIONAL INSTITUTE OF TECHNOLOGY, WARANGAL

Certificate

This is to certify that the work presented in the thesis entitled *"**Donor doped $BaSnO_3$, SnO_2 Metal Oxide Photoanodes and Prickly Pear Fruit Extract Photosensitizer Alternatives for Dye Sensitized Solar Cells"*** is a bonafide work done by **Mr. N. PURUSHOTHAM REDDY** under my supervision and was not submitted elsewhere for the award of any degree.

Dr. D. Paul Joseph
Assistant Professor
Research Supervisor

Date: 26-11-2021
Place: NIT Warangal

Acknowledgements

I would like to express sincere thanks to my research supervisor, **Dr. D Paul Joseph**, Assistant Professor, Department of Physics, NIT Warangal for his constructive guidance, relentless encouragement, and his love for research that motivated me throughout my research work.

I very much appreciate that he has given me the freedom to pursue my research interests for the completion of this research work. I would remain grateful to him for his invaluable advice, availability to discuss ideas, and willingness to share his knowledge expertise, and innumerable help that he rendered throughout my research career.

I express my sincere thanks to the ***Director***, National Institute of Technology, Warangal, for having given me the opportunity to carry out the research work and allowing me to submit it in the form of a research thesis.

I express my sincere thanks to Prof. **D. Dinakar**, Head, Department of Physics, NITW, for his valuable suggestions and support. I also express my sincere thanks to the former heads of the department of Physics, NITW, for their valuable help, support and for providing good infrastructure to carry out my research work.

I am indebted to my doctorial scrutiny committee members **Prof. Narasaiah**, Department of Metallurgical and Materials Engineering, NITW, **Dr. Kusum Kumari,** and **Dr. V. Jayalakshmi**, Assistant Professors, Department of Physics, NITW, for their valuable suggestions and comments on my research work during the doctoral scrutiny committee meetings.

I express my sincere thanks to **DST-SERB, Govt. of India** for the financial support in the form of a fellowship research grant under the file No.: YSS/2014/000191.

I sincerely thank **Dr. V. Ganapathi,** DST-Inspire faculty, ARCI, Hyderabad, for his valuable suggestions and support to carry out my research work. I also thank Ms. **Reshma** Dileep for assistance in fabricating and testing H-LBSO and natural dye based DSSCs.

I am very much thankful to **Dr. Rakesh Kumar**, Assistant Professor, department of Physics, NITW, for his help in recommending me to Dr. Murali Banovoth, University of Hyderabad, to carry out my research related work.

I sincerely thank **Dr. Murali Banovoth**, Assistant Professor, School of Chemistry, University of Hyderabad, for his valuable suggestions, constant support, and for permitting me to carry out device fabrication and characterization in his laboratory. I also thank his scholar Mr. **R. Santhosh** for his innumerable help in characterizations and assistance in device fabrication. I acknowledge the support and input for this work obtained through the 'UGC Networking Resource Centre', School of Chemistry, University of Hyderabad.

I am very much thankful to **Dr. M. Kovendhan**, Department of Environmental Engineering, Inha University, Incheon, South Korea for his help in various measurements related to my research work.

I thank **Dr. Jean Maria Fernandes**, Adhoc Faculty, department of Physics, NITW, for her help in proofreading my manuscripts and thesis.

I am thankful to senior faculty members of our department, **Prof. S.V.S. Ramana Reddy**, **Prof. Sai Sankar, Prof. L. Ramgopal Reddy, Prof. R. L. N. Sai Prasad, Prof. K. Venugopal Reddy**, for their encouragement and support.

I take this opportunity to express my gratitude to **Dr. B. Sobha, Dr. T. Venkatappa Rao, Dr. P. Abdul Azeem, Dr. P. Syam Prasad, Dr. Sourabh Roy, Dr. K. Thangaraju, Dr. D. Haranath, Dr. K Udaykumar, Dr. Vijay Kumar, Dr. Surya K. Ghosh, Dr. Hitesh Borkar, Dr. Aalu Boda**, Department of Physics, National Institute of Technology, Warangal for their advice and encouragement.

I would also like to extend my sincere thanks to **Prof. M. K. Mohan** for permitting me to use CAM facilities to carry out my experiments. I would also like to thank **Mr. Srinivas** and **Mrs. Ramya**, Technicians, NIT Warangal for their help to record XRD and SEM-EDX characterizations.

With all happiness, I acknowledge the cheerful assistance rendered by all my senior research colleagues **Dr. S. Rajkumar, Dr. V. Himamaheswara Rao, Dr. M. Mohan Babu, Dr. R. Ramarajan Mr. D. Gnyaneshwar, Dr. Lal Singh, Dr. Ashish Kumar, Dr. P. M. Pratheeksha**, for their encouragement throughout my research in the department of Physics, NITW.

I thank all the research colleagues **Ms. Sravanthi, Mr. M. Nagaraju, Dr. Srinath, Mr. VDR Pavan, Ms. N. Manjula, Mr. G. Buchaiah, Mr. B. Ramesh**, and other co-research scholars for their munificent support throughout my research.

I especially thank my junior research scholars **Mr. R. Muniramaiah and Mr. Gouranga Maharana** for their great help in drafting and proofreading my thesis as well as their constant love and support.

I sincerely thank **Dr. K. S Dhathathreyan, Dr. Imran Jafri, Dr. Rajalakshmi, Dr. Balaji, Dr. Ramya**, Center for Fuel Cell Technology (CFCT), ARCI, Chennai for their encouragement and valuable suggestions during my early stage of continuing research.

I thank **Dr. N. Manjula, Dr. Anusri, Mr. T. Ramesh, Dr. Preethi Jayaraj, Mr. Naik, Mr. Imran**, CFCT-ARCI, Chennai, for their suggestions, encouragement, and support.

I wish to express my heartfelt thanks to my teachers of 1st class to 12th, especially **Mr. Eswar Reddy, Mrs. Chittemma, Mr. Nataraj, Mr. R. Ramesh, Mrs. Susheeladevi, Mrs. Krishnaveni, Mr. Chandra Reddy, Mr. Arun Kumar, Mr. Kareem Mullai, Mr. Govinda Reddy, Mr. Uday Kumar, Mr. Babu, Mrs. Nagalakshmi, Mrs. Symaladevi** who encouraged and guided me during early stages of my education so as to establish my career.

I wish to express my heartfelt thanks to **Prof. K. Dayananda Reddy (**Head, Chemistry Department, PVKN Govt. College Chittoor), **Dr. Hemalatha, Dr. Giribabu, Dr. Srinivasuslu, Dr. Subramanyam Naidu, Mr. P. Shanmugam,** Department of Physics, PVKN Govt. College Chittoor, **Dr. K. Ramaiah, Dr. A. Narasimhuluchetty, Mr. P. Haribabu, Dr. Bhanuprakash (**Department of Chemistry, PVKN Govt. College Chittoor), for helping me to establish my career from B.Sc graduation.

I sincerely thank **Prof. S. Uthanna**, **Prof. OM. Hussain**, Department of Physics, Thin Films and Vacuum Technology laboratory, Sri Venkateswara University, Tirupati, for their constant support and encouragement during my post graduation course especially on thin films.

I thank all my relatives **Mr. N. Narasimha Reddy, Mrs. N. Munniyamma, Mrs. A. Lakshmi, Mr. Errama Reddy, Late. N. Gangulu Reddy, Mrs. N. Bujjamma, Mr. N. Raja Reddy, Mrs. Chilakamma, Mr. N. Nagaraja Reddy, Mrs. N. Vanitha, Mrs. B. Bujjamma, Mr. B. Somasekar Reddy, Mrs. A. Anuradha, Mr. A. Hariprasad Reddy, Mr. N. Udayasankar Reddy, Mr. N. Nagaraja Reddy, Ms. Meenakshi, Mr. N. Bharat Reddy, Mr. N. Hemanth Reddy,** and all the people of my beautiful village (Jangala Palli) for their encouragement.

My heartfelt thanks are to my beloved friends **Mr. M. Anil Kumar, Mr. P. Bhaskar Rao, Dr. K. Chandra Shekar, Dr. N. V. Raveendra, Dr. Reddy Sekhar, Mr. Reddy Prakash, Mr. M. Kumar, Mr. Vijay, Mr. Mahesh Reddy, Mr. Praveen Kumar, Mr. G. Prasad Babu, Dr. Goli Nagaraju, Mr. N. Jayachandra Reddy, Mr. B. Sadashiva Reddy, Mr. N. Venu Reddy,** and all other friends for their love, encouragement, and great support.

Finally, no word can express my deep sense of gratitude towards my parents **Mr. N. Jayarama Reddy** and **Mrs. N. Pushpa** for their love, encouragement, moral support, and the sacrifice they did throughout my life. With all their patience, prayers and faith in the Almighty, waited all these long years to see me reaching this stage.

I wholeheartedly would like to thank my beloved brothers **Dr. N. Damodar Reddy, Dr. N. Kumarswamy Reddy, Mr. N. Bhaskar Reddy, Mr. N. Bhupathi Reddy** for inspiring me to pursue my ambitions and pushing me to work hard towards my goal. All of you are the driving force behind my success and your intense caring and support in every aspect has influenced my life. I also thank my brother's son and daughters, **Mr. N. Bhargav Reddy, Ms. Laasya, Ms. Novika, Ms. Veeksha,** and my sisters-in-law **Mrs. N. Hemaltha and Mrs. N. Usha,** and my wife **N. Kalpana** for their affection, love and constant support which cheered me up and boosted me whenever needed. Their blessings and care always gave me new fervor and gusto to do something more with perfection. I thank all my other relatives who have been very supportive and who encouraged me in all my endeavors.

Finally, I thank **God the Almighty** for giving me the knowledge, vision, and ability to proceed and "make it so". It is only through His grace, that any achievement can truly be accomplished.

Date:

Place: NIT Warangal **N. PURUSHOTHAM REDDY**

"I have gone through so many different stages changing ideas and goals while searching for the right kind of life for me. You are always ready to help me at all times. You are the one who gave me strength and energy whenever I needed. I can't return encouragement, care, and loving words of praise. In quite the way you did for me through all my life. But there is one gift that I can give, It's all the love you've earned."

Dedicated to

MY BELOVED

PARENTS & BROTHERS

Preface

Today, the world is increasingly interested in clean alternate energy sources to produce electricity without environmental damage and carbon footprint, unlike traditional fossil fuels that cause severe environmental pollution, which has motivated researchers to explore alternative means for obtaining renewable energy from plentiful natural resources. Solar energy is the most abundant and prominent renewable source for environmentally clean energy which can be harnessed via different routes. A dye-sensitized solar cell (DSSC) is one such renewable energy device that can convert solar radiation into usable electrical energy. With the growing demand for clean and sustainable energy, DSSCs are extensively explored as potential alternatives to supplement the existing technology due to their captivating properties, such as cost-effectiveness, ease of fabrication, eco-friendliness, non-toxicity, light-weight, and good conversion efficiency even under cloudy and artificial light conditions. For the past two decades, DSSC devices have been explored using various photoanode materials, electrolytes, and sensitizers to improve their performance and long-term stability. To develop DSSCs with high efficiency, it is crucial to optimize the semiconducting material by tuning its optical properties, electrical properties, and morphology. The challenges associated with DSSCs are the choice of photoanode material, nano-structuring of the electrodes, photosensitizers, electrolytes, and device architecture, which are yet to be investigated in-depth to achieve high efficiency with good reproducibility. These aspects are the motivation for the present work on the investigation of alternative materials for achieving high efficiency and stability of DSSC devices. Based on this motivation, appropriate alternative materials for photoanode materials, transparent conducting electrodes (TCE), and natural dye are investigated in this thesis.

In DSSCs, mesoporous TiO_2 is widely used as photoanode material highly influencing the photovoltaic performance by playing a crucial role in transporting the photo-generated

electrons. However, the TiO_2-based photoanode can cause photo-bleaching of dye molecules upon solar irradiation, particularly in the UV region, which is a significant drawback for practical applications. Alternatively, researchers have focused on ternary oxide semiconductors such as Zn_2SnO_4, $SrSnO_3$, and $BaSnO_3$ due to their favorable ionization potential, bandgap, and electron affinity that can be easily tuned by doping with appropriate impurities during the synthesis process. Among the ternary oxides, $BaSnO_3$ is a promising n-type semiconductor with a perovskite structure possessing a wide bandgap of 3.2 eV and structural stability around 1000 °C. It exhibits high carrier mobility, facilitating fast diffusion of electrons in the conduction band and faster dye adsorption ability compared to binary oxide photoanodes.

Apart from photoanode materials, transparent conducting oxide (TCO) electrodes also play a crucial role in the performance of DSSCs by enhancing the electronic conductivity by functioning as a current collector supporting the semiconducting layer. The TCOs have two important features; one is high optical transparency which allows sunlight to enter into the device without much absorption, and secondly, low electrical resistivity to facilitate effective electron transfer to improve the conductivity. Alternative 'Sb' doped SnO_2 thin film is optimized and explored to supplement the conventional fluorine doped SnO_2 based TCO.

Alternative dyes extracted from natural sources are also widely investigated as photosensitizers due to their eco-friendliness, cost-effectiveness, non-toxicity, and abundance. These natural dyes are capable of absorbing photons having wavelengths in the visible region of the solar spectrum. Overall, the major objective of DSSC research is to identify and optimize appropriate cost-effective and eco-friendly alternative material components by facile processes for achieving high efficiency and stability of the devices.

In this thesis work, alternative photoanode materials La-doped $BaSnO_3$ (LBSO) and Sb-doped $BaSnO_3$ (ABSO), alternative Sb-doped SnO_2 (ATO) transparent conducting electrode, and alternative natural dye extracted from prickly pear fruit for use as a photosensitizer in

DSSCs are systematically investigated. The obtained results are analyzed and divided into eight chapters and the gist of which is briefly outlined as follows,

Chapter-1: This chapter gives an overview of the basics of solar energy and photovoltaic technology. The development of DSSCs, device architecture, working mechanism, and the materials involved are briefly outlined. A brief description of various material components employed as photoanodes and transparent conducting electrodes (TCE) is also given. Properties of various types of binary/ternary metal oxides, photosensitizers, and electrolytes are explained in sufficient detail. This chapter is concluded with the motivation, objectives, and scope of the thesis.

Chapter-2: This chapter depicts the principle behind various experimental methods and analytical instruments used in this thesis. Hydrothermal and facile peroxide routes for the synthesis of ternary oxides are described in detail. Deposition of TCE thin film by spray pyrolysis is given in detail and also outlines the importance of natural dyes and their extraction from prickly pear fruits for use as a photosensitizer in DSSCs. An overview of working principles of various characterization instruments along with specifications as well as complete steps of DSSC device fabrication processes and related characterization instrumentation details are also presented.

Chapter-3: This chapter elaborates the structural, morphological, optical, and electrical properties of the hydrothermally synthesized nanostructured La-doped $BaSnO_3$ ternary oxides for use as photoanode in DSSCs. Upon increasing the dopant concentration of La, the morphology disintegrates and tends towards a mixed nanorod-nanoparticle feature for 0.03% La-doped $BaSnO_3$ sample as confirmed from the SEM and TEM measurements. A significant variation in the bandgap is observed upon doping with 'La' into the $BaSnO_3$ system. Among all the devices, highest power conversion efficiency of 1.23% is observed for the 0.03% La-doped $BaSnO_3$ sample. The efficiency is lower compared to standard TiO_2 based devices due

to bigger-sized rod-like particles grown by hydrothermal method which may not lead to effective dye adsorption.

Chapter-4: This chapter presents the results of ternary La-doped $BaSnO_3$ nanoparticles synthesized using facile peroxide route to overcome the grain size issue encountered in chapter 3. The synthesized samples are studied for their structural, optical, and morphological characteristics, and also used as photoanodes in DSSCs. The pure and La-doped samples are confirmed with a single-phase cubic perovskite structure of $BaSnO_3$. A mixed nanocuboids/nanoparticles morphology is observed for the LBSO3 sample. The absorption studies show a slight increase in optical bandgap upon doping with 'La'. Dye loading measurements are also carried out to determine the effect of morphology on the dye adsorption capability of the pure (BSO) and La-doped (LBSO1, LBSO3, and LBSO5) photoanodes. The absorption of dye solution corresponding to post $TiCl_4$ treated LBSO3 film shows higher dye loading than that of the BSO film within a mere 60 minutes. The post-treated DSSC exhibits improved efficiency of 5.96% for LBSO3 cell against 4.37% of the pre-treated LBSO3 cell. Additionally, the DSSC performance stability test carried out for 16 days shows retention of ~ 80% of its initial PCE.

Chapter-5: This chapter deals with 'Sb' doped $BaSnO_3$ as photoanode explored for its performance in DSSCs. A facile-peroxide route was used to synthesize pure and Sb-doped perovskite $BaSnO_3$ (ABSO) nanoparticles. The synthesized samples were characterized for their structural, morphological, and optical properties. The DSSCs fabricated using the synthesized BSO and ABSO samples as photoanodes show reasonably good photovoltaic performance with a maximum power conversion efficiency of 4.06% for 0.01% 'Sb' doped photoanode.

Chapter-6: This chapter describes the details of Sb-doped SnO_2 (ATO) transparent conducting thin films deposited over a 5x5 cm^2 area of glass substrates using the facile spray pyrolysis technique. The ATO film deposited at 420 °C is found to possess good transmittance

with a wide bandgap and low sheet resistance compared to pure TO film. Further, it shows good electrical properties with high carrier concentration and mobility. The film exhibits thermal stability around 400 °C. The stabilized ATO film used as an alternative to FTO in DSSC exhibits an efficiency of 4.05%.

Chapter-7: In this chapter, prickly pear fruit extract is explored as an alternative photosensitizer for use in DSSCs. The natural photosensitizer is isolated from prickly pear fruits by a facile extraction process and is studied for its structural, optical, chemical, and electronic properties. The UV-Vis DRS and FTIR spectra of the extract confirm the presence of betacyanin with high absorption around 534 nm in the visible region, and well-anchored hydroxyl groups onto the TiO_2 surface are also confirmed from XPS analysis. The fabricated DSSC using prickly pear extract as photosensitizer exhibits conversion efficiency of 0.56 % with a high fill factor of 85%.

Chapter-8: The final chapter presents the summary and conclusions drawn from the investigations carried out on photoanode materials, TCE, and natural photosensitizer when used in DSSCs. This chapter presents the comparison of performance parameters of DSSCs of all the optimized La- and Sb-doped $BaSnO_3$ photoanodes, alternative ATO based TCE, and prickly pear fruit extract photosensitizer. This chapter is finally concluded with perspectives for future work.

****

List of Symbols

Symbol	Description
D	Average crystallite size
β	Full Width at Half Maximum (FWHM)
θ	Diffraction angle
θ_w	Wenzel's contact angle
θ_Y	Young's contact angle
d	Inter-planar spacing
Å	Angstrom
'a', 'b', and 'c'	Lattice constants
TC_{hkl}	Texture coefficient
α	Absorption coefficient
h	Planck's constant
ν	Frequency
λ	Wavelength
E_g	Band gap
ρ	Resistivity
n_c	Carrier concentration
μ_e	Mobility
R_{Sheet}	Sheet resistance
R_s	Series resistance

V	Measured voltage
I	Applied current
$\Omega/\square$	Ohm per square
σ	Conductivity
N	Defect density
E_k	Kinetic energy
Φ	Work function
I_{sc}	Short circuit current
V_{oc}	Open-circuit voltage
J_{sc}	Short-circuit current density
FF	Fill factor
P_{max}	Maximum output power
I_{max}	Maximum current
V_{max}	Maximum voltage
P_{in}	Incident light power
η	Power conversion efficiency
Z_R	Resistive impedance
Z_C	Capacitive reactance impedance
Z'	Real part of impedance
Z''	Imaginary part of impedance
$T\%$	Transmittance percentage

List of Abbreviations

Abbreviation	Description
PV	Photovoltaic
TW	Terawatt
DSSC	Dye sensitized solar cell
QDSSC	Quantum dot sensitized solar cell
OPV	Organic photo voltaics
PSC	Perovskite solar cell
AU	Astronomical unit
AM	Air mass
CdTe	Cadmium telluride
CdS	Cadmium sulfide
CIGS	Copper indium gallium selenide
TCO	Transparent conducting oxide
TCE	Transparent conducting electrode
TO	Tin oxide
ITO	Indium tin oxide
FTO	Fluorine doped tin oxide
ATO	Antimony doped tin oxide
BSO	Barium stannate
LBSO	Lanthanum doped barium stannate
ABSO	Antimony doped barium stannate
ETL	Electron transport layer
HTL	Hole transport layer
WE	Working electrode
CE	Counter electrode
LHE	Light harvesting efficiency
LUMO	Lowest unoccupied molecular orbital
HOMO	Highest occupied molecular orbital
IPCE	Incident photon conversion efficiency

RMS	Root mean square
BM-shift	Moss–Burstein shift
VBM	Valence band maximum
CBM	Conduction band minimum
FoM	Figure of merit
XRD	X-ray diffraction
SEM	Scanning electron microscope
FESEM	Field emission scanning electron microscope
TEM	Transmission electron microscope
HR-TEM	High resolution transmission electron microscope
SAED	Selected area electron diffraction
XPS	X-ray photoelectron spectroscopy
FTIR	Fourier transform infrared spectroscopy
PL	Photoluminescence
AFM	Atomic force microscopy
PVD	Physical vapor deposition
CVD	Chemical vapor deposition
PLD	Pulsed laser deposition
CA	Contact angle
JCPDS	Joint committee on powder diffraction standards
EDS	Energy dispersive X-ray spectroscopy
UV-Vis-NIR	Ultraviolet-visible-near infrared
OLED	Organic light emitting diode
EIS	Electrochemical impedance spectroscopy

List of Figures

List of Tables

Contents

CHAPTER: 1

Overview of solar energy and photovoltaics

1.1 Introduction to Renewable energy and its need

Today, our global society is galloping towards an acute energy crisis due to a shortage of fossil fuels from natural resources. Currently, the supply of energy sources widely relies on fossil fuels such as oil, coal, and natural gas which are depleting at a foreseeably rapid rate due to overuse [1]. Over the last two decades, a steep decline in fossil fuels as well as increasing environmental pollution due to the release of a large amount of various harmful pollutant gases such as SO_2 and CO_2, etc. as mentioned in Fig. 1.1 are the causes of the greenhouse effect. According to the USA energy information administration (EIA) 2019 reports, greenhouse gas emissions are equal to 6558 million metric tons[2]. Hence, non-renewable energy sources lead to severe environmental damage to the earth. To minimize these environmental issues, the search for alternative renewable energy sources has intensified. Renewable energy systems do not produce any air pollution or greenhouse gases. Using renewable energy (mainly solar energy) can have a positive effect on the environment when non-renewable energy is either replaced or supplemented or reduced by the use of other forms of renewable energy resources.

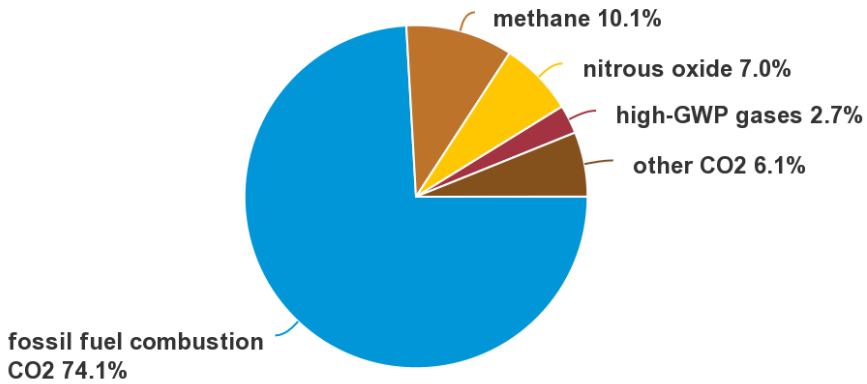

Fig. 1.1. Greenhouse gas emissions and their percentage as per EIA 2019 reports.

Due to the rapid depletion of non-renewable energy resources causing dramatically increasing concerns about environmental issues, researchers worldwide are motivated to focus on sustainable and renewable energy resources needed for future generations in a global society. Currently, renewable energy sources are one of the most important requirements for the advancement of technologies of modern society. The wise use of sustainable and renewable energy sources as an alternative to fossil fuels is of great importance to our society and also for the protection of our planet. To transcend these issues, alternative renewable energy sources are considered to be the need of the hour. There are several primary renewable means of energy such as solar, hydroelectricity, wind, tidal energy, etc. [3] that are depicted in Fig. 1.2. Among these, solar energy is the most abundant (~ 11%) and clean renewable energy source available to us[4].

A photovoltaic (PV) device can convert light energy from the Sun into electricity using the generated photoelectrons. In this regard, the Sun acts as a renewable and sustainable energy supply by providing an enormous, free, and inexhaustible energy source in the form of solar radiation. The total solar radiation per year is approximately 3×10^{24} J: and out of the 1.7×10^{5} terawatts (TW) solar energy which strikes on the surface of the earth, the overall annual solar energy received by the earth's atmosphere is 342 Wm^{-2}. Out of this, 30% of solar radiation is lost in the form of scattering or by reflection back to space. The remaining 70% (~ 239 Wm^{-2}) of solar radiation is used as an energy source for converting into electricity [5], which is significantly huge energy obtained in one hour compared to the energy requirement of the entire world for one year. The energy consumption in the world is reported to be 18 TW per year which is estimated to increase to 27.6 TW in 2050 [6]. Based on these statistics, world energy consumption is continuously increasing with the population growth day by day, and utilization of renewable technology such as solar energy provides a clear vision of opportunities to meet the global energy demands for the present and future needs.

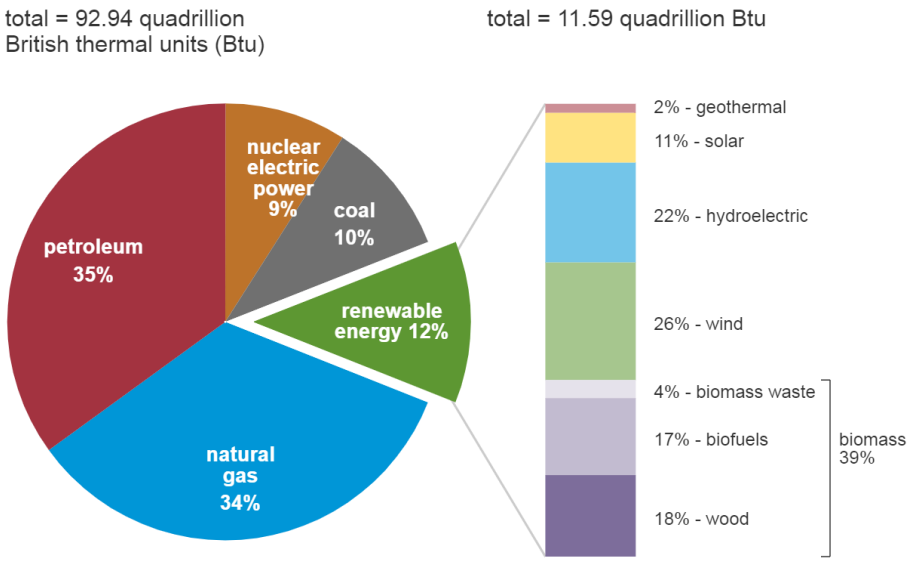

Fig. 1.2. Statistics of energy consumption from various sources in the U.S for the year 2020.

1.1.1 Background of photovoltaic technology

The mention of a photovoltaic cell can be traced back to nearly 150 years and was first introduced by French physicist Alexandre Edmond Becquerel in 1839 [7]. He observed that light incident on an electrode placed in an electrolyte solution resulted in a photo-voltage, and this phenomenon is called light energy conversion. Later, it was named as photovoltaic (PV) effect and this phenomenon could be understood more precisely based on the photoelectric effect which was theoretically explained by Albert Einstein in 1904. These photovoltaic devices were then assembled in Bell labs in 1954 with an efficiency of 4.5-6% (Si-based solar cell) [8].

Solar cells are divided into three generations. The first-generation solar cells are Silicon solar cells, second-generation solar cells are thin-film solar cells such as GaAs, CdTe, and $Cu(In,Ga)(S,Se)_2$ CIGS. The third-generation solar cells constitute dye sensitized solar cells (DSSCs), quantum dot sensitized solar cells (QDSSCs), organic photovoltaics (OPVs), and perovskite solar cells (PSCs). All generations of solar cells are individually explained in the sections below.

1.2 Overview of Solar Energy and Photovoltaic Technologies

1.2.1 Solar energy spectrum

The sun is a natural and perpetual energy source that emits electromagnetic radiation in the form of light. The main reason behind the sun's radiation is the occurrence of nuclear fusion reactions in its core [9]. The maximum temperature at the surface of the Sun is nearly 5778 K. Sunlight (Solar spectrum) consists of 50 % infrared, 40 % visible, and 10 % ultra violet radiation. The amount of energy released from the sun will be measured in terms of the solar constant. The solar constant is the amount of solar radiation received per unit area per unit time by a surface normal to the Sun's rays.

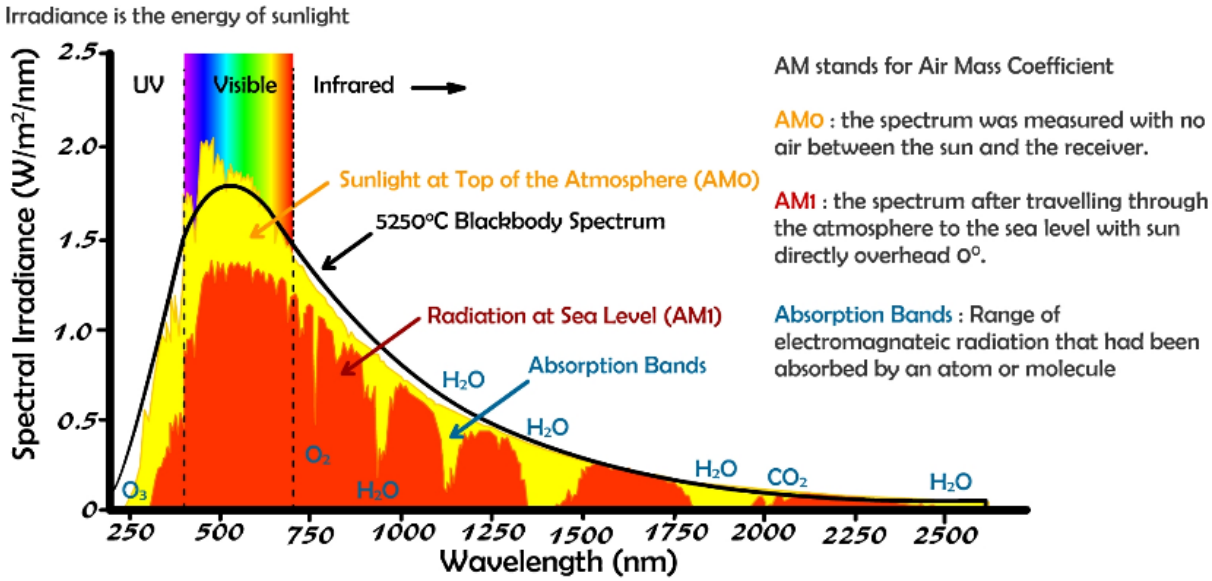

Fig. 1.3. Solar radiation spectrum spanning from UV to IR region.

The value of the solar constant is nearly equal to 1,353 W/m^2 in space at a distance of one astronomical unit (AU) from the sun, but in the case of the earth's surface, the light gets attenuated by the earth's atmosphere, thereby reducing the solar constant value to nearly 1,000 W/m^2 in clear atmospheric conditions when the sun is near the zenith. The light intensity and spectral distribution of the radiation arriving at the earth's surface depend on the composition

of the atmosphere, as well as the path length of the radiation traversing through the atmosphere. Air mass (AM) is described according to the path length through the atmosphere as shown in Fig. 1.3. The solar radiation spectrum shows the solar radiation outside the earth's atmosphere denoted by AM 0 and at sea level denoted by AM 1.5.

1.2.2 Air mass

The solar irradiance on the earth's surface is estimated by the sun's position (Zenith angle) and the distance of the atmospheric layer that absorbs the solar radiation. The loss of incident radiation in the atmosphere due to differences in solar zenith angle is called as air mass (AM) coefficient. Here, solar radiation depends on the location of the incident light, atmospheric conditions, time, and the distance between the earth and the sun. When sunlight enters the earth's atmosphere, it experiences phenomena such as absorption, reflection, refraction, and scattering due to which light gets distorted and its intensity decreases when it reaches the earth's surface. The coefficient AM is defined by the quotient of the optical path length L of solar radiation traversing through the earth's atmosphere and the path length L_0 at the zenith (eq. 1.1). This parameter can be described by the solar cell efficiency under normalized conditions. The solar cells are tested under the standard spectral distribution of the incident light at AM 1.5G as shown in Fig. 1.4. The air mass is expressed by the following equation,

$$AM = L/L_0 = 1/\cos \theta_Z \tag{1.1}$$

where θ_Z is the zenith angle.

1.2.3 Solar tracking

The concentrated solar thermal and solar photovoltaics have optics that directly receives the sunlight, and hence, the solar trackers should be angled precisely to gather the incident light energy. Every concentrated solar system has trackers; otherwise, they do not harvest energy

effectively unless directed properly towards the sun's motion. Single-axis solar trackers move on an axis back and forth in only one direction.

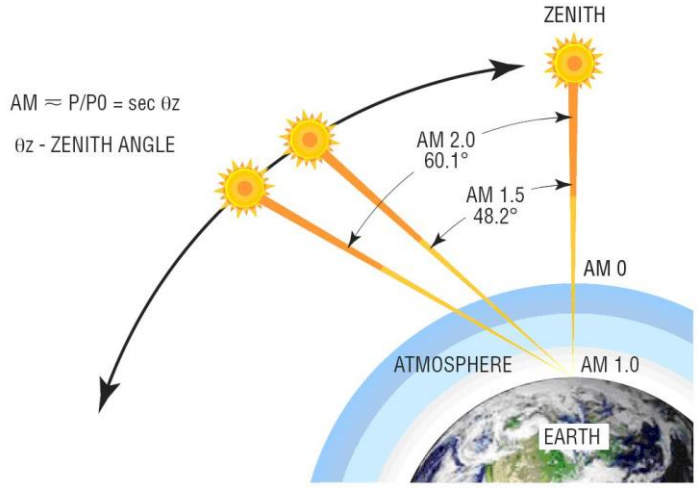

Fig. 1.4. The air mass coefficient dependency and the zenith angle.

Various types of solar trackers like vertical, tilted, polar aligned, and horizontal, move as implied by their names. In any solar application, the efficiency is improved when the modules are continually aligned to the optimum angle as the sun traverses the sky. Improved efficiency means improved yield, and the use of trackers can make a significant difference to the revenue generated from a large solar plant. This is the reason why solar trackers are widely used in utility-scale solar installations.

1.2.4 Generations of solar cells

The solar cell is a device that converts the incident light directly into usable electrical energy based on the photovoltaic effect, which involves both physical and chemical phenomena. In 1839, French physicist Alexandre Edmond Becquerel demonstrated the photovoltaic effect. The first solar cell device was made by Charles Frits (1883) with compounds of selenium. Later, Bell laboratories developed traditional silicon solar cells in 1954. Solar cells are classified into three generations based on their performance and design which are discussed in the following sections.

1.2.4.1 First generation solar cells

First-generation (1st) solar cells are traditional solar cells. These are made using crystalline silicon wafers. These cells are presently the commercially dominant technology and occupy more than 86% of the solar cell production. Based on the level of crystallinity of silicon (Si), the 1st generation solar cells are classified into mono-crystalline, multi-crystalline, amorphous, and hybrid 'Si' solar cells. The highest efficiency of single crystalline solar cells has reached nearly 27 % which is close to the Shockley-Queisser limit for 'Si' based devices (≅ 30 % under AM 1.5) [10]. They have a longer life than that of non-Si solar cells, and high power conversion efficiency compared to multi-crystalline solar cells. However, mono-crystalline solar cells have limited applications due to their complex manufacturing process and very high production cost. The 1st generation solar cells have dominant rooftop applications, and due to their high performance as well as high stability, these 1st generation silicon solar cells are industrialized worldwide to cater to applications in various fields. Owing to their performance and robustness, the 1st generation 'Si' solar cells are dominating the market. However, owing to their rigidity and requirement of stringent production protocols, they have limitations for novel flexible applications. Additionally, their special requirements such as high manufacturing cost, and environmental hazards involved during the processing of silicon lead to the demand for a better alternative. Hence, to supplement silicon-based PV technology, researchers have alternatively developed second-generation solar cells.

1.2.4.2 Second-generation solar cells

Second-generation (2nd) solar cells are based on thin-film technology which uses thin layers of semiconductor materials. These thin-film solar cells were introduced in 1970 [11]. Examples of 2nd generation solar cells are GaAs [12], cadmium telluride (CdTe)/cadmium sulphide (CdS) solar cells[13] and copper indium gallium selenide (CIGS) solar cells[14]. Thin

film technology is a relatively easy technology for designing solar cells due to consumption of very less material, cost effectiveness, and high efficiency compared to the 1st generation solar cells. These 2nd generation solar cells exhibit an efficiency of about 10-15 %[15][16]. The main advantage of these solar cells is the growth of thin films on bendable substrates that can be easily incorporated into the device architecture. Moreover, they can be used in several advanced applications like self-powered smart windows in cars/buildings, textile products, foldable devices, etc. The main drawbacks of the 2nd generation solar cells are the need to be grown in high vacuum conditions, high temperature treatments, the environmental toxicity of cadmium, as well as the rarity and high cost of indium. Hence, to overcome these limitations, third-generation (3rd) solar cells are developed by replacing CdTe and CIGS with facilely synthesized low-cost metal oxide semiconductors like TiO_2, ZnO, SnO_2, Nb_2O_5, etc.

1.2.4.3 Third-generation solar cells

The structure of the 3rd generation solar cells is very different from the commercially available 1st and 2nd generation solar cells since they use semiconductor nanomaterials as one of their main components. Several issues have been observed in 1st generation solar cells which are expensive and employ electronic grade silicon crystals at elevated temperatures for growth and processing of wafers, and technology incompatible with the environment. The 2nd generation solar cells are comparatively cheaper and present efficiency of only 10-15% which limits their marketing. To overcome these challenges, the 3rd generation solar cells are designed using organic and/or nanocrystalline materials. They are commercially not yet available and research on these solar cells is limited to laboratory scale and prototypes, and they still require elaborate exploration. The 3rd generation solar cells are mainly multi-junction or tandem solar cells, polymeric solar cells, dye-sensitized solar cells (DSSC)[17], quantum dot solar cells (QDSSCs)[18][19], organic solar cells (OSCs)[20] and perovskite solar cells (PSCs)[21]. Among these, multi-junction cells exhibit a maximum conversion efficiency of 40 %. Polymer-

based solar cells have several advantages such as cost effectiveness, light weight, and suitability for mass production technology. Hence, the 3rd generation solar cells have many possibilities, and scope for improvement in efficiency and development of cost-effective devices for widespread use, eventually leading to commercialization.

For the past two decades, research interest in DSSCs is enormous due to their cost effectiveness and facile fabrication procedures, environment-friendliness, and relatively low-cost production. The market has a high interest in 3rd generation systems mainly due to their applicability in portable devices like self-powered chargers, backpacks, key boards, etc. The DSSCs are suitable for roll-to-roll mass production technology on rigid or bendable substrates using polymers on a massive scale for the market. Fig. 1.5 shows the efficiency and cost per unit power of the 3rd generation cells. The aim of these PVs is to decrease the price below the $1/W level of the 2nd generation PVs to $0.50/W - $0.20/W or lower by considerably increasing their efficiencies, while retaining environmental and cost aspects of thin film technologies. To attain high efficiency, the Shockley-Queisser limit can be overcome using multiple energy thresholds and single bandgap devices. Increasing the efficiency strongly leverages lower costs because the area required for the desired power output is also reduced [22][23].

As per the US-EIA reports, the global DSSC market size was estimated at USD 90.5 million in 2019 and is expected to increase at a compound annual growth rate (CAGR) of 12.4% from the year 2020 to 2027 as shown in Fig. 1.6. The motive of DSSC technology is expected to address three main energy needs of the future, namely economic growth, energy security, and environmental safety. The highest efficiencies for various solar harvesting technologies across the globe are shown in Fig. 1.7.

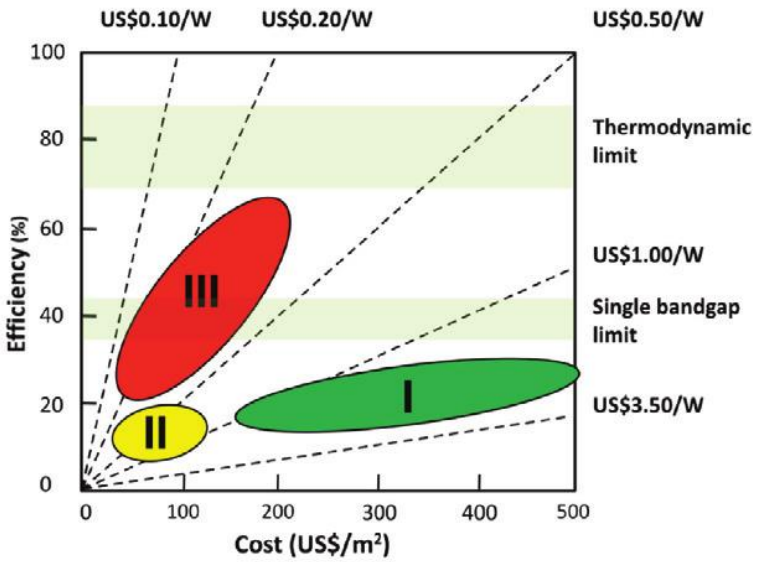

Fig. 1.5. Efficiency and cost for 1st, 2nd and 3rd generation photovoltaic technologies [22].

The DSSC market is confined only to portable and disposable electronics, and it will take a huge leap in many other sectors. The dye-sensitized solar cell market is forecasted to grow by over $130 million by the year 2023. DSSCs are widely used in flexible optoelectronics, portable electronics, and solar jackets. The flexible DSSC can be utilized for decoration in colored smart windows to generate electricity due to its flexibility, variety of colors, and shapes. The high degree of transparency, lightweight, and plausibility for flexible devices make it suitable for designing self-powered integrated windows, walls, and roofs in buildings.

1.3 Dye-sensitized solar cells

1.3.1 A Brief history of DSSCs

Solar energy can be harnessed via different routes, and for the last three decades, photovoltaic cells or solar cells have been developed to minimize the production cost and enhance device efficiency and stability. The DSSCs constitute a sub-category of these PV devices and have generated much interest due to steady improvements in their efficiency and stability. In 1870, Vogel et al. first developed the idea of DSSC, and they demonstrated that silver halide emulsions may be sensitized by adding a dye that extended the photoactivity to longer

wavelengths[24]. After several years, James Moser invented the idea of dye enhancement in applications ranging from photography to photoelectrochemical devices using the dye erythrosine on silver halide electrodes[25]. The same concept was implemented by Hishiki and Gerischer by introducing ZnO and dyes like rose Bengal and cyanine[26][27].

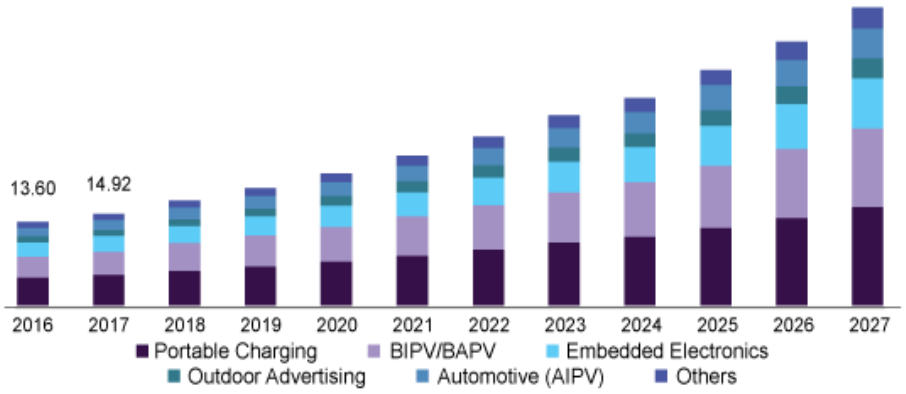

Fig. 1.6. Growth rate of various market sectors implementation in the U.S for DSSC based device applications predicted for the period 2016-2027 (USD in Millions) [US-EIA reports-2020].

Daltrozzo and Tributsch introduced Rhodamine B as a new dye into the ZnO system, and subsequently, they observed electron transport to be the dominant mechanism for both photographic and photo-electrochemical sensitization phenomena[28]. In 1977, Spitler and Calvin replaced ZnO with TiO_2 in the cells and were able to elucidate the results of current density which was reported to depend on two factors of the dye, namely, the quantity of dye adsorbed on the TiO_2 surface and the pH of the dye solution [29]. From the late 1980s to the 1990s, new research appeared in the field of solar cells initiated by Grätzel and his co-workers, reporting the use of synthetic dye series in the TiO_2 system. The DSSC first designed by O'Regan and Gratzel in 1991 achieved 7.1 % energy conversion efficiency using TiO_2 as a photoanode and ruthenium based synthetic dye. These solar cells were called Grätzel solar cells in honor of the inventor[30] [17]. Later in 2014, researchers improved the device efficiency of these synthetic dye-based solar cells from 7.1 % to 13% using porphyrin [17][31]. DSSCs are

much easier to fabricate and are insensitive to environmental contaminants. They are also processable under ambient atmospheric conditions. Recently, the efficiency of DSSCs was enhanced to values exceeding 14% using Triarylamine (TAA) based dyes as sensitizers [32].

1.3.2 Device structure of DSSC

The schematic of the basic device structure of nanocrystalline-TiO_2-based DSSC is shown in Fig. 1.8. The DSSC device mainly consists of five components; (i) transparent conducting oxide (TCO) electrode which is generally fluorine (F) doped tin oxide (FTO) glass substrate, (ii) Nano crystalline wide bandgap semiconductor electron transporting layer (ETL) coated onto FTO which serves as working electrode (WE), (iii) a dye as photosensitizer anchored onto the surface of TiO_2 nanoparticles, (iv) redox mediator containing iodine/triiodide (I_3^-/I^-) redox couple as electrolyte and (v) platinum (Pt) coated FTO glass substrate as a counter electrode (CE).

The working electrode plays an important role in the functioning of DSSC for light absorption. It is made up of TiO_2 nanoparticles (10-20 nm) coated onto the FTO glass substrate. The TiO_2 porous nanocrystalline particle-coated FTO glass substrates are then immersed in a dye solution for a particular duration to facilitate dye absorption onto the surface of the TiO_2 particles. Here, the TiO_2 surface anchored with the photosensitizer dye plays an important role in the generation of photo-excited electrons which are injected into the conduction band of the TiO_2 layer, leading to better functioning of the DSSC. The platinum-coated FTO glass substrate acts as a cathode in the DSSC and is referred to as a counter electrode. Usually, the electrolyte solution containing an I_3^-/I^- redox couple acts as a mediator between the two electrodes and is responsible for the dye regeneration.

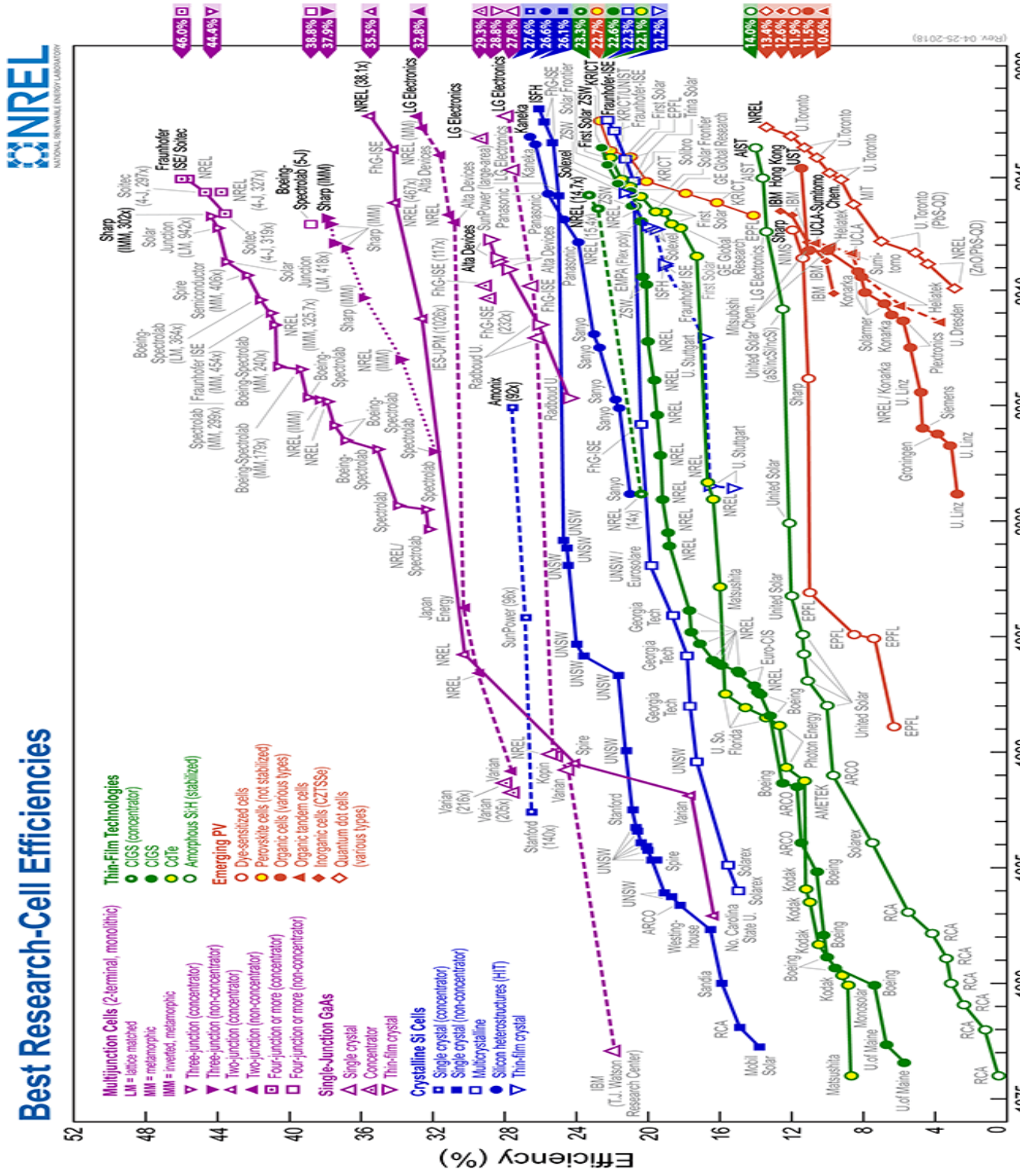

Fig. 1.7. The chart showing various photovoltaic technologies around the globe and their best efficiencies from 1975 to 2020 [National renewable energy laboratory (NREL), USA].

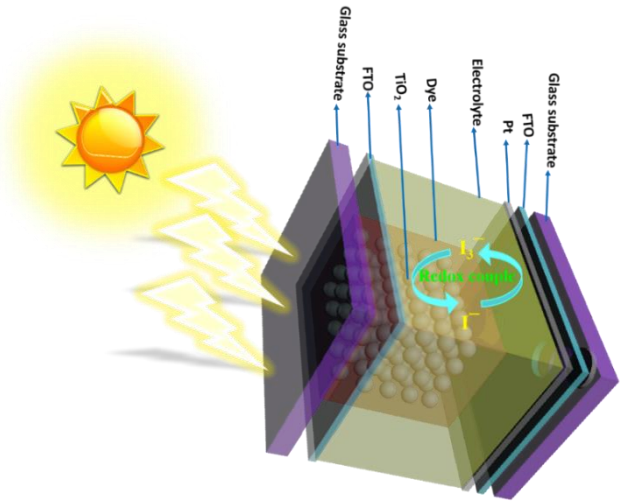

Fig. 1.8. Schematic representation of the basic DSSC device structure with its components.

1.3.3 Working principle of the DSSC

The DSSC device has multi-components as shown in Fig. 1.8. The working principle of DSSC involves multistep processes as represented in Fig. 1.9. When sunlight illuminates the working electrode side, the dye adsorbed TiO_2 photoanode generates photocurrent in the circuit which is described using different steps as follows:

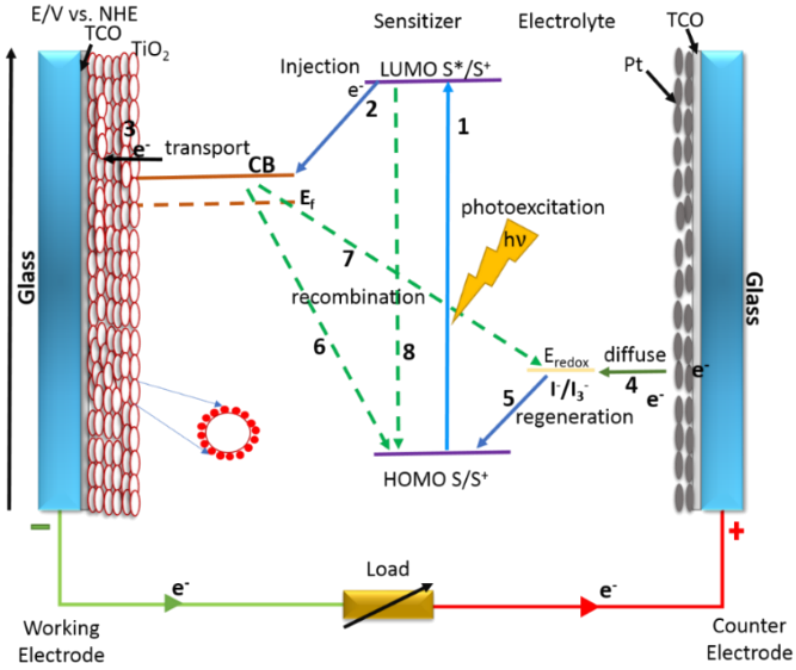

Fig. 1.9. Working principle of the DSSC device.

(1) The dye-photosensitizer (S) absorbs a photon that promotes electrons, leading to the excited state (S*) (eq. 1.2).

(2) The excited electrons are then injected from the excited sensitizer into the conduction band of the semiconducting nanoparticles according to eq. 1.3.

(3) The injected electrons percolate through the mesoporous semiconductor TiO_2 nanoparticles and are collected at the counter electrode, and subsequently transported to the external circuit.

(4) Through the external circuit, the electrons reach the counter-electrode and interact with the redox mediator, turning it to its reduced form.

(5) The resulting oxidized dye is eventually restored to the initial neutral state of the redox mediator by receiving electrons from the iodide (I^-) ions in the redox mediator, generating I_3^-, and this process is represented in eq. 1.4 which is known as the dye regeneration process.

In order to complete the circuit at the counter electrode side, electrons are donated to I_3^- and it regenerates into I^- as indicated by eq. 1.5.

$$S + hv \rightarrow S^* \quad \textit{(Light absorption)} \tag{1.2}$$

$$S^* \rightarrow S^+ + e^- \quad \textit{(Electron injection)} \tag{1.3}$$

$$2S^+ \textit{ (on } TiO_2\textit{)} + 3I^- \rightarrow 2S \textit{ (on } TiO_2\textit{)} + I_3^- \tag{1.4}$$

$$I_3^- + 2e^- \textit{ (Pt)} \rightarrow 3I^- \quad \textit{(Redox mediator reduction)} \tag{1.5}$$

$$S^+ \textit{ (on } TiO_2\textit{)} + (TiO_2) \rightarrow e^- \textit{ (on } TiO_2\textit{)} \tag{1.6}$$

$$I_3^- + 2e^- (TiO_2) \rightarrow 3I^- \tag{1.7}$$

$$S^* \rightarrow S \textit{ (On } TiO_2\textit{)} \tag{1.8}$$

(6) However, when the solar cell is functioning (i.e., during the electron flow cycle), undesirable side processes such as the recombination of injected carriers either with the oxidized dye or with I_3^- at the TiO_2 surface simultaneously take place as per eq. 1.6 and eq. 1.7, respectively.

(7) Non-radiation relaxation of photo-excited dye deteriorating the DSSC device performance is represented by eq. 1.8.

Finally, the overall performance of DSSC can be measured based on sunlight-to-electric power conversion efficiency (η).

$$\eta = \frac{V_{OC} J_{SC} FF}{P_{in}} \times 100\% \qquad (1.9)$$

where V_{OC} is the open-circuit voltage, J_{SC} is the photocurrent density, FF is the fill factor and P_{in} is the power of incident photons.

The open-circuit voltage (V_{OC}) is measured from the potential difference between the fermi-level of the electrons in the semiconducting layer and the redox potential of the electrolyte. Similarly, the short circuit current density (J_{SC}), based on the incident light harvesting efficiency (LHE), is determined from the carrier injection and extraction efficiencies. The fill factor is calculated as the highest power output divided by the product of J_{SC} and V_{OC}. The overall conversion efficiency of a DSSC is tested under standard irradiation conditions (100 mW/cm^2, AM 1.5).

1.4 Components of DSSC

The DSSCs containing several components have scope for exploration by altering the dye/photoanode/electrolyte/counter-electrode combinations. It is quite challenging to fine-tune the properties of each component in a DSSC towards ideal conditions to increase the overall performance of the assembled device. The issues with PV stability and performance are the

main shortcomings in the commercialization of DSSCs. Hence, research is focused on the development of alternative components for more stable, flexible, environment-resistant, cost-effective, and highly efficient DSSCs. Intense exploration is ongoing for the development of alternative components to identify promising semiconducting photoanode materials, dyes, electrolytes, counter electrodes as well as their integration to improve the photovoltaic performance and durability of the assembled DSSCs.

1.4.1 Semiconductor photoanode

In general, the photoanode is a few micron (10-20 μm) thick film with a mesoporous layer consisting of arrays of semiconductor nanoparticles of size ranging between 10-20 nm with high surface area for efficient dye absorption. The highly porous feature is effective for mass transport through diffusion. Bandgap alignment with the sensitizer helps effective electron injection and rapid charge transport with high mobility. Here, the electronic properties are mostly dependent on the bandgap of the semiconductor nanoparticles which influences the electron transfer and performance of the device. Moreover, the electron transport rate in the semiconductor film is mostly influenced by the crystallinity, morphology, and surface area of the material. All these factors with combined improvements contribute to a higher charge collection efficiency[33][34]. In DSSCs, several wide bandgap metal oxide semiconductors like TiO_2 [35], ZnO [36], SnO_2 [37], niobium oxide (Nb_2O_5) [38][39] and zinc stannate (Zn_2SnO_4)[40] have been used as photoanode materials. Among them, TiO_2 is a stable photoelectrode material with good electrochemical properties, abundance, excellent dye loading, high chemical stability, non-toxicity, mesoporous nature, wide bandgap, and high surface area. The TiO_2 nanoparticles-based photoanode gives a higher efficiency compared to that of ZnO, SnO_2, and Nb_2O_5 semiconducting oxides [35][37][38]. In 1991, Grätzel and his co-workers confirmed that TiO_2 is an ideal semiconductor for DSSC applications [17].

The composition of metal oxide semiconductors, bandgap, morphology, and thickness of the semiconducting layer influence the charge gathering, electron transport, and light-harvesting aspects. In DSSCs, an effective electron transport layer should have a high surface area to enhance dye adsorption for efficient photon-harvesting, and it should be transparent to visible light, thereby reducing the loss of incident photons [41][42]. The conduction band energy should be lower than the lowest unoccupied molecular orbital (LUMO) level of the dye for sufficient injection of photo-excited electrons. High mobility is preferred to reduce the electron recombination rate in the redox electrolyte system. In addition, semiconducting materials containing hydroxyl groups are beneficial for the effective attachment of dye onto their surface [43][44].

1.4.2 Photosensitizer

The dye (Photosensitizer) has a crucial role in absorbing and converting Sun's energy into electrical energy. In DSSC, the photosensitizer is chemically attached to the surface of semiconductor nanoparticles. Here, the photosensitizer acts as an electron pump by absorbing the solar radiation (visible region) and pumping electrons from the excited dye molecule into the conduction band of the semiconductor. The dye molecules regenerate the electron from the electrolyte (charge mediator) and this cycle is repeated [17]. To fulfill such needs, the dye must have the following aspects:

1) An efficient photosensitizer should absorb a wide range of wavelengths from visible to near IR-region of the solar spectrum.
2) It should adsorb or be anchored strongly on the surface of the semiconductor nanoparticles.
3) It should possess a high molar extinction coefficient (ε, M^{-1}, cm^{-1}) to enable efficient light harvesting.

4) The lowest unoccupied molecular orbital (LUMO) [45] level of the dye must remain higher than the conduction band edge of the semiconductor while the highest occupied molecular orbital (HOMO) [45] level of the dye should be lower than the energy level of the redox mediator to permit efficient regeneration of the oxidized dye [46][47] (see Fig. 1.9).
5) The performance of DSSCs also depends on the molecular structure of the synthetic photosensitizer [48].
6) Photosensitizers are preferred to have enough stability for carrying out several cycles of power conversion and performance for many years without any significant degradation[34].

The sensitizing dyes are categorized into three groups, depending on their compositions:

1) Metal complex sensitizers using metals such as ruthenium [49], Osmium [50], cobalt [51], iron [52], copper [53] and rhenium [54].
2) Metal-free organic sensitizers such as coumarin [55], triarylamine [56], indoline [57], etc.
3) Natural dyes such as Chlorophylls [58], Flavonoids [59] and betalains [60].

1.4.2.1 Metal-based complex sensitizers

Metal complex-based dyes are composed of chromophores of Ruthenium complex and are frequently used because they are the most effective photo sensitizers having both anchoring and ancillary ligands. The capability of dye absorption onto TiO_2 depends on the anchoring ligands, and at the same time, ancillary ligands make up for the overall properties of the sensitizer. By modifying these two ligands, one can improve the efficiency of solar cells [34]. The history of these complexes dates back to the 1970s when tris(2,2'-bipyridyl)Ru(II) was investigated as a redox sensitizer [61]. Since 1993, N3 dye (cis-RuL2-$(NCS)_2$) is the standard compared to other Ru(II) complexes for efficient charge transfer. Nazeeruddin and his co-workers proposed several superior Ruthenium dye-based complexes as charge-transfer sensitizers on TiO_2 nanoparticles. Using these Ruthenium dye complexes, they reported that

the conversion efficiency of solar energy to electricity is ≅ 11% under simulated AM 1.5 conditions [62]. The metal complex dyes are effective sensitizers due to their high efficiency, excellent chemical stability, favorable photoelectrochemical properties, and strong absorption over the range of visible spectrum [63][64].

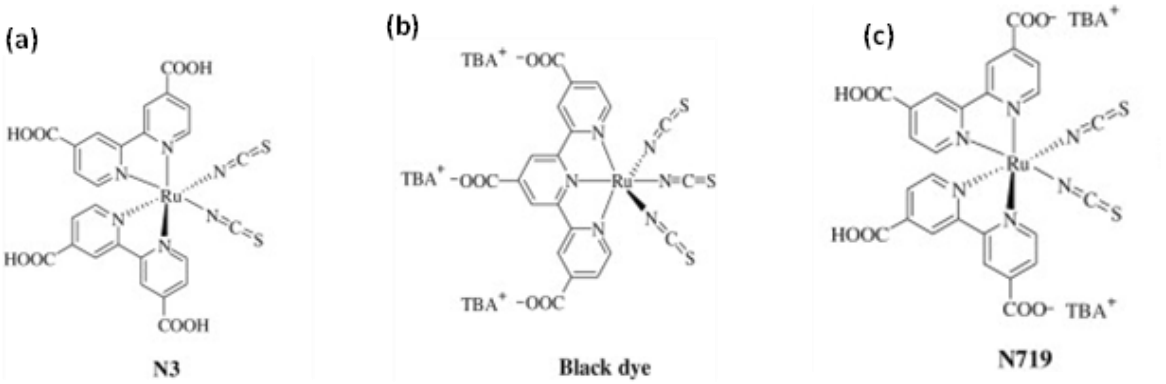

Fig. 1.10 General molecular structures of Ru-based N3, N749 (Black dye) and N719 dyes.

Table 1.1 Photovoltaic performances (at 1 sun irradiation) of the most popular dyes based on ruthenium(II)-complex photosensitizers

Dye	J_{sc} (mA cm^{-2})	V_{oc} (V)	FF	η (%)	Reference
N3	18.20	0.720	73	10	[65]
N749	20.53	0.720	70	10.4	[49]
N719	17.73	0.846	75	11.2	[66]
Ru(dcphn)$_2$(SCN)$_2$	12.50	0.740	71	6.6	[67]
N945	19.0	0.728	71	10.8	[68]
C101 R=C$_6$H$_{13}$	17.94	0.778	79	11.0	[69]
C106 R = –S–C$_6$H$_{13}$	18.28	0.749	77	11.3	[70]
K19	14.61	0.711	67	7.0	[71]
Z910	17.20	0.777	76	10.2	[72]
YE05	17.0	0.800	74	10.1	[73]
DX1	21.4	0.664	70	10	[74]

The same group has developed two other dyes, namely tris(isothiocyanato)-2,20, 2”-terpyridyl-4,40, 4”-tricarboxylate)Ru(II) complex, that is denoted as N749 (Fig.1.10b) [65][49][75] and Di-tetrabutylammonium cis-bis(isothiocyanato)bis(2,2’-bipyridyl-4,4’-dicarboxylato ruthenium(II), called as N719 dye (Fig.1.10c) [76]. Currently, these three are the most efficient ruthenium-based organometallic sensitizers that are used in DSSCs, which have shown a power conversion efficiency of close to 12%. Fig. 1.10 shows the molecular structures of N3, N719, and N749 dyes. Even though the ruthenium (II) based sensitizers show relatively higher efficiency and stability, there are many drawbacks associated with these dyes, for example; the ruthenium complex contains an expensive heavy metal and is also harmful to the environment. Moreover, its production cost is high due to the complexity of the synthesis process, and it also tends to deteriorate in the presence of water [77][78].

1.4.2.2 Metal free-organic sensitizers

Metal-free organic sensitizers gained interest since the year 2000. Currently, metal-free organic sensitizer-based DSSCs have improved the electrical conversion efficiency from 4% to 9%. The main advantages of these sensitizers are cost-effectiveness, ease of synthesis process, structural simplicity, tunability, environment-friendliness, and higher absorption coefficient compared to the ruthenium complex-based sensitizers. However, compared to metal-based sensitizers, the efficiency is low for metal-free organic sensitizers.

Generally, the design of metal-free organic sensitizers has a donor and acceptor incorporated π-conjugated bridge (D-π-A) as shown in Fig. 1.11. The characteristics of a metal-free organic sensitizer are dependent on the carrier donating/accepting ability and the electronic properties of the π bridge [79]. Presently, most of the organic sensitizers are π- bridge conjugated based dyes like oligothiophene, coumarin, phenoxazine, fluorine, and oligoene. In the case of organic sensitizers, the donor is synthesized with dialkyl amine and the acceptor is synthesized with

carboxylic acid and cyanoacrylic acid [79][80] . Fig. 1.11 shows a sensitizer anchored onto TiO_2 nanoparticles through the acceptor part of the dye molecule. Recently, a DSSC fabricated using porphyrin dyes having donor-π-bridge-acceptor structure has shown a conversion efficiency of 13% with $[Co(bpy)_3]^{2+/3+}$ redox couple under simulated 1.5 AM solar illumination[31]. However, the metal-free organic dyes also have some drawbacks like low absorption bands compared to the metal-based sensitizers, leading to a reduction in photon harvesting ability. The other disadvantages include significant low stability, tedious purification steps, and toxicity of the dyes or their by-products which act as pollutants [80]. The natural dyes are discussed later in detail under section 1.5.4.

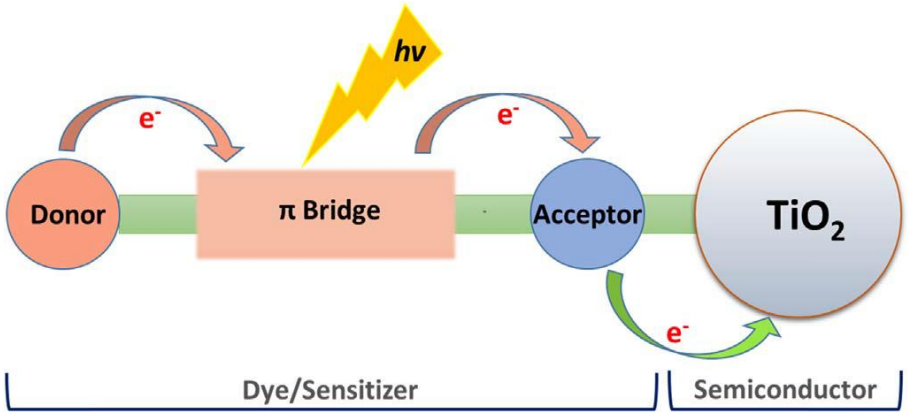

Fig. 1.11. Design of metal-free organic dye sensitizer showing the donor-π-bridge-acceptor structure.

1.4.3 Electrolyte

Generally, the electrolyte plays an essential role in a DSSC for the regeneration of the dye after injection of a carrier into the TiO_2 band. Simultaneously, the electrolyte works as a conducting medium that transports the electronic charge between the working and counter electrodes. The properties of the electrolyte are extremely important for maintaining the long-term stability of DSSCs. Electrolytes should have high ionic conductivity, good interfacial contact with semiconductor nanoparticles, transparency to visible light, non-corrosiveness to the counter electrode, and should not affect the stability of dye molecule upon contact. In

DSSCs, electrolytes are classified into three types, namely liquid electrolyte, solid-state electrolyte, and quasi-solid electrolyte [81][82], and are discussed in the following sections.

1.4.3.1 Liquid electrolytes

Liquid electrolytes are generally sub-classified into two types, depending on their composition as organic electrolyte and ionic liquid electrolyte. Usually, the organic electrolyte consists of a redox couple, solvent, and additives. As demonstrated over several years, iodine-triiodide (I^-/I_3^-) redox couple has been recognized as the most popular electrolyte due to its high solubility, rapid dye regeneration process, low light absorption in the visible region, appropriate redox potential, and very slow recombination rate between the injected electrons into TiO_2 band and triiodide (I_3^-) [83]. However, few undesirable intrinsic properties also exist for liquid electrolytes, such as absorption of a specific wavelength (430 nm) in the visible region, corrosion of noble metals on the counter electrodes (Pt, Au), and an upper limit on open-circuit voltage (V_{OC}) of 0.9 V. These factors significantly limit the further improvement of a DSSC using liquid electrolyte system. However, there are several alternative redox couples such as Br^-/ Br_3^-, $SCN^-/(SCN)_2$, $SeCN^-/(SeCN)_2$, etc. that have been used as a supplement [84][85]. The next type is the ionic electrolyte which contains cations with a group of organic salts (e.g., pyridinium, imidazolium) and anions from halides or pseudo-halide family [34][86][87]. The main advantages of these are high ionic conductivity, higher chemical and thermal stability, and minimal vapor pressure which are beneficial for high-efficiency DSSCs. The main drawback of liquid electrolytes is the evaporation of volatile iodine ions that decreases the charge carrier concentration and creates sealing problems, leading to degradation of cell performance and long-term stability issues [34]. Therefore, efforts have been directed towards development of an alternative solid-state electrolyte.

1.4.3.2 Solid-state electrolyte

The stability of a DSSC is influenced by electrolyte volatility and leakage of liquid electrolytes. To minimize these drawbacks, solid-state electrolytes can be optimized for further research and commercialization. Several inorganic electrolytes are investigated with p-type materials such as CuI, CuBr, CuSCN and organic polymers; for example; PEDOT (poly (3, 4-ethylene dioxythiophene), spiro-MeOTAD (2, 20, 7, 70-tetrakis (N, N-di- 4-methoxyphenylamino)-9,90-spirobifluorene), and P3HT (poly(3-hexylthiophene)) have been successfully used in solid-state DSSCs (SS-DSSC) [88][89]. In SS-DSSCs, a higher charge recombination rate is observed due to poor electrical contact between the photoanode and HTM, which is the main factor leading to low efficiency (~3.8%) of DSSCs using solid-state electrolytes [90][85].

1.4.3.3 Quasi solid-state electrolytes

A quasi solid-state electrolyte is a blend of polymer and a liquid electrolyte that can easily establish good contact with the photoanode. Polymer electrolytes such as poly(ethylene oxide), poly(vinylidine fluoride), and polyvinyl acetates contain redox couples that are generally employed as quasi solid-state electrolytes to minimize volatilization and leakage issues of liquid electrolytes [92][90]. Interestingly, quasi solid-state electrolytes have better stability, good electrical conductivity, and better interfacial contact compared to other types of electrolytes. However, these electrolytes have a specific disadvantage since they highly depend on the service temperature of the device, and high temperature causes phase changes from a gel state to a solution state [93][94].

1.4.4 Counter electrodes

To obtain fast reaction kinetics for the redox couple, the electro-catalytic reduction reaction at the counter electrode side is very important to result in good performance of the DSSCs. The role of the redox couple is to act as a mediator for the regeneration of dye molecules[95]. The dye molecules are regenerated into triiodide and reduced to iodine ions at the counter electrode side. Hence, the counter electrode should be a good conductor and must possess a lower voltage for the reduction of the redox mediator [96]. Moreover, the counter electrode materials should have high exchange current densities and minimal charge transfer resistance. Usually, the counter electrode is deposited with a 'Pt' catalyst onto the conductive FTO substrate for efficient transfer of electrons from the external circuit back to the electrolyte, and reduce oxidation from the redox couple to carry the photocurrent of a DSSC [48][97]. To date, platinum (Pt) is the standard photo catalyst for the counter electrode because it has very good catalytic activity and stability for I_3^- reduction in electrolytes [98][48]. The thickness of the Pt counter electrode is ≅ 200 nm and it can be deposited by various methods such as sputtering, spray pyrolysis, electrodeposition, and vapor deposition of H_2PtCl_6 solution onto TCO substrates [99][100][101]. The Pt electrode has higher conductivity, stability, and catalytic activity. However, Pt is scarce, and hence, its cost is high due to which it is not suitable for large-scale commercial production of DSSCs, and it also has durability issues [102]. Therefore, stabilization of carbon nanotubes, graphene, conductive polymers, etc. which are alternatives to Pt has been given importance by researchers [103][104]. Hsu et al. found that CoS is a cost-effective alternative material to supplement Pt-based electrode for DSSC applications. The roughness factor and high surface area of CoS make it an efficient material to supplement Pt-based DSSCs. A highly efficient CoS cathode material which yields a power conversion efficiency of ≅ 8.1 % has been reported in literature [105].

1.5 Alternative materials for DSSCs

In this thesis work, the focus is on the stabilization of alternative photoanodes by exploring suitable ETL materials, TCO substrates, and natural dye extracts for DSSC applications. In DSSCs, the semiconductor nanoparticle layer leads the main role in the functioning of the device. For the last two decades, several materials have been tested as photoanodes in DSSCs; for example, binary (TiO_2, SnO_2, ZnO, and Nb_2O_5, etc.) and ternary metal oxides (Zn_2SnO_4, $BaTiO_3$, $CdSnO_3$, $BaSnO_3$, SrTiO3, etc.) have been investigated extensively.

1.5.1 Binary oxide photoanodes

In DSSCs, several binary metal oxides like TiO_2[17], ZnO[106], SnO_2[107], and Nb_2O_5[108] have been tested as ETLs. These binary oxides have an energy bandgap varying between 3 eV and 3.2 eV. The most commonly used wide bandgap semiconductor as photoanode material in DSSCs is mesoporous TiO_2 (3.2 eV) due to its excellent properties like high conduction band edge, surface area, electron affinity, and dye adhering aspects. With these properties, TiO_2 nanoparticles exhibit the highest efficiency of 13% among all the materials that are investigated [31]. Moreover, TiO_2 is a cost-effective, non-toxic, bio-compatible material with good stability. ZnO is another wide bandgap semiconductor considered as photoanode in DSSCs due to similar bandgap value and work function as that of TiO_2. ZnO has higher carrier mobility (1-5 $cm^2\ V^{-1}\ s^{-1}$) [109] compared to that of TiO_2 (0.1–1 $cm^2\ V^{-1}\ s^{-1}$) [110] [111]. Maximum efficiency of 7.5% has been achieved for ZnO nanoparticle aggregates [112]. Niobium pentoxide (Nb_2O_5) is an n-type material with a bandgap value between 3.2 eV and 4.0 eV, and it has so far shown an efficiency of 6% when used in the form of nanorods [108]. The photovoltaic performance of selected binary oxides is shown in Table 1.2.

Tin oxide (SnO_2) shows properties suitable for use in DSSC as photoanode and it has higher electron mobility (100-200 $cm^2 V^{-1} s^{-1}$) [113] and a larger energy bandgap (3.8 eV) than that of TiO_2. SnO_2 also shows transparency greater than 80% in the visible region. The highest conversion efficiency of 6.8% for the hierarchical SnO_2 octahedra photoanode has been reported [107]. Few other nano dimensional binary metal oxides like Al_2O_3, V_2O_5, ZrO_2, and Fe_2O_3 are also used as photoanodes in DSSCs [114][115]. In comparison to simple binary oxides, multi-cation ternary oxides present additional possibilities to modify the material's physico-chemical properties by tuning the composition and nano-dimensional features like size, porosity, etc.

Table 1.2 Photovoltaic parameters of various dye sensitized binary photoanode materials

Photoanode	**Dye**	**J_{SC} ($mAcm^{-2}$)**	**V_{OC} (V)**	**FF**	**η (%)**	**Ref. No**
TiO_2 nanoparticles	N3	17.77	0.79	0.748	10.6	[95]
TiO_2 nanoparticles	ADEKA-1 + LEG4	18.36	1.01	0.77	14.3*	[116]*
TiO_2 nanoparticles	SM 315	18.1	0.91	0.78	13	[31]
TiO_2 nanorods	N719	16.52	0.772	0.746	9.5	[117]
TiO_2 nanochains	N719	15.95	0.75	0.61	7.46	[118]
ZnO nanoparticles	N719	18.11	0.62	0.585	6.58	[119]
ZnO nanowires	SK1	12.04	0.71	0.64	5.7	[120]
ZnO hierarchical aggregates	N719	19.8	0.64	0.59	7.5	[106]
ZnO nanorods	N719	10.7	0.71	0.62	4.7	[121]
Nb_2O_5 nanorods	N719	11.2	0.74	0.66	6.03	[122]
Nb_2O_5 nanopores	N3	10	0.7	0.58	4.1	[123]
Nb_2O_5 nanochannels	N3	17.6	0.639	0.39	4.48	[124]
* Champion efficiency						

1.5.2 Ternary oxide photoanodes

There is enormous scope to introduce various types of oxides as photoanodes in DSSC. One can modify the composition or employ doping and study the physical, chemical, and optical properties of complex ternary oxide systems. Generally, alkaline earth stannates $ASnO_3$ (A = Zn, Ca, Sr, and Ba, etc.,) are the most frequently explored materials, mainly due to the ease of tuning their electronic properties by substitution of donor/acceptor cation (sometimes anion). These ternary oxides are also quite stable at high temperatures (around 1000 ˚C). To overcome certain limitations (low electron transport and diminished lifetime) of binary oxides [125], efforts have been made to replace/supplement the binary oxides with ternary oxides such as Zn_2SnO_4, $SrTiO_3$, $BaTiO_3$, $BaSnO_3$, $CdSnO_3$, and $BiFeO_3$ for fabrication of photoanodes in the recent years [126][127][128][129][130] and the efficiencies are shown in table 1.3.

Table 1.3. Photovoltaic parameters of various ternary photoanode materials

S.No	Photoanodes	V_{OC} (V)	J_{SC} (mA/cm^2)	FF	Efficiency (%)	Ref.
1.	Zn_2SnO_4	0.63	9.1	0.65	3.7	[126]
2.	$SrTiO_3$	0.78	3.0	0.70	1.8	[129]
3.	$BaTiO_3$	0.53	10.65	0.33	1.93	[129]
4.	$CdSnO_3$	0.43	7.43	0.45	1.42	[128]
5.	$BiFeO_3$	0.75	7.0	0.58	3.02	[130]
6.	$BaSnO_3$	0.78	16.68	0.44	5.68	[131]

Among these, Zn_2SnO_4, $SrTiO_3$, and $BaSnO_3$ are the widely studied photoanode materials. One of the many advantages of these ternary oxides is the viability to easily modify their energy bandgap, work function, and electrical properties by changing the dopant element and its concentration. Due to the availability of a large range of multi-cation oxides and the feasibility of tuning them, it is exciting to explore their applicability in DSSCs. Strontium titanium oxide ($SrTiO_3$) has a similar band-gap and structure as that of TiO_2 (3.2 eV), but its conduction band

(CB) is positioned at a relatively higher level than that of TiO_2, causing a higher open-circuit voltage (V_{OC}) and a fairly low conversion efficiency due to the specific surface area of the material [132].

1.5.2.1 Zinc stannate

Zinc stannate (Zn_2SnO_4) is a direct wide bandgap material with values between 3.3 eV and 3.8 eV which makes it appealing for DSSC applications. It has an inverse spinel structure of octahedrally coordinated Sn^{4+} atoms. In this material, half of the Zn^{2+} atoms in the structure of Zn_2SnO_4 are in the tetrahedral site, while other half are in the octahedral site. It can improve the efficiency depending on the orientations of ZnO and SnO_2 sub lattice in the Zn_2SnO_4 structure [126]. The position of its conduction band is slightly higher than that of anatase TiO_2, and this metal oxide has a significantly better conduction property compared to TiO_2. Another advantage of Zn_2SnO_4 is its stability and higher corrosion resistance compared to ZnO due to its larger pH stability range [133]. The studies have shown that Zn_2SnO_4 based photoanode materials tolerate the stability problems associated with ZnO ETL against acidic dyes [126]. In this sense, the ternary Zn_2SnO_4 is more attractive than its binary oxide compounds such as SnO_2 and ZnO. Among these ternary oxide materials, the recently reported $BaSnO_3$ perovskite material has shown promising photoanode properties for use in DSSC and is explored and discussed in sufficient detail in the following sections of this thesis.

1.5.2.2 Barium stannate

Barium stannate ($BaSnO_3$) belongs to the family of alkaline earth stannates, and is an important n-type semiconductor with a perovskite structure (energy bandgap $\cong$ 3.2 eV) exhibiting higher electron mobility (~320 $cm^2\ V^{-1}\ s^{-1}$) facilitating fast diffusion of electrons in the conduction band. This compound has stability up to 1000 °C and rapid dye adsorption ability than that of the binary oxides [134][135]. The pure $BaSnO_3$ crystal system has an ideal cubic perovskite

structure with a space group of *Pm3̄m*. In perovskite structure, the Sn^{4+} and Ba^{2+} cations/atoms occupy the corner and middle of the cube, respectively, and Sn^{4+} is coordinated to six O^{2-} anions, forming a perfect octahedron. Subsequently, each oxygen atom occupies the middle of the cube edge and is coordinated with two Sn atoms. This periodic arrangement of atoms in $BaSnO_3$ results in a perovskite structure [136]. It is found that distortion of SnO_6 octahedron leads to a reduction in the conductivity of $BaSnO_3$. The $BaSnO_3$ has received increased attention in the past decade for its superior optical and electrical properties in various applications including capacitors, high dielectric ceramics, sensors, dye-sensitized solar cells, etc. [137][138][139][127]. $BaSnO_3$ plays an important role as an electron transport layer (photoanode) in DSSCs. Recently, there have been many reports on $BaSnO_3$ based photoanodes for DSSCs with an overall conversion efficiency ranging from 1.1 to 6.86% [127][140]. Zhang *et al.* reported that dye-sensitized $BaSnO_3$ could be used as a photoanode in DSSCs owing to its fast dye adsorption capability than the conventional binary oxide materials [135]. Guo *et al.* reported $BaSnO_3$ nanoparticles used as photoanode which, exhibited a power conversion efficiency (PCE) of 1.1% [141]. Recently, Rajamanikam *et al.* reported PCE of 0.71% without surface treatment and scattering layer [131]. In 2018, the same group reported surface treatment on the $BaSnO_3$ layer resulting in enhanced efficiency of 5.64% for 5% Sr doped BSO. Moreover, as in perovskite solar cells (PSCs), the mesoporous $BaSnO_3$ layer shows better performance as well as excellent photo stability compared to that of TiO_2 [142]. The material properties can be tuned by doping, where the dopants may donate carriers and/or create defect levels in the band which may play a significant role in improving the optical as well as electrical properties, thereby improving the overall performance of the device in which it is employed. It is quite easy to modify the optical and electronic properties of $BaSnO_3$ by manipulating the composition and/or by doping with transition and rare earth impurity ions [143][144] to improve the performance and stability of the photoanodes in DSSCs.

1.5.3 Transparent conducting oxides in DSSCs

Apart from the semiconducting oxides that are used as photoanodes, transparent conducting oxide (TCO) substrates also play a crucial role in increasing the performance of DSSCs due to their effective electronic conductivity. A thin layer of TCO can act as a current collector and supports the photoanode (semiconducting oxide) in DSSCs. The TCOs have two key aspects; one is high optical transparency that allows Sun's light to enter into the device without much absorption of the incident radiation, and secondly, low sheet resistance to facilitate the effective charge transfer process which improves the performance. The indium tin oxide (ITO, 90% In_2O_3: 10% Sn) film exhibits high transparency over 85 % and a resistivity value of about 10^{-4} Ω cm. ITO has been widely used as a transparent conducting electrode in optoelectronic devices, liquid crystal displays, and solar energy conversion device applications. Moreover, the optical and electrical properties of ITO films depend on the deposition method [145][146]. However, the low resistivity property of ITO films changes to high resistivity with increasing calcination temperature when used in DSSC device fabrication. Particularly, in DSSC fabrication, the photoanode material involves coating and sintering of TiO_2 paste on conducting substrates at high temperature (≅ 450 ˚C) to improve the electrical contact, but the sheet resistance of ITO increases drastically at high temperature (> 300 ˚C), leading to a decrease in power conversion efficiency [17]. Apart from ITO, SnO_2 and ZnO doped with donor elements are also frequently used as TCOs. However, these well-known semiconducting materials have some limitations such as instability of oxygen content, variations in surface work function, fatigue, and degradation [147][148]. In general, pure SnO_2, ZnO, and In_2O_3 materials do not possess the desired TCO properties. These desired optical and electrical properties are obtained by suitably doping impurities such as pentavalent (n-type) and trivalent (p-type) elements. Most importantly, the selection of dopant materials depends on their valency, charge state, effective mass, ionic radii, cost-effectiveness, and natural abundance.

Here, Table 1.4 shows some of the host and doping elements for designing TCO materials with desirable properties. Fluorine-doped tin oxide (FTO) has properties similar to that of ITO which makes it viable for use in DSSCs. The FTO substrates have 70-80% transparency in the visible range, which is roughly 10% lesser than that of the ITO electrodes. The sheet resistance of FTO (≅ 12 Ω/□) is comparable to that of ITO glass substrate and it has good resistance stability with temperature. Compared to the ITO substrates, FTO has comparably low transparency, similar conductivity, and cost effectiveness [149]. The comparison of DSSC properties using ITO and FTO conducting glass substrates was reported by Sima et al., where the sheet resistance of ITO increases from the initial 18 Ω/□ to 52 Ω/□ upon annealing at 450 ˚C, whereas the sheet resistance of FTO is nearly invariant (18 Ω/□). The cell efficiency of the ITO based DSSC was reported to be 2.24%, and for an identical cell using FTO, it was 9.6% [150]. The availability of raw materials and the applicability of facile and cost-effective deposition techniques are some of the key factors for choosing binary TCOs. Other than the electrical properties and efficiency, some of the limitations of traditional ITO based transparent conducting oxides are limited availability and the high cost of indium. ITO substrates are sensitive to thermal treatment (beyond a temperature limit, around 325 °C), possess limited transparency in the near IR region, and are brittle in nature [151].

The FTO is widely used as an alternative electrode for ITO in several optoelectronic devices, and specifically in DSSC due to its high conductivity and excellent thermal stability of sheet resistance (up to 450° C) which is better than that of ITO [152]. However, there are certain limitations for FTO when compared to ITO which are transparency, difficulty in doping of fluorine into the anionic sites of the host SnO_2 lattice, and high surface roughness, resulting in leakage current [153].

Table 1.4. Parameters relevant to the host and dopant materials for making effective TCOs

Group	Element	Oxidational state	Ionic radius (Å)	Co-ordination Number
Host lattice SnO_2/ZnO	O	-2	1.35/1.36/1.38/1.41/1.42	2/3/4/6/8
	Sn	+4	0.69/0.76/0.83/0.89/0.95	4/5/6/7/8
	Zn	+2	0.6/0.68/0.74/0.9	4/5/6/8
Donor/Acceptor elements	F	-1	1.28/1.3/1.31	2/3/4
	Al	+3	0.39/0.48/0.54	4/5/6
	In	+3	0.62/0.8/0.92	4/6/8
	Sb	+3	0.76/0.8/0.76	4/5/6
		+5	0.6	6

Hence, researchers are interested in finding suitable supplementary material for ITO and FTO electrodes. In this scenario, SnO_2 is identified as one of the promising alternative host materials, which by doping with suitable dopant elements can be tuned for better optical and electrical properties (*i.e.*, transparency and conductivity). In general, FTO electrodes are deposited over thick glass substrates (usually 2.2 mm thick) to withstand the high temperature involved during the deposition of the electrode. This thickness of the glass substrate significantly affects the transparency and haze of the finished electrode. In this thesis, as an alternative, Sb doped into the SnO_2 (with Sb in 5+ charge state) yielding free carriers to the lattice increasing the conductivity of the film are explored for their applicability in DSSCs as a transparent conducting electrode.

1.5.4 Natural dyes

Natural photosensitizers are alternatives to expensive synthetic dyes which are cost-effective on a large scale when extracted from natural plant sources such as colorful flowers, fruits, leaves, etc. Natural dyes are used as a photosensitizer in DSSCs since natural pigments have several beneficial features like facile preparation methods, abundance, high absorbance, easy extraction and processing, cost effectiveness, environment friendly nature, and most essentially, elimination of the use of noble metals [154][155]. In DSCCs, the dye sensitizer has the most basic role of primary charge separation by photo-excitation of electrons. The excited electrons must have the ability to get injected into the conduction band of the semiconducting material (Electron transport material). Here, natural photosensitizers are classified into carotenoids, flavonoids, or chlorophylls, and betalains as shown in Table 1.5.

1.5.4.1 Carotenoids

Carotenoid structures allow a short wavelength absorption in the visible region [156]. These pigments are found in several flowers, fruits, and also in some microorganisms. They exhibit bright orange, red, and yellow colors. Carotenoids have two major sub-categories known as xanthophylls that contain oxygen molecules and carotenes which contain purely hydrocarbons[157]. The carotenoids have been successfully used in DSSCs as a photosensitizer and show conversion efficiency of 2.6% [158]. Meanwhile, co-sensitizing them with carotenoids and chlorophyll derivatives has been shown to improve the efficiency to 4.2%[159].

1.5.4.2 Chlorophyll

Chlorophyll is a green pigment present in the leaves of green plants, algae, and also in cyanobacteria. Chlorophyll absorbs light photons having red, blue, and violet wavelengths, and it derives color by reflecting green wavelength. Firstly, Kay and Grätzel reported

chlorophyllderivatives for sensitization on nanoporous TiO_2[58]. After this report, several research groups demonstrated chlorophyll as a photosensitizer in DSSCs [160][161]. Chlorophyll is mainly derived from chlorophyllides (Chl-a and Chl-b) and pheophytins. Interestingly, the most efficient photosensitizer chlorophyll 'a' derivative is methyl trans-32-carboxy-phyropheophorbide. Chlorophyll 'a' can bind with TiO_2 and ZnO semiconductor nanoparticles through bidentate chelating and monodentate modes. The chemical structures of chlorophyll are shown in Fig. 1.12.

1.5.4.3 Flavonoids

Flavonoids are the important active group of natural pigments that are associated with angiosperms, contributing color to the flowers by absorbing almost all the colors in the visible region. Flavonoids are described as a network of natural pigments that includes the structure of a C6-C3-C6 carbon framework with two phenyl rings linked by three carbon rings that specifically form a phenyl benzopyran functionality[59]. Flavonoids include subclasses like anthocyanins, aurones, chalcones, flavones and flavonols. Among these, anthocyanin is the most efficient photosensitizer for use in DSSCs compared to other chlorophyll sub-classes. In the case of flavonoids, the charged electrons transfer from HOMO to LUMO levels at lower energy. The pigment molecule is energized by a broad absorption peak in the visible region[162]. These flavonoids are highly adsorbed to the surface of TiO_2 by replacing OH^- counter ions from the Ti sites that combine with a proton donated by the flavonoid structure[163]. The basic chemical structures of flavonoids are presented in Fig. 1.12.

Table 1.5 Photovoltaic parameters of dyes extracted from various natural sources.

Plant sourc/Flowers	Structural class	J_{SC} (mA cm^{-2})	V_{OC} (V)	FF (%)	η (%)	Extraction Solvent	Ref.
			Flowers				
Ixora sp. (Rubiaceae)	Anthocyanins	6.26	0.35	47	0.96	Ethanol	[164]
Rhododendron	Anthocyanins	1.61	0.58	61	0.57	Ethanol	[165]
Erythrina variegata	Carotenoid, Chlorophyll	0.78	0.48	55	n.a.	Fractionated extract	[63]
Red Bougainvillea glabra	Betacyanin	2.34	0.26	74	0.45	Acidic H_2O	[166]
Red Bougainvillea spectabilis	Betalain	2.29	0.28	76	0.48	Acidic H_2O	[166]
Hibiscus rosa-sinensis	Anthocyanin	3.31	0.145	55	1.08	Ethanol	[167]
			Fruits				
Blueberry	Anthocyanins	4.1	0.30	55	0.69	Ethanol	[168]
Kuduk-kuduk (Melastoma malabathricum L.)	Anthocyanins	3.18	0.45	52	0.83	Ethanol	[169]
Fructus lycii	Carotene	0.53	0.68	46	0.17	Ethanol	[165]
Capsicum	Carotenoid	0.23	0.41	63	n.a.	Fractionated extract	[165]
Wild Sicilian Prickly Pear	Betalain	8.2	0.38	38	1.19	Aqueous acid	[170]
Mulberry fruit	Anthocyanins	1.89	0.56	49	0.55	Ethanol	[171]
Canarium odontophyllm	Anthocyanins	2.45	0.39	62	0.59	Ethanol	[164]
Blackberry	n.a.	5.85	0.32	57	1.07	Aqueous acid	[172]
			Leaves				
Codiaeum variegatum	Anthocyanins	4.03	0.44	55	1.08	Ethanol	[167]
Ipomoea	Chlorophyll	0.91	0.54	56	0.28	H_2O	[173]
Punica granatum (Pomegranate)	Chlorophyll	2.05	0.56	52	0.59	-	[171]
Ficus reusa	Chlorophyll, carotenoids	7.85	0.52	29	1.18	H_2O	[174]
Rhoeo spathacea	Chlorophyll, carotenoids	10.9	0.5	27	1.49	H_2O	[174]
Garcinia subelliptica	Chlorophyll, carotenoids	6.48	0.32	33	0.69	H_2O	[174]
Red cabbage	Anthocyanins	2.25	0.62	70	0.97	Aqueous extract	[175]
Pandan leaves	Chlorophyll	1.91	0.48	56	0.51	Ethanol	[176]
			Seeds				
Coffee	n.a.	0.85	0.55	69	0.33	H_2O	[165]
Black Rice	Anthocyanins	2.09	0.47	57	0.56	Ethanol	[176]
Lawsonia inermis seed	Lawsone	2.99	0.50	70	1.47	H_2O	[177]

1.5.4.4 Betalains

Betalains constitute another set of water-soluble nitrogen-containing vegetable pigments and are potential absorbers of visible light for DSSC applications. Betalain dyes are extracted from colored plants, flowers, fruits, and some vegetative tissues of plants belonging to Caryophyllales and Basidiomycota families [178][60]. In general, these dyes have orange and red colors which are due to red-violet betacyanin and yellow betaxanthin. For example, prickly pear fruit extract contains dyes of betanin and indicaxanthin as well. Red beetroot has betanin and vulgaxanthin, showing a deep red coloration. However, betalains are further categorized as betacyanins and betaxanthins whose molecular structures are shown in Fig. 1.13 (a and b).

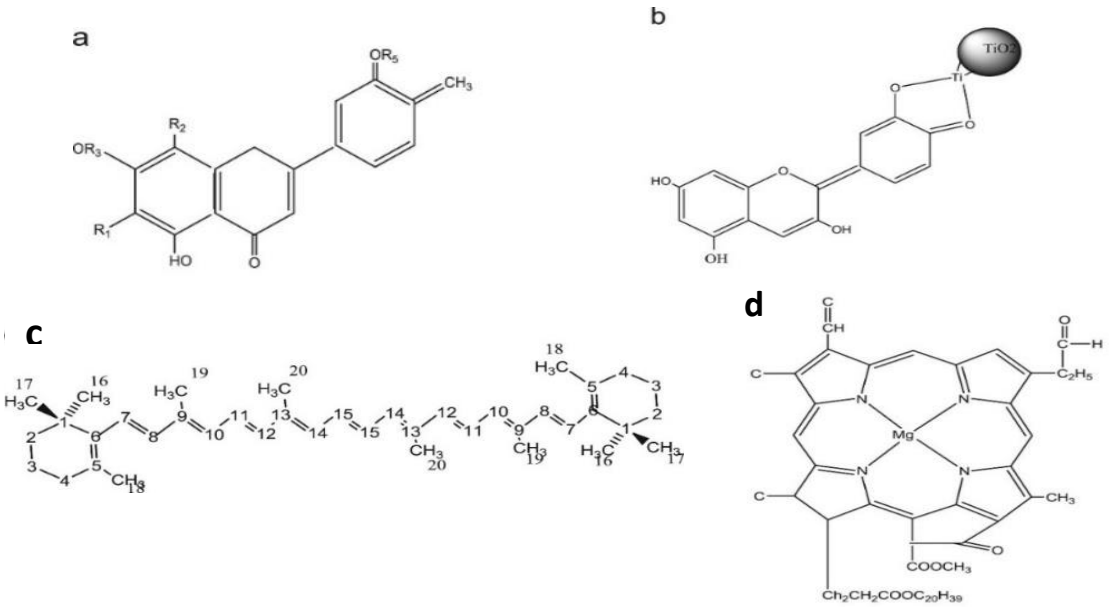

Fig. 1.12. Basic chemical structures of (a) anthocyanin, (b) flavonoid, (c) carotenoid and (d) chlorophyll.

Both these dyes were first extracted from beetroot and named '*Betalains'* by Mabry and Dreiding in 1968 [179][155]. Significant exploration has been done for the last fifteen years on betalains dyes that are extracted from the leaf and grain of amaranth[180], prickly pear fruit[181], beetroot[182], and bougainvillea[183]. In particular, betalains show strong absorption in the visible range of the electromagnetic spectrum and have been considered as a

good candidate for DSSCs due to their capability as electron donors [155]. In 2002, the first report on betalains extract used as a photosensitizer in DSSCs with an efficiency of 0.44% and 0.014% for TiO_2 and ZnO, respectively, was published[184]. From these results, the observed low efficiency is attributed to the fewer injected electrons from the excited dye molecule to the conduction band of ZnO compared to the TiO_2 based DSSC[184]. The second report was published in 2008 by McHale and his co-workers where they extracted betalains from red beetroot, and also derived betalains sensitizers like betanin, betanidin, betaxanthin, and melanin. They have reported a maximum efficiency of 0.67% in DSSC sensitized with the derivative betanin[182]. Therefore, considering these results, the extracted betalains dyes from natural pigments such as fruits and roots act as alternative photosensitizers for use in DSSC. In this work, considering the beneficial features of natural dyes, the focus is on the dye-extraction from the less-explored prickly pear fruits (Cactus) to be used as a photosensitizer for DSSCs [185]. Cactus (*Opuntia ficus-indica*) generally known as prickly pear belongs to a family of Cactaceae. This plant yields sweet, nutritionally rich edible fruits, and its tender cladodes are also used for making a salad.

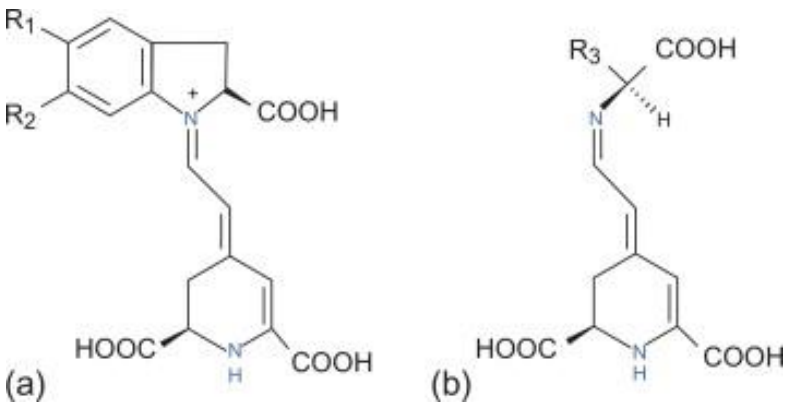

Fig. 1.13. Chemical structure of (a) betacyanins and (b) betaxanthins derivative compounds

1.5.4.5 Description of Cactus (Opuntia ficus-Indica)

Opuntia ficus-Indica is a shrub containing about 130 genera and about 1500 species that are well-adapted to arid lands throughout the globe in countries like South Africa, Middle East, the Mediterranean basin, Australia, and India [186]. The cladodes (large pads) are green to blue-green, containing few spines up to 2.5 cm or they may be spineless. Prickly pear grows with flat and rounded cladodes as well as smooth and fixed spines. The cactus flowers are typically large with yellow color and its fruits are deep red with arillate seeds. The Opuntia ficus-Indica plants grow in areas with weather conditions having an extended dry spell followed by hot summer and occasional rainy seasons with low humidity. Prickly pear is a rich source of betalains and has deep red-purple color due to the presence of betacyanin in the extract. Complete details of the prickly pear fruit extraction and properties of the dye are discussed in chapters 2 and 7, respectively.

1.5.5 Figures of Merit of DSSCs

The performance of a dye-sensitized solar cell is generally determined from the parameters of the J-V characteristic curves which include,

(1) Short circuit current density (J_{SC}, mA/cm^2)

(2) Open-circuit voltage (V_{OC}, V)

(3) Fill factor (FF) and

(4) Conversion efficiency (η, %).

Current from a solar cell is generally determined from the equation given below,

$$I = I_{SC} - I_0 \left(e^{\frac{qv}{kT}} - 1 \right) \qquad (1.10)$$

where I_{SC} is the short circuit current, I_0 is the reverse saturation current, q is the electron charge, k is the Boltzmann constant and T is the temperature in kelvin [187].

1.5.5.1 Short circuit current

Short circuit current (I_{SC}) is determined under one sunlight radiation and indicates the photocurrent per unit area (mA/cm^2) of the cell. Generally, I_{SC} is defined as the ratio of maximum output current to the cell area. The I_{SC} depends on many factors including the area of the solar cell, the total amount of photons absorbed, the wavelength of the incident solar radiation, charge collection ability of the solar cell, and finally operational conditions and material properties.

1.5.5.2 Open circuit voltage

Open circuit voltage (V_{OC}) is the highest voltage that a solar cell can yield from the external circuit and corresponds to the quasi-fermi level (determined from the separation of the hole and electron quasi-fermi level (E_F, -0.5 V to -0.4 eV *vs*. normal hydrogen electrode (NHE), for TiO_2) of the semiconductor and redox potential of the charge mediator (-0.4 eV vs. NHE, for I_3^-/I^- redox couple) [188]. The maximum open circuit voltage can be measured when I_{SC} equals zero. The V_{OC} is indicated on the I-V curve in Fig. 1.14 and is not dependent on the cell area. The V_{OC} is invariable under constant illumination and temperature conditions. The maximum I_{SC} is found when the device is short-circuited, while under open-circuit conditions, no current can pass through. At this condition, the voltage is highest and V_{OC} is expressed as:

$$V_{OC} = V_T - I_0\left(1 + \frac{I_{OC}}{I_0}\right) \tag{1.11}$$

where V_T is the thermal voltage, and I_o is the reverse saturation current density.

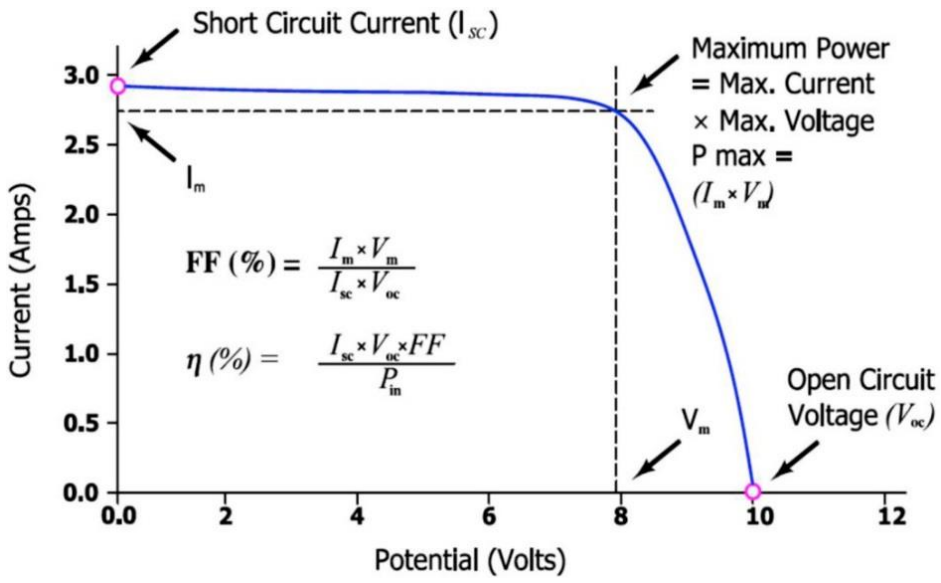

Fig. 1.14. The I-V characteristic curve of a solar cell with key parameters indicated [187].

1.5.5.3 Fill factor

Fill factor (FF) is determined from the ratio of the highest power output from a solar cell to the product of short-circuit current and open-circuit voltage. The fill factor can be defined as,

$$FF = \frac{P_{max}}{J_{SC} \cdot V_{OC}} \tag{1.12}$$

where P_{max} is the maximum output power of the cell per unit area ($P_{max} = I_{max} \times V_{max}$). In an I-V curve, the fill factor is described by the product of J_{SC} and V_{OC} which is a rectangle with maximum area as shown in Fig. 1.14.

1.5.5.4 Power conversion efficiency

Power conversion efficiency *(η)* of a solar cell is defined as the ratio between the highest electrical output power and energy of the incident power (P_{in}). The incident power equals to the irradiance of the AM 1.5 normalized to 1000 W/m^2 at room temperature. The total power conversion efficiency of a DSSC is determined from J_{SC}, V_{OC}, FF, and P_{in}. The power conversion efficiency can be calculated using the relation,

$$\eta = \frac{P_{max}}{P_{in}} = \frac{J_{SC} \cdot V_{OC} \cdot FF}{P_{in}} \times 100\ \% \quad (1.13)$$

Here, P_{in} is determined by the aspects of the light spectrum that is incident upon the device.

1.5.5.5 Incident photon to current conversion efficiency

Incident photon to current conversion efficiency (IPCE) or external quantum efficiency (EQE) of the solar cell is measured from the ratio of the number of generated photoelectrons ($N_{electrons}$) that flow in the external circuit to the number of photons incident on the active surface area under monochromatic light irradiation with a given wavelength (λ):

$$IPCE\ (\lambda) = \frac{N_{electron}}{N_{photons}} \quad (1.14)$$

The IPCE can be expressed in another form which is the product of the photon-harvesting efficiency [LHE(λ)] for a wavelength λ, the quantum yield of electron injection (Φ_{inj}) from the excited state of the dye to the conduction band of the semiconductor, and collection efficiency (Φ_{coll}) of the injected electron at the front electrode [187]:

$$IPCE = LHE(\lambda)\Phi_{inj}\Phi_{coll} \quad (1.15)$$

where the LHE(λ) is defined as , $LHE(\lambda) = 1 - 10^{-A}$ (1.16)

Here, exponent A represents the dye absorbance (also referred to as optical density). The values of IPCE mainly depend on the absorption properties, the quantity of sensitizer that is adsorbed on the surface of the semiconductor as well as on the Φ_{inj} and Φ_{coll}.

1.6 Current status and future prospects of DSSC

Over the past two decades, DSSCs have proven their potential in becoming one of the essential means of future energy due to their cost-effectiveness, ease of fabrication, long-term stability, and as well as steadily improving conversion efficiency levels. The DSSCs perform

better in diffuse light and elevated-temperature environments compared to other types of PV technologies. There can be several challenges for the implementation of large-scale production and industrial applications of DSSCs such as low power conversion efficiency compared to the 1st and 2nd generation solar cells, and low stability which need to be overcome. The maximum power conversion efficiency achieved for DSSC is 13% (without any co-sensitization) [31]. However, for full commercialization, efficiency levels need to be improved to more than 20% to compete with the existing technologies. Apart from efficiency, some of the other challenges are improvement of DSSC device stability as well as reduction of material and manufacturing costs mainly due to expensive ruthenium-based dyes. The power conversion efficiency of DSSCs strongly depends on the sensitizers, photoanode material, and light absorption ability. However, for the past 20 years, considerable work has been executed to develop panchromatic dye sensitizers that are expected to be a breakthrough in cost and performance compared to synthetic Ru-based dyes. In 2009, Kojima et al. first proposed the use of inorganic-organic hybrid halogen perovskite $CH_3NH_3PbI_3$ nanocrystals as sensitizers in DSSCs, owing to their high absorption coefficient, instead of conventional synthetic ruthenium-based N719 dye [189]. However, the efficiency was not very high (≅ 4%) due to the rapid dissolution of the perovskite compound in liquid electrolyte. Subsequently, in heterojunction solar cell devices, Etgar et al. demonstrated that $CH_3NH_3PbI_3$ acts as a sensitizer as well as a hole transport material. For the last six years, the efficiency of solid-state perovskite solar cells (PSCs) has reached from 3% to 22% [190], which has opened up a new era of solar cell technology with immense scope. Besides high efficiency, improving stability is another important issue in PSCs which needs to be addressed. Though the efficiency of perovskite solar cells is promising, their stability issues and the toxicity of lead are serious concerns.

In DSSCs, instability is mainly due to the leakage of liquid electrolyte and few other reasons such as dye desorption, changes in the structure of dye in the presence of iodine (liquid

electrolyte) as well as the influence of the working electrode and degradation of Pt catalyst (counter electrode). To prevent electrolyte leakage, it is beneficial to replace the liquid electrolyte with solid-state electrolyte (hole transport material, HTM), and Pt catalyst can be supplemented with graphene-based carbonaceous materials which possess high electrochemical stability under prolonged potential cycling [191]. Upon solving these issues, Grätzel has estimated the lifetime of optimized DSSC modules to about 20 years [192].

Apart from improving the performance, it is also essential to minimize the material and production costs. In DSSCs, the most expensive component is the noble metal based synthetic dye which also uses toxic precursors involving tedious preparation steps. To minimize these costs and issues related to the synthesis of dye, alternative dyes are extracted from natural resources. Generally, compared to synthetic dyes, natural dyes are widely available, easy to extract, non-toxic, environment-friendly, cost-effective, and also completely bio-degradable [193]. For several natural dyes, the efficiency can be further improved by choosing a suitable co-sensitizer and stabilizer. In a DSSC, the second most expensive material is the transparent conducting substrate [194]. As an alternative to FTO, graphene-based transparent conducting electrodes (TCEs) are found to be effective with a low sheet resistance (30 Ω/□) and high transmittance (> 90%) [195]. Graphene-based materials can play a double role as conducting substrate and catalyst in DSSC, almost reducing the cost by four times [196]. However, it is a challenge to optimize the layers of graphene over a large area, and hence, researchers are exploring alternative oxide based transparent conducting electrodes like SnO_2 and ZnO doped with appropriate donor elements as already discussed in section 1.5.3. It is expected that the DSSC technology will be promising to supplement the future energy requirements, considering the economic factor and environmental protection.

1.7 Scope and objectives of the thesis

High efficiency, non-toxicity, good stability, and cost-effective production are the desired features of a solar cell. Existing commercial solar cells are expensive due to raw materials and manufacturing costs. The cost per watt can be justified either by lowering the manufacturing cost or by increasing efficiency. Hence, it is necessary to enhance the efficiency and long-term stability by altering various components of DSSCs. The efficiency of a DSSC depends on the major components like photoanode material, dye-sensitizer, electrolyte, and transparent conducting electrodes. The main focus of this thesis is on exploring alternative materials which can serve as photoanode compared to the existing conventional ETL materials, as well as transparent conducting oxide (TCO) electrode to supplement FTO, and natural dyes instead of expensive synthetic dyes in DSSCs by using relatively simple and cost-effective synthesis techniques.

The objectives of the thesis based on these alternative materials are listed below:

- To investigate the status of alternative photoanodes based on ternary oxides/ transparent conducting electrodes / natural dye-sensitizers through extensive literature survey, and selection of suitable materials and synthesis methods which can contribute to new knowledge in the area of DSSCs.
- To synthesize nanostructured ternary $BaSnO_3$ and La/Sb doped $BaSnO_3$ particles for varying their composition using two different techniques, namely hydrothermal method, and facile peroxide co-precipitation method to achieve high surface area and nano-dimensional features.
- To characterize the optimized nanostructured ternary $BaSnO_3$ and La/Sb doped $BaSnO_3$ particles for their structural, optical, and morphological properties using appropriate techniques.

- To fabricate DSSC devices based on the optimized ternary $BaSnO_3$ compounds doped with La/Sb and to assess the impact of dopants on the charge transfer properties and power conversion efficiency.
- To deposit a large area (5x5 cm^2) Sb doped SnO_2 thin film onto glass substrates by spray pyrolysis and to characterize them for their optical and electrical properties to serve as an alternative transparent conducting oxide electrode in DSSCs.
- To extract and stabilize natural dye-sensitizer from prickly pear fruit and to investigate its optical properties to use it as a photosensitizer in DSCCs.

References

[1] S. Update, Energy Reserves from page 4, (2015). http://www.wise-uranium.org/stk.html?src=stkd03e.

[2] Where greenhouse gases come from - U.S. Energy Information Administration (EIA), (n.d.).

[3] R. Perez, M. Perez, A Fundamental Look At Energy Reserves For The Planet, Int. Energy Agency SHC Program. Sol. Updat. 50 (2009) 4–6. http://www.iea-shc.org/data/sites/1/publications/2015-11-A-Fundamental-Look-at-Supply-Side-Energy-Reserves-for-the-Planet.pdf.

[4] Homepage - U.S. Energy Information Administration (EIA), (n.d.).

[5] M. Hart, Hubris: The troubling science, economics, and politics of climate change, Lulu. com, 2015.

[6] S. Yun, Y. Qin, A.R. Uhl, N. Vlachopoulos, M. Yin, D. Li, X. Han, A. Hagfeldt, New-generation integrated devices based on dye-sensitized and perovskite solar cells, Energy Environ. Sci. 11 (2018) 476–526.S

[7] A.-E. Becquerel, Recherches sur les effets de la radiation chimique de la lumiere solaire au moyen des courants electriques, CR Acad. Sci. 9 (1839) 1.

[8] D.M. Chapin, C.S. Fuller, G.L. Pearson, A new silicon p-n junction photocell for converting solar radiation into electrical power, J. Appl. Phys. 25 (1954) 676–677.

[9] S. Sharma, K.K. Jain, A. Sharma, Solar Cells: In Research and Applications—A Review, Mater. Sci. Appl. 06 (2015) 1145–1155.

[10] W. Shockley, H.J. Queisser, Detailed balance limit of efficiency of p-n junction solar cells, J. Appl. Phys. 32 (1961) 510–519.

[11] R.W. Birkmire, E. Eser, POLYCRYSTALLINE THIN FILM SOLAR CELLS : Present Status and Future Potential, (1997).

[12] X. Sheng, L. Shen, T. Kim, L. Li, X. Wang, R. Dowdy, P. Froeter, K. Shigeta, X. Li, R.G. Nuzzo, Doubling the power output of bifacial thin-film GaAs solar cells by embedding them in luminescent waveguides, Adv. Energy Mater. 3 (2013) 991–996.

[13] C.S. Ferekides, U. Balasubramanian, R. Mamazza, V. Viswanathan, H. Zhao, D.L. Morel, CdTe thin film solar cells : device and technology issues, 77 (2004) 823–830.

[14] F. Kessler, D. Herrmann, M. Powalla, Approaches to flexible CIGS thin-film solar cells, 481 (2005) 491–498.

[15] S. Benagli, D. Borrello, E. Vallat-Sauvain, J. Meier, U. Kroll, J. Hötzel, J. Bailat, J. Steinhauser, M. Marmelo, G. Monteduro, High-efficiency amorphous silicon devices on LPCVD-ZnO TCO prepared in industrial KAI-M R&D reactor, in: 24th Eur. Photovolt. Sol. Energy Conf., 2009: pp. 21–25.

[16] Y. Kuang, M. Di Vece, J.K. Rath, L. Van Dijk, R.E.I. Schropp, Elongated nanostructures for radial junction solar cells, 106502 (n.d.).

[17] B. O'Regan, M. Grätzel, A low-cost, high-efficiency solar cell based on dye-sensitized colloidal TiO2 films, Nature. 353 (1991) 737–740.

[18] M.C. Beard, J.M. Luther, A.J. Nozik, Multiple exciton generation in semiconductor quantum dots and electronically coupled quantum dot arrays for application to third- generation photovoltaic solar cells, Colloid. Quantum Dot Optoelectron. Photovoltaics. 9780521198 (2010) 112–147.

[19] M.R. Kim, Quantum-Dot-Based Solar Cells: Recent Advances, Strategies, and Challenges, (2015).

[20] T. Ameri, P. Khoram, J. Min, C.J. Brabec, M.O.E.L.U. Mo, Organic Ternary Solar Cells : A Review, (2013) 4245–4266.

[21] S. Kazim, M.K. Nazeeruddin, M. Grätzel, S. Ahmad, Perovskite as light harvester: A game changer in photovoltaics, Angew. Chemie - Int. Ed. 53 (2014) 2812–2824.

[22] M.A. Green, Third generation photovoltaics: Ultra-high conversion efficiency at low cost, Prog. Photovoltaics Res. Appl. 9 (2001) 123–135.

[23] G. Conibeer, photovoltaics, Mater. Today. 10 (2007) 42–50.

[24] W. West, First hundred years of spectral sensitization, Photogr. Sci. Eng. 18 (1974) 35–48.

[25] J. Moser, Notiz über Verstärkung photoelektrischer Ströme durch optische Sensibilisirung, Monatshefte Für Chemie Und Verwandte Teile Anderer Wissenschaften. 8 (1887) 373.

[26] S. Namba, Y. Hishiki, Color sensitization of zinc oxide with cyanine dyes1, J. Phys. Chem. 69 (1965) 774–779.

[27] H. Gerischer, M.E. Michel-Beyerle, F. Rebentrost, H. Tributsch, Sensitization of charge injection into semiconductors with large band gap, Electrochim. Acta. 13 (1968) 1509–1515.

[28] E. Daltrozzo, ON THE MECHANISM OF SPECTRAL SENSITIZATION: RHODAMIN B SENSITIZED ELECTRON TRANSFER TO ZINC OXIDE., (1975).

[29] M.T. Spitler, M. Calvin, Electron transfer at sensitized TiO2 electrodes, J. Chem. Phys. 66 (1977) 4294–4305.

[30] K. Kalyanasundaram, N. Vlachopoulos, V.K.A. Monnier, M. Grátzel, Sensitization of TI02 in the Visible Light Region Using Zinc Porphyrins, (1987) 2342–2347.

[31] S. Mathew, A. Yella, P. Gao, R. Humphry-Baker, B.F.E. Curchod, N. Ashari-Astani, I. Tavernelli, U. Rothlisberger, M.K. Nazeeruddin, M. Grätzel, Dye-sensitized solar cells with 13% efficiency achieved through the molecular engineering of porphyrin sensitizers, Nat. Chem. 6 (2014) 242–247.

[32] J. Wang, K. Liu, L. Ma, X. Zhan, Triarylamine : Versatile Platform for Organic , Dye-Sensitized , and Perovskite Solar Cells, (2016).

[33] S. Chai, T. Lau, J. Dayou, C.S. Sipaut, R.F. Mansa, Development in Photoanode Materials for High Efficiency Dye Sensitized Solar Cells, 4 (2014).

[34] J. Gong, J. Liang, K. Sumathy, Review on dye-sensitized solar cells (DSSCs): Fundamental

concepts and novel materials, Renew. Sustain. Energy Rev. 16 (2012) 5848–5860.

[35] E. Poiytechnique, D. Lausanne, Ellectrical and optical properties of Ti02 anatase thin films, 75 (1994) 0–5.

[36] Ü. Özgür, Y.I. Alivov, C. Liu, A. Teke, M.A. Reshchikov, S. Do, V. Avrutin, APPLIED PHYSICS REVIEWS A comprehensive review of ZnO materials and devices, (2005) 1–103.

[37] Y. Fukai, Y. Kondo, S. Mori, E. Suzuki, Highly efficient dye-sensitized SnO 2 solar cells having sufficient electron diffusion length, 9 (2007) 1439–1443.

[38] P. Guo, M.A. Aegerter, RU (II) sensitized Nb 2 O 5 solar cell made by the sol-gel process, 351 (1999) 290–294.

[39] M.-R. Ok, R. Ghosh, M.K. Brennaman, R. Lopez, T.J. Meyer, E.T. Samulski, Surface patterning of mesoporous niobium oxide films for solar energy conversion, ACS Appl. Mater. Interfaces. 5 (2013) 3469–3474.

[40] B. Tan, E. Toman, Y. Li, Y. Wu, Zinc Stannate (Zn 2 SnO 4) Dye-Sensitized Solar Cells, (2007) 4162–4163.

[41] A. Listorti, B.O. Regan, J.R. Durrant, Electron Transfer Dynamics in Dye-Sensitized Solar Cells, (2011) 3381–3399.

[42] M. Gra, Solar Energy Conversion by Dye-Sensitized Photovoltaic Cells, 44 (2005) 6841–6851.

[43] S. Ito, T.N. Murakami, P. Comte, P. Liska, C. Grätzel, M.K. Nazeeruddin, M. Grätzel, Fabrication of thin film dye sensitized solar cells with solar to electric power conversion efficiency over 10%, Thin Solid Films. 516 (2008) 4613–4619.

[44] L.M. Peter, Dye-sensitized nanocrystalline solar cells, Phys. Chem. Chem. Phys. 9 (2007) 2630–2642.

[45] K. Fukui, T. Yonezawa, H. Shingu, A molecular orbital theory of reactivity in aromatic hydrocarbons, J. Chem. Phys. 20 (1952) 722–725.

[46] G.J. Meyer, Efficient light-to-electrical energy conversion: nanocrystalline TiO2 films modified with inorganic sensitizers, (1997).

[47] C.A. Kelly, G.J. Meyer, Excited state processes at sensitized nanocrystalline thin film semiconductor interfaces, Coord. Chem. Rev. 211 (2001) 295–315.

[48] M.R. Narayan, Review: Dye sensitized solar cells based on natural photosensitizers, Renew. Sustain. Energy Rev. 16 (2012) 208–215.

[49] M.K. Nazeeruddin, P. Pechy, T. Renouard, S.M. Zakeeruddin, R. Humphry-Baker, P. Comte, P. Liska, L. Cevey, E. Costa, V. Shklover, Engineering of efficient panchromatic sensitizers for nanocrystalline TiO2-based solar cells, J. Am. Chem. Soc. 123 (2001) 1613–1624.

[50] G. Sauve, M.E. Cass, S.J. Doig, I. Lauermann, K. Pomykal, N.S. Lewis, High Quantum Yield Sensitization of Nanocrystalline Titanium Dioxide Photoelectrodes with cis-Dicyanobis (4, 4 ‘-dicarboxy-2, 2 ‘-bipyridine) osmium (II) or Tris (4, 4 ‘-dicarboxy-2, 2 ‘-bipyridine) osmium (II) Complexes, J. Phys. Chem. B. 104 (2000) 3488–3491.

[51] H. Nusbaumer, J.-E. Moser, S.M. Zakeeruddin, M.K. Nazeeruddin, M. Grätzel, CoII (dbbip) 22+ complex rivals tri-iodide/iodide redox mediator in dye-sensitized photovoltaic cells, J. Phys. Chem. B. 105 (2001) 10461–10464.

[52] S. Ferrere, New photosensitizers based upon [FeII (L) 2 (CN) 2] and [FeIIL3], where L is substituted 2, 2′-bipyridine, Inorganica Chim. Acta. 329 (2002) 79–92.

[53] S. Sakaki, T. Kuroki, T. Hamada, Synthesis of a new copper (I) complex,[Cu (tmdcbpy) 2]+(tmdcbpy= 4, 4′, 6, 6′-tetramethyl-2, 2′-bipyridine-5, 5′-dicarboxylic acid), and its application to solar cells, J. Chem. Soc. Dalt. Trans. (2002) 840–842.

[54] G.M. Hasselmann, G.J. Meyer, Diffusion-limited interfacial electron transfer with large apparent driving forces, J. Phys. Chem. B. 103 (1999) 7671–7675.

[55] K. Hara, Z.-S. Wang, T. Sato, A. Furube, R. Katoh, H. Sugihara, Y. Dan-Oh, C. Kasada, A. Shinpo, S. Suga, Oligothiophene-containing coumarin dyes for efficient dye-sensitized solar cells, J. Phys. Chem. B. 109 (2005) 15476–15482.

[56] G. Zhang, H. Bala, Y. Cheng, D. Shi, X. Lv, Q. Yu, P. Wang, High efficiency and stable dye-sensitized solar cells with an organic chromophore featuring a binary π-conjugated spacer, Chem. Commun. (2009) 2198–2200.

[57] L. Schmidt-Mende, U. Bach, R. Humphry-Baker, T. Horiuchi, H. Miura, S. Ito, S. Uchida, M. Grätzel, Organic dye for highly efficient solid-state dye-sensitized solar cells, Adv. Mater. 17 (2005) 813–815.

[58] A. Kay, M. Graetzel, Artificial photosynthesis. 1. Photosensitization of titania solar cells with chlorophyll derivatives and related natural porphyrins, J. Phys. Chem. 97 (1993) 6272–6277.

[59] E. Grotewold, The science of flavonoids, Springer, 2006.

[60] D. Strack, T. Vogt, W. Schliemann, Recent advances in betalain research, Phytochemistry. 62 (2003) 247–269.

[61] S. Yanagida, Y. Yu, K. Manseki, Iodine/iodide-free dye-sensitized solar cells, Acc. Chem. Res. 42 (2009) 1827–1838.

[62] M.K. Nazeeruddin, A. Kay, I. Rodicio, E. Muller, P. Liska, N. Vlachopoulos, M. Gratzel, Conversion of Light to Electricity by Charge-Transfer Sensitizers (X = Cl ", Br ", I ", CN ", and SCN ~) on Nanocrystalline Ti02 Electrodes, (1993) 6382–6390.

[63] S. Hao, J. Wu, Y. Huang, J. Lin, Natural dyes as photosensitizers for dye-sensitized solar cell, 80 (2006) 209–214.

[64] A.R. Hernandez-Martinez, M. Estevez, S. Vargas, F. Quintanilla, R. Rodríguez, Natural pigment-based dye-sensitized solar cells, J. Appl. Res. Technol. 10 (2012) 38–47.

[65] M.K. Nazeeruddin, A. Kay, I. Rodicio, R. Humphry-Baker, E. Müller, P. Liska, N. Vlachopoulos, M. Grätzel, Conversion of light to electricity by cis-X2bis (2, 2'-bipyridyl-4, 4'-dicarboxylate) ruthenium (II) charge-transfer sensitizers (X= Cl-, Br-, I-, CN-, and SCN-) on nanocrystalline titanium dioxide electrodes, J. Am. Chem. Soc. 115 (1993) 6382–6390.

[66] M.K. Nazeeruddin, S.M. Zakeeruddin, R. Humphry-Baker, M. Jirousek, P. Liska, N. Vlachopoulos, V. Shklover, C.-H. Fischer, M. Grätzel, Acid− Base equilibria of (2, 2 '-Bipyridyl-4, 4 '-dicarboxylic acid) ruthenium (II) complexes and the effect of protonation on charge-transfer sensitization of nanocrystalline titania, Inorg. Chem. 38 (1999) 6298–6305.

[67] K. Hara, H. Sugihara, Y. Tachibana, A. Islam, M. Yanagida, K. Sayama, H. Arakawa, G. Fujihashi, T. Horiguchi, T. Kinoshita, Dye-sensitized nanocrystalline TiO2 solar cells based on ruthenium (II) phenanthroline complex photosensitizers, Langmuir. 17 (2001) 5992–5999.

[68] M.K. Nazeeruddin, T. Bessho, L. Cevey, S. Ito, C. Klein, F. De Angelis, S. Fantacci, P. Comte, P. Liska, H. Imai, A high molar extinction coefficient charge transfer sensitizer and its application in dye-sensitized solar cell, J. Photochem. Photobiol. A Chem. 185 (2007) 331–337.

[69] F. Gao, Y. Wang, D. Shi, J. Zhang, M. Wang, X. Jing, R. Humphry-Baker, P. Wang, S.M. Zakeeruddin, M. Grätzel, Enhance the Optical Absorptivity of Nanocrystalline TiO 2 Film with High Molar Extinction Coefficient Ruthenium Sensitizers for High Performance Dye-Sensitized Solar Cells, J. Am. Chem. Soc. 32 (2008) 10720–10728.

[70] Y. Cao, Y. Bai, Q. Yu, Y. Cheng, S. Liu, D. Shi, F. Gao, P. Wang, Dye-sensitized solar cells with a high absorptivity ruthenium sensitizer featuring a 2-(hexylthio) thiophene conjugated bipyridine, J. Phys. Chem. C. 113 (2009) 6290–6297.

[71] P. Wang, C. Klein, R. Humphry-Baker, S.M. Zakeeruddin, M. Grätzel, A high molar extinction coefficient sensitizer for stable dye-sensitized solar cells, J. Am. Chem. Soc. 127 (2005) 808–809.

[72] P. Wang, S.M. Zakeeruddin, J.E. Moser, R. Humphry-Baker, P. Comte, V. Aranyos, A. Hagfeldt, M.K. Nazeeruddin, M. Grätzel, Stable new sensitizer with improved light harvesting for nanocrystalline dye-sensitized solar cells, Adv. Mater. 16 (2004) 1806–1811.

[73] T. Bessho, E. Yoneda, J.-H. Yum, M. Guglielmi, I. Tavernelli, H. Imai, U. Rothlisberger, M.K. Nazeeruddin, M. Grätzel, New paradigm in molecular engineering of sensitizers for solar cell applications, J. Am. Chem. Soc. 131 (2009) 5930–5934.

[74] T. Kinoshita, J.T. Dy, S. Uchida, T. Kubo, H. Segawa, Wideband dye-sensitized solar cells employing a phosphine-coordinated ruthenium sensitizer, Nat. Photonics. 7 (2013) 535–539.

[75] M.K. Nazeeruddin, P. Pechy, M. Grätzel, Efficient panchromatic sensitization of nanocrystallineTiO2 films by a black dye based on atrithiocyanato–ruthenium complex, Chem. Commun. (1997) 1705–1706.

[76] M. Grätzel, Conversion of sunlight to electric power by nanocrystalline dye-sensitized solar cells, J. Photochem. Photobiol. A Chem. 164 (2004) 3–14.

[77] H. Tributsch, Dye sensitization solar cells: a critical assessment of the learning curve, Coord. Chem. Rev. 248 (2004) 1511–1530.

[78] R. Faccio, L. Fernández-Werner, H. Pardo, A. W Mombru, Current trends in materials for dye sensitized solar cells, Recent Pat. Nanotechnol. 5 (2011) 46–61.

[79] Y. Ooyama, Y. Harima, Photophysical and electrochemical properties, and molecular structures of organic dyes for dye-sensitized solar cells, ChemPhysChem. 13 (2012) 4032–4080.

[80] A. Hagfeldt, G. Boschloo, L. Sun, L. Kloo, H. Pettersson, Dye-sensitized solar cells, Chem. Rev. 110 (2010) 6595–6663.

[81] A.F. Nogueira, C. Longo, M.-A. De Paoli, Polymers in dye sensitized solar cells: overview and perspectives, Coord. Chem. Rev. 248 (2004) 1455–1468.

[82] H. Kusama, H. Arakawa, Influence of pyrazole derivatives in I−/I3− redox electrolyte solution on Ru (II)-dye-sensitized TiO2 solar cell performance, Sol. Energy Mater. Sol. Cells. 85 (2005) 333–344.

[83] J. Wu, Z. Lan, S. Hao, P. Li, J. Lin, M. Huang, L. Fang, Y. Huang, Progress on the electrolytes for dye-sensitized solar cells, Pure Appl. Chem. 80 (2008) 2241–2258.

[84] B. V Bergeron, A. Marton, G. Oskam, G.J. Meyer, Dye-sensitized SnO2 electrodes with iodide and pseudohalide redox mediators, J. Phys. Chem. B. 109 (2005) 937–943.

[85] T. Daeneke, Y. Uemura, N.W. Duffy, A.J. Mozer, N. Koumura, U. Bach, L. Spiccia, Aqueous Dye-Sensitized Solar Cell Electrolytes Based on the Ferricyanide–Ferrocyanide Redox Couple, Adv. Mater. 24 (2012) 1222–1225.

[86] M. Marszalek, F.D. Arendse, J. Decoppet, S.S. Babkair, A.A. Ansari, S.S. Habib, M. Wang, S.M. Zakeeruddin, M. Grätzel, Ionic Liquid–Sulfolane Composite Electrolytes for High-Performance and Stable Dye-Sensitized Solar Cells, Adv. Energy Mater. 4 (2014) 1301235.

[87] F. Li, J.R. Jennings, X. Wang, L. Fan, Z.Y. Koh, H. Yu, L. Yan, Q. Wang, Influence of ionic liquid on recombination and regeneration kinetics in dye-sensitized solar cells, J. Phys. Chem. C. 118 (2014) 17153–17159.

[88] G. Hodes, D. Cahen, All-solid-state, semiconductor-sensitized nanoporous solar cells, Acc. Chem. Res. 45 (2012) 705–713.

[89] D. Bi, L. Yang, G. Boschloo, A. Hagfeldt, E.M.J. Johansson, Effect of different hole transport materials on recombination in CH3NH3PbI3 perovskite-sensitized mesoscopic solar cells, J. Phys. Chem. Lett. 4 (2013) 1532–1536.

[90] D. Li, D. Qin, M. Deng, Y. Luo, Q. Meng, Optimization the solid-state electrolytes for dye-sensitized solar cells, Energy Environ. Sci. 2 (2009) 283–291.

[91] J. Yum, P. Chen, M. Grätzel, M.K. Nazeeruddin, Recent developments in solid-state dye-sensitized solar cells, ChemSusChem Chem. Sustain. Energy Mater. 1 (2008) 699–707.

[92] M.B. Achari, V. Elumalai, N. Vlachopoulos, M. Safdari, J. Gao, J.M. Gardner, L. Kloo, A quasi-liquid polymer-based cobalt redox mediator electrolyte for dye-sensitized solar cells, Phys. Chem. Chem. Phys. 15 (2013) 17419–17425.

[93] N. Manfredi, A. Bianchi, V. Causin, R. Ruffo, R. Simonutti, A. Abbotto, Electrolytes for quasi solid-state dye-sensitized solar cells based on block copolymers, J. Polym. Sci. Part A Polym. Chem. 52 (2014) 719–727.

[94] Y.-F. Chan, C.-C. Wang, C.-Y. Chen, Quasi-solid DSSC based on a gel-state electrolyte of PAN with 2-D graphenes incorporated, J. Mater. Chem. A. 1 (2013) 5479–5486.

[95] M. Grätzel, Dye-sensitized solar cells, J. Photochem. Photobiol. C Photochem. Rev. 4 (2003) 145–153.

[96] S. Yun, P.D. Lund, A. Hinsch, Stability assessment of alternative platinum free counter electrodes for dye-sensitized solar cells, Energy Environ. Sci. 8 (2015) 3495–3514.

[97] A. Yella, H.-W. Lee, H.N. Tsao, C. Yi, A.K. Chandiran, M.K. Nazeeruddin, E.W.-G. Diau, C.-Y. Yeh, S.M. Zakeeruddin, M. Grätzel, Porphyrin-sensitized solar cells with cobalt (II/III)–based redox electrolyte exceed 12 percent efficiency, Science (80-.). 334 (2011) 629–634.

[98] A. Luque, S. Hegedus, Handbook of photovoltaic science and engineering, John Wiley & Sons, 2011.

[99] G. Tsekouras, A.J. Mozer, G.G. Wallace, Enhanced performance of dye sensitized solar cells utilizing platinum electrodeposit counter electrodes, J. Electrochem. Soc. 155 (2008) K124.

[100] S. Anandan, Recent improvements and arising challenges in dye-sensitized solar cells, Sol. Energy Mater. Sol. Cells. 91 (2007) 843–846.

[101] G. Khelashvili, S. Behrens, C. Weidenthaler, C. Vetter, A. Hinsch, R. Kern, K. Skupien, E. Dinjus, H. Bönnemann, Catalytic platinum layers for dye solar cells: a comparative study, Thin Solid Films. 511 (2006) 342–348.

[102] Q.W. Jiang, G.R. Li, X.P. Gao, Highly ordered TiN nanotube arrays as counter electrodes for dye-sensitized solar cells, Chem. Commun. (2009) 6720–6722.

[103] P. Li, J. Wu, J. Lin, M. Huang, Y. Huang, Q. Li, High-performance and low platinum loading Pt/Carbon black counter electrode for dye-sensitized solar cells, Sol. Energy. 83 (2009) 845–849.

[104] A. Kay, M. Grätzel, Low cost photovoltaic modules based on dye sensitized nanocrystalline titanium dioxide and carbon powder, Sol. Energy Mater. Sol. Cells. 44 (1996) 99–117.

[105] S.-H. Hsu, C.-T. Li, H.-T. Chien, R.R. Salunkhe, N. Suzuki, Y. Yamauchi, K.-C. Ho, K.C.-W. Wu, Platinum-free counter electrode comprised of metal-organic-framework (MOF)-derived cobalt sulfide nanoparticles for efficient dye-sensitized solar cells (DSSCs), Sci. Rep. 4 (2014) 1–6.

[106] N. Memarian, I. Concina, A. Braga, S.M. Rozati, A. Vomiero, G. Sberveglieri, Hierarchically assembled ZnO nanocrystallites for high-efficiency dye-sensitized solar cells, Angew. Chemie. 123 (2011) 12529–12533.

[107] Y.-F. Wang, K.-N. Li, C.-L. Liang, Y.-F. Hou, C.-Y. Su, D.-B. Kuang, Synthesis of hierarchical SnO 2 octahedra with tailorable size and application in dye-sensitized solar cells with enhanced power conversion efficiency, J. Mater. Chem. 22 (2012) 21495–21501.

[108] M. Wei, Z. Qi, M. Ichihara, H. Zhou, Synthesis of single-crystal niobium pentoxide nanobelts, Acta Mater. 56 (2008) 2488–2494.

[109] K. Keis, E. Magnusson, H. Lindström, S.-E. Lindquist, A. Hagfeldt, A 5% efficient photoelectrochemical solar cell based on nanostructured ZnO electrodes, Sol. Energy Mater. Sol. Cells. 73 (2002) 51–58.

[110] R.G. Breckenridge, W.R. Hosler, Electrical properties of titanium dioxide semiconductors, Phys. Rev. 91 (1953) 793.

[111] M. Quintana, T. Edvinsson, A. Hagfeldt, G. Boschloo, Comparison of dye-sensitized ZnO and TiO2 solar cells: studies of charge transport and carrier lifetime, J. Phys. Chem. C. 111 (2007) 1035–1041.

[112] A.K. Chandiran, M. Abdi-Jalebi, M.K. Nazeeruddin, M. Grätzel, Analysis of electron transfer properties of ZnO and TiO2 photoanodes for dye-sensitized solar cells, ACS Nano. 8 (2014) 2261–2268.

[113] J. Qian, P. Liu, Y. Xiao, Y. Jiang, Y. Cao, X. Ai, H. Yang, TiO2-coated multilayered SnO2 hollow microspheres for dye-sensitized solar cells, Adv. Mater. 21 (2009) 3663–3667.

[114] V. Pfeifer, P. Erhart, S. Li, K. Rachut, J. Morasch, J. Brötz, P. Reckers, T. Mayer, S. Rühle, A. Zaban, Energy band alignment between anatase and rutile TiO2, J. Phys. Chem. Lett. 4 (2013) 4182–4187.

[115] C.C. Raj, R. Prasanth, Review article A critical review of recent developments in nanomaterials for photoelectrodes in dye sensitized solar cells, J. Power Sources. 317 (2016) 120–132.

[116] K. Kakiage, Y. Aoyama, T. Yano, K. Oya, J. Fujisawa, M. Hanaya, Highly-efficient dye-sensitized solar cells with collaborative sensitization by silyl-anchor and carboxy-anchor dyes, Chem. Commun. 51 (2015) 15894–15897.

[117] B.H. Lee, M.Y. Song, S.-Y. Jang, S.M. Jo, S.-Y. Kwak, D.Y. Kim, Charge transport characteristics of high efficiency dye-sensitized solar cells based on electrospun TiO2 nanorod photoelectrodes, J. Phys. Chem. C. 113 (2009) 21453–21457.

[118] C. Chen, J. Wang, Z. Ren, G. Qian, Z. Wang, One-dimension TiO 2 nanostructures: oriented attachment and application in dye-sensitized solar cell, CrystEngComm. 16 (2014) 1681–1686.

[119] M. Saito, S. Fujihara, Large photocurrent generation in dye-sensitized ZnO solar cells, Energy Environ. Sci. 1 (2008) 280–283.

[120] D. Barpuzary, A.S. Patra, J. V Vaghasiya, B.G. Solanki, S.S. Soni, M. Qureshi, Highly Efficient One-Dimensional ZnO Nanowire-Based Dye-Sensitized Solar Cell Using a Metal-Free, D−π−A-Type, Carbazole Derivative with More than 5% Power Conversion, ACS Appl. Mater. Interfaces. 6 (2014) 12629–12639.

[121] A.R. Rao, V. Dutta, Achievement of 4.7% conversion efficiency in ZnO dye-sensitized solar cells fabricated by spray deposition using hydrothermally synthesized nanoparticles, Nanotechnology. 19 (2008) 445712.

[122] H. Zhang, Y. Wang, D. Yang, Y. Li, H. Liu, P. Liu, B.J. Wood, H. Zhao, Directly Hydrothermal Growth of Single Crystal Nb3O7 (OH) Nanorod Film for High Performance Dye-Sensitized

Solar Cells, Adv. Mater. 24 (2012) 1598–1603.

[123] J.Z. Ou, R.A. Rani, M.-H. Ham, M.R. Field, Y. Zhang, H. Zheng, P. Reece, S. Zhuiykov, S. Sriram, M. Bhaskaran, R.B. Kaner, K. Kalantar-zadeh, Elevated Temperature Anodized Nb2O5: A Photoanode Material with Exceptionally Large Photoconversion Efficiencies, ACS Nano. 6 (2012) 4045–4053.

[124] R. Abdul Rani, A.S. Zoolfakar, J. Subbiah, J.Z. Ou, K. Kalantar-Zadeh, Highly ordered anodized Nb2O5 nanochannels for dye-sensitized solar cells, Electrochem. Commun. 40 (2014) 20–23.

[125] J.S. Shaikh, N.S. Shaikh, S.S. Mali, J. V. Patil, K.K. Pawar, P. Kanjanaboos, C.K. Hong, J.H. Kim, P.S. Patil, Nanoarchitectures in dye-sensitized solar cells: Metal oxides, oxide perovskites and carbon-based materials, Nanoscale. 10 (2018) 4987–5034.

[126] B. Tan, E. Toman, Y. Li, Y. Wu, Zinc stannate (Zn2SnO4) dye-sensitized solar cells, J. Am. Chem. Soc. 129 (2007) 4162–4163.

[127] S.S. Shin, J.S. Kim, J.H. Suk, K.D. Lee, D.W. Kim, J.H. Park, I.S. Cho, K.S. Hong, J.Y. Kim, Improved quantum efficiency of highly efficient perovskite BaSnO 3-based dye-sensitized solar cells, ACS Nano. 7 (2013) 1027–1035.

[128] G. Natu, Y. Wu, Photoelectrochemical study of the ilmenite polymorph of CdSnO3 and its photoanodic application in dye-sensitized solar cells, J. Phys. Chem. C. 114 (2010) 6802–6807.

[129] Y. Okamoto, Y. Suzuki, Perovskite-type SrTiO3, CaTiO3 and BaTiO3 porous film electrodes for dye-sensitized solar cells, J. Ceram. Soc. Japan. 122 (2014) 728–731.

[130] G.S. Lotey, N.K. Verma, Synthesis and characterization of BiFeO3 nanowires and their applications in dye-sensitized solar cells, Mater. Sci. Semicond. Process. 21 (2014) 206–211.

[131] N. Rajamanickam, P. Soundarrajan, V.K. Vendra, J.B. Jasinski, M.K. Sunkara, K. Ramachandran, Efficiency enhancement of cubic perovskite BaSnO3 nanostructures based dye sensitized solar cells, Phys. Chem. Chem. Phys. 18 (2016) 8468–8478.

[132] S. Burnside, J.-E. Moser, K. Brooks, M. Grätzel, D. Cahen, Nanocrystalline mesoporous strontium titanate as photoelectrode material for photosensitized solar devices: increasing photovoltage through flatband potential engineering, J. Phys. Chem. B. 103 (1999) 9328–9332.

[133] J. Chen, L. Lu, W. Wang, Zn 2SnO 4 nanowires as photoanode for dye-sensitized solar cells and the improvement on open-circuit voltage, J. Phys. Chem. C. 116 (2012) 10841–10847.

[134] S. Raghavan, T. Schumann, H. Kim, J.Y. Zhang, T.A. Cain, S. Stemmer, High-mobility BaSnO3 grown by oxide molecular beam epitaxy, Apl Mater. 4 (2016) 16106.

[135] Y. Zhang, H. Zhang, Y. Wang, W.F. Zhang, Efficient visible spectrum sensitization of BaSnO3 nanoparticles with N719, J. Phys. Chem. C. 112 (2008) 8553–8557.

[136] H. Mizoguchi, P. Chen, P. Boolchand, V. Ksenofontov, C. Felser, P.W. Barnes, P.M. Woodward, Electrical and Optical Properties of Sb-Doped BaSnO3, Chem. Mater. 25 (2013) 3858–3866.

[137] R. Vivekanandan, T.R.N. Kutty, Hydrothermal synthesis of Ba (Ti, Sn) O3 fine powders and dielectric properties of the corresponding ceramics, Ceram. Int. 14 (1988) 207–216.

[138] E.C. Subbarao, Ceramic dielectrics for capacitors, Ferroelectrics. 35 (1981) 143–148.

[139] S. Tao, F. Gao, X. Liu, O.T. Sørensen, Ethanol-sensing characteristics of barium stannate prepared by chemical precipitation, Sensors Actuators B Chem. 71 (2000) 223–227.

[140] A. Roy, P.P. Das, P. Selvaraj, S. Sundaram, P.S. Devi, Perforated BaSnO3 Nanorods Exhibiting Enhanced Efficiency in Dye Sensitized Solar Cells, ACS Sustain. Chem. Eng. 6 (2018) 3299–3310.

[141] F. Guo, G. Li, W. Zhang, Barium staminate as semiconductor working electrodes for dye-sensitized solar cells, Int. J. Photoenergy. 2010 (2010).

[142] L. Zhu, Z. Shao, J. Ye, X. Zhang, X. Pan, S. Dai, Mesoporous BaSnO 3 layer based perovskite solar cells, Chem. Commun. 52 (2016) 970–973.

[143] X. Luo, Y.S. Oh, A. Sirenko, P. Gao, T.A. Tyson, K. Char, S.-W. Cheong, High carrier mobility in transparent Ba1− xLaxSnO3 crystals with a wide band gap, Appl. Phys. Lett. 100 (2012) 172112.

[144] B.H. Li, Y.W. Tang, L.J. Luo, T. Xiao, D.W. Li, X.Y. Hu, M. Yuan, Fabrication of porous BaSnO 3 hollow architectures using BaCO 3 @SnO 2 core-shell nanorods as precursors, Appl. Surf. Sci. 257 (2010) 197–202.

[145] I. Hamberg, C.G. Granqvist, Evaporated Sn-doped In2O3 films: Basic optical properties and applications to energy-efficient windows, J. Appl. Phys. 60 (1986) R123–R160.

[146] S. Ngamsinlapasathian, T. Sreethawong, Y. Suzuki, S. Yoshikawa, Doubled layered ITO/SnO2 conducting glass for substrate of dye-sensitized solar cells, Sol. Energy Mater. Sol. Cells. 90 (2006) 2129–2140.

[147] G. Thomas, Invisible circuits, Nature. 389 (1997) 907–908.

[148] Z.K. Tang, G.K.L. Wong, P. Yu, M. Kawasaki, A. Ohtomo, H. Koinuma, Y. Segawa, Room-temperature ultraviolet laser emission from self-assembled ZnO microcrystallite thin films, Appl. Phys. Lett. 72 (1998) 3270–3272.

[149] F. Yang, Thin film solar cells grown by organic vapor phase deposition, Princeton University, 2008.

[150] C. Sima, C. Grigoriu, S. Antohe, Comparison of the dye-sensitized solar cells performances based on transparent conductive ITO and FTO, Thin Solid Films. 519 (2010) 595–597.

[151] Z. Chen, B. Cotterell, W. Wang, E. Guenther, S.-J. Chua, A mechanical assessment of flexible optoelectronic devices, Thin Solid Films. 394 (2001) 201–205.

[152] V. Consonni, G. Rey, H. Roussel, D. Bellet, Thickness effects on the texture development of fluorine-doped SnO2 thin films: The role of surface and strain energy, J. Appl. Phys. 111 (2012) 33523.

[153] P.D.C. King, R.L. Lichti, Y.G. Celebi, J.M. Gil, R.C. Vilão, H. V Alberto, J.P. Duarte, D.J. Payne, R.G. Egdell, I. McKenzie, Shallow donor state of hydrogen in In 2 O 3 and SnO 2: Implications for conductivity in transparent conducting oxides, Phys. Rev. B. 80 (2009) 81201.

[154] N.T.R.N. Kumara, A. Lim, C. Ming, M. Iskandar, Recent progress and utilization of natural pigments in dye sensitized solar cells : A review, Renew. Sustain. Energy Rev. 78 (2017) 301–317.

[155] G. Calogero, A. Bartolotta, G. Di Marco, A. Di Carlo, F. Bonaccorso, Vegetable-based dye-sensitized solar cells, Chem. Soc. Rev. 44 (2015) 3244–3294.

[156] C. Zhu, C. Bai, G. Sanahuja, D. Yuan, G. Farré, S. Naqvi, L. Shi, T. Capell, P. Christou, The regulation of carotenoid pigmentation in flowers, Arch. Biochem. Biophys. 504 (2010) 132–141.

[157] E. Murillo, D. Giuffrida, D. Menchaca, P. Dugo, G. Torre, A.J. Meléndez-Martinez, L. Mondello, Native carotenoids composition of some tropical fruits, Food Chem. 140 (2013) 825–836.

[158] X.-F. Wang, Y. Koyama, H. Nagae, Y. Yamano, M. Ito, Y. Wada, Photocurrents of solar cells sensitized by aggregate-forming polyenes: enhancement due to suppression of singlet–triplet annihilation by lowering of dye concentration or light intensity, Chem. Phys. Lett. 420 (2006) 309–315.

[159] X.-F. Wang, A. Matsuda, Y. Koyama, H. Nagae, S. Sasaki, H. Tamiaki, Y. Wada, Effects of plant carotenoid spacers on the performance of a dye-sensitized solar cell using a chlorophyll derivative: enhancement of photocurrent determined by one electron-oxidation potential of each carotenoid, Chem. Phys. Lett. 423 (2006) 470–475.

[160] A. Kay, R. Humphry-Baker, M. Graetzel, Artificial photosynthesis. 2. Investigations on the mechanism of photosensitization of nanocrystalline TiO2 solar cells by chlorophyll derivatives, J. Phys. Chem. 98 (1994) 952–959.

[161] G. Calogero, I. Citro, G. Di Marco, S.A. Minicante, M. Morabito, G. Genovese, Brown seaweed pigment as a dye source for photoelectrochemical solar cells, Spectrochim. Acta Part A Mol. Biomol. Spectrosc. 117 (2014) 702–706.

[162] P. Maher, T. Akaishi, K. Abe, Flavonoid fisetin promotes ERK-dependent long-term potentiation and enhances memory, (2006).

[163] M. Narayan, A. Raturi, Investigation of some common Fijian flower dyes as photosensi-tizers for dye sensitized solar cellsabstract, Appl. Sol. Energy. 47 (2011) 112–117.

[164] N. Kumara, P. Ekanayake, A. Lim, L.Y.C. Liew, M. Iskandar, L.C. Ming, G.K.R. Senadeera, Layered co-sensitization for enhancement of conversion efficiency of natural dye sensitized solar cells, J. Alloys Compd. 581 (2013) 186–191.

[165] H. Zhou, L. Wu, Y. Gao, T. Ma, Dye-sensitized solar cells using 20 natural dyes as sensitizers, J. Photochem. Photobiol. A Chem. 219 (2011) 188–194.

[166] A.R. Hernandez-Martinez, M. Estevez, S. Vargas, F. Quintanilla, R. Rodriguez, New dye-sensitized solar cells obtained from extracted bracts of Bougainvillea glabra and spectabilis betalain pigments by different purification processes, Int. J. Mol. Sci. 12 (2011) 5565–5576.

[167] A. Yusoff, N. Kumara, A. Lim, P. Ekanayake, K.U. Tennakoon, Impacts of temperature on the

stability of tropical plant pigments as sensitizers for dye sensitized solar cells, J. Biophys. 2014 (2014).

[168] F. Teoli, S. Lucioli, P. Nota, A. Frattarelli, F. Matteocci, A. Di Carlo, E. Caboni, C. Forni, Role of pH and pigment concentration for natural dye-sensitized solar cells treated with anthocyanin extracts of common fruits, J. Photochem. Photobiol. A Chem. 316 (2016) 24–30.

[169] N. Kumara, N. Hamdan, M.I. Petra, K.U. Tennakoon, P. Ekanayake, Equilibrium isotherm studies of adsorption of pigments extracted from Kuduk-kuduk (Melastoma malabathricum L.) pulp onto TiO2 nanoparticles, J. Chem. 2014 (2014).

[170] G. Calogero, G. Di Marco, S. Cazzanti, S. Caramori, R. Argazzi, A. Di Carlo, C.A. Bignozzi, Efficient dye-sensitized solar cells using red turnip and purple wild sicilian prickly pear fruits, Int. J. Mol. Sci. 11 (2010) 254–267.

[171] H. Chang, Y.-J. Lo, Pomegranate leaves and mulberry fruit as natural sensitizers for dye-sensitized solar cells, Sol. Energy. 84 (2010) 1833–1837.

[172] G. Calogero, J.H. Yum, A. Sinopoli, G. Di Marco, M. Grätzel, M.K. Nazeeruddin, Anthocyanins and betalains as light-harvesting pigments for dye-sensitized solar cells, Sol. Energy. 86 (2012) 1563–1575. https://doi.org/10.1016/j.solener.2012.02.018.

[173] H. Chang, H.M. Wu, T.L. Chen, K.D. Huang, C.S. Jwo, Y.J. Lo, Dye-sensitized solar cell using natural dyes extracted from spinach and ipomoea, J. Alloys Compd. 495 (2010) 606–610.

[174] W.H. Lai, Y.H. Su, L.G. Teoh, M.H. Hon, Commercial and natural dyes as photosensitizers for a water-based dye-sensitized solar cell loaded with gold nanoparticles, J. Photochem. Photobiol. A Chem. 195 (2008) 307–313.

[175] C.-Y. Chien, B.-D. Hsu, Performance enhancement of dye-sensitized solar cells based on anthocyanin by carbohydrates, Sol. Energy. 108 (2014) 403–411.

[176] M.M. Noor, M.H. Buraidah, M.A. Careem, S.R. Majid, A.K. Arof, An optimized poly (vinylidene fluoride-hexafluoropropylene)–NaI gel polymer electrolyte and its application in natural dye sensitized solar cells, Electrochim. Acta. 121 (2014) 159–167.

[177] S. Ananth, P. Vivek, T. Arumanayagam, P. Murugakoothan, Natural dye extract of lawsonia inermis seed as photo sensitizer for titanium dioxide based dye sensitized solar cells, Spectrochim. Acta Part A Mol. Biomol. Spectrosc. 128 (2014) 420–426.

[178] A. Cronquist, A.L. Takhtadzhi͡an, An integrated system of classification of flowering plants, Columbia university press, 1981.

[179] T.J. Mabry, Recent advances in phytochemistry., Phytochemistry. 6 (1967) 159–160.

[180] F.C. Stintzing, D. Kammerer, A. Schieber, H. Adama, O.G. Nacoulma, R. Carle, Betacyanins and phenolic compounds from Amaranthus spinosus L. and Boerhavia erecta L., Zeitschrift Für Naturforsch. C. 59 (2004) 1–8.

[181] D. Butera, L. Tesoriere, F. Di Gaudio, A. Bongiorno, M. Allegra, A.M. Pintaudi, R. Kohen, M.A. Livrea, Antioxidant activities of Sicilian prickly pear (Opuntia ficus indica) fruit extracts and

reducing properties of its betalains: betanin and indicaxanthin, J. Agric. Food Chem. 50 (2002) 6895–6901.

[182] D. Zhang, S.M. Lanier, J.A. Downing, J.L. Avent, J. Lum, J.L. McHale, Betalain pigments for dye-sensitized solar cells, J. Photochem. Photobiol. A Chem. 195 (2008) 72–80.

[183] S. Heuer, S. Richter, J.W. Metzger, V. Wray, M. Nimtzt, D. Strack, Betacyanins from bracts of Bougainvillea glabra, Phytochemistry. 37 (1994) 761–767.

[184] D. Zhang, N. Yamamoto, T. Yoshida, H. Minoura, Natural dye sensitized solar cells, Trans. Res. Soc. JAPAN. 27 (2002) 811–814.

[185] G. Calogero, G. Di Marco, Red Sicilian orange and purple eggplant fruits as natural sensitizers for dye-sensitized solar cells, Sol. Energy Mater. Sol. Cells. 92 (2008) 1341–1346.

[186] U. Osuna-martínez, J. Reyes-esparza, L. Rodríguez-fragoso, Cactus (Opuntia ficus-indica): A Review on its Antioxidants Properties and Potential Pharmacological Use in Chronic Diseases, Nat. Prod. Chem. Res. 2 (2014) 2–9.

[187] M.A.M. Al-Alwani, A.B. Mohamad, N.A. Ludin, A.A.H. Kadhum, Dye-sensitised solar cells: Development, structure, operation principles, electron kinetics, characterisation, synthesis materials and natural photosensitisers, Renew. Sustain. Energy Rev. 65 (2016) 183–213.

[188] A. Hagfeldt, M. Graetzel, Light-induced redox reactions in nanocrystalline systems, Chem. Rev. 95 (1995) 49–68.

[189] A. Kojima, K. Teshima, Y. Shirai, T. Miyasaka, Organometal halide perovskites as visible-light sensitizers for photovoltaic cells, J. Am. Chem. Soc. 131 (2009) 6050–6051.

[190] M. Habibi, F. Zabihi, M.R. Ahmadian-Yazdi, M. Eslamian, Progress in emerging solution-processed thin film solar cells–Part II: Perovskite solar cells, Renew. Sustain. Energy Rev. 62 (2016) 1012–1031.

[191] L. Kavan, J.-H. Yum, M. Grätzel, Graphene nanoplatelets outperforming platinum as the electrocatalyst in co-bipyridine-mediated dye-sensitized solar cells, Nano Lett. 11 (2011) 5501–5506.

[192] J. Gong, K. Sumathy, Q. Qiao, Z. Zhou, Review on dye-sensitized solar cells (DSSCs): Advanced techniques and research trends, Renew. Sustain. Energy Rev. 68 (2017) 234–246.

[193] S. Shalini, S. Prasanna, T.K. Mallick, S. Senthilarasu, Review on natural dye sensitized solar cells: Operation, materials and methods, Renew. Sustain. Energy Rev. 51 (2015) 1306–1325.

[194] J. Kalowekamo, E. Baker, Estimating the manufacturing cost of purely organic solar cells, Sol. Energy. 83 (2009) 1224–1231.

[195] S. Bae, H. Kim, Y. Lee, X. Xu, J.-S. Park, Y. Zheng, J. Balakrishnan, Roll-to-roll production of 30-inch graphene films for transparent electrodes, Nat. Nanotechnol. 5 (2010) 574–578.

[196] F. Bonaccorso, L. Colombo, G. Yu, M. Stoller, V. Tozzini, A.C. Ferrari, Graphene, related two-dimensional crystals, and hybrid systems for energy conversion and storage, Science (80-.). 347 (2015).

CHAPTER: 2

Experimental methods and instrumentation techniques

2. Introduction

This chapter gives a detailed description of various synthesis methods used for the preparation of nanostructured particles of ternary oxide materials, as well as spray-coated conductive electrodes for use in dye-sensitized solar cells. The natural dye extraction for use in dye-sensitized solar cells (DSSCs) is also elaborated along with instrumentation details that are employed for material characterization throughout the thesis work.

This chapter is divided into four major sections, the first section gives a general introduction to synthesis methods of nanoparticles. The second section describes thin film growth related to spray pyrolysis and its mechanism. In addition, the custom-built spray pyrolysis unit used in the present work for film deposition is also described. The third section deals with the importance of natural dyes and the extraction of natural dyes from natural sources for use in DSSCs. The fourth section deals with the description of the instrumentation of techniques such as XRD, FE-SEM, TEM, XPS, FTIR, Hall effect, etc. used in this thesis work. This section also describes the fabrication of the DSSC device along with the instrumentation used for their characterization.

2.1 Nanomaterials for energy conversion

Recent technological advancements show that nanomaterials and nanostructures play a crucial role in several domains, particularly energy conversion applications. Nanomaterials offer new possibilities and also introduce new challenges since they are different from micro-sized and bulk counterparts dimensionally as well as in their physical and chemical properties. In the last few decades, research has been focused on the synthesis of novel nanomaterials with improved properties using cost-effective synthesis approaches. The synthesis method-

dependent material properties have been well documented in the literature. However, in this thesis, the focus is only on specific methods employed to control the particle size and nanostructures for use as photoanode in DSSCs. These methods include hydrothermal synthesis and facile peroxide-precipitate technique to achieve the size-controlled synthesis of nanoparticles.

The choice of the synthesis method can be a key factor in determining the effectiveness of the electron transport layer. The preparation methods of ternary oxides and their physical properties are the most important aspects to be considered for the enhancement of device efficiency. However, nanoparticle synthesis methods employing environment-friendly economical processes should have greater control over particle size distribution, morphology, purity of the sample, quantity, and quality, which has always been a challenge for researchers. In this thesis, two different synthesis methods are followed to prepare ternary oxides of pure and doped $BaSnO_3$ nanostructured particles towards development of dye-sensitized solar cells with high efficiency.

2.2 Synthesis methods for preparing nanostructured oxide materials

2.2.1 Hydrothermal method

The hydrothermal method is one of the most widely used and important techniques for advanced material processing, particularly for the synthesis of nanostructured materials towards a variety of technological applications, such as ceramics, electronics, optoelectronics, photovoltaics, biomedical, magnetic data storage, etc. The term ‘hydrothermal’ comes from the earth sciences. Typical processing conditions of the hydrothermal method require high temperatures and a high-pressure apparatus called ‘autoclave’ [1–4]. The general hydrothermal operating condition is that the range of boiling point of water should be from 100 °C to 374 °C. The hydrothermal method is very useful when there is difficulty in dissolving precursor

solutions at low temperatures, and it also enables the growth of nanostructures at high vapor pressure near their melting point at normal conditions. The size of the particle and morphology of the samples prepared by using this technique can be controlled by altering variables, such as concentrations of reactant solution, temperature, pressure, choice of additives/solvents, and aging period. Hydrothermally synthesized materials can be anhydrous, crystalline, or amorphous, depending on the processing conditions maintained during synthesis. The advantage of this technique is that particle size and shape can be controlled simultaneously by varying the chemical compositions, stoichiometry, etc. The powders synthesized using this method have a crystalline structure in most of the cases and do not require calcination processes (or very low temperature) and milling treatment, and large-scale production of nano and micro-sized particles is also possible. However, the main drawback of the hydrothermal technique is the difficulty in controlling the nanoparticle growth processes. One more drawback is the requirement of a long-time duration to raise the temperatures of the solution in an autoclave setup.

2.2.2 Facile peroxide precipitation method

The peroxide precipitate route is a facile technique where one can use a variety of solvents including hydrogen peroxide. The facile peroxide precipitation route is an important technique for the synthesis of oxide nanomaterials. This technique involves precipitation reactions and simultaneous occurrence of nucleation, growth, and agglomeration processes as shown in the schematic representation in Fig. 2.1. Typically, a controlled release of cations and anions assist in regulating the nucleation and growth kinetics, which helps in the preparation of monodispersed nanoparticles [5]. The products synthesized from the facile peroxide route are insoluble species and are generally formed under conditions of high super-saturation. During the nucleation process, numerous smaller particles are formed; whereas, in secondary processes, the Ostwald ripening and aggregation formed affects the size,

morphology and properties of the product phase. One of the main characteristics of this technique is the formation of oxides from an aqueous solution as well as a non-aqueous solution with possibilities to modify the surface states of the products homogeneously. The precipitation is followed by filtering, drying, and calcination steps. This technique is a simple and fast preparation method with easier control of particle size and composition. The average particle size can be controlled by varying parameters such as reaction period in an aqueous medium, pH of the medium, reaction temperature, and molar ratio/or concentration of the salts. Moreover, this synthesis process does not involve any expensive organic solvents.

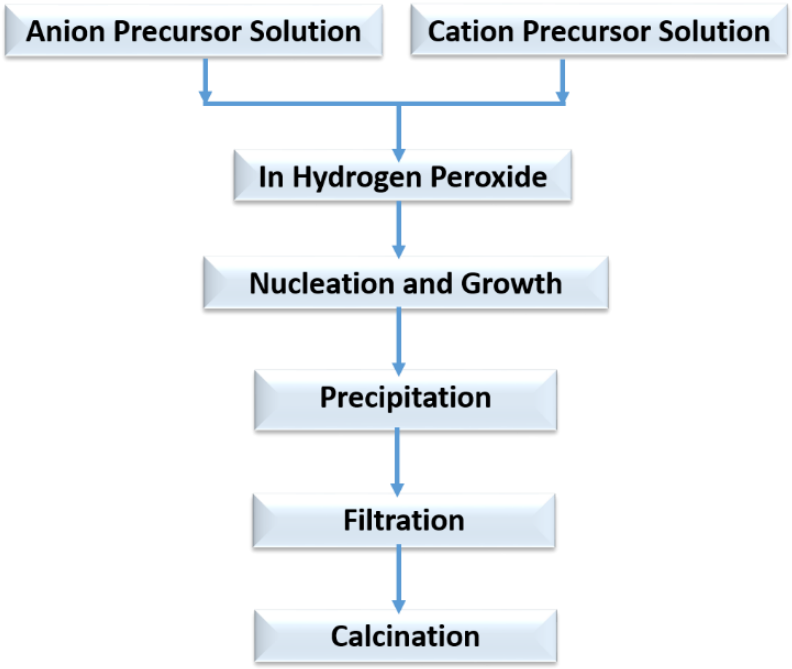

Fig. 2.1. Schematics of the facile peroxide synthesis route.

2.3 Chemical spray deposition of transparent conductive substrates

Chamberlin and Skarman in 1966 developed solar cells by depositing cadmium sulfide films using chemical spray pyrolysis method [6]. Due to the simplicity of this method and its suitability for large-scale production, it has attracted many researchers to develop thin films of

transparent conducting oxides (TCO) on suitable substrates. In the spray deposition process, a precursor solution employing a pressurized neutral gas arrives at the substrate in the form of very fine droplets. The deposition parameters can be varied to result in thin films with controlled porosity, desired refractive index, and stoichiometry. The chemical spray pyrolysis unit mainly consists of a spray nozzle, precursor stock solution, hot plate with a controller, and air compressor or gas propellant. Airblast is usually used to deposit large-area films, and generally, a stepper motor is used to move the spray nozzle or substrate for depositing uniform thin films [7]. However, in the present work, the spray nozzle is kept static (Fig. 2.3(a)). The quality and properties of the films depend largely on the preparation conditions such as substrate temperature, spray rate, the concentration of the solution, etc. [8]. Spray pyrolysis has been utilized not only for depositing thin films of simple binary and ternary oxides but also to obtain films of complex metallic spinel oxides, and multi-component transparent conducting oxides (TCOs) for use as electrodes and conducting substrates in various applications [9,10].

2.3.1 Mechanism of spray deposition and film formation

Thin-film deposition by using the spray pyrolysis technique can be divided into three major steps:

1) Atomization of the precursor solution, 2) transportation of the resultant aerosol, and 3) controlled decomposition of the precursor aerosol on the surface of the substrate [11]. During atomization, a custom-made atomizer with a fine nozzle (≅ 0.3 mm) was used to spray the precursor solution [8]. In an aerosol, the droplet is transported onto the surface of the heated substrate and it eventually evaporates. In the spray pyrolysis method, it is desired that a maximum number of droplets strike the substrate. The precursor to a solvent concentration should be optimal and not exceed the solubility limit of the solute. This should be maintained since it may lead to porous and hollow particle formation which is not desired since it might increase the film roughness and deteriorate the physical properties of the film.

During decomposition, many processes such as spreading of the droplet, evaporation of the residual solvent, and decomposition of the precursor occur simultaneously when an aerosol droplet hits the substrate's surface. With an increase in the substrate temperature, some of the following processes occur which are proposed by Viguie and Spitz [12].

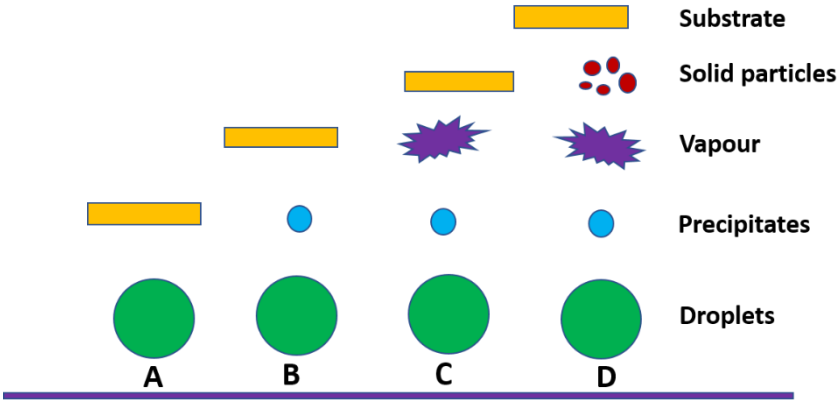

Fig. 2.2. Viguie and Spitz mechanism of spray deposition processes.

1. In-process A: In the low substrate temperature regime, the aerosol droplet strikes onto the substrate and does not decompose fully due to insufficient temperature.
2. In process B: At intermediate substrate temperature, the solvent evaporates fully during the flight of the droplet itself, and only dry precipitates hit the substrate, resulting in incomplete decomposition.
3. In process C: At the intermediate to higher temperatures, the solvent evaporates just before the aerosol droplet reaches the substrate and results in subsequent decomposition/oxidation of the solute on the surface of the substrate, resulting in a true CVD-like process.
4. Process D: The precursor vaporizes before it hits the substrate, and eventually, solid particles are formed upon reaction in the vapor phase itself.

Fig. 2.2 shows various stages of the Viguie and Spitz process which gives complete information on the aerosol dynamics. The film formation also depends on the process of droplet landing,

reaction, and evaporation of the solvent, which are related to droplet size and its momentum. Lampkin [13] showed that for fixed gas pressure and nozzle to substrate distance, depending on flow direction and velocity of the droplet, a droplet may flatten, slide along the surface, or hover motionless. An ideal deposition condition is the arrival of the droplet onto the substrate's surface just as the solvent is completely removed. In this thesis work, thin films are deposited over glass substrates using a static single nozzle spray technique. The main advantages of the spray technique are cost-effectiveness and easy control of the deposition parameters. Moreover, it does not require vacuum and high-quality targets for deposition.

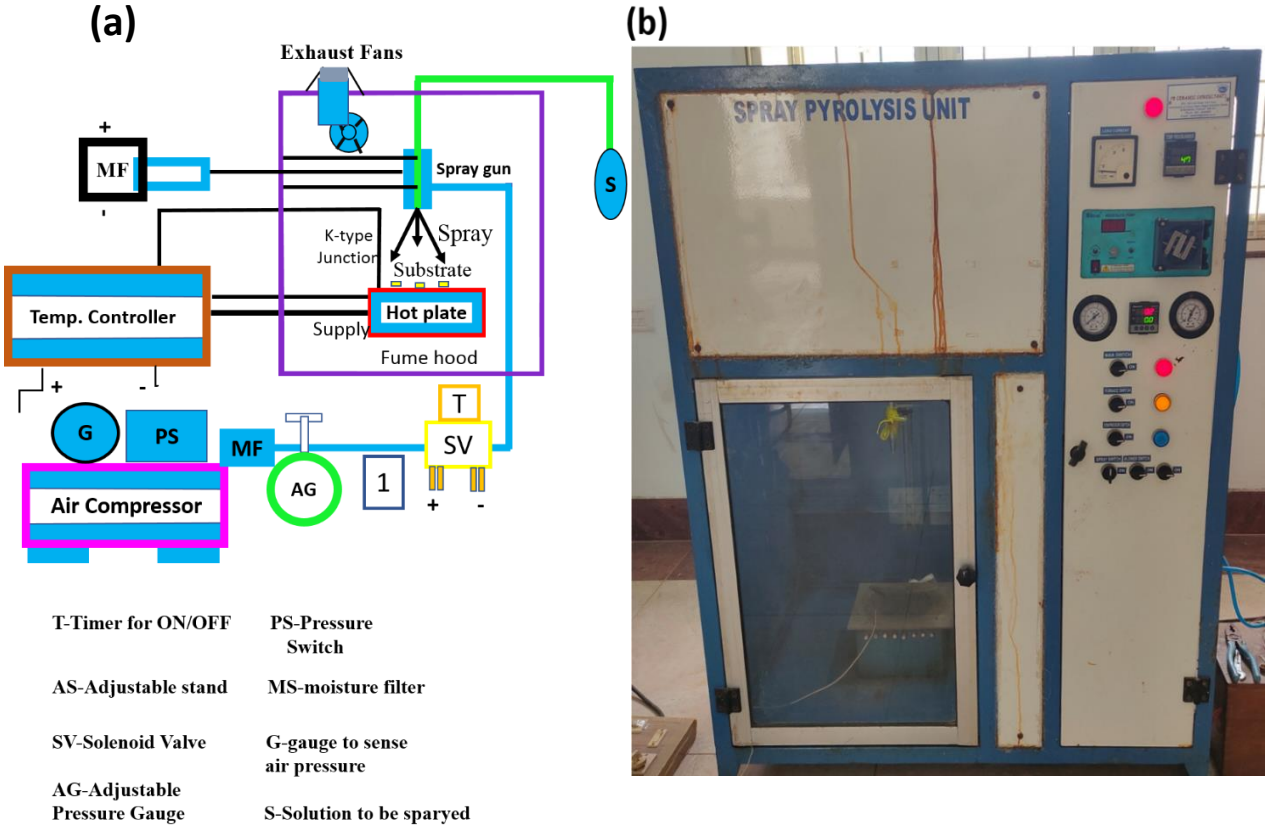

Fig. 2.3. (a) Schematics of chemical spray pyrolysis unit and (b) photograph of the custom-made instrument.

The main drawback of this technique is the time-consuming process and relative difficulty in controlling thickness and roughness, unlike PVD methods. In this thesis work, a chemical spray pyrolysis instrument shown in Fig. 2.3 (b) is used for the deposition of an antimony doped tin oxide (Sb-doped SnO_2) thin film as a transparent conducting oxide (TCO) which is an alternative to Fluorine doped tin oxide (FTO).

2.4 Extraction of dye from prickly pear fruit

Natural dyes are used as a photosensitizer in DSSCs since natural pigments have abundant sources, high availability, high absorbance, easy extraction, and are also environment friendly [14,15]. In this thesis work, considering the advantages and beneficial features of natural dyes, the focus is on the extraction of natural dyes from natural pigments of the fruits and roots of prickly pear (Cactus) to be used as a photosensitizer for DSSCs [16,17].

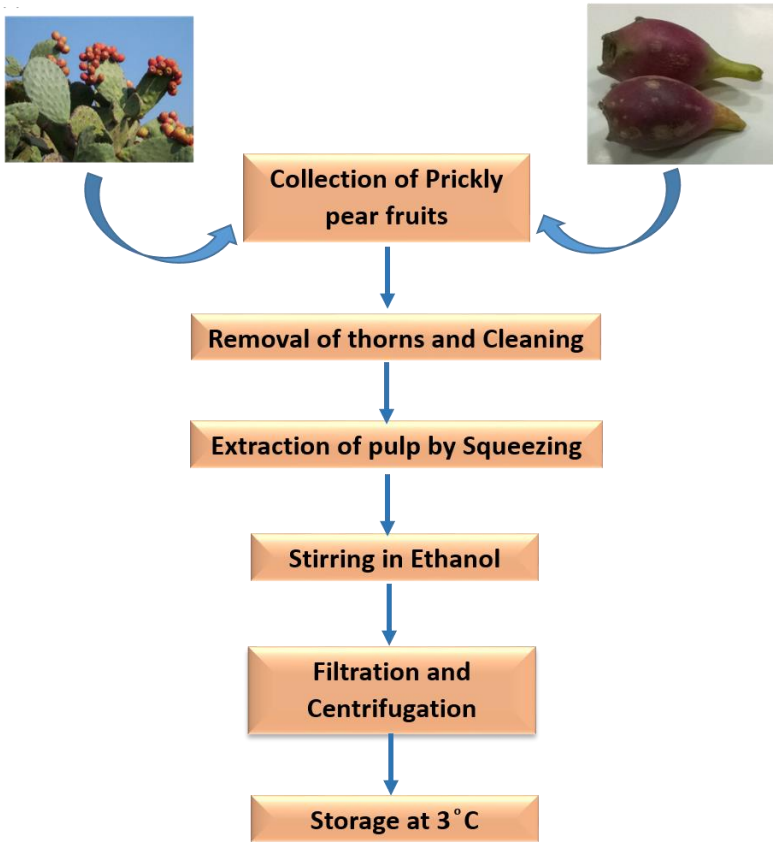

Fig. 2.4. Dye extraction process from the prickly pear fruit of cactus (Opuntia ficus Indica) plant.

2.4.1 *Preparation of natural dye solution*

Fully ripened prickly pear fruit pulp approximately around 50 g was taken and 50 ml of ethanol was added to it. This mixture was stirred for 2 h to extract a red-colored solution at room temperature. The red-colored extract was then filtered and centrifuged at 7000 rpm for 15 min at room temperature. This was followed by decanting to separate it from a suspension of insoluble particles like fibers and pulp. The extract was then carefully transferred into air-tight containers and externally covered with aluminum foil to protect it from light and then preserved in a refrigerator at 3 °C for further use. This process is schematically represented in Fig. 2.4.

2.5 Characterization techniques

2.5.1 X-Ray diffraction

X-ray diffraction (XRD) is the most efficient and commonly used technique to study the crystallographic structure of samples. It is a powerful non-destructive analytical technique that is commonly employed to determine the crystal structure, quality of the sample, phase purity, chemical composition, grain size, and strain in the material [18]. The schematic representation of the basic principle of X-ray diffraction is illustrated in Fig. 2.5. Diffraction occurs when a collimated monochromatic X-ray beam is incident on the sample. When an X-ray beam is incident on the sample, elastic scattering of the electron cloud of individual atoms takes place and spots are generated on a recording media. These spots depend on the size, shape, and symmetry position of the unit cell of the sample under study. Constructive interference occurs only for specific angles (θ) correlating with those planes (hkl) where the path difference is the integral multiple (n) of wavelength. Based on this, Bragg's law of X-ray diffraction is given by,

$$2d\ sin\theta = n\lambda \tag{2.1}$$

where λ is the incident wavelength of X-ray, d_{hkl} is the interplanar spacing between the respective hkl planes, 'θ' is the scattering angle, and 'n' is an integer known as diffraction order. To satisfy Bragg's condition, X-rays are diffracted at a particular angle by the oriented crystallites. Knowing the λ of the incident radiation and the angle θ, the interatomic spacing can be determined using this law. The peaks in the diffraction pattern acquire a nonzero width due to various factors such as instrumental resolution, finite grain size, and random strain [19]. The scan mode angle varies from θ-2θ where the incident X-ray beam makes an angle of θ with the surface of the sample. The movement of the detector is coupled to the X-ray source such that an angle 2θ is made with the incident direction of the X-ray beam. The resulting spectrum is plotted between the recorded intensity and 2θ. The reflection by the incident X-ray beam may occur in several directions but the measurement is taken only at one location that requires the condition where the angle of incidence (θ_i) equals the angle of reflectance (θ_r). When this condition is satisfied, the measurement of reflected X-ray intensity is possible.

Smaller-sized crystallites and significant strain are present in nanomaterials due to dimensional effects which cause peak broadening and shift in peak position compared to standard data. The change in d-spacing can be measured from the shift in peak position and it can give the variation in lattice constant under strain. The crystallite size (D) is calculated using Scherrer's formula.

$$D = \frac{K\lambda}{\beta cos\,\theta} \tag{2.2}$$

where K is the shape factor (≅ 0.9 for non-spherical particles), λ is the wavelength of incident radiation for Cu K_α, β is the full-width at half maxima of the diffraction lines. In this thesis work, characterization of the synthesized nanopowders and films is carried out at room temperature using X'pert High Scorer-Panalytical Diffractometer with a Cu K_α target of radiation; λ=1.5406 Å (Model: XPERT-PRO). The X-ray diffraction spectrum is input to an

advanced program such as Rietveld refinement and the data is compared with the Joint committee on powder X-ray diffraction standards (JCPDS) PCPDFwin database.

2.5.2 Field emission scanning electron microscopy

Field emission scanning electron microscopy (FESEM) is a tool of choice for researchers and industries due to its scope to image the structure of materials at submicron resolutions, and is a type of electron microscope capable of producing high-resolution images of a sample's surface. The FESEM gives an ultra-high magnification of the specimen at a very fine scale of 100-nanometer range. It is the most useful instrument to analyze the topography, morphology, and chemical composition of materials with a high resolution and depth focus [20]. A schematic representation of FESEM is depicted in Fig. 2.6.

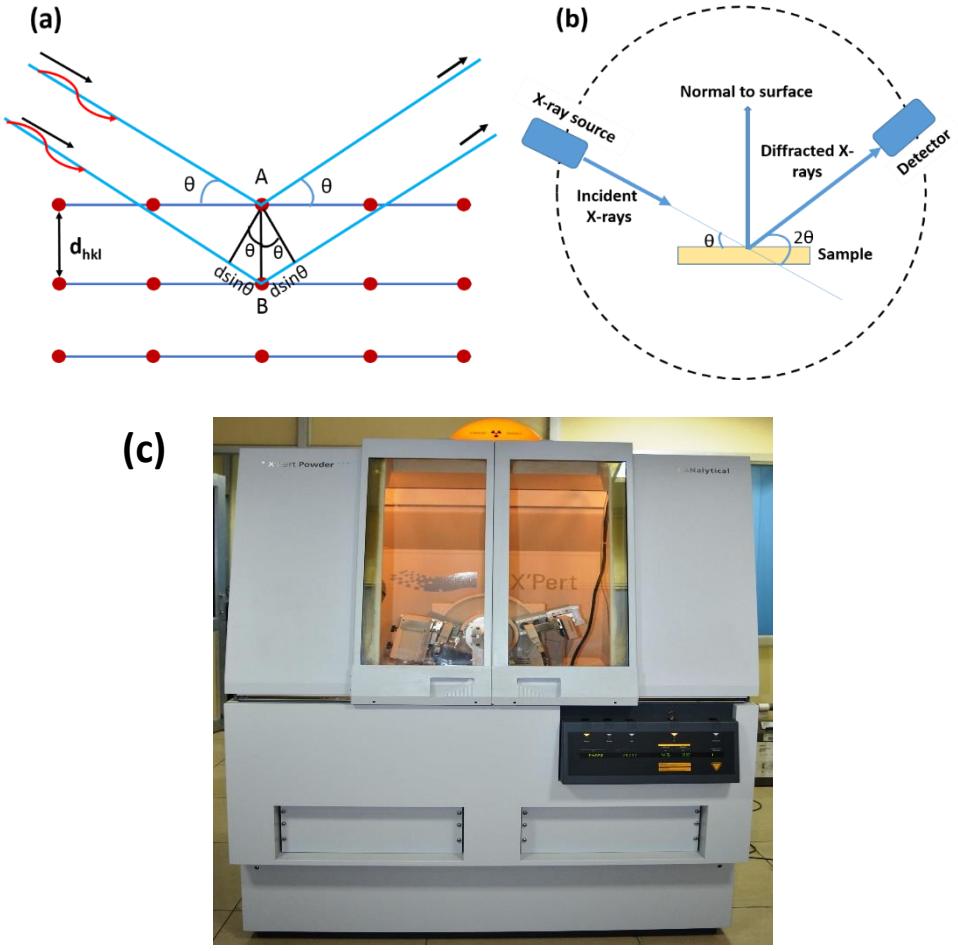

Fig. 2.5. (a) Schematic representation of Bragg's law, (b) geometry of powder X-ray diffractometer and (c) the photograph of XRD instrument.

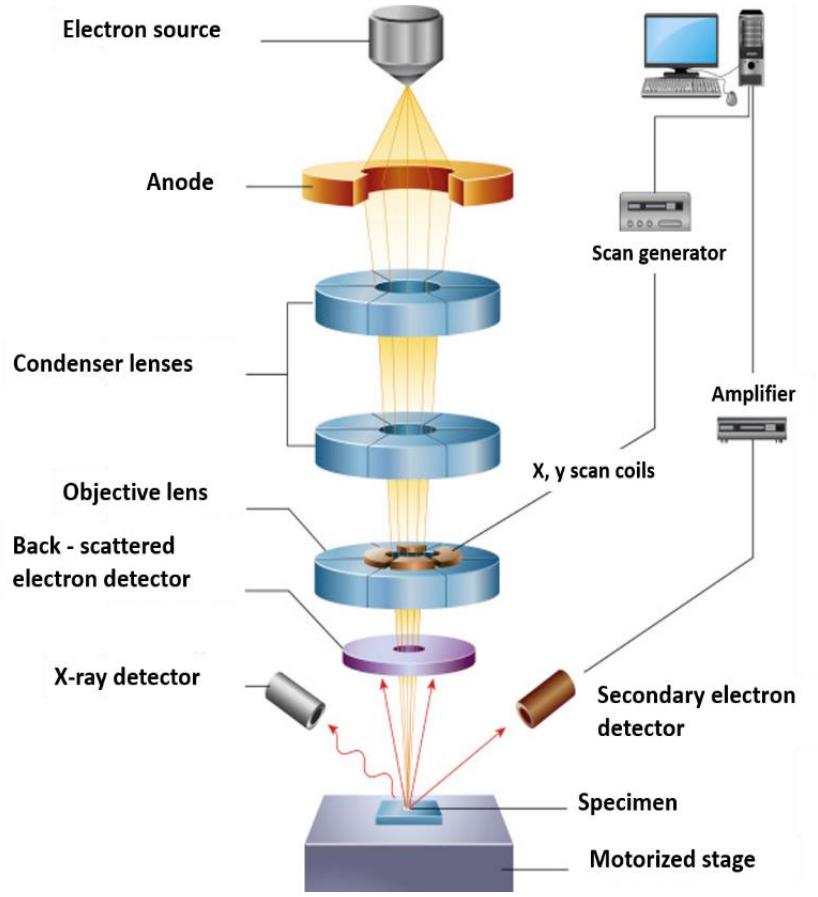

Fig. 2.6. Schematics of FESEM with core components showing the working principle [21].

In a typical FESEM, thermionic electrons are emitted from a tungsten filament cathode electron gun. The electron gun having an energy ranging from 0.2 keV to 0.4 keV is focused with spot condenser lenses of diameter 0.4 nm to 5 nm. These highly accelerated electrons interact with the surface of the sample in two ways; one is by elastic scattering and the other by inelastic scattering. Elastic scattering happens when the energy exchange between the electron beam and the sample results in the reflection of high-energy electrons called primary electrons. Inelastic scattering is a result of the emission of secondary electrons from each spot on the sample. The velocity and angle of the secondary electrons relate to the structure of the sample. The secondary electrons are observed through a detector that produces an electric signal. This electric signal is amplified and transformed to be displayed as variations in the brightness of the image on the monitor or stored as a digital image.

Energy dispersive X-ray (EDX) is an analytical technique that is widely used for chemical analysis as well as qualitative elemental information and composition of the sample. For this thesis work, the surface morphology and chemical composition of the synthesized samples were analyzed using JEOL – JAPAN JSM 840-A and HITACHI, S-4300SE instruments.

2.5.3 Transmission electron microscopy

The transmission electron microscopy (TEM) technique is a suitable choice for the analysis of the structure and composition of the nanostructured specimen. The TEM consists of an electron gun, electrostatic lenses to focus electrons (both above and below the specimen), and a transmitted electron detection system. The transmission electron microscopy is the most powerful imaging technique wherein high-energy electrons are transmitted through the specimen and are focused by the post specimen lenses to result in an image. The photons are detected using a charged coupled device (CCD) and the image recorded by the parallel recording device can be viewed on a phosphor screen. The basic principle of TEM operation is the use of electron beam instead of light photons. A typical schematic of a TEM is shown in Fig. 2.7[21]. TEM contains a higher number of electromagnetic lenses than SEM. The electromagnetic lenses are arranged sequentially along the electron beam direction as an electron column. The column constitutes tungsten filament for thermionic emission of electrons, electrodes for the acceleration of electrons, electromagnetic lenses, sample holder, and CCD camera. Using electron energy, the condenser lenses present above the specimen focus the electrons into a beam of controlled diameter and convergence. The objective lens aligns the transmitted electrons to form the diffraction pattern and first image. Projection lenses magnify the images/diffraction pattern into the detection system of the CCD array and detect the image using a computer monitor. The atomic resolution becomes feasible in TEM because the wavelength of electrons is much smaller than that of the photons (2.5 pm at 200 keV). Most effectively, TEM is useful for the determination of particle size, shape, and to study their

arrangements in the sample [22]. Moreover, the d-spacing between lattice planes can be determined using the selected area electron diffraction pattern (SAED) technique in TEM using the relation:

$$dr = \lambda L \tag{2.3}$$

Where L is the distance between the sample and photographic plate, $L\lambda$ is known as the camera constant and r is the radius of the diffraction ring. In the present work, TEM measurements were performed using TALOS - F200S G2 instrument operating at 200 KV with a CMOS camera (4k x 4k) as an EDS detector.

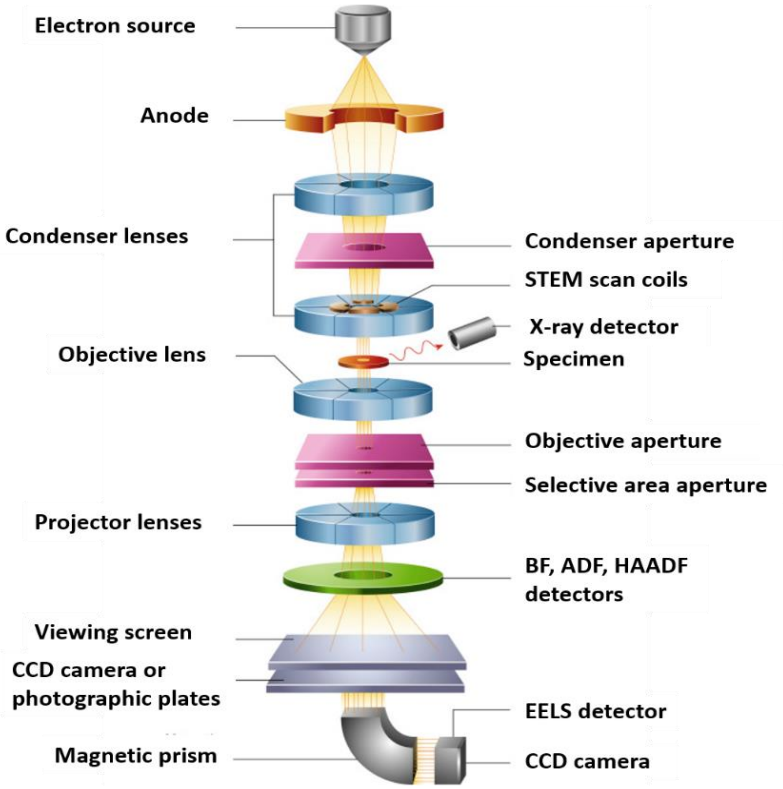

Fig. 2.7. Schematics of core components of the TEM

2.5.4 X-ray photoelectron spectroscopy

X-ray photoelectron spectroscopy (XPS) is an important technique used to quantitatively measure the charge state, elemental composition variation, and also to determine the binding energy of the elements present in a given sample. The XPS utilizes energy-dispersive analysis and photo-ionization of the emitted photoelectrons to explore the

composition and electronic state of the surface of the sample. The XPS is based on the photoelectric effect, where X-rays are continuously incident on the surface of the sample and atoms absorb the X-ray photon energy (hν), leading to ejection of electrons from a core level with maximum kinetic energy. The kinetic energy of each of the emitted electrons can be determined using a photoelectric equation given by

$$E_k = h\nu - E_g - e\Phi \tag{2.4}$$

where E_k is the kinetic energy of the electron, Eg is the binding energy of the electron measured relative to the chemical potential, hν is the photo energy, and Φ is the work function for a specific surface of the material. The eq. 2.4 gives the minimum energy to remove an electron from the surface of the material [23]. The ejected electrons are a function of their binding energies which are characteristic of their constituent elements. For each element, there is characteristic binding energy associated with each core atomic orbital, i.e., each element will give rise to a characteristic set of peaks in the XPS spectrum with respective binding energies. The intensity of the peaks indicates the presence of elements and concentration in specific charge states with respective binding energies. XPS is a surface sensitive technique due to the detection of generated Auger electrons that escape from the surface. The photoelectrons have less kinetic energy due to their inelastic mean free path in the sample. Due to inelastic collisions with the surface of the sample, the photoelectrons originating more than 20 Å to 50 Å beneath the surface cannot escape with sufficient energy to be detected. The schematics of working principle of X-ray photoelectron microscope (XPS) is shown in Fig. 2.8. In this thesis, samples are characterized using Theta probe angle-resolved X-ray photoelectron spectrometer (ARXPS) with 180° double-focusing hemispherical analyzer and PARXPS detector; a monochromatic X-ray source is used with micro-focused Al Kα and the X-ray spot size is 15 to 400 μm.

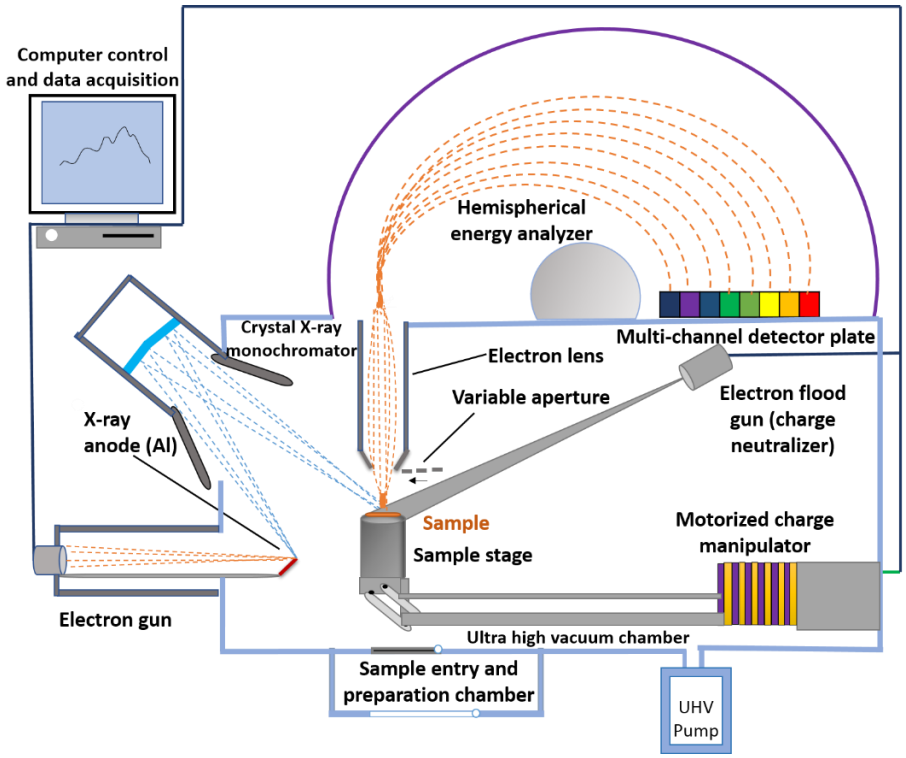

Fig. 2.8. Schematics of X-ray photoelectron spectrometer.

2.5.5 UV-Visible-diffuse reflectance spectroscopy

Ultraviolet-visible spectroscopy (UV-Vis) is a widely used technique to study the optical properties such as absorption, transmittance, and reflectance of the samples (liquids, solids, thin films, and powders). UV-Vis spectroscopy deals with the recorded absorption signals due to electronic transitions in the material. In semiconductors, when the energy of incident photons exceeds the bandgap, absorption takes place and the spectrometer records a corresponding signal; whereas, on the metal surface, free electrons vibrate coherently with the incident frequency, leading to resonant absorption. The two different operation modes of UV-Vis spectroscopy are, (1) Transmission mode and (2) reflection mode. Usually, in transmission mode, thin films and colloidal nanoparticles which are well dispersed in solvents are used. Optical measurements can be characterized by diffuse reflectance spectroscopy (DRS) mode for opaque thin films and those nanoparticles which are not dispersible in solvents. The optical phenomenon is known as diffuse reflectance and is commonly used in the UV-Visible region to obtain molecular spectroscopic information. The spectrum information is obtained by the

collection and analysis of surface reflected electromagnetic radiation as a function of wavelength (λ). The basic principle of a UV-Visible instrument is the alternative separation of a source light beam into two by a chopper; where one of the beams is passed through the sample and another beam through the reference sample. The detector, usually a photodiode alternates between measuring the sample and reference beams. The sample absorbs energy from a beam of radiation and the amount of energy absorbed depends on the number of samples. The amount of radiation absorbed at each wavelength is measured to get the spectrum. Here, the quantity and concentration of the sample are deciding factors for absorption. Using the Beer-Lambert law, one can determine the concentration of the absorbing species.

$$A = \log_{10}(I_0/I) = \varepsilon c l \qquad (2.5)$$

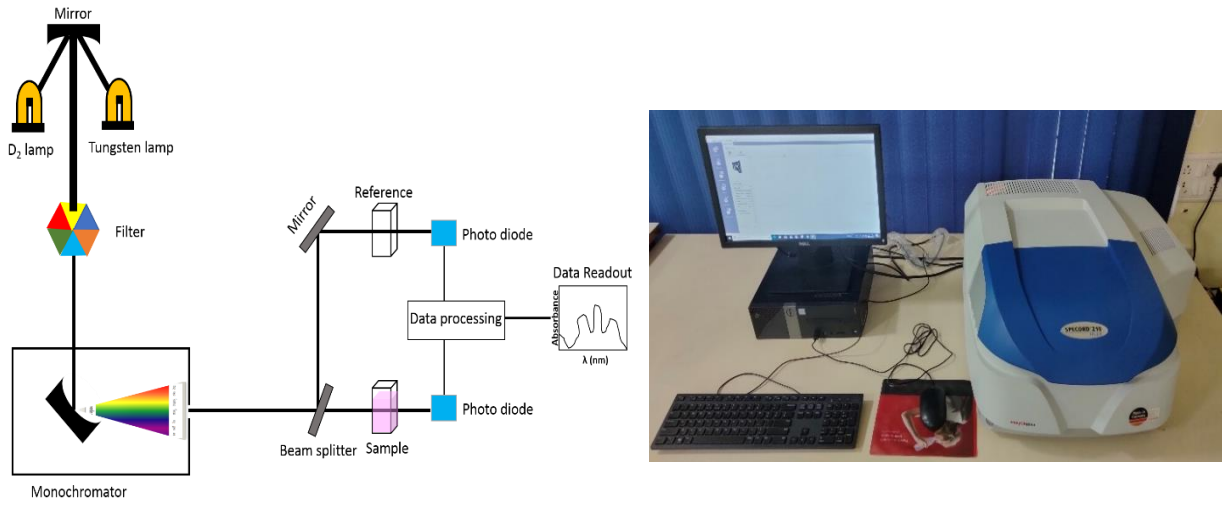

Fig. 2.9. (a) Schematic representation of basic working principle of UV-Visible spectroscopy and (b) photograph of an UV-Vis DRS spectrometer.

where A is the measured absorbance, I_0 is the intensity of the incident light, I is the transmitted intensity, L is the path length through the sample, c is the concentration of the absorbing species and ε is the extinction coefficient. The bandgap is estimated using the Tauc relation [24]. The basic working mechanism, schematic diagram, and photograph of the UV-Visible spectrometer are shown in Fig. 2.9. In this thesis, UV-VIS DRS spectrometer measurements are carried out

using Analytik Jena SPECORD 210 PLUS double-beam spectrometer in the wavelength range from 185 to 1200 nm with five variable slit widths.

2.5.6 Fourier transform infrared spectroscopy analysis

Fourier transform infrared spectroscopy (FTIR) is a useful traditional method to identify the presence of typical functional groups in a molecule of either organic or inorganic compounds. The principle of FTIR is based on vibrations of the atoms within a molecule of a compound which leads to the identification of the types of chemical bonds in the molecule [25]. This technique is useful to quantify some components of the unknown mixture and for the analysis of solids, liquids, and gases. The infrared absorption spectrum represents a molecular fingerprint (Stretching and bending modes). IR spectrometer involves different modes such as twisting, bending, rotation, and vibrational motions of atoms in a molecule. The sample interacts with IR radiations and the incident radiation is absorbed at particular wavelengths where the simultaneous occurrence of the multiplicity of vibrations takes place, leading to transmission of all other frequencies. The resulting absorbed energy and frequencies give the IR spectrum. The FTIR measurements in this thesis are carried out in the IR frequency range from 4000 to 400 cm^{-1}. Fig. 2.10 shows the schematics of the components and photograph of an FTIR spectrometer. Typical FTIR spectrometer components are IR source, sample cell, beam splitter, amplifier, A/D converter, and detector. The electromagnetic radiation from a monochromatic source is passed through an interferometer to the sample before reaching the detector. The interferometer has a beam splitter which is used to split the light source into two arms. Each of those light beams is reflected back to the beam splitter. The interferogram receives the resulting signals with all the frequencies simultaneously. The individual vibrational frequencies can be decoded by the Fourier transformations which provide information about the spectrum analysis using a computer. In this thesis work, the functional groups present in the

dye extracted from prickly pear fruit are analyzed using PerkinElmer Spectrum - 100 (4000-400 cm^{-1} range) FTIR spectrometer.

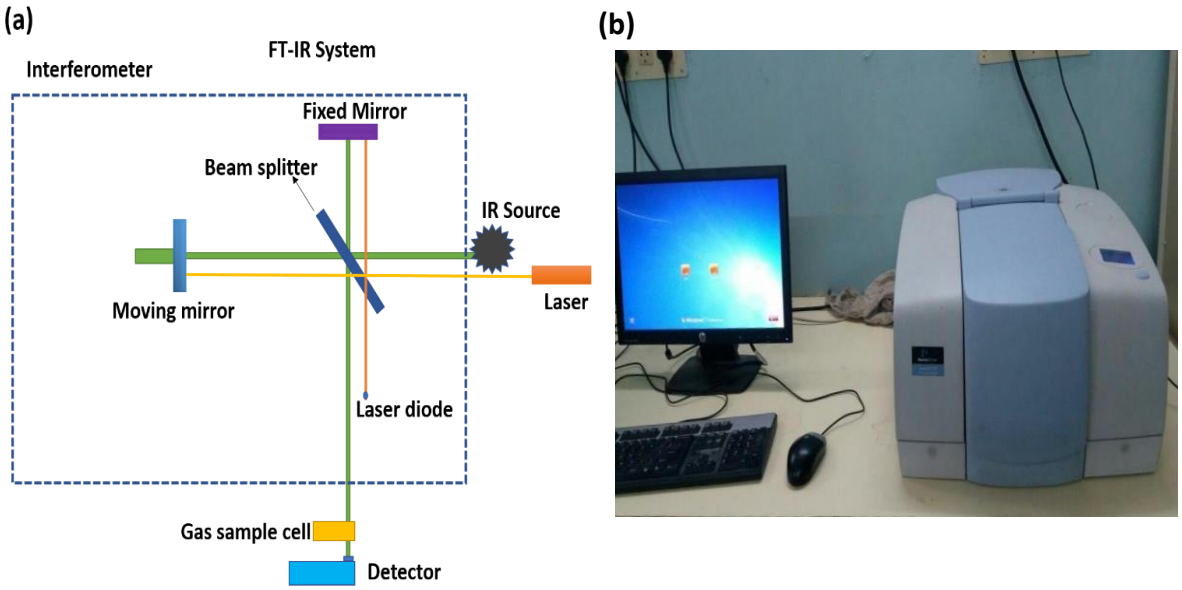

Fig. 2.10. (a) Schematic representation of working principle of FTIR spectroscopy and (b) photograph of an FTIR spectrometer.

2.5.7 Atomic force microscopy

The Atomic Force Microscopy (AFM) is a type of cantilever-based instrument with a high resolution developed by Binnig and Rohrer [26]. An AFM can generally measure vertical and horizontal deflections of a cantilever with Pico meter resolution. To achieve high-resolution imaging measurements, optical cantilevers are mostly used in atomic force microscopes comparable to an interferometer. The optical lever functions by reflecting off a laser beam from the back of the cantilever. The basic working principle and block diagram of AFM are shown in Fig. 2.11. The AFM mainly consists of a laser source, cantilever, and detector. The impact of the attractive or repulsive force between the tip and the sample is recorded as an AFM image. Here, the forces are not measured directly but estimated using Hooke's law by measuring the deflection of the lever by knowing the stiffness of the cantilever [27].

The cantilever deflections emerge due to the electrostatic force between the tip and the sample, and also due to the attraction of Vander Waals forces between the inter-atomic species. Therefore, the atomic force microscope measures contours of constant attractive or repulsive forces. If the tip is scanned over the surface of the sample, then the deflection of the cantilever can be recorded as an image that represents the topology of the sample's surface (deflection image). The detection is made so sensitive that the forces can be detected as small as a few pico-newton. In the present work, the surface topology of the thin films is characterized using NT-MDT Solver Pro microscope in the semi-contact mode and Nova software is used to analyze the imaged data.

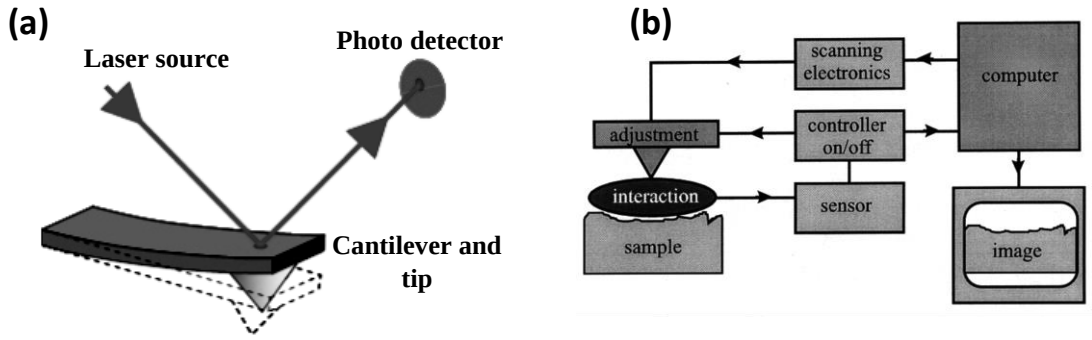

Fig. 2.11. (a) Schematics of operation of optical lever by reflecting a laser beam from the back of cantilever (b) block diagram of the entire unit.

2.5.8 Thickness measurement by stylus profilometer

Thickness is the most important parameter for thin films. A profilometer is a basic tool that quickly measures the physical thickness of films, provided a sharp edge of the film is available. Various methods are adapted for measuring the film thickness. Some of the thickness measurement methods available are ellipsometry, multiple beam interferometry, spectrophotometry, and stylus profilometry. Among these, the stylus profilometer is an accurate and reliable technique.

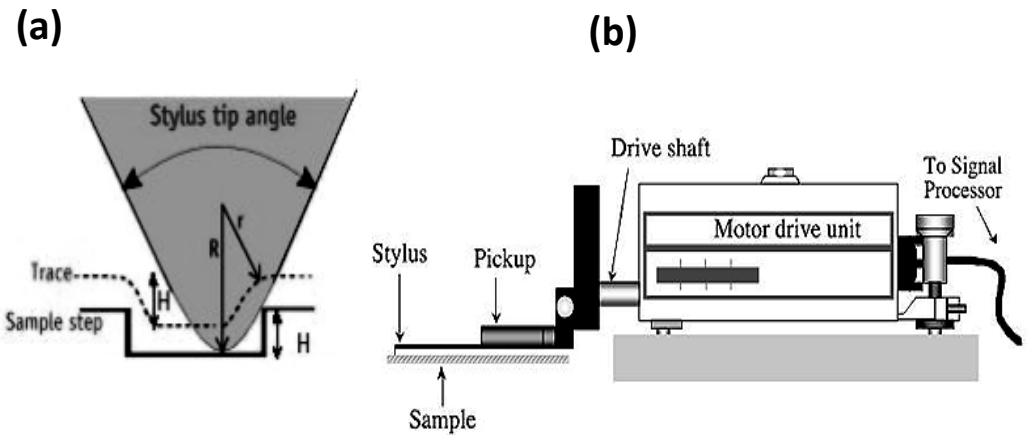

Fig. 2.12. (a) Schematics of **s**tylus profiler tip over the surface of sample and (b) depiction of the entire unit.

A stylus profilometer drags a diamond tip on the film surface with very feeble pressure to generate information about the surface topography [28]. The motion of the tip actuates a Linear Variable Differential Transducer (LVDT) that converts movement into an equivalent electrical signal. LVDT is a highly sensitive transducer but the tip of the profiler is conical and has a finite round shape that interacts with the surface of the sample being scanned. The vertical sensitivity is in the nanometer range but steep edge profiles are distorted due to the shape of the tip (Fig. 2.12). This technique also measures the profile along a line on the sample surface, and many such lines must be scanned to map the entire surface. The involvement of contact with the surface is the major drawback of this technique since it either alters the surface or damages the probe tip. The measurements in this thesis are carried out using DektakXT, Bruker.

2.5.9. Hall effect and linear four-probe

Hall effect is an important measurement to determine the electrical properties of thin films for transparent conducting electrodes (TCE) applications. The electrical transport properties of thin films depend on their thickness as well as structural and surface properties. The electrical transport properties can be estimated from Hall effect measurement using van der-Pauw geometry and one can also distinguish the type of conduction (n-type or p-type),

measure the carrier concentration, mobility, and conductivity of the semiconducting materials. The basic working principle of the Hall effect and photograph of the instrument are shown in Figs. 2.13 a and b. The Hall effect states that when a current-carrying conductor (I_H) or semiconductor is placed in a perpendicular magnetic field (B), a voltage can be measured at a right angle to the current path. This effect of obtaining measurable voltage difference (V_H) is the so-called Hall effect [27]. In this work, Hall measurements are carried out using the Ecopia instrument (Model: HMS 3000, Resistivity range 10^{-4} to 10^{7} Ω cm). To determine the sheet resistance and resistivity of thin films, a homemade four-probe setup is used along with the Keithley multimeter 2010. The sheet resistance of the film is calculated using the relation,

$$R_{Sheet} = F \times (V/I)\ (\Omega/\square) \qquad (2.6)$$

where F (4.532) is the correction factor for the probe configuration used, I is the current applied, and V is the voltage drop measured. The photograph of the homemade four-probe unit is shown in Fig. 2.13c.

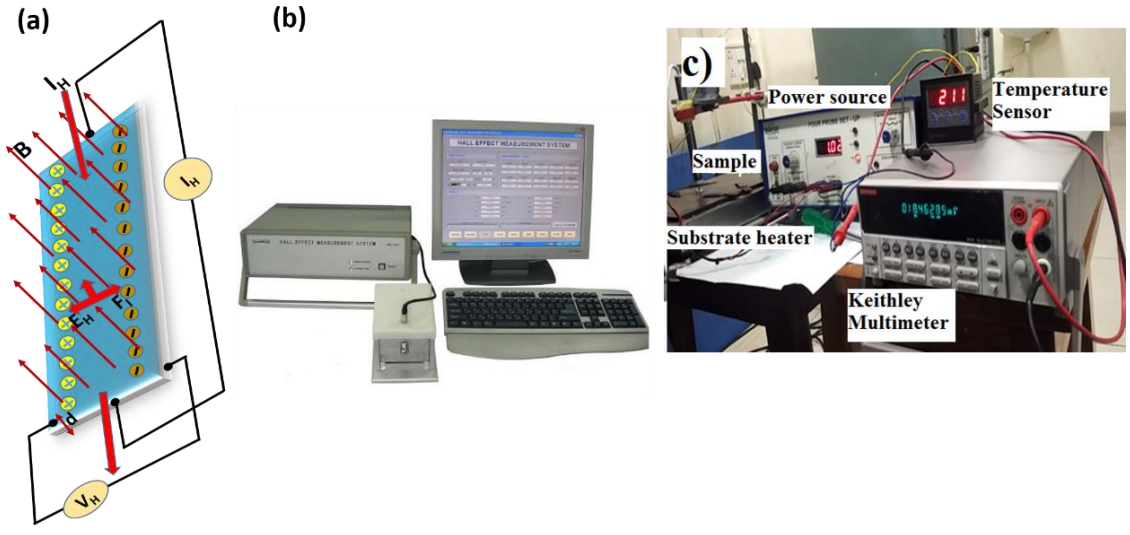

Fig. 2.13. (a) Schematics of working principle of Hall effect, (b) photographs of Hall effect instrument and (c) homemade linear four probe unit.

2.5.10 Contact angle measurement

The contact angle (CA) measurement is a tool used to understand the surface characteristics of the film or any solid surface when it comes into contact with a liquid droplet, and is a key parameter in surface science. The shape of a liquid droplet on the solid's surface reveals the aspects of surface wettability. It mainly depends on the interaction between the liquid and solid at the interface (or point of contact). Wettability provides a simple and reliable means for surface engineering. Surface wettability research can be used as a diagnostic method to evaluate beforehand the quality/performance of coated thin films when used as photoanode in DSSCs. This helps to understand indirectly the dye loading capacity [29,30] or the electrolyte infiltration behavior of a photoanode film without actual device fabrication [31]. The surface tension of droplets reflects the surface energy which is directly related to the surface properties.

From the theoretical point of view, Young's equation remains the fundamental equation in the science of surface wetting [32]. Assuming an ideal solid surface, it relates the contact angle of a drop on a surface to the specific energies of the solid–vapor (γ_{sv}), the liquid-vapor (γ_{lv}), and solid-liquid (γ_{sl}) interfaces.

$$\gamma_{lv} \cos \theta_Y = \gamma_{sv} - \gamma_{sl} \qquad (2.7)$$

Several parameters can affect the contact angle value; those are surface roughness, functional groups present on the surface, porosity, surface energy, and impurities or cleanliness. Among these, surface roughness is considered to be a parameter controlling the surface contact angles. Based on the surface roughness values, the Wenzel and Cassie models are generally used to explain the contact angle [33]. The schematics of the contact angle instrument with the necessary components is shown in Fig. 2.14.

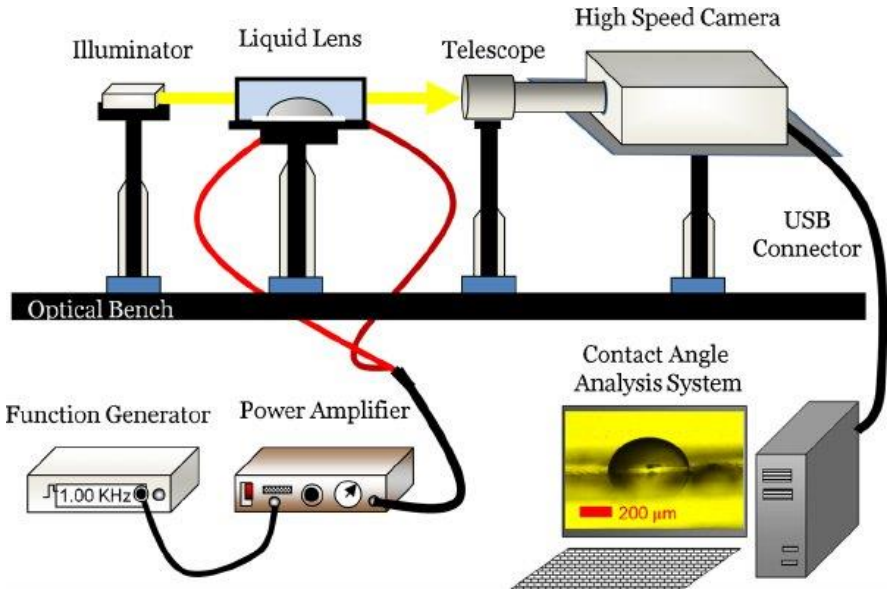

Fig. 2.14. Schematics of the experimental set up used to measure the contact angle.

The Wenzel equation is given as follows [34],

$$cos\theta_W = r_W cos\theta_Y \qquad (2.8)$$

where θ_W and θ_Y are Wenzel's contact angle (measured) and Young's contact angle (for ideal surface), respectively. r_W is Wenzel's roughness factor defined as the ratio of the actual area of a rough surface to the geometric projected area.

2.6 Fabrication and characterization of Dye sensitized solar cells

2.6.1 Device fabrication

2.6.1.1 Substrate cleaning

Transparent conducting Fluorine doped tin oxide (FTO) glass substrates were purchased from Greatcell Solar Materials Pvt. Ltd. (sheet resistance 7 Ω/□, Australia). For the DSSC device fabrication process, FTO glass substrates were cut into pieces of size 1.6 cm x 1.2 cm using a diamond cutter. The FTO substrates were ultrasonically cleaned following a standard procedure in a sequence with soap solution, de-ionized water, acetone, isopropyl alcohol (IPA), and finally rinsed with ethanol and dried with nitrogen gas. The ultrasonically cleaned FTO

glass substrates were placed in a UV-Ozone cleaner equipped with high intensity Ozone UV lamp (Holmarc Tabletop UV-Ozone cleaner, Model: HO-TH-UVT250) to effectively oxidize residuals from the substrate surface. These UV-Ozone treated FTO glass substrates were used for the DSSC fabrication process.

2.6.1.2 Preparation of semiconductor nanoparticle paste for DSSC device fabrication

The cleaned FTO glass substrates were surface-treated with 0.05 M of $TiCl_4$ aqueous solution pre-treated for 30 min at 80 ºC and then rinsed with double deionized (DI) water followed by annealing at 500 ºC for 30 min. Then, a fine homogeneous paste was prepared using a mixture of nanopowders, 10 wt.% of ethylcellulose, 5 wt.% of α-terpineol (Sigma Aldrich), and ethanol using a homogenizer and gradually mixed to get a viscous paste. This viscous paste was continuously ground using pestle and mortar for 30 min to form a homogeneous paste. The prepared nanostructured paste was coated onto FTO glass substrates by doctor-blade method with a cell area of 0.25 cm^2 with subsequent annealing at 500 °C for 30 min under ambient atmosphere.

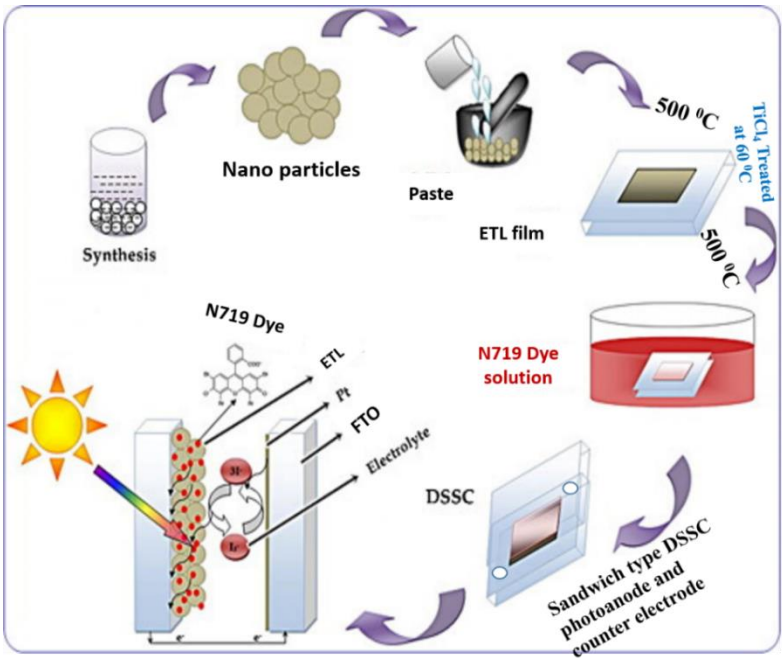

Fig. 2.15. Schematics of DSSC device fabrication steps using the synthesized semiconductor nanoparticles.

2.6.1.3 Assembling of DSSC device

For dye adsorption, the annealed films were soaked in 0.5 mmol of N719 dye (Greatcellsolar, Australia) solution dissolved in absolute ethanol under ambient conditions. To exclude the loosely adsorbed dye molecules on the surface, the films were thoroughly rinsed with ethanol. To prepare the counter electrodes, FTO substrates were first drilled using a diamond drill bit (model DREMEL 240) of diameter 0.7 mm for injecting the electrolyte into the DSSC cell. The platinum counter electrodes were prepared by drop-casting 5 mM chloroplatinic acid hexahydrate (H_2PtCl_6) dissolved in isopropyl alcohol on ultrasonically cleaned FTO substrates which were subsequently treated at 500 °C for 30 min under ambient atmosphere. Finally, both the photoanode and platinized counter electrodes were sandwiched using hot melt film (55 µm, Surlyn, Greatcellsolar) between them. For the electrolyte preparation, 0.5 M of 1-butyl-3 methylimidazolium iodide (BMII), 0.06 M of iodine (I_2), 0.1 M of LiI, 0.5 M of tert-butyl pyridine (tBP) were mixed in acetonitrile solvent and the entire mixture was stirred for 5 h. All these chemicals were procured from Alfa aesar and made use of without additional purification. After sandwiching both electrodes, the prepared I^-/I_3^- liquid electrolyte was infiltered through the drilled holes from the counter electrode side of the fabricated DSSC cell, and the drilled holes were covered with a thin glass coverslip at the rear side of the DSSC device.

2.6.2 I-V Characterization

A solar simulator is a device that can provide illumination approximate to natural sunlight for the measurement of current-voltage (I-V) characteristics of the fabricated DSSC devices. The simulator constitutes a Xenon lamp arc with an output power of 300 W and an illumination area around 2 x 2 inches. The standard condition of illumination at AM 1.5 spectrum with incident power 100 mW/cm^2 at room temperature 298 K is used for measurements. The Sun (source) is at an oblique angle of 48.2° which leads to a longer optical

path length through the Earth's atmosphere. I-V measurement is the most important tool to measure the photoconversion efficiency and figure of merit in solar cell devices. The I-V measurements yield parameters such as short circuit current (I_{SC}), current density (J_{SC}), open-circuit voltage (V_{OC}), fill factor (FF), maximum output power (P_{max}), maximum current (I_{max}), maximum voltage (V_{max}) and efficiency (η). All these parameters are already elaborated in section 1.5.5. These parameters are compared with that of a reference cell to determine the spectral mismatch factors for different devices. The solar simulator is optimized using Newport standard silicon reference cell. In this thesis, I-V measurements of the fabricated DSSC devices were performed using Oriel class AAA solar simulator (Model: 94023A, Class AAA, IEC/JIS/ASTM, Xenon lamp with 450 W power, illumination area is 2 x 2 inch). The photograph of the solar simulator is shown in Fig. 2.16.

Fig. 2.16. Photograph of the solar simulator with I-V measurement set up.

2.6.3 External Quantum efficiency

The basic idea in an external quantum efficiency experiment is to know the ratio between the number of photogenerated carriers per incident photons, as a function of the wavelength λ, under short circuit conditions,

$$EQE(\lambda) = \frac{n_e(\lambda)}{n_{ph}(\lambda)} \qquad (2.9)$$

This ratio is by definition taken when no voltage is applied to the solar cell. It is then possible to obtain the Jsc created by the solar cell under any wavelength, by integrating both quantities such as the short circuit current density under standard test conditions can be derived from EQE as follows,

$$J_{sc} = q \int_0^{\infty} \Phi(\lambda) EQE(\lambda)\, d\lambda \qquad (2.10)$$

In this equation, q is the electron charge and Φ(λ) is the photon flux corresponding to the AM1.5 spectrum.

2.6.4 Electrochemical impedance spectroscopy analysis

Electrochemical impedance spectroscopy (EIS) is an important technique to study electron transport kinetics and charge recombination processes in semiconducting metal oxides. To explore the charge transport kinetics of the fabricated DSSC devices, a frequency range from 10^{-1} to 10^{6} Hz was chosen with an arc amplitude of 10 mV for measurements of Nyquist and Bode plots. The Nyquist plot consists of three semicircles attributed to the impedances at various interfaces of the device. The first semicircle is the charge resistance (Z_2) between Pt/electrolyte interfaces at the high-frequency region, the second semicircle corresponds to the resistance (Z_3) at the interface of photoanode/Dye/electrolyte at the mid-frequency region and the third semicircle accounts for the diffusion of I_3- Z_1 in the electrolyte as shown in Fig. 2.17b. The series resistance (Z_1) is determined at a high-frequency range over 1 MHz and influences the resistance between the FTO and electron transport layer (nanoparticle-film interface). Based on Ohm's law, the complex impedance can be expressed as

$$Z\,(\omega) = \frac{V(t)}{I(t)} \qquad (2.12)$$

where V(t) is the voltage, I(t) is the AC current and ω is the frequency of the AC signal.

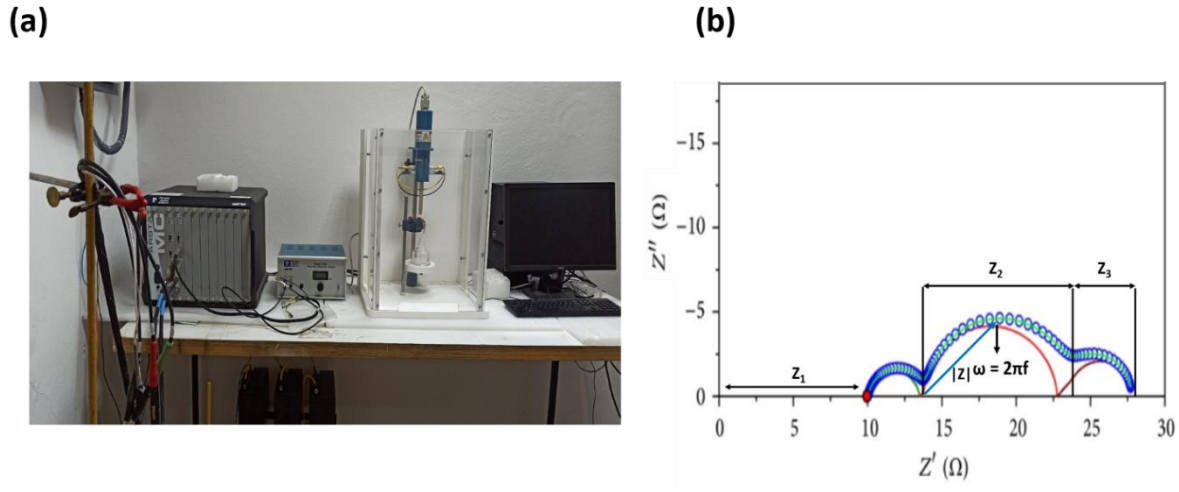

Fig. 2.17. (a) Photograph of EIS instrument and (b) model diagram of typical Nyquist plot.

For a sinusoidal system, the impedance of the resistor (Z_R) can be expressed as $Z_R = R$ and the capacitive reactance or impedance (Z_C) can be expressed as $Zc = \frac{1}{i\omega c}$. In cartesian coordinates, the complex impedance of an electrochemical system can be expressed as,

$$Z(\omega) = Z' + iZ'' \qquad (2.13)$$

where Z' and Z'' are the real and imaginary parts of Z, respectively. The photograph of the EIS instrument and model diagram of the Nyquist plot are shown in Fig. 2.17 (a and b). In this thesis, EIS analysis of the fabricated DSSC devices was carried out using PARSTAT MC (Model: PMC–200) multichannel potentiostat instrument, and data analysis was done using ZSimpwin software.

References

[1] G.W. Morey, Hydrothermal synthesis, J. Am. Ceram. Soc. 36 (1953) 279–285.

[2] L.G. Benning, T.M. Seward, Hydrosulphide complexing of Au (I) in hydrothermal solutions from 150–400 C and 500–1500 bar, Geochim. Cosmochim. Acta. 60 (1996) 1849–1871.

[3] A. Rabenau, The role of hydrothermal synthesis in preparative chemistry, Angew. Chemie Int. Ed. English. 24 (1985) 1026–1040.

[4] S. Sōmiya, R. Roy, Hydrothermal synthesis of fine oxide powders, Bull. Mater. Sci. 23 (2000) 453–460.

[5] C. Burda, X. Chen, R. Narayanan, M.A. El-Sayed, Chemistry and properties of nanocrystals of different shapes, Chem. Rev. 105 (2005) 1025–1102.

[6] P.S. Patil, Versatility of chemical spray pyrolysis technique, Mater. Chem. Phys. 59 (1999) 185–198.

[7] A.R. Balkenende, A. Bogaerts, J.J. Scholtz, R.R.M. Tijburg, H.X. Willems, Thin MgO layers for effective hopping transport of electrons, Philips J. Res. 50 (1996) 365–373.

[8] R.R. Chamberlin, J.S. Skarman, Chemical spray deposition process for inorganic films, J. Electrochem. Soc. 113 (1966) 86.

[9] G.J. Exarhos, X.-D. Zhou, Discovery-based design of transparent conducting oxide films, Thin Solid Films. 515 (2007) 7025–7052.

[10] A. Gupta, G. Koren, E.A. Giess, N.R. Moore, E.J.M. O'Sullivan, E.I. Cooper, Y1Ba2Cu3O7− δ thin films grown by a simple spray deposition technique, Appl. Phys. Lett. 52 (1988) 163–165.

[11] D. Perednis, L.J. Gauckler, Thin film deposition using spray pyrolysis, J. Electroceramics. 14 (2005) 103–111.

[12] J.C. Viguie, J. Spitz, Chemical vapor deposition at low temperatures, J. Electrochem. Soc. 122 (1975) 585–588.

[13] C.M. Lampkin, L. CM, Aerodynamics of nozzles used in spray pyrolysis, (1979).

[14] H. Hug, M. Bader, P. Mair, T. Glatzel, Biophotovoltaics: Natural pigments in dye-sensitized solar cells, Appl. Energy. 115 (2014) 216–225.

[15] G. Calogero, A. Bartolotta, G. Di Marco, A. Di Carlo, F. Bonaccorso, Vegetable-based dye-sensitized solar cells, Chem. Soc. Rev. 44 (2015) 3244–3294.

[16] G. Calogero, G. Di Marco, Red Sicilian orange and purple eggplant fruits as natural sensitizers for dye-sensitized solar cells, Sol. Energy Mater. Sol. Cells. 92 (2008) 1341–1346.

[17] G.C. DiMarco, S. Caramori, S. Cazzanti, R. Argazzi, A. DiCarlo, C.A. Bignozzi, Efficient Dye-Sensitized Solar Cells Using Red Turnip and Purple Wild Sicilian Prickly Pear Fruits, (2010).

[18] B.E. Warren, X-ray Diffraction, Courier Corporation, 1990.

[19] B.D. Cullity, S.R. Stock, Elements of x-ray diffraction, Prentice Hall, Up. Saddle River, NJ. (2001) 388.

[20] C.W. Oatley, D. McMullan, K.C.A. Smith, The development of the scanning electron

microscope, Beginnings Electron Microsc. (1985) 443–482.

[21] B.J. Inkson, Scanning Electron Microscopy (SEM) and Transmission Electron Microscopy (TEM) for Materials Characterization, Elsevier Ltd, 2016.

[22] P. Buseck, J. Cowley, L. Eyring, High-resolution transmission electron microscopy: and associated techniques, Oxford University Press, 1989.

[23] C.J. Powell, P.E. Larson, Quantitative surface analysis by X-ray photoelectron spectroscopy, Appl. Surf. Sci. 1 (1978) 186–201.

[24] J. Tauc, R. Grigorovici, A. Vancu, Optical properties and electronic structure of amorphous germanium, Phys. Status Solidi. 15 (1966) 627–637.

[25] G. Binnig, H. Rohrer, Helvetica Phys. Acta 55, 726 (1982), Sci Am. 253 (1985) 50.

[26] C.F. Quate, C. Gerber, C. Binnig, Atomic force microscope, Phys. Rev. Lett. 56 (1986) 930–933.

[27] L.J. van der Pauw, A method of measuring the resistivity and Hall coefficient on lamellae of arbitrary shape, Philips Tech. Rev. 20 (1958) 220–224.

[28] J.B.P. Williamson, Paper 17: Microtopography of surfaces, in: Proc. Inst. Mech. Eng. Conf. Proc., SAGE Publications Sage UK: London, England, 1967: pp. 21–30.

[29] A. Roy, P.P. Das, P. Selvaraj, S. Sundaram, P.S. Devi, Perforated BaSnO3 Nanorods Exhibiting Enhanced Efficiency in Dye Sensitized Solar Cells, ACS Sustain. Chem. Eng. 6 (2018) 3299–3310.

[30] P. Pratim Das, A. Roy, S. Das, P.S. Devi, Enhanced stability of Zn_2SnO_4 with N719, N3 and eosin y dye molecules for DSSC application, Phys. Chem. Chem. Phys. 18 (2016) 1429–1438.

[31] M.A. Gaikwad, M.P. Suryawanshi, P.S. Maldar, T.D. Dongale, A. V Moholkar, Nanostructured zinc oxide photoelectrodes by green routes M-SILAR and electrodeposition for dye sensitized solar cell, Opt. Mater. (Amst). 78 (2018) 325–334.

[32] T. Young, III. An essay on the cohesion of fluids, Philos. Trans. R. Soc. London. (1805) 65–87.

[33] K. Liu, X. Yao, L. Jiang, Recent developments in bio-inspired special wettability, Chem. Soc. Rev. 39 (2010) 3240–3255.

[34] R.N. Wenzel, Resistance of solid surfaces to wetting by water, Ind. Eng. Chem. 28 (1936) 988–994.

CHAPTER: 3

Hydrothermally grown nanostructured La-doped $BaSnO_3$ as photoanodes in DSSC

This chapter deals with the structural, morphological, optical, and electrical properties of the hydrothermally synthesized nanostructured La-doped $BaSnO_3$ ternary oxides for use as photoanode in DSSCs. The hydrothermal method with optimal pressure and temperature components yields interesting morphological nanostructures with high crystallinity and low agglomeration. Attempts are made to dope the Ba sites in $BaSnO_3$ with La ions by hydrothermal method. After characterizing the samples, the optimal nanostructured La-doped $BaSnO_3$ samples were also tested as alternative photoanodes in DSSCs. The effect of grain morphology and shape of the nanostructured La doped $BaSnO_3$ on the performance of DSSC are elaborated in this chapter.

3.1. Introduction

Dye-sensitized solar cells (DSSCs) are the third-generation solar cells that have received increased attention due to their low cost, environmentally-friendly nature, ease of fabrication, and high power conversion efficiency (PCE) as reported by Grätzel's group in 1991 using mesoporous TiO_2 [1,2]. The most widely used photoanode in DSSC is TiO_2 which is a wide-band-gap electron transport material suitable for photon harvesting. Other than TiO_2, binary oxide materials like ZnO, SnO_2, and Nb_2O_5 have also been investigated as electron transport materials in DSSCs [3–8]. Recently, researchers are focusing their attention on the ternary metal oxide materials based on their relevant valence orbital and electronic properties. Alkaline earth stannate materials with the general formula $RSnO_3$ (R = Ba, Sr and Ca) are studied by several researchers due to their vast technological applicability in areas like dielectrics, sensors, photocatalytic activity, and optoelectronics, etc. [9–14]. To overcome limitations of existing

binary photoanode oxides such as TiO_2 and ZnO, efforts have been made to explore the ternary metal oxide semiconductors such as Zn_2SnO_4, $BaTiO_3$, $SrTiO_3$, and $BaSnO_3$ (BSO) due to their ionization potential and electron affinity that can be easily modified by changing the atomic component by adopting appropriate synthesis strategy [15–20]. Perovskite $BaSnO_3$ is an n-type semiconducting material having wide band-gap energy of 3.2 eV suitable for band-gap tuning for photovoltaic and optoelectronic applications by doping with appropriate dopant elements [21,22]. The detailed structural aspects of this compound are as discussed previously in Chapter-1, Section 1.5.2.1**.** The perovskite structure offers the advantage of two different cation sites, one at the Ba^{2+} site and the other at Sn^{2+} site. In this way, the band structure and electronic properties of BSO can be tuned by substitution at the metallic lattice sites to enhance the properties for DSSC applications.

Presently, researchers adopt various methods such as solid-state reaction, co-precipitation, sol-gel, and other wet-chemical routes to prepare nanostructured $BaSnO_3$ materials. In all these reported methods, it has been observed that various parameters, synthesis process, reaction time, controlled reaction temperature, etc. influence the properties of nanostructured material. The prepared nanocrystalline $BaSnO_3$ powder should be of high phase purity, better crystallinity, a large surface area, and low agglomeration. To achieve these aspects, in this chapter, we have optimized conditions to obtain single-phase nanostructured pure and La-doped $BaSnO_3$ (La-BSO) material via hydrothermal method. The hydrothermal method with optimal pressure and temperature components yields interesting morphological nanostructures with high crystallinity and low agglomeration. An attempt is made to dope the Ba sites of $BaSnO_3$ with La by hydrothermal method and explored for the structural, morphological, and optical properties and are also tested as a photoanode in DSSCs.

3.2. Experimental methods

3.2.1 Materials

Barium chloride di-hydrate ($BaCl_2.2H_2O$) from Himedia, stannic chloride pentahydrate ($SnCl_4.5H_2O$, Sigma Aldrich), lanthanum (III) chloride heptahydrate ($LaCl_3.7H_2O$) from Himedia, and NaOH from Finar were used as precursors for preparing the pure and La-doped BSO compounds. The Ru complex-based dye molecules (N719, Dyesol), α-terpineol, and chloroplatinic acid were procured from Sigma Aldrich. A 0.5 M of 1-butyl-3 methylimidazolium iodide (BMII), 0.06 M of iodine (I_2), 0.1 M of LiI, 0.5 M of tert-butyl pyridine (tBP) were prepared in acetonitrile solvent to serve as an electrolyte. All the procured chemicals were used as such without any further purification. Deionized water was used as the main solvent for the synthesis of the samples.

3.2.2 Synthesis of nanostructured BSO and La-BSO

To synthesize BSO and La-BSO samples, appropriate amounts of the starting materials $BaCl_2.2H_2O$ and $SnCl_4.5H_2O$ were separately dissolved in 50 ml of deionized water and then mixed together. After continuous stirring for 1 h, aqueous NaOH was added until precipitates were formed and the suspension was continuously stirred further for 1h. The resultant slurry was transferred into a teflon-lined stainless-steel autoclave and heated at 180 °C for 24 h in an oven. Afterward, the precipitates from the autoclave were washed several times with deionized water to remove the byproducts until pH ≅ 7 was attained. The precipitates were then dried at 80 °C overnight. To dope La ions at the Ba sites of $BaSnO_3$, $LaCl_2.6H_2O$ precursor was added into the above solution depending on 'x' (x = 0, 0.01%, 0.03%, and 0.05%) to result in a $Ba_{1-x}La_xSnO_3$ compound. These 'as-prepared' samples were annealed at 1000 °C for 2 h in air and are referred to as BSO and La-BSO.

3.2.3 Synthesis of BSO and La-BSO paste

The binder was prepared with 95 wt % (19 g) of α-terpineol and 5 wt % (1 g) of ethyl cellulose by stirring overnight. 500 mg of La-BSO nanoparticles were weighed and ground for 30 min for de-agglomeration. Then, the La-BSO nanoparticles along with a stock binder solution in the ratio of 1 mg: 0.875 mg were ground for 15 min. Later, this mixture was added with pristine α-terpineol in the ratio of 1 mg: 1.25 mg and continuously ground using mortar and pestle until a smooth, homogenous paste was obtained. A similar procedure was followed for preparing the paste of all the prepared samples.

3.2.4 Photoanode preparation:

The prepared BSO and La-BSO paste was coated onto cleaned FTO glass substrates by marking an area of 0.25 cm^2 by doctor blading technique followed by annealing at 500 °C for 30 min. These annealed BSO and La-BSO films were treated in 0.04 M $TiCl_4$ aqueous solution at 100 °C for 1 h. The $TiCl_4$ treated electrodes were then rinsed in ethanol and DI water followed by annealing at 500 °C for 30 min in an ambient atmosphere.

3.2.5 Assembling of DSSC

After $TiCl_4$ treatment, the BSO and La-BSO films were soaked in a dye solution (0.3 mM of N719 dye prepared in absolute ethanol) at room temperature for 12 h. After the dye adsorption, the films were thoroughly washed with ethanol to remove the physically adsorbed dye molecules. The counter electrodes were drilled with fine holes to fill the electrolyte solution. The thin platinum layer was then coated onto the counter electrodes with chloroplatinic acid (10 mM in IPA) by spreading manually using a micro-pipette. After coating, the platinum films were then annealed at 500 °C for 30 min in air. Sandwich-type DSSCs were then assembled using the dye adsorbed films and platinum-coated FTO substrates with a hot-melted film (~60 µm, Surlyn spacer) between them at 130 °C using a hot plate. Finally, the

prepared iodide-based liquid electrolyte was infiltrated into the cell through the hole from the counter electrode side and sealed using coverslip glass and surlyn spacer.

3.3. Results and Discussion

3.3.1 Crystal structure analysis

The Rietveld refined (FullProf.2k, Version 7.00) XRD patterns of the hydrothermally synthesized nanostructured BSO and La-BSO samples obtained after annealing the powders at 1000 °C for 2h are shown in Fig. 3.1 (a-d). The Rietveld refinement of XRD data confirms the formation of single-phase samples with space group P*m-3m* having cubic symmetry. The pure BSO and La-BSO crystal structures are shown in Fig. 3.1 (e) and (f). The refined lattice parameters and cell volume of all the samples are listed in Table 3.1. The observed marginal decrease in lattice constant implies contraction of the lattice which might be due to the smaller ionic radius of La^{3+} (1.36 Å) when compared to that of Ba^{2+} (1.61 Å) [23,24]. The crystallite size obtained using the Scherrer formula (eq. 2.2) for the strongest (110) reflection peaks are 39 nm, 35 nm, 26 nm, and 34 nm for BSO, 0.01%, 0.03%, and 0.05% La-BSO samples, respectively. When La ion content increases from 0 to 0.05% in the BSO system at the Ba sites, a reduction in crystallite size is observed up to 0.03%, and an increase in size is observed for 0.05% La concentration. It is observed that the (110) diffraction peak slightly shifts to a lower angle upon doping of La^{3+} ions as shown in Fig. 3.1(g). This subtle shift in the peak position of (110) major plane upon substitution of La compared to undoped BSO implies the substitution of La into the Ba sites in $BaSnO_3$ perovskite structure.

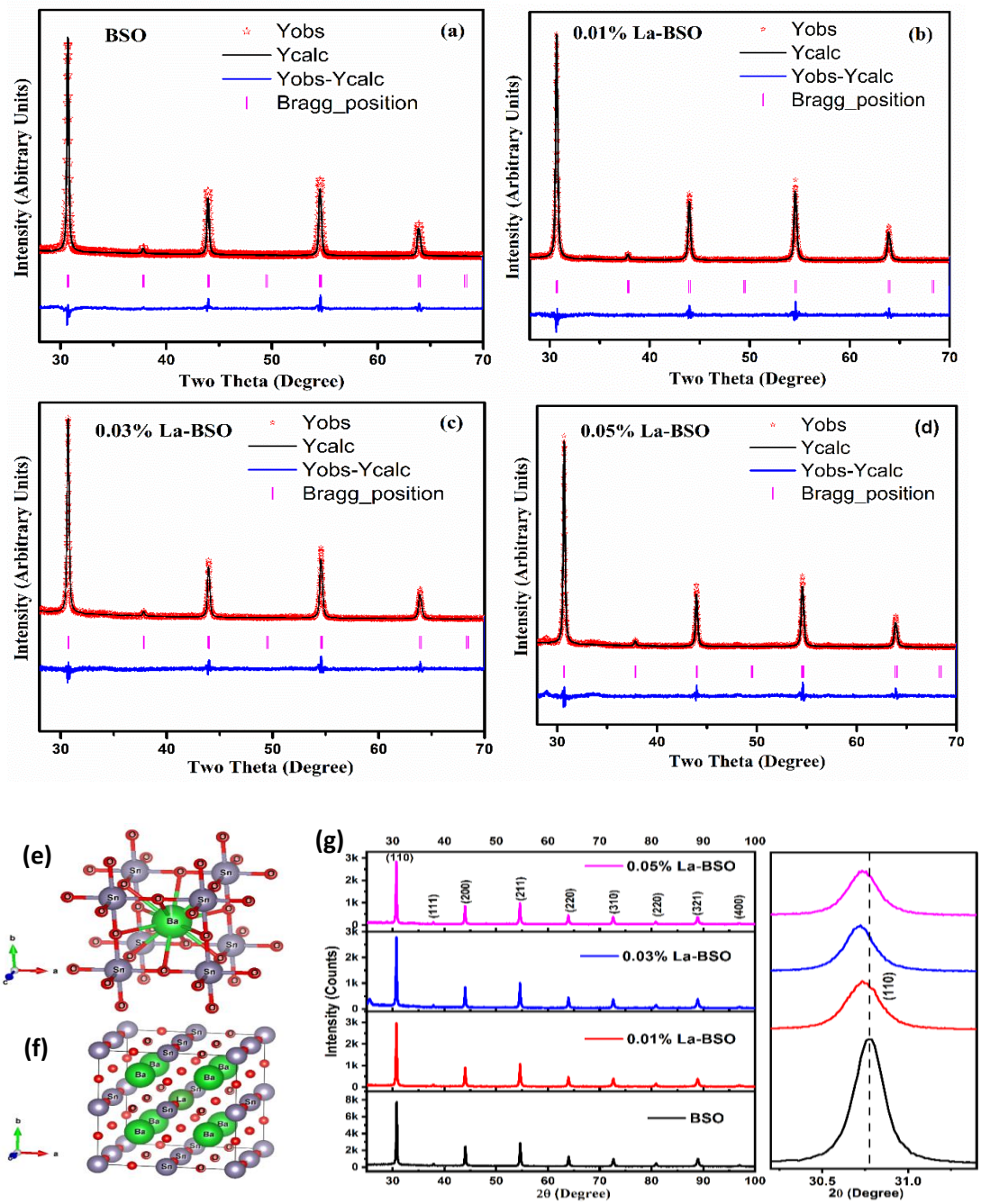

Fig. 3.1. Rietveld refinement of the XRD patterns of (a) pure BSO, (b) 0.01%, (c) 0.03% and (d) 0.05% La-BSO samples. Representative crystal structure images of (e) pure BSO and (f) La-BSO sample. (g) XRD patterns of La-doped BSO samples after annealing at 1000 °C/2h in air and expanded view of (110) plane indicates the peak shift as a function of La doping.

Table 3.1. Structural parameters and elemental composition of pure BSO and La-BSO samples.

Parameter	BSO	0.01% La-BSO	0.03% La-BSO	0.05% La-BSO
Lattice constants a = b = c (Å)	4.1191(2)	4.1189(1)	4.1187(2)	4.1191(2)
Cell volume	69.89	69.88	69.87	69.89
Chi^2	2.51	1.35	2.60	1.69
Elemental composition from EDX (Wt %)				
Ba	43.19	49.29	39.40	39.83
Sn	35.73	36.38	49.68	45.48
O	21.08	20.85	9.19	11.27
La	-	0.18	1.73	3.42

3.3.2 Scanning electron microscopy analysis

Morphological features of the hydrothermally prepared pure and La-BSO powders characterized by scanning electron microscopy (SEM) are shown in Fig. 3.2 (a-d). Here, it is observed that the pure BSO sample to has thicker rod-like features as shown in Fig. 3.2(a). Upon introducing 0.01% La ions, the morphology slightly changes from nanorods to a mixed morphology with coexisting particulate-like features as seen in Fig. 3.2(b). At 0.03 % of La doping, it is seen that this mixed morphology feature increases in number as shown in Fig. 3.2(c). Finally, for 0.05% La doping concentration, the agglomeration of nanoparticles has increases, thereby reducing the rod-like structures which are vividly seen in Fig. 3.2(d). The presence of Ba, Sn, O, and La elements are confirmed from the energy-dispersive X-ray (EDX) analysis shown in Fig. 3.2 (e-h). The elemental composition of hydrothermally synthesized BSO and La-BSO samples measured from energy-dispersive X-ray (EDX) analysis presented in Table 3.1 indicates near-stoichiometry with only a nominal deviation from the desired composition. The SEM images indicate the formation of mixed nanorods-particles morphology as a function of La doping which is graphically represented in Fig. 3.3(i).

3.3.3 Transmission electron microscopy analysis

Figure 3.3 (a-f) shows the transmission electron microscopy (TEM), high-resolution TEM, (HR-TEM), and selected area electron diffraction (SAED) patterns of the nanostructured BSO and 0.03 % La-BSO samples. The TEM image of the BSO sample indicates the presence of rod-like features with length around 200 – 460 nm and diameter around 50 – 90 nm (Fig. 3.3a), confirming the features observed in the SEM images (Fig. 3.2a). The d-spacing value of lattice fringes estimated from the HR-TEM image of BSO is 0.278 nm corresponding to the (110) crystallographic plane of the cubic BSO system (Fig. 3.3b). The SAED pattern of BSO (Fig. 3.3c) shows crystallographic reflections corresponding to (110), (111), (200), and (211) planes that match with the cubic phase of BSO, which also corroborates with the XRD analysis shown in Fig. 3.1. Figure 3.3(d) confirms the mixed nanorod-nanoparticle morphology for 0.03% La-BSO as evidenced in the SEM image Fig. 3.2c. The length and width of the nanorods are in the range 90 nm -115 nm and around 19 nm, respectively. The size of the nanoparticles in the 0.03% La-BSO with mixed morphology is in the range 13 nm - 26 nm. Upon doping La into the BSO system, the rod-like morphology disintegrates and tends towards a mixed rod-particle nanostructure. This distinct changeover to mixed nanorod-nanoparticle morphology results in the La-doped BSO samples prepared by the hydrothermal method. This observation indicates that the hydrothermal method along with La concentration yield control over the morphology of the La-BSO system. From Fig. 3.3(e), the measured d-spacing values of 0.272 nm belong to the (110) crystallographic plane. The SAED pattern shown in Fig. 3.3(f) shows a clear signature of polycrystalline nature with rings corresponding to the (110), (111), and (200) planes of the BSO system [25]. The SAED pattern of pure BSO indicate distinct spots (Fig. 3.3c) implying high crystallinity. Upon doping with La, the crystallinity reduces significantly due to the changeover in morphology, leading to a ring pattern (Fig. 3.3f), implying polycrystalline nature.

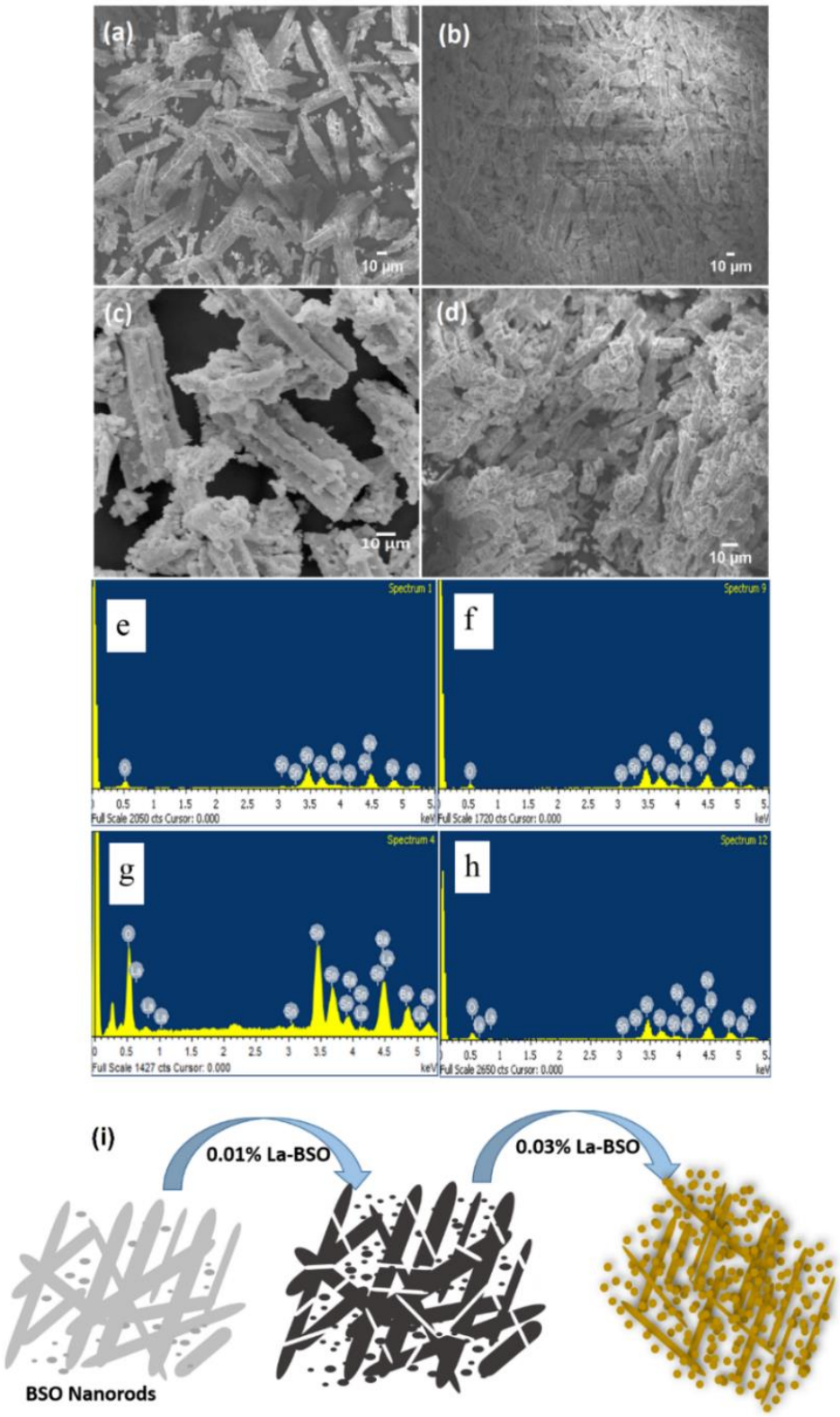

Fig. 3.2. SEM images as a function of La doping (a) Pure BSO (b) 0.01% La-BSO, (c) 0.03% La-BSO and (d) 0.05% La-BSO. The composition of samples from EDX analysis is shown in (e-h) and (i) graphical representation of formation of mixed nanorods-particles morphology as a function of La doping.

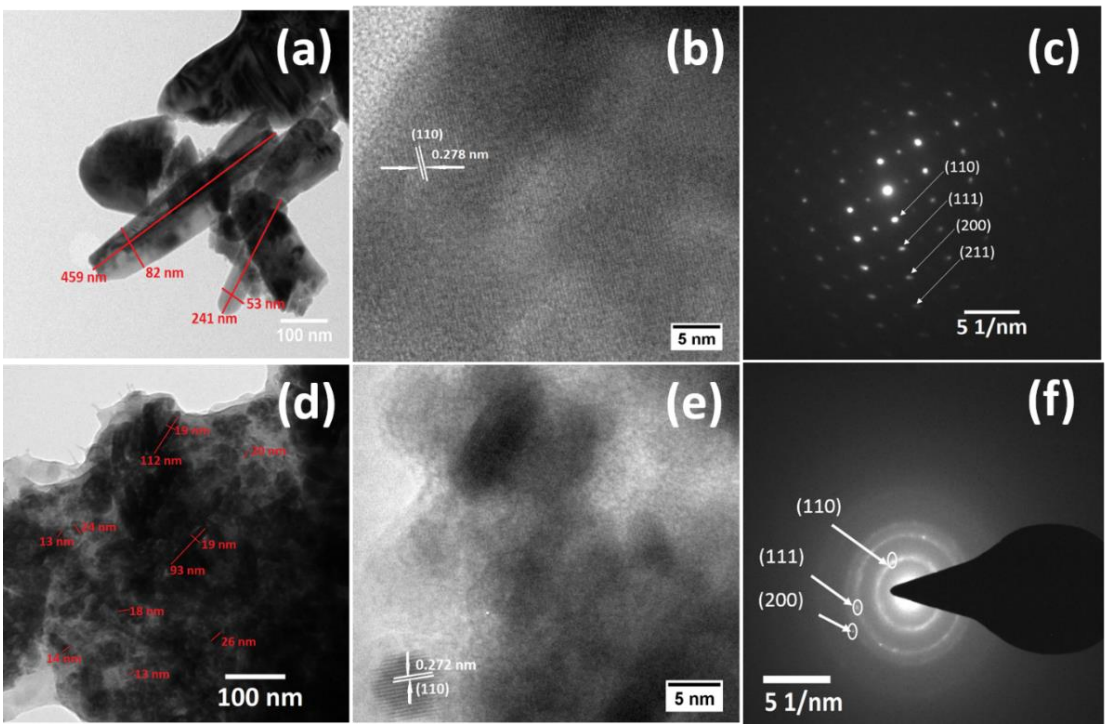

Fig. 3.3. The TEM, HR-TEM and SAED patterns of pure BSO (a-c) and 0.03% La-BSO (d-f) indicating nanorods-nanoparticles mixed morphologies.

3.3.4 X-ray photoelectron spectroscopy analysis

The X-ray photoelectron spectroscopy (XPS) analysis is carried out to perceive the chemical state and binding energy of the elemental composition present in the BSO and La-BSO samples. The core levels of Ba-3d, Sn-3d, O-1s, and La-3d obtained from the XPS measurement of BSO and 0.01%, 0.03%, 0.05% La-BSO are shown in Fig. 3.4(a-d). The Ba 3d state's binding energy is found to show a small shift upon doping La into the Ba sites with a significant reduction in intensity. The Ba $3d_{5/2}$ peak is observed at 779.58 eV, 780.08 eV and 780.10 eV, 780.28 eV for BSO, 0.01%, 0.03% and 0.05% La-BSO samples, respectively, indicating systematic variation in binding energy. Moreover, the Ba $3d_{3/2}$ state peak at 794.98 eV, 795.38 eV, 795.42 eV and 795.48 eV corresponding to pure BSO, 0.01%, 0.03% and 0.05% La-BSO samples, respectively, are also shifted systematically. These shifts compared to BSO are due to the La^{3+} ions being incorporated into the Ba lattice sites of the perovskite structure.

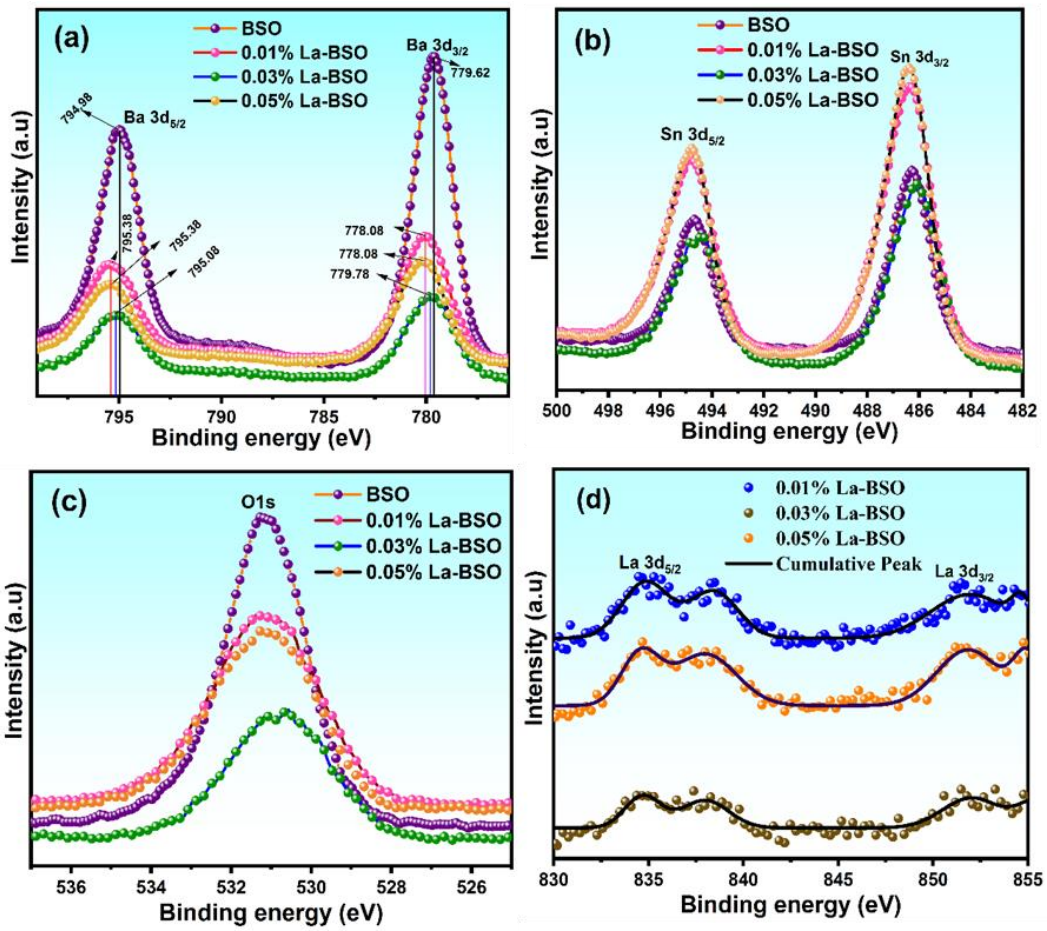

Fig. 3.4. The XPS spectra showing the comparison of core levels (a) Ba-3d, (b) Sn-3d, (c) O-1s and (d) fitted La-3d states of the La-BSO samples.

Subsequently, Fig. 3.4b shows the double spectral peaks of BSO and La-BSO samples corresponding to the Sn $3d_{3/2}$ and Sn $3d_{5/2}$ states with binding energy peaks appearing at 494.78 eV and 486.38 eV, respectively, matching with the reported values [26]. Figure 3.4c exhibits a symmetric O1s peak centered around 531.18 eV without a significant shift for the pure BSO and all the La-BSO samples. The O1s peaks are nearly symmetric and characteristic of O^{2-} ions that form the Ba-O-Sn lattice [27]. Upon doping with La, the intensity of O1s peaks also decreases significantly. Figure 3.4d shows the Gaussian function fitted doublet peaks of 0.01%, 0.03%, and 0.05% La-BSO samples. The broad overlapping peaks are fitted to obtain the exact peak position values. The characteristic peaks of La $3d_{5/2}$ and La $3d_{3/2}$ are identified at the binding energies 834.3 eV and 851.7 eV, respectively, for the La-BSO samples. Satellite peaks

of La $3d_{5/2}$ and La $3d_{3/2}$ are also observed at binding energy values 838.4 eV and 854.7 eV, respectively [28]. These doublet peaks of La $3d_{5/2}$ and La $3d_{3/2}$ are due to the bonding and anti-bonding states between the $3d^9\ 4f^0$ of $3d^9\ 4f^1L$ configuration [29,30].

3.3.5 Optical properties

The diffuse reflectance spectra (DRS) of BSO and La (0.01%, 0.03%, and 0.05%) doped BSO nanostructured powders measured in the range 350 nm to 800 nm and the estimation of band-gap are shown in Fig. 3.5. A significant reduction in the reflectance intensity upon doping with 'La' compared to the BSO sample implies that the sample absorbs photons of the corresponding wavelengths effectively (Fig. 3.5a). The band-gap of powder materials can be estimated from the onset of the linear region of the diffuse reflectance spectra. The sharp rise in percent reflectance constitutes the linear region with the greatest slope that is attributed to an exponential drop in the absorption coefficient. The onset of this linear region is a universal method of determining absorption edges from which the band-gap can be deduced without estimating the absorption coefficient by extrapolating the linear fit to R=0 [31] as shown in Fig. 3.5b. The linear fit intercept of the DRS spectra at R=0 of the BSO sample yields a band-gap value of 3.40 eV.

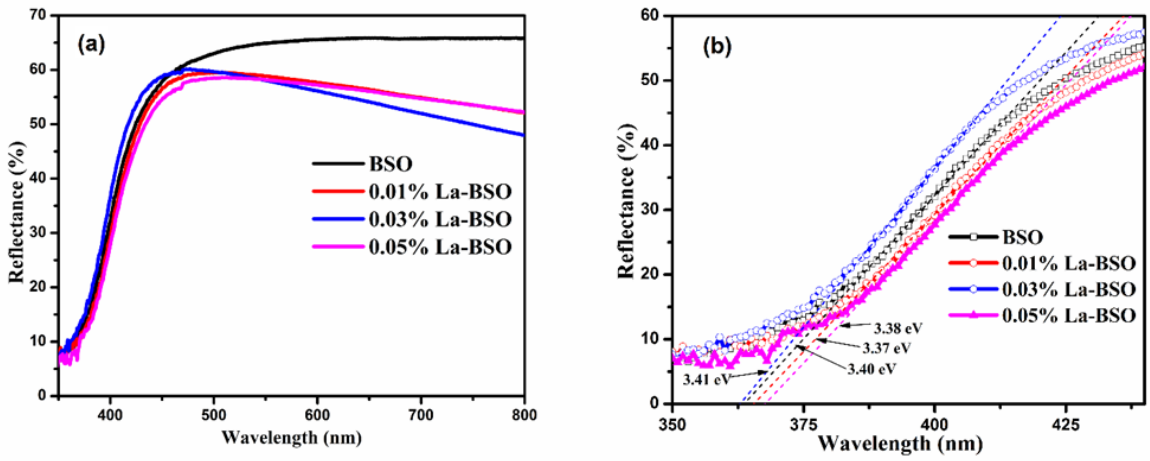

Fig. 3.5. Diffuse reflectance spectra of (a) BSO and 0.01%, 0.03% and 0.05% La-BSO powders and (b) Intercept of the linear fit of the DRS spectra yielding the band-gap.

No systematic trend in the variation of the bandgap is observed with La doping. Upon doping 0.01 %, 0.03% and 0.05% of La into the BSO system, the band-gap value slightly decreases to 3.37 eV for 0.01% La-doped sample and slightly increases to 3.41 eV for 0.03% La doping and then significantly decreases to 3.38 eV for 0.05% La doping. Among the doped samples, 0.03% La-BSO has a higher value of bandgap. The observed distinct changeover in the morphology of the La-BSO samples prepared by hydrothermal method leading to mixed nanorods-nanoparticles might be the reason for the 0.03% La doped BSO to have a slightly higher value of bandgap which may be beneficial for photon harvesting. The possibility of band-gap alteration by way of doping and/or synthesis by hydrothermal method indicates the suitability of the material for further exploration towards band-gap engineering and tuning its property for photovoltaic applications.

3.3.6 Photovoltaic performance of fabricated DSSCs

The comparison of the J-V characteristics of the DSSCs fabricated using the BSO and La- (0.01%, 0.03%, and 0.05%) BSO samples as photoanodes is shown in Fig. 3.6. The photovoltaic parameters of the devices are summarized in Table 3.2. The fill factor (FF) and power conversion efficiency (η) are calculated according to eq. 1.12 & eq. 1.13. A reasonable conversion efficiency of 1.23% is observed with a higher J_{SC} of 2.57 mA/cm^2 for the 0.03% La-BSO photoanode possessing the mixed nanorod-nanoparticle morphology. These values are significantly higher compared to that of BSO based photoanode. From Table 3.2, it is obvious that the efficiency increases while increasing the La doping content from pure BSO to 0.03 % La doping. The current density (J_{SC}) is significantly raised to an extent of 2.57 mA/cm^2 for 0.03% La-BSO which is due to the mixed morphology, leading to an appreciable increase in the surface to volume ratio. To confirm the PCEs and their corresponding $J_{SC,}$ the external quantum efficiencies (EQEs) of devices fabricated using BSO and 0.03% La-BSO are measured

Table 3.2. Current density-voltage (J-V) parameters of BSO and 0.01%, 0.03% and 0.05% La-BSO based DSSC devices.

Device ID	**Voc (V)**	**Jsc (mA/cm^2)**	**FF**	**η (%)**
BSO	0.54	1.10	0.51	0.31
0.01% La-BSO	0.59	1.18	0.59	0.42
0.03% La-BSO	0.62	3.05	0.65	1.23
0.05% La-BSO	0.60	1.87	0.62	0.68

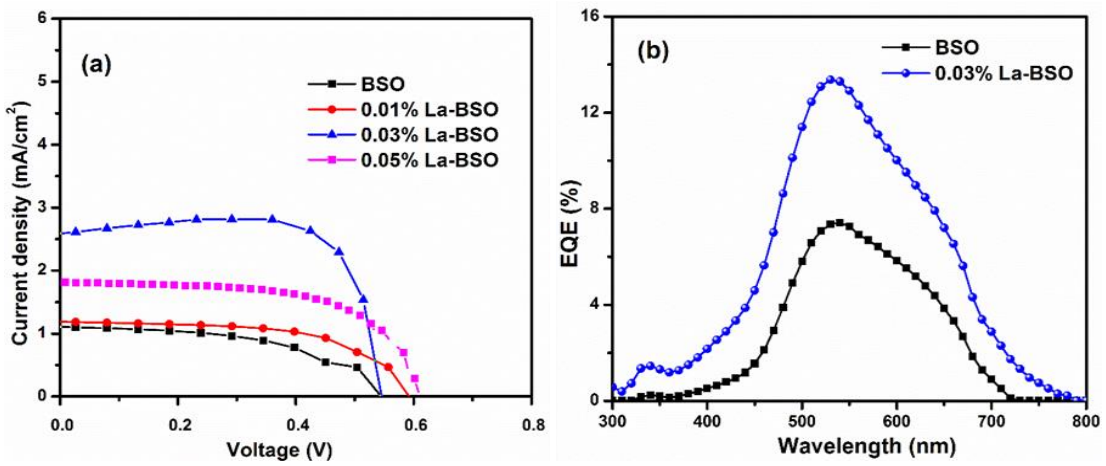

Fig. 3.6. (a) Photovoltaic performance of the $BaSnO_3$ and La-doped $BaSnO_3$ photoanode based DSSCs, and (b) External quantum efficiency (EQE) of BSO and 0.03% La-BSO devices measured under AM 1.5G, 100 mW/cm^2.

and compared (Fig. 3.6b). The PCE was gradually increases with La concentration and among all the DSSC devices, the 0.03% La-BSO sample has a higher conversion efficiency of 1.23%. (Shown in Table 3.2). With further increase in the La concentration to 0.05% La, the PCE decreases considerably. Here, it is noticed that the V_{OC} varies a little for all the devices. It is also evident that the variation of current density (J_{SC}) is follows the trend of conversion efficiency with a maximum value of 2.57 mA/cm^2. The external quantum efficiency spectrum of selected BSO and 0.03% La-BSO is measured in the wavelength range from 300-800 nm. The EQE value of BSO is around 7% and it increases upon doping with La. A maximum external quantum efficiency value of 14% is obtained at 530 nm for the 0.03% La-BSO devices

as shown in Fig. 3.6b, implying better light-harvesting efficiency than that of the BSO device in the entire wavelength range from 300-800 nm.

3.3.7 Electrochemical studies

Considering the above results, to elucidate the plausible reason for the increase in the performance of LBSO, the devices are characterized by electrochemical impedance spectroscopy (EIS) to investigate the interfacial charge transport and recombination properties. Nyquist plot and the equivalent circuit diagram (inset of Fig. 3.7) of the DSSCs fabricated using BSO and 0.03% La-BSO samples are measured from 0.01 Hz to 1 MHz as shown in Fig. 3.7. Usually, in the EIS study of DSSC devices, at higher frequency, the intercept on the real axis is the series resistance (R_S) which includes the contact resistance, resistance of FTO glass substrate, and bulk resistance of CE material. The R_S value of the DSSC devices is nearly the same due to the use of the same electrolyte (I^-/I_3^-) and counter electrodes (Pt). At the high-frequency region, the BSO and 0.03% La-BSO devices show similar semicircle behavior and charge-transfer resistance (R_{CE}) at the CE side. Here, the interest is on the charge-transfer resistance (R_{CT}) at the interfaces of La-BSO/dye/electrolyte in the high-frequency region. The DSSC device fabricated using 0.03% La-BSO exhibits a lower R_{CT} value of 8.40 Ω compared to a value of 9.26 Ω for the device made using the BSO sample. The lower value of R_{CT} of 0.03% La-BSO indicates a better charge carrier transportation compared to BSO. The 0.03% La-doped $BaSnO_3$ sample having mixed nanorods-nanoparticles morphology facilitates more dye adsorption, leading to a lesser value of R_{CT} which may reduce the charge recombination, leading to a better value of J_{SC}. The FF and J_{SC} are higher when the R_S is smaller, which is also consistent with the results of photovoltaic performance [27]. The electronic properties of LBSO facilitate efficient charge transport due to the mixed morphology induced by La doping and imply the ternary $BaSnO_3$ to be a potential system for tuning as an efficient photoanode for application in DSSCs.

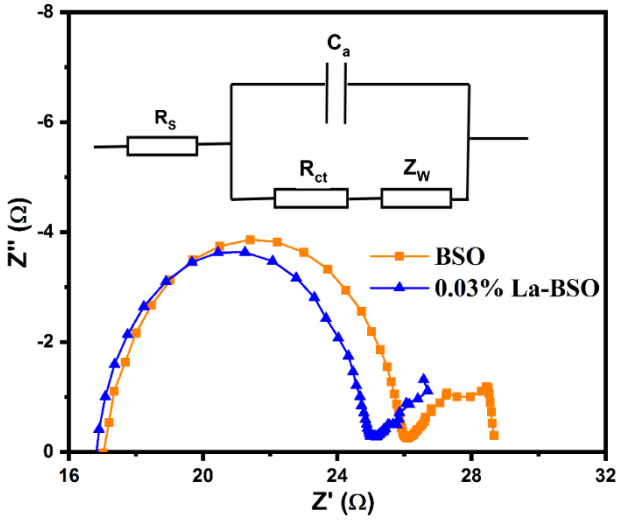

Fig. 3.7. Nyquist plot of DSSC devices fabricated using BSO and 0.03% La-BSO photoanodes and the inset is the equivalent circuit diagram.

3.4. Conclusions

In summary, the La impurity ions are successfully doped at the Ba sites of the perovskite ternary $BaSnO_3$ and stabilized as a single-phase compound. Doping of La in $BaSnO_3$ by hydrothermal method plays a significant role in inducing a changeover to mixed nanorod-nanoparticle morphology. Band-gap alteration by doping with La is promising for fine-tuning the properties of perovskite $BaSnO_3$ material as per the requirement. Among the doped samples, the high conversion efficiency of 1.23 % with a higher short circuit current density of 2.57 mA/cm^2 is obtained for the DSSC fabricated using 0.03% La-BSO. Although the results are interesting, the observed efficiency is comparatively lesser (compared to standard TiO_2 based devices) due to bigger-sized rod-like particles grown by the hydrothermal method which might not have led to effective dye adsorption. Hence, it was opted for preparing the same composition by a facile peroxide route envisaging to achieve fine grain size with a larger surface area, which is dealt in the following chapter.

References

[1] B. O'Regan, M. Grätzel, A low-cost, high-efficiency solar cell based on dye-sensitized colloidal TiO2 films, Nature. 353 (1991) 737–740.

[2] M. Grätzel, Photoelectrochemical cells, Nature. 414 (2001) 338–344.

[3] Q. Zhang, T.P. Chou, B. Russo, S.A. Jenekhe, G. Cao, Aggregation of ZnO nanocrystallites for high conversion efficiency in dye-sensitized solar cells, Angew. Chemie. 120 (2008) 2436–2440.

[4] T.P. Chou, Q. Zhang, G.E. Fryxell, G.Z. Cao, Hierarchically Structured ZnO Film for Dye-Sensitized Solar Cells with Enhanced Energy Conversion Efficiency, Adv. Mater. 19 (2007) 2588–2592.

[5] E.N. Kumar, R. Jose, P.S. Archana, C. Vijila, M.M. Yusoff, S. Ramakrishna, High performance dye-sensitized solar cells with record open circuit voltage using tin oxide nanoflowers developed by electrospinning, Energy Environ. Sci. 5 (2012) 5401–5407.

[6] A. Birkel, Y.-G. Lee, D. Koll, X. Van Meerbeek, S. Frank, W. Tremel, Highly efficient and stable dye-sensitized solar cells based on SnO_2 nanocrystals prepared by microwave-assisted synthesis, Energy Environ. Sci. 5 (2012) 5392–5400.

[7] J.Z. Ou, R.A. Rani, M.-H. Ham, M.R. Field, P. Reece, S. Zhuiykov, S. Sriram, M. Bhaskaran, R.B. Kaner, K. Kalantar-zadeh, Elevated Temperature Anodized Nb2O5: A Photoanode Material with Exceptionally Large Photoconversion Efficiencies, ACS Nano. 6 (2012) 4045–4053.

[8] R. Bhattacharjee, I.-M. Hung, Effect of different concentration Li-doping on the morphology, defect and photovoltaic performance of Li–ZnO nanofibers in the dye-sensitized solar cells, Mater. Chem. Phys. 143 (2014) 693–701.

[9] L. Geske, V. Lorenz, T. Müller, L. Jäger, H. Beige, H.-P. Abicht, V. Mueller, Dielectric and electromechanical characterisation of fine-grain $BaTi_{0.95}Sn_{0.05}O_3$ ceramics sintered from glycolate-precursor powder, J. Eur. Ceram. Soc. 25 (2005) 2537–2542.

[10] U. Lampe, J. Gerblinger, H. Meixner, Nitrogen oxide sensors based on thin films of $BaSnO_3$, Sensors Actuators B Chem. 26 (1995) 97–98.

[11] S. Tao, F. Gao, X. Liu, O.T. Sørensen, Ethanol-sensing characteristics of barium stannate prepared by chemical precipitation, Sensors Actuators B Chem. 71 (2000) 223–227.

[12] X. Han, X. Li, X. Long, H. He, Y. Cao, A dielectric and ferroelectric solid solution of $(1- x)$ $BaSnO_3PbTiO_3$ with morphotropic phase boundary, J. Mater. Chem. 19 (2009) 6132–6136.

[13] S. V Manorama, V.J. Rao, Preparation and characterization of barium stannate: application as a liquefied petroleum gas sensor, J. Mater. Sci. Mater. Electron. 12 (2001) 137–142.

[14] S. Hodjati, K. Vaezzadeh, C. Petit, V. Pitchon, A. Kiennemann, NOx sorption–desorption study: application to diesel and lean-burn exhaust gas, Catal. Today. 59 (2000) 323–334.

[15] B. Tan, E. Toman, Y. Li, Y. Wu, Zinc stannate (Zn2SnO4) dye-sensitized solar cells, J. Am. Chem. Soc. 129 (2007) 4162–4163.

[16] Y. Okamoto, Y. Suzuki, Perovskite-type SrTiO3, $CaTiO_3$ and $BaTiO_3$ porous film electrodes for

dye-sensitized solar cells, J. Ceram. Soc. Japan. 122 (2014) 728–731.

[17] S. Burnside, J.-E. Moser, K. Brooks, M. Grätzel, D. Cahen, Nanocrystalline mesoporous strontium titanate as photoelectrode material for photosensitized solar devices: increasing photovoltage through flatband potential engineering, J. Phys. Chem. B. 103 (1999) 9328–9332.

[18] J. Dou, X. Li, Y. Li, Y. Chen, M. Wei, Fabrication of Zn_2SnO_4 microspheres with controllable shell numbers for highly efficient dye-sensitized solar cells, Sol. Energy. 181 (2019) 424–429.

[19] J. Dou, Y. Li, J. Wu, Improving the photovoltaic performance of Zn_2SnO_4 solar cells by doping Sr^{2+}/Ba^{2+} ions: Efficient electron injection and transfer, Sol. Energy. 165 (2018) 122–130.

[20] F. Xie, Y. Li, T. Xiao, D. Shen, M. Wei, Efficiency improvement of dye-sensitized $BaSnO_3$ solar cell based surface treatments, Electrochim. Acta. 261 (2018) 23–28.

[21] F. Guo, G. Li, W. Zhang, Barium staminate as semiconductor working electrodes for dye-sensitized solar cells, Int. J. Photoenergy. 2010 (2010).

[22] D.W. Kim, S.S. Shin, S. Lee, I.S. Cho, D.H. Kim, C.W. Lee, H.S. Jung, $BaSnO_3$ perovskite nanoparticles for high efficiency dye-sensitized solar cells, ChemSusChem. 6 (2013) 449–454.

[23] C. Huang, X. Wang, X. Wang, X. Liu, Q. Shi, X. Pan, X. Li, Preparation of $BaSnO_3$ and $Ba_{0.96}La_{0.04}SnO_3$ by reactive core–shell precursor: formation process, CO sensitivity, electronic and optical properties analysis, RSC Adv. 6 (2016) 25379–25387.

[24] Y. Ohkubo, T. Saito, Y. Murakami, A. YOKOYAMA, Y. KAWASE, Acta Crystallogr., Sect. A: Cryst. Phys., Diffr., Theor. Gen. Crystallogr. Mater. Trans. 43 (2002) 1469–1474.

[25] N. Rajamanickam, P. Soundarrajan, K. Jayakumar, K. Ramachandran, Improve the power conversion efficiency of perovskite $BaSnO_3$ nanostructures based dye-sensitized solar cells by Fe doping, Sol. Energy Mater. Sol. Cells. 166 (2017) 69–77.

[26] Y. Jiang, Y. Li, M. Yan, N. Bahlawane, Abnormal behaviors in electrical transport properties of cobalt-doped tin oxide thin films, J. Mater. Chem. 22 (2012) 16060–16065.

[27] A. Roy, P.P. Das, P. Selvaraj, S. Sundaram, Perforated $BaSnO_3$ Nanorods Exhibiting Enhanced Efficiency in Dye Sensitized Solar Cells, ACS Sustain. Chem. Eng. 6 (2018) 3299–3310.

[28] J. Zhang, Z. Zhao, X. Wang, T. Yu, J. Guan, Z. Yu, Z. Li, Z. Zou, Increasing the oxygen vacancy density on the TiO_2 surface by La-doping for dye-sensitized solar cells, J. Phys. Chem. C. 114 (2010) 18396–18400.

[29] B.C. Luo, J. Zhang, J. Wang, P.X. Ran, Structural, electrical and optical properties of lanthanum-doped barium stannate, Ceram. Int. 41 (2015) 2668–2672.

[30] A.J. Nelson, J.J. Adams, K.I. Schaffers, Photoemission investigation of the electronic structure of lanthanum–calcium oxoborate, J. Appl. Phys. 94 (2003) 7493–7495.

[31] N. Purushothamreddy, R.K. Dileep, G. Veerappan, M. Kovendhan, D.P. Joseph, Prickly pear fruit extract as photosensitizer for dye-sensitized solar cell, Spectrochim. Acta Part A Mol. Biomol. Spectrosc. 228 (2020) 117686.

CHAPTER: 4

Facile peroxide route synthesized La-doped $BaSnO_3$ nanoparticles as photoanodes for enhanced performance of DSSCs

This chapter presents the results of the ternary La-doped $BaSnO_3$ nanoparticles synthesized using the facile peroxide route to overcome the particle size issue encountered in sample preparation by the hydrothermal method in the previous chapter. The La-doped $BaSnO_3$ samples optimized using the facile peroxide route are studied for their structural, morphological, and optical properties for use as photoanodes in DSSCs. A strategy of double surface treatment of photoanodes is adapted to enhance the dye loading ability and is confirmed by dye loading measurements. The 0.03% La doped $BaSnO_3$ sample with mixed morphology (nanocuboid-nanoparticles) is found to be effective for the dye adsorption property. Additionally, the DSSC performance stability test is performed for 16 days, and it shows that ~ 80% of the initial PCE is retained. These results show that doping BSO with La by facile peroxide route is beneficial for designing high-performance and long stability DSSCs. The experimental results obtained are presented and discussed in sufficient detail in the following sections.

4.1 Introduction

The captivating properties of dye-sensitized solar cells (DSSCs), such as cost-effectiveness, ease of fabrication, eco-friendliness, non-toxicity, lightweight, good performance in diverse light conditions, and promising conversion efficiency always attracts researchers to explore more in this field[1–3]. For the past two decades, the DSSC devices have been explored by using various photoanode materials, electrolytes, and sensitizers to improve photovoltaic performance and long-term stability. In DSSCs, the promising photoanode material is

mesoporous TiO_2. It acts as an electron transport layer (ETL), which has a significant influence on the photovoltaic performance of the device. Despite high efficiencies reported for a couple of decades using the mesoporous TiO_2 material, there is also a significant number of reports with lower efficiency [4–8]. Even though several binary semiconducting oxides such as ZnO, SnO_2, and Nb_2O_5 have been reported as alternative ETLs in DSSCs [9–15], none exhibit better performance than the conventional mesoporous TiO_2 based ETL. Among these, TiO_2 has been mainly investigated as an efficient binary oxide material for DSSCs, owing to their higher power conversion efficiency, ease of preparation, low preparation costs, etc. [16,17]. However, the binary TiO_2 oxide-based photoanode can cause photobleaching of dye molecules under solar irradiation, mainly in the ultraviolet region, which is a significant drawback for their long-term stability in practical applications [18,19].

To surmount the drawbacks in binary oxides, intense exploration is undertaken on ternary oxide semiconductors such as Zn_2SnO_4, $SrTiO_3$, $BaTiO_3$, $SrSnO_3$, and $BaSnO_3$ (BSO) [20–28]. Ternary metal oxides have been chosen since their ionization potential and electron affinity can be easily tuned by adding or doping impurities to modify the valence electron's ionic or covalent bond energy via altering their atomic composition during the synthesis process [27,29]. Among all of these, $BaSnO_3$ is one of the promising n-type semiconducting oxides with a perovskite structure having a wide bandgap of 3.2 eV exhibiting higher electron mobility (~ 320 $cm^2 V^{-1} s^{-1}$) which facilitates fast diffusion of the electrons in the conduction band [27], expeditious electron transport [28], and structural stability up to 1000 °C, and rapid dye adsorption ability compared to binary oxides TiO_2 and ZnO [30,31]. $BaSnO_3$ has several applications due to which its optical and electrical properties can be easily tuned by modifying atomic composition, appropriate doping, and grain size [32]. Owing to these properties, BSO is also employed as transparent conducting electrodes (TCEs) [33] and gas sensors [34] apart from DSSC applications [35]. Recently, few reports have been published on the photovoltaic

performance of $BaSnO_3$ in DSSCs. Zhang *et al.* reported that dye-sensitized $BaSnO_3$ could be used as a photoanode in DSSCs, owing to its fast dye adsorption capability than that of the conventional binary oxide materials [36]. Guo *et al.* reported DSSCs using $BaSnO_3$ nanoparticles used as photoanode, which exhibit a power conversion efficiency (PCE) of 1.1% [35]. Recently, Rajamanikam *et al.* reported PCE of 0.71% without surface treatment and scattering layer [37]. In 2018, the same group reported surface treatment on the $BaSnO_3$ layer, resulting in enhanced efficiency of 5.64% for Sr (5%) doped BSO [38]. Moreover, the BSO has been used as an ETL in perovskite solar cells which exhibit enhanced conversion efficiency of around 21% by doping with La and excellent photostability compared to mesoporous TiO_2 [39]. We have recently reported efficiency of 1.56% using nanostructured La-doped $BaSnO_3$samples synthesized by the hydrothermal method [40] which is discussed in chapter 3.

From the literature reports, one can note that the La-doped $BaSnO_3$ (LBSO) is a potential candidate to enhance the photovoltaic performance by using it as an ETL. Various methods have been adapted in literature to synthesize doped BSO materials; such as sol-gel, co-precipitation, hydrothermal, solid-state, and oxalate chemical routes. A novel facile peroxide precipitate route has been adopted to synthesize nanostructured BSO and LBSO particles to enhance the dye adsorption capacity and DSSC device performance with high efficiency. Until now, fewer reports exist on LBSO being explored as an electron transport material in DSSCs. However, the optimization of electron transport materials significantly impacts the photovoltaic performance of DSSCs. In this chapter, the successful synthesis and characterization of nanostructured BSO and LBSO particles with high crystallinity by the facile peroxide-precipitate route are presented. The prepared BSO and LBSO nanoparticles investigated using several characterization techniques are explained in detail for their structural, optical, and electronic properties. These optimized nanoparticles are also used as an ETL in DSSCs. The electron lifetime and charge transferability are also analyzed using electrochemical impedance

spectroscopy (EIS) to realize the difference in the photocurrent density and photovoltaic performance of the DSSCs.

4.2. Experimental section

4.2.1 Synthesis and characterization of $Ba_{1-x}La_xSnO_3$ nanoparticles

All the chemicals were of reagent grade used without any further purification and all the reactions were performed in ambient conditions. The $BaSnO_3$ nanoparticles were prepared from a solution made using $SnCl_4.5H_2O$ and $BaCl_2.2H_2O$ dissolved in an aqueous hydrogen peroxide solution (170 ml, 30%, OCI). For doping of La at the Ba sites of $BaSnO_3$, La $(NO_3)_3$. $6H_2O$ solution (appropriate amount separately dissolved in hydrogen peroxide) was added into the above precursor solution depending on 'x' (x = 0, 0.01, 0.03, and 0.05) to result in a $Ba_{1-x}La_xSnO_3$ compound. While stirring, to suppress the agglomeration of the particles, 5 mmol. (0.96 g) of citric acid ($C_6H_8O_7$) was added to the above solution. To induce precipitation, ammonia solution was added slowly to the above precursor mixture, until it reaches a pH value of 10 with constant stirring. After adding the ammonia solution, the transparent solution turned to milky white color and gradually became particulate in nature due to the completion of the precipitation process. The resultant precipitated mixture was continuously stirred maintaining the temperature in-between 40 °C to 60 °C in a water bath for 12 h to obtain crystalline precipitates. After 12 h of reaction, white precipitates were formed which were thoroughly washed with distilled water and centrifuged in ethanol. The obtained product was vacuum dried at room temperature and then annealed at 900 °C for 2 h in an air atmosphere to result in nanocrystalline $BaSnO_3$ and La-doped $BaSnO_3$ particles. The nanocrystalline $Ba_{1-x}La_xSnO_3$ (x = 0, 0.01, 0.03, and 0.05) samples are coded as BSO, LBSO1, LBSO3 and LBSO5 where, 1, 3 and 5 indicate x = 0.01, 0.03 and 0.05 of

La atomic percentage, respectively. For the sake of convenience, the La doped BSO samples are collectively referred to as LBSO in this chapter.

4.2.2 Preparation of BSO and LBSO Electrode

Pastes of nanocrystalline BSO and LBSO samples were made using the synthesized particles and were coated onto ultrasonically cleaned and ozone treated fluorine-doped tin oxide (FTO) glass substrates by the doctor-blade method. Firstly, a fine homogeneous paste was prepared with a mixture of BSO (or LBSO) nanopowders, 10 wt% of ethyl cellulose, and 5 wt% of α-terpineol (Sigma Aldrich) and ethanol by gradually mixing to result in a viscous mixture. This was continuously ground using pestle and mortar for 30 min to form a homogeneous viscous paste. Here, the double surface treatment with $TiCl_4$ strategy is adapted. Firstly, for the pre-treatment step, the cleaned FTO glass substrates were surface treated with 0.05 M of $TiCl_4$ aqueous solution pre-treated for 30 min at 80 ˚C and then rinsed with double deionized water followed by annealing at 500 ˚C for 30 min. The prepared BSO and LBSO pastes were coated onto $TiCl_4$ pre-treated FTO glass substrates by doctor-blade method for a cell area of 0.25 cm^2 which was then annealed at 500 °C for 30 min in air atmosphere and these electrodes are named as TCL/BSO and TCL/LBSO, respectively. For the post-treatment step, another set of pre-surface-treated TCL/BSO and TCL/LBSO films were treated once again with 0.05 M of $TiCl_4$ aqueous solution at 80 °C for 30 min and then annealed at 500 °C for 30 min, which are named as TCL/BSO/TCL and TCL/LBSO/TCL respectively.

4.2.3 Fabrication of DSSC

For the dye adsorption, the pre-and post-surface-treated BSO and LBSO films were soaked in 0.5 mmol of N719 dye (Greatcellsolar, Australia) solution prepared in absolute ethanol by stirring at room temperature merely for 1 h. Here, it is to be noted

that the dye adsorption duration is much shorter than that for traditional electron transport materials, *e.g.*, 12 h for TiO_2, 12 h for Zn_2SnO_4, 120 h for $BiFeO_3$, etc. [41–43]. After the dye adsorption, the films were thoroughly rinsed with ethanol to remove the physically adsorbed dye molecules on the surface of the films. The platinum counter electrodes were coated by drop-casting using 5 mM chloroplatinic acid hexahydrate (H_2PtCl_6, Sigma Aldrich) dissolved in isopropyl alcohol over cleaned FTO substrates and were subsequently annealed at 500 °C for 30 min under an ambient atmosphere. The sandwich-type DSSC was assembled using dye adsorbed BSO/LBSO photoanodes and platinum-coated counter electrodes. The photoanode and platinized counter electrodes were sandwiched using hot melt film (55 µm, Surlyn, Greatcellsolar, Australia). The electrolyte was prepared with 0.5 M of 1-butyl-3 methylimidazolium iodide (BMII), 0.06 M of iodine (I_2), 0.1 M of LiI, and 0.5 M of *tert*-butyl pyridine (*t*BP), all mixed in acetonitrile solvent. All the chemicals were purchased from Alfa aesar and used without further purification. After sandwiching both the electrodes, the prepared I^-/I_3^- liquid electrolyte was infiltrated through the pre-drilled holes from the rear side of the counter electrode.

4.3. Results and discussion

4.3.1 Structural and morphological analysis

The synthesized BSO and LBSO nanocrystalline powders annealed at 900 °C for 2 h in an air atmosphere are characterized by XRD analysis. Fig. 4.1(a) shows the schematic crystal structure of the perovskite $Ba_{1-x}La_xSnO_3$ compound. The sample's purity and phase structure are carefully examined using the XRD patterns shown in Fig. 4.1b. The ideal cubic perovskite structure is evident for both the pure and La doped $BaSnO_3$ samples with the space group *Pm3m* as shown in Fig. 4.1(a). The obtained diffraction results match well to the JCPDS card no. 74-0780, indicating phase purity of

the cubic perovskite structure reported with a lattice parameter of a = 0.4117 nm for $BaSnO_3$ compound. The obtained XRD patterns of all the samples confirm the formation of a single-phase without any impurities like lanthanum oxides (La_2O_3, $La_2Sn_2O_7$). Good crystallinity and purity for the BSO and LBSO nanoparticles are ensured. One cannot observe any significant difference between the XRD patterns of BSO and LBSO samples (Fig. 4.1b). Thus, it can be confirmed that La ions are doped into the Ba sites of the BSO crystal lattice system.

Table 4.1: Rietveld refinement parameters of $Ba_{1-x}La_xSnO_3$ (x = 0, 0.01, 0.03, and 0.05) nanoparticles.

Sample code	a = b = c (Å)	Volume (Å^3)	R_p	R_{wp}	R_e	Chi^2
BSO	4.1186(3)	69.8649	17.2	17.3	12.7	1.85
LBSO1	4.1185(2)	69.8600	21.4	19.8	12.3	2.34
LBSO3	4.1170(2)	69.7854	17.4	19.1	11.9	2.58
LBSO5	4.1168(2)	69.7759	21.0	20.3	12.8	2.52

The crystal structure analysis of all the samples is also performed with Rietveld refinement based on the XRD data as shown in Fig. 4.2 (a-d) and the obtained lattice refinement parameters are given in Table 4.1. Upon increasing the concentration of La^{3+} (radius = 1.36 Å) ions into the Ba (Ba^{2+} radius = 1.61 Å) sites from x = 0 to 0.05, all the samples show the same cubic structure with the space group of *Pm3m*. From Table 4.1, we can see that the lattice parameters and unit cell volumes decrease monotonically due to the smaller ionic radius of the La^{3+} ions[44]. Additionally, the crystallite size is also calculated using the Scherrer equation (eq. 2.2).

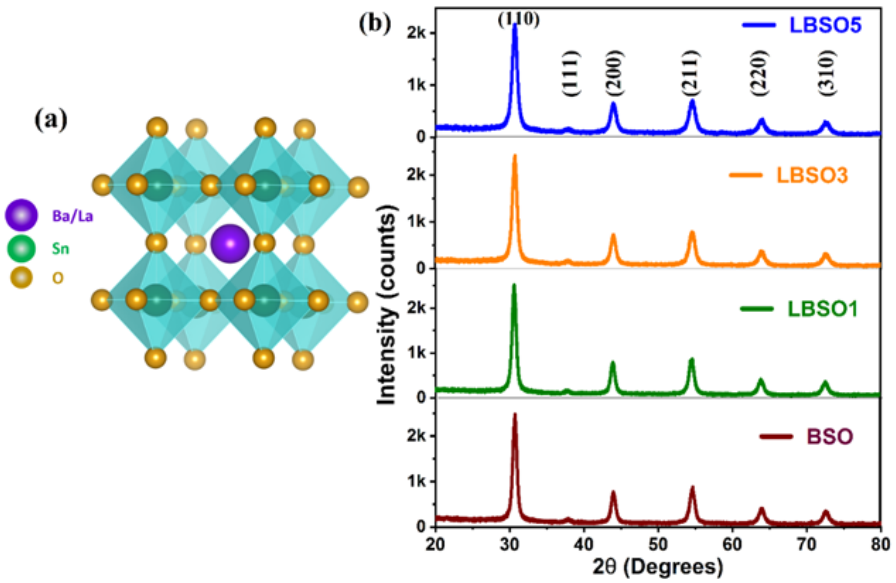

Fig. 4.1. (a) Perovskite crystal structure of La-doped $BaSnO_3$ compound and (b) The X-ray diffraction patterns of BSO and LBSO nanoparticles.

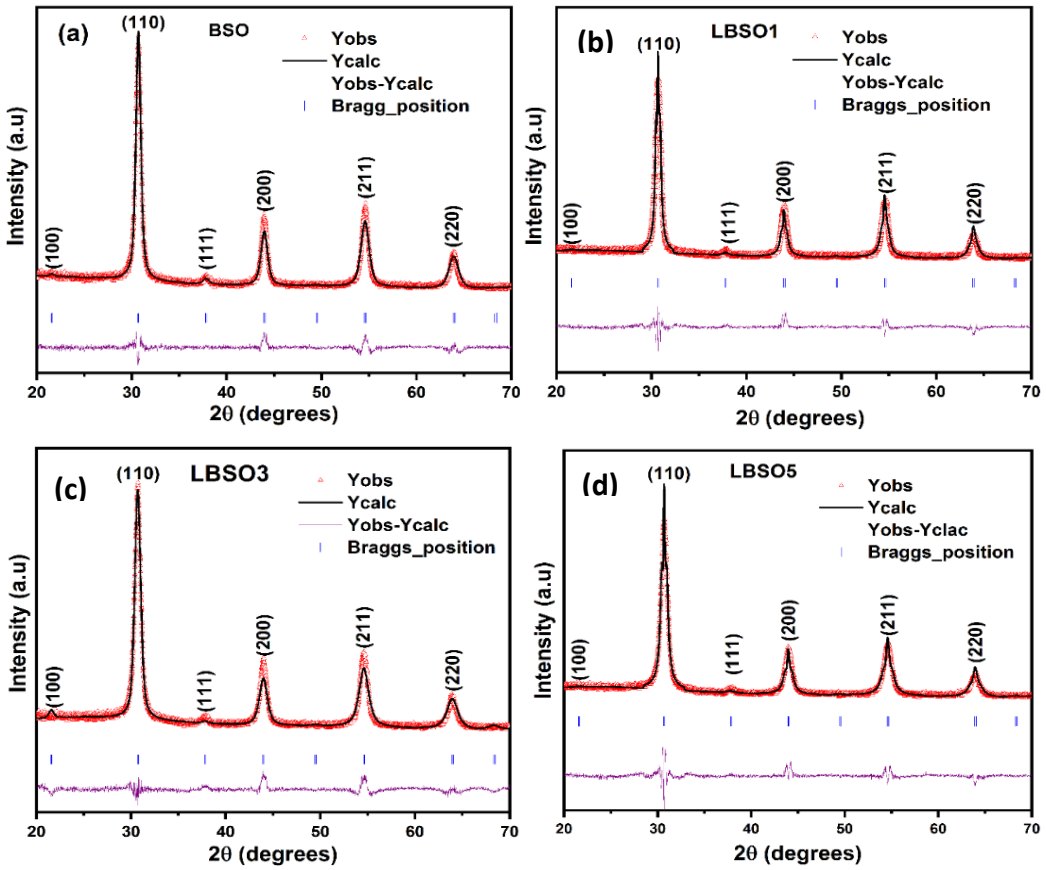

Fig. 4.2. The Rietveld refinement of X-ray diffraction patterns of (a) BSO, (b) LBSO1, (c) LBSO3 and (d) LBSO5 samples.

The calculated crystallite size using the FWHM of the strongest (110) crystallographic plane is found to be 12.4 nm, 12.6 nm, 11.09 nm, and 10.10 nm for BSO, LBSO1, LBSO3, and LBSO5, respectively.

The surface morphological features of the synthesized nanostructured BSO and LBSO particles are obtained by controlled experimental parameters. The FE-SEM images of nanostructured BSO and LBSO samples are shown in Fig. 4.3 (a-d). The average particle size of La-doped samples is found to be in the range ~20 to 30 nm. The cross-sectional FE-SEM image of the coated photoanode layer is shown in the inset of Fig. 4.3a and c for BSO and LBSO3 films, respectively.

In general, the crystallinity of the synthesized nanostructured particles is crucial in improving the charge transport characteristics in the ETLs. Therefore, the crystallinity and morphological features of the BSO and LBSO3 samples are further explored by TEM measurements which are shown in Fig. 4.4 (a-g). The TEM images of BSO (Fig. 4.4a) show irregular nanosized particles and the LBSO3 exhibit mixed nanocuboids/nanoparticles as shown in Fig. 4.4 (d & e). Hence, when doped with La, a mixed morphology is observed with vivid nanocuboids/nanoparticles (see Fig. 4.4d). The calculated width and breadth of the LBSO3 nanocuboids are in the range ~18–24 nm and ~20–26 nm, respectively. The average particle size is also determined as 18 nm and 15 nm for the BSO and LBSO3 samples, respectively. High-resolution transmission electron microscopy (HR-TEM) images at 10 nm scale (nanocuboids for LBSO3, see Fig. 4.4d) are shown in Fig. 4.4(b) and Fig. 4.4(f) for BSO and LBSO3, respectively.

The HR-TEM images reveal that the bulk of the nanostructured particles are nearly defect-free, as evident from the lattice fringes. The lattice fringes of d-spacing (inset of Fig. 4.4(b & f) are determined to be around 2.92 Å and 2.98 Å for BSO and LBSO3, respectively, which corresponds to the (110) diffraction plane of the cubic structure of the BSO system.

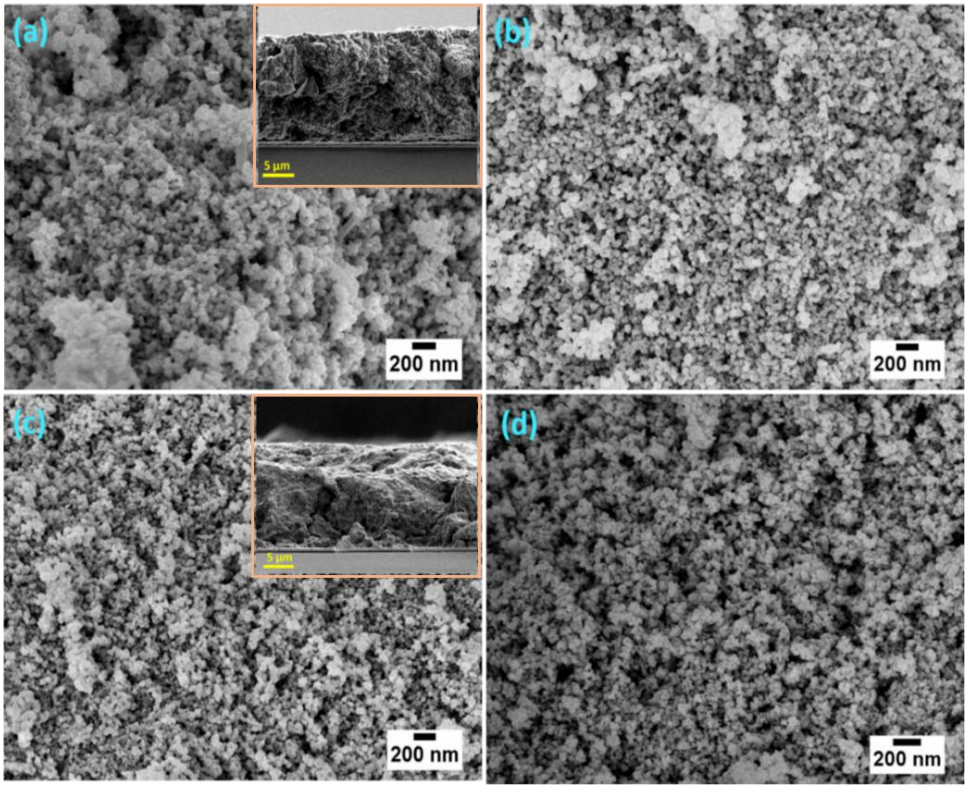

Fig. 4.3. FE-SEM images showing the surface morphologies of (a) BSO, (b) LBSO1, (c) LBSO3 and (d) LBSO5 nanoparticles. Insets of (a) and (c) are the cross-sectional images of BSO and LBSO3 photoanodes.

The SAED patterns of BSO and LBSO3 are shown in Fig. 4.4c and Fig. 4.4g, respectively. The pattern shows that the synthesized nanostructured particles of BSO and LBSO3 samples exhibit a highly crystalline nature with single-phase crystal structure, which also corroborates with the XRD patterns. The energy-dispersive X-ray spectroscopy (EDS) analysis for elemental composition confirms the presence of La in BSO nanoparticles and the results are shown in Fig. 4.4(h). It is confirmed that Ba, Sn, and O elements are present in the sample in the desired composition without any other impurities from the EDS data. The inset of Fig. 4.4(h) is the EDS data for the BSO sample. In Fig. 4.4(h), the major peaks at 0.85 KeV, 4.12 KeV, and 4.51 KeV belong to La, confirming its presence in the LBSO system.

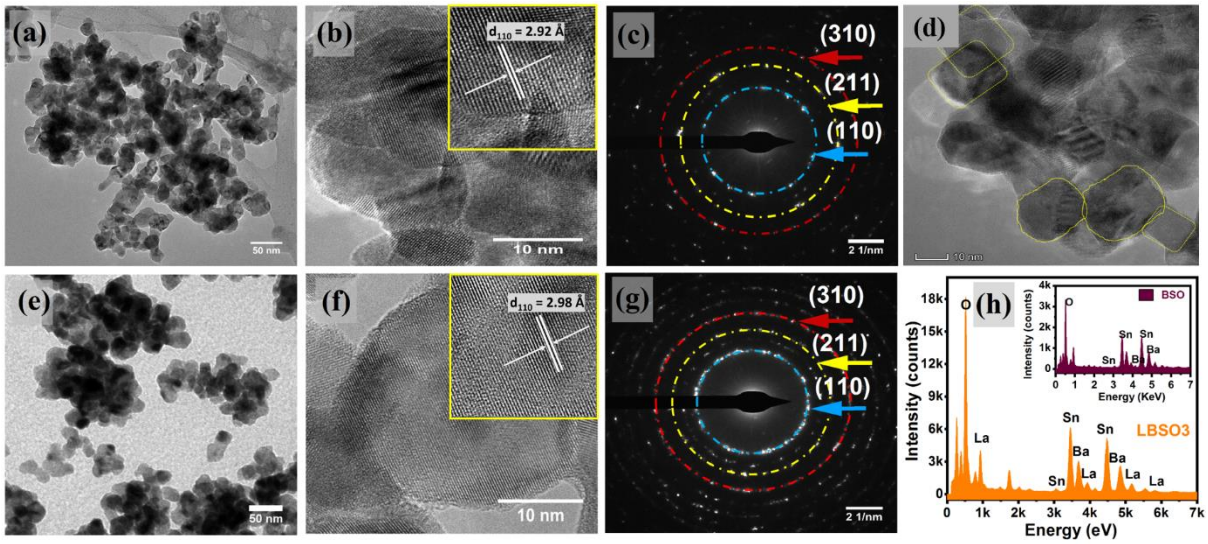

Fig. 4.4. The TEM, HR-TEM, and SAED pattern of (a-c) BSO and (e-g) LBSO3, respectively, (d) Mixed nanocuboid/nanoparticle morphology of LBSO3 at a higher magnification of 10 nm scale, and (h) EDS analysis of LBSO3 (inset is for BSO) nanostructured samples. The HR-TEM images in the insets of (b) BSO and (f) LBSO3 are the lattice

4.3.2 Optical properties

Fig. 4.5(a) shows the UV-Visible absorption spectra (UV-Vis DRS) of BSO, LBSO1, LBSO3, and LBSO5 samples recorded from 200-900 nm at room temperature. The absorption of all the samples is higher in the visible region and it is notably higher for the LBSO3 sample (Fig. 4.5 a). The energy bandgap calculated from well-known 'Tauc' plots for the single-phase nanostructured BSO, LBSO1, LBSO3, and LBSO5 samples are 3.23 eV, 3.24 eV, 3.25 eV, and 3.29 eV, respectively (Inset of Figs. 4.5 a). The incorporation of La dopant ions is supported by the respective changes in the percentage of diffuse reflectance spectra of the synthesized samples (Fig. 4.5 b). The change in energy bandgap with increasing La content is possibly caused by the Sn-O bond hybridization.

The electronic energy band diagram of perovskite $BaSnO_3$ is schematically shown in Fig. 4.5c. Usually, the perovskite ternary oxide's energy band is influenced by the Sn-O bond hybridization. Here, the La dopant significantly changes the conduction band minimum (CBM)

state by orbital hybridization. The perovskite $BaSnO_3$ energy band comprises CBM and valence band maximum (VBM) by Sn 5s/5p and O 2p orbitals, respectively. Here, the VBM is dominated by the O 2p orbitals, and at the same time, CBM is dominated by the Sn 5s/5p orbitals. Upon increasing the La^{3+} ions at the Ba^{2+} sites, the unit cell volume decreases, and the average bond length also reduces due to the decrease in the unit cell volume. The increasing strength of Sn-O bond hybridization causes large crystal field splitting, resulting in the upward shift of CBM and an increase in the bandgap of LBSO samples [45–48]; this is the so-called Burstein-Mass shift which indicates a large conduction band (CB) dispersion [46]. This indicates that the La substitution effectively changes the band position and bandgap of the perovskite $BaSnO_3$ compound, thereby enabling optimization of band offset between the sensitized dye and the ETL in DSSCs.

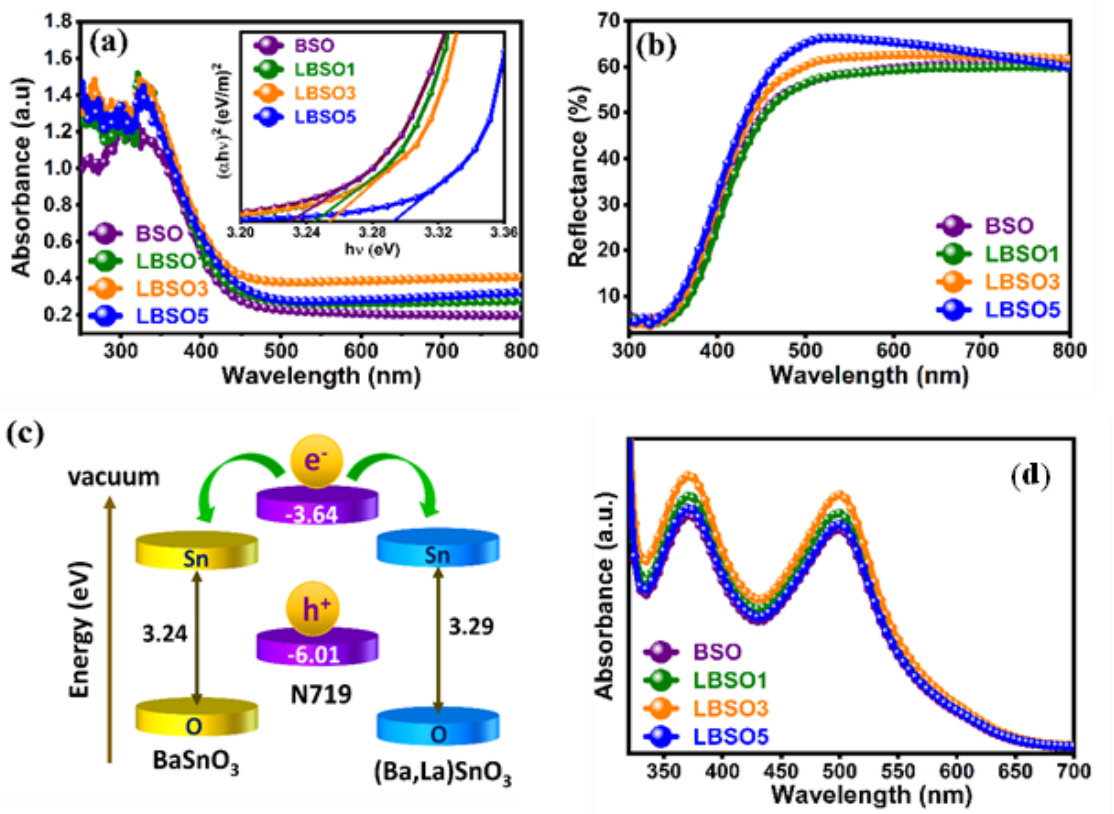

Fig. 4.5. (a) UV-Vis absorption spectra (inset is the Tauc plot), (b) diffuse reflectance spectra, (c) Schematic representation of the energy band diagram and (d) Absorption spectra of 0.5 mM of N719 dye loaded onto BSO and LBSO photoanodes.

Dye loading measurements were carried out to determine the effect of mixed (nanocuboids/nanoparticles) morphology on the dye adsorption capability of the BSO, LBSO1, LBSO3, and LBSO5 films. The dye loading capacity is evaluated by measuring the amount of N719 dye desorbed from the photoanode into the solvent, as shown in Fig. 4.5(d). The absorption of dye solution corresponding to the surface treated LBSO3 film is higher than that of the BSO film. For the pre- and post-surface treated LBSO films, the amount of dye loading increases with La content and it reaches the maximum absorption intensity up to $x = 0.03$ and decreases afterward for $x = 0.05$. The higher dye adsorption for LBSO3 may be due to the composite nanocuboids/nanoparticles morphology.

4.3.3 X-ray photoelectron spectroscopy analysis

The X-ray photoelectron spectroscopy measurement was performed, and the results are shown in Fig. 4.6 (a to b). From Fig. 4.6(a), the characteristic doublet peaks of Ba are observed at binding energies of 779.2 eV and 794.70 eV ascribed to Ba $3d_{5/2}$ and Ba $3d_{3/2}$ for BSO and LBSO3 samples, respectively. The peaks both have symmetrical shapes, indicating that the La-doped BSO nanoparticles have a highly crystalline nature [27]. Fig. 4.6(b) shows the doublet peaks at 485.78 eV and 494.26 eV corresponding to Sn $3d_{5/2}$ and Sn $3d_{3/2}$, respectively, and no shift is observed in the Sn 3d spectra. The symmetric peak at 530.18 eV is attributed to O 1s spectra and is shown in Fig. 4.6(c). It is the characteristic O^{2-} ion peak in the BSO metal oxide lattice framework. From Fig. 4.6(d), the La 3d spectra of LBSO3 exhibit two prominent peaks at 833.50 eV and 851.34 eV corresponding to La $3d_{5/2}$ and La $3d_{3/2}$, levels respectively. The XPS data ensures the presence of La dopant ions in the BSO nanoparticles in the most stable valence states of +II, +IV, -II, and +III for Ba, Sn, O, and La elements, respectively, in the cubic perovskite $BaSnO_3$ compound.

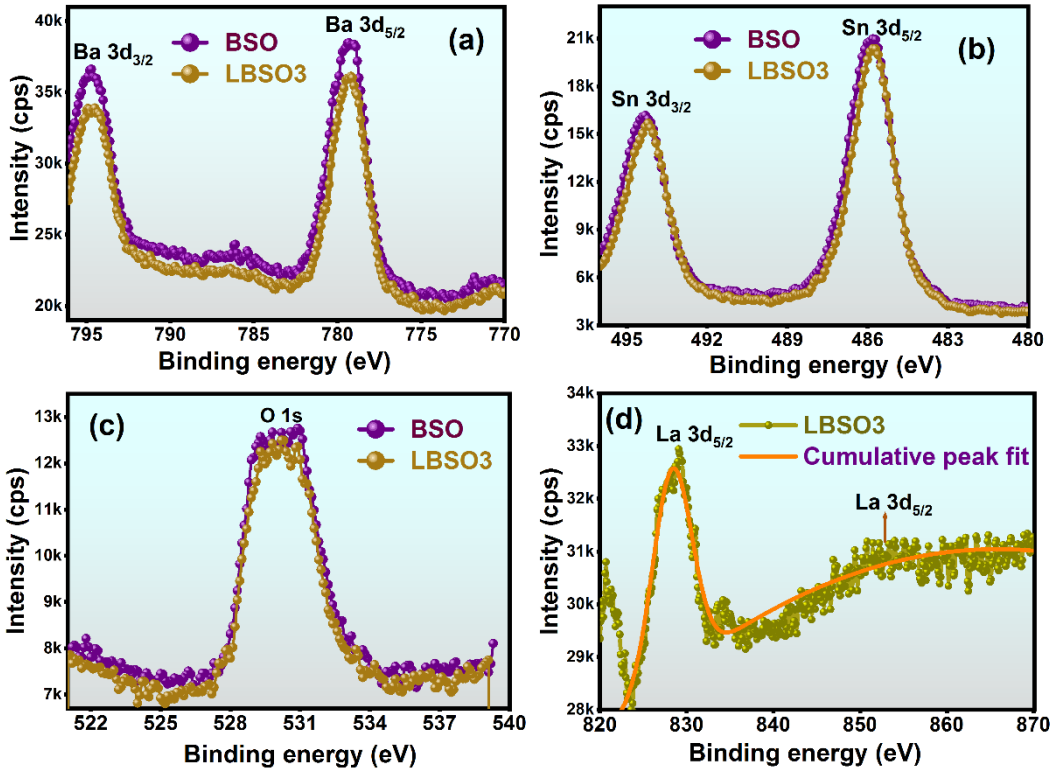

Fig. 4.6. The XPS spectra showing the core levels of (a) Ba 3d, (b) Sn 3d, (c) O1s, and (d) La 3d of BSO and LBSO3 samples.

4.3.4 Performance of pre and post surface treated photoanode based DSSCs

To demonstrate the potential use of La substituted $BaSnO_3$ perovskite material as an ETL in photovoltaics, DSSCs are fabricated using pre-and post-surface-treated BSO and LBSO photoanodes and tested for their photocurrent density-voltage (J-V) characteristics. The amount of dye loading on the surface of photoanodes strongly affects the photocurrent density, thereby the overall DSSC device performance is also influenced. The optimized DSSC devices are measured under simulated solar illumination of 100 mW cm^{-2}. Briefly, for the pre-treatment, the cleaned FTO substrates were immersed in 0.05 M of $TiCl_4$ aqueous solution at 80 °C for 1h and used to deposit the BSO and LBSO nanostructured particles, and are referred to as TCL/BSO and TCL/LBSO in this chapter. The pre-treated BSO and LBSO photoanode (TCL/BSO and TCL/LBSO) based device J-V curves are shown in Fig. 4.7(a) and also the J-V parameters are listed in Table 4.2. Among these pre-treated cells, a maximum current density

of 8.95 mA/cm^2 and conversion efficiency of 4.37% is achieved for the LBSO3 cell, and also the maximum external quantum efficiency (EQE) ~42% is observed for the LBSO3 device (shown in Fig. 4.7b).

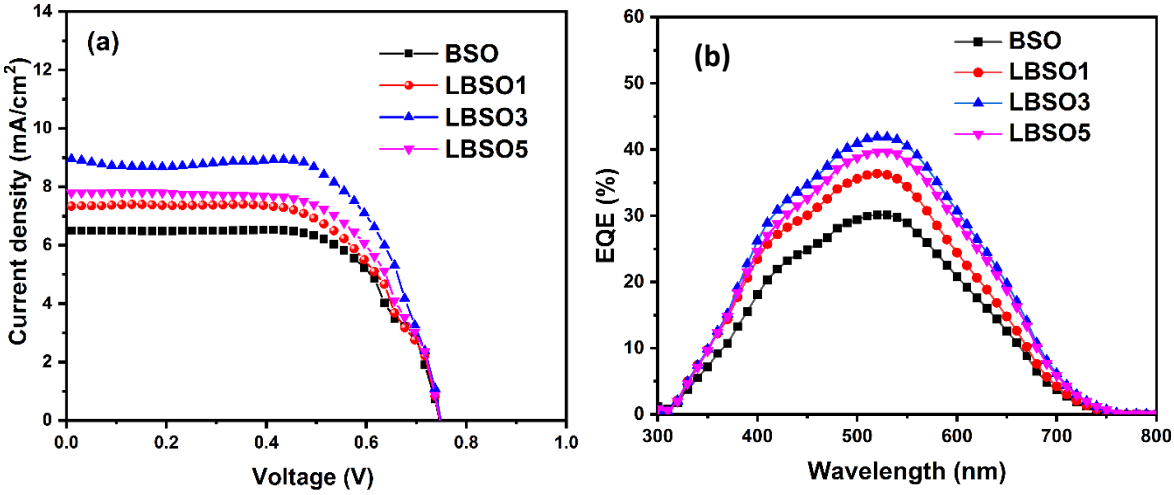

Fig. 4.7. (a) Pre-surface treated photocurrent density-voltage (J-V) curves of DSSCs fabricated with BSO and LBSO photoanodes, (b) External quantum efficiency (EQE) measurements of pre-surface treated BSO and LBSO photoanodes.

Table 4.2. The current density-voltage (J-V) parameters of pre-surface treated nanostructured BSO and LBSO photoanodes.

Device code	V_{OC} (V)	J_{SC} (mA/cm^2)	FF (%)	η (%)
TCL/BSO	0.737	6.50	67.42	3.23
TCL/LBSO1	0.738	7.33	64.23	3.48
TCL/LBSO3	0.742	8.95	65.73	4.37
TCL/LBSO5	0.739	7.79	65.36	3.76

Another set of pre-surface treated BSO and LBSO photoanodes were further treated with $TiCl_4$ solution and are referred to as TCL/BSO/TCL and TCL/LBSO/TCL (refers to post-surface treatment devices). It has been reported that there is a possibility of enhancing the cell efficiency due to pre-surface treatment with $TiCl_4$ on the FTO substrate [49]. Here, $TiCl_4$ forms a very

thin layer of TiO_2 on FTO and improves the bonding strength between FTO and the TiO_2 layer so that it increases the conductivity at the interface between the thin layer of TiO_2 and FTO when BSO or LBSO layer is coated over it. Moreover, it also reduces recombination between electrons within the electrolyte that contains the electron-hole pairs; these processes can enhance the current density, and subsequently, improve the power conversion efficiency of the DSSCs [34,49,50]. Therefore, by performing the post surface treatments on photoanodes, dye loading increases (see Fig. 4.5d), thereby increasing the photon absorption and leading to an increase in current as well as power conversion efficiency of the devices. The J-V curves are shown in Fig. 4.8a and the parameters are listed in Table 4.3 for the post-surface-treated BSO and LBSO photoanode based devices. The post-treated DSSC device exhibits best power conversion efficiency (η) of 5.96% with a current density (J_{sc}) of 14.37 mA cm^{-2}, open-circuit voltage (V_{oc}) of 0.722 V, and fill factor (FF) of 57.56 % for the LBSO3 sample. Upon further increasing the La substitution (x = 0.05), it results in decreased power conversion efficiency to 4.21%. This decrease may be caused by the reduced injection efficiency from dye to ETL due to the higher CBM of the ETL for x = 0.05 La substitution as discussed in section 4.3.2. (*i.e.*, higher bandgap value of 3.29 eV). Among all the tested devices, the TCL/LBSO3/TCL photoanode based device shows highest performance which is mainly attributed to the high V_{OC} and J_{SC} values. Moreover, higher electron density and efficient electron injection created by doping with La into the BSO system may induce the built-in potential between the dye and semiconducting layer [51], which may be the reason for the increased V_{OC} and J_{SC} for LBSO3 nanostructured particles. Finally, the power conversion efficiency is enhanced remarkably with pre/post-surface treated La-doped BSO electrodes. These results imply very promising performance in photovoltaics by doping La^{3+} cations into the BSO lattice.

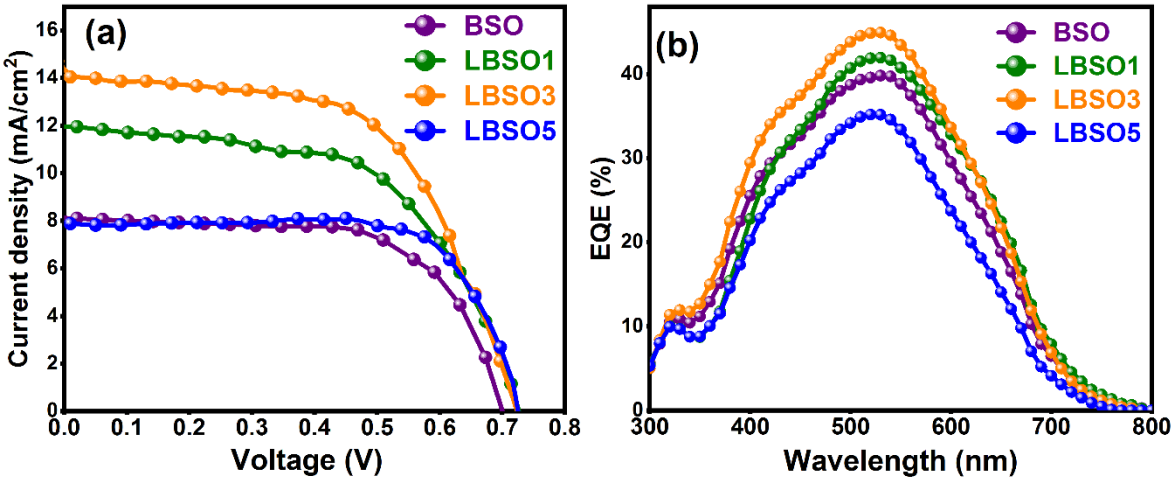

Fig. 4.8. The characteristics of (a) photocurrent density-voltage (J-V) curves and (b) external quantum efficiency (EQE) measurements of DSSCs fabricated using post-treated BSO and LBSO as photoanodes.

Table 4.3. Photocurrent density-voltage (J-V) parameters of the post $TiCl_4$-treated BSO and LBSO photoanode based DSSC devices.

Device code	V_{OC} (V)	J_{SC} (mA/cm^2)	FF (%)	η (%)
TCL/BSO/TCL	0.701	8.11	66.51	3.71
TCL/LBSO1/TCL	0.722	11.94	57.58	4.97
TCL/LBSO3/TCL	0.722	14.37	57.56	5.96
TCL/LBSO5/TCL	0.724	7.88	73.86	4.21

Figure 4.8b shows the incident photon to current conversion efficiency spectra of the post-treated BSO and LBSO based DSSCs. The measured IPCE spectra indicate that all the fabricated DSSCs show broad spectra over the 300-800 nm wavelength range with a maximum efficiency of ≅ 45% peaking around 520 nm. Figure 4.8b represents that the intensity of the IPCE increases while increasing the incorporation of La^{3+} ions into BSO from x= 0 to 0.03 and then decreases for 0.05 La-doped BSO; the same trend is observed

in J_{SC} (Fig. 4.8a). The EQE is also measured for the $TiCl_4$ pre-treated BSO and LBSO photoanode based cells and the spectra are shown in Fig. 4.7(b) for comparison.

4.3.5 Electrochemical impedance spectroscopy analysis

Electrochemical impedance spectroscopy (EIS) is measured to investigate the interfacial reactions of photoexcited electrons and electron transport kinetics within the fabricated DSSC devices. The Nyquist (including equivalent circuit) and Bode plots of post-treated BSO and LBSO based DSSC devices measured from 0.1 Hz to 10^6 Hz are shown in Fig. 4.9 (a & b). According to the equivalent circuit model fitting, the series resistance (R_s) values can be recognized as the resistance at the interface of FTO and photoanode material and the values are shown in Table 4.4. The R_S values of the DSSCs based on BSO, LBSO1, LBSO3, and LBSO5 determined according to the equivalent circuit are 17.90 Ω, 18.39 Ω, 19.40 Ω, and 18.02 Ω, respectively. All the devices show nearly identical charge transfer resistance in the high-frequency region, which is mainly due to the similar electrolyte (I^-/I_3^-) and counter electrodes (Pt) used for all the DSSCs. The mid-frequency region shows a bigger semicircle in Nyquist plots corresponding to charge transfer resistance (R_{CT2}) of oxide/dye/electrolyte interfaces, which strongly depends on the band-bending due to heterostructured photoanodes [38]. Here, the interest is on the R_{CT2} at the device's oxide/dye/electrolyte interface. From Fig. 4.9(a), it is clear that the radius or size of the semicircle decreases while increasing the La doping content in the BSO system (up to $x = 0.03$). The observed resistance values at the oxide/dye/electrolyte interface are 16.80 Ω, 14.76 Ω, 12.84 Ω, and 15.71 Ω for pure BSO, LBSO1, LBSO3, and LBSO5 devices, respectively. The lower R_{CT2} value for the device with LBSO3 leads to an efficient charge carrier transportation, demonstrating lesser electron transport resistance and fewer electrons going back to the redox mediator at the oxide/dye/electrolyte interface. Hence, the change in the current density is

attributed to the difference in the charge transferability. To show the variation in charge transfer resistances of pre-and post-treated devices, the EIS data of best-performing LBSO3 based DSSCs are shown for comparison in Fig. 4.10. Among these, the post-treated LBSO3 photoanode based cell exhibits lowest series resistance (R_S) of 19.20 Ω compared to the 22.01 Ω of the pre-treated device (calculated from Fig. 4.10). Similarly, the charge transfer resistance (R_{CT2}) value are 13.47 Ω and 12.84 Ω for pre and post treated LBSO3 devices, respectively. These results imply better charge transfer and enhanced performance of the LBSO3 photoanode-based DSSC device after the $TiCl_4$ post-treatment._Additionally, the electron lifetime (τ_e) values are evaluated from the Bode plot (Fig. 4.9(b)) as a function of frequency using EIS model relation $\tau_e \approx 1/\omega_{max}$, where ω_{max} is the maximum peak frequency at the R_{CT2} region. The analysis shows noticeable differences in the electron lifetime values in the order of LBSO3 (6.96 ms) > LBSO1 (6.26 ms) > BSO (5.84 ms) > LBSO5 (5.74 ms). Here, lower R_{CT2} and longer electron lifetime facilitate faster electron transport to ETL, resulting in slower electron recombination and increase in the electron capture ability [52–54]. The electron lifetime for the DSSC using post-treated LBSO3 is longer than those using the other pure BSO and LBSO photoanodes due to the proper substitution of La ions into the Ba sites of the BSO lattice, which act as charge trapping sites.

Table 4.4. Electrochemical impedance parameters of post $TiCl_4$ treated BSO and LBSO photoanode based DSSC devices.

Device Name	R_S (Ω)	R_{CT2} (Ω)	τ_e (ms)
TCL/BSO/TCL	17.90	16.80	5.84
TCL/LBSO1/TCL	18.39	14.76	6.26
TCL/LBSO3/TCL	19.20	12.84	6.96
TCL/LBSO5/TCL	18.02	15.71	5.74

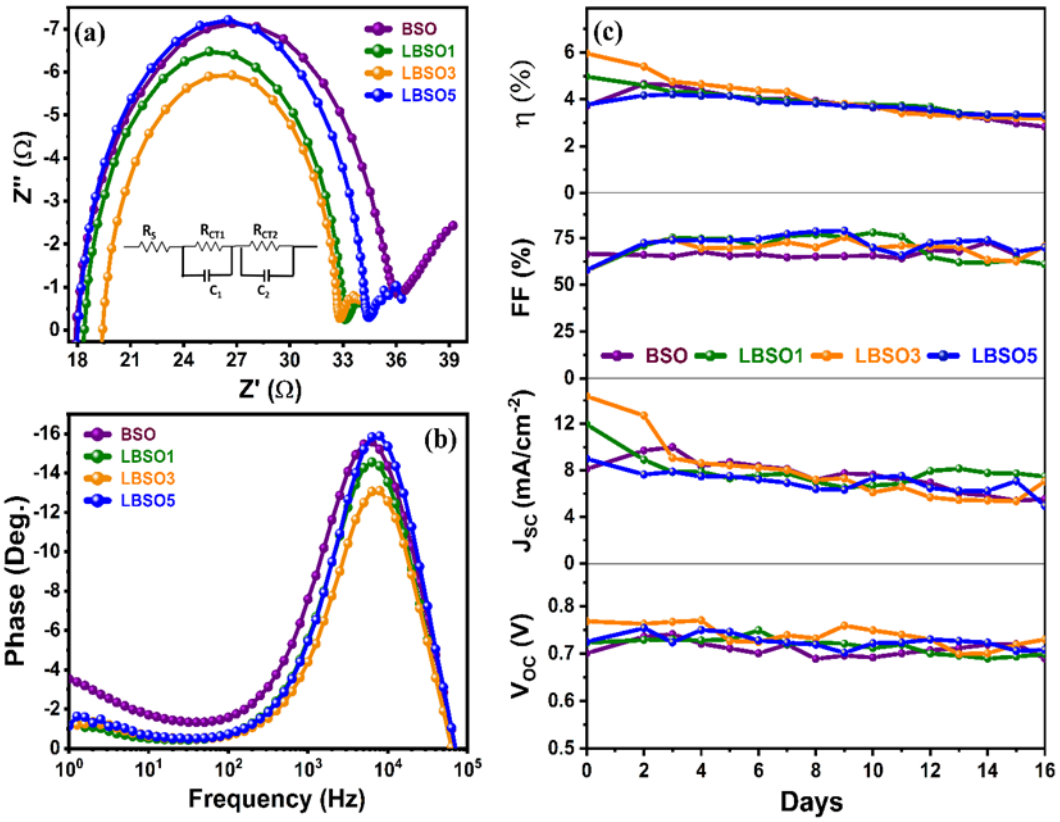

Fig. 4.9. The EIS spectra of DSSC devices fabricated using post-treated BSO and LBSO photoanodes, (a) Nyquist plot and the inset is the equivalent circuit diagram, (b) Bode plots. (c) The stability test of N719 dye-sensitized BSO and LBSO photoanode based devices stored for 16 days in air under ambient conditions.

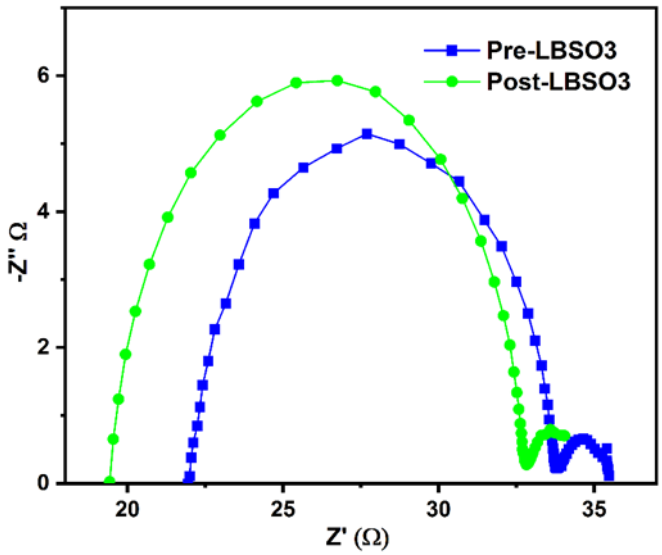

Fig. 4.10. Comparison of Nyquist plot of fabricated DSSC devices using pre and post treated LBSO3 (TCL/LBSO3 and TCL/LBSO3/TCL) photoanode based

4.3.6 Effect of surface treatments

It is well known that apart from J_{SC} and V_{OC}, fill factor (FF) is another critical parameter in evaluating the performance of DSSC devices. Significantly, series resistance, built-in voltage, and fabrication conditions of devices affect the FF and J_{SC} of the DSSCs [55,56]. Here, it is believed that the attenuation of FF of post-treated cells is due to an increment in series resistance for LBSO devices over BSO device. Also, it is observed that the charge transfer resistance R_{CT2} reduces with La concentration doped into the BSO system. Therefore, this implies that post-surface treatment results in an unprecedented escalation in the dye molecule adsorption, as shown in Fig. 4.5(d). These results may convey that the pre- and post-treatment of BSO, LBSO1, LBSO3, and LBSO5 surfaces provide more specific binding states. Potentially, the pre- and post-treatments of the surface may diminish the fraction of the TiO_2 surface area that may be inaccessible for the dye due to steric constraints [30]. These results clearly show that the La-doped BSO photoanodes are beneficial to increase the electron conduction for the efficient performance of the DSSC devices.

4.3.7 Long term stability test

The stability test of the fabricated DSSC devices using post treated BSO, LBSO1, LBSO3, and LBSO5 photoanodes was carried out and the results are shown in Fig. 4.9c. The devices stored in ambient conditions for 16 days were measured daily for their performance. The obtained performance parameters such as V_{OC}, J_{SC}, FF, and η are plotted against the number of days. During this 16-day test, the photovoltaic performance was remarkably stable, with only a moderate decrease in the value of performance parameters as seen in Fig. 4.9c. Interestingly, the nanostructured BSO and LBSO photoanode based DSSC devices still retained ~80% of their initial PCE at the end of 16 days stability test. Thus, the long-term stability for La-doped BSO-based DSSCs elucidates its potential use in future solar cells.

4.4 Conclusions

In summary, crystalline La-doped $BaSnO_3$ nanostructured particles were successfully synthesized *via* a facile peroxide-chemical route and coated as ETLs in DSSCs. Here, La is doped in the BSO system for varying concentration and is studied for their structural and optical properties to perceive their favorable interactions in the photoanode interface of DSSCs. A specific quantity of x = 0.03 La content leads to the formation of $BaSnO_3$ samples with vivid nanocuboid/nanoparticle composite morphologies, which is very effective in exhibiting expeditious dye adsorption compared to pristine BSO photoanode (within a short duration of 60 min). The pre-treated LBSO3 based cell shows a maximum power conversion efficiency of 4.37%. A typical post-$TiCl_4$ treatment of photoanode further enhances the conversion efficiency to 5.96% for LBSO3 cells, which is attributed to the increased electron lifetime and charge transferability as confirmed from the EIS analysis. This is one of the highest efficiencies without using any scattering layer over the nanostructured La-doped $BaSnO_3$, which shows great potential for its use as photoanode in DSSCs. Based on these results, it is believed that further exploration of La doping into BSO will provide a valuable perception for designing the high-performance and long-term stability of DSSCs.

References

[1] M. Grätzel, The advent of mesoscopic injection solar cells, Prog. Photovoltaics Res. Appl. 14 (2006) 429–442.

[2] Brian O'Regan & Michael Grätzel, A low-cost, high-efficiency solar cell based on dye-sensitized colloidal TiO_2 films, Nature. 353 (1991) 737–740.

[3] A. Yella, H.-W. Lee, H.N. Tsao, C. Yi, A.K. Chandiran, M.K. Nazeeruddin, E.W.-G. Diau, C.-Y. Yeh, S.M. Zakeeruddin, M. Grätzel, Porphyrin-sensitized solar cells with cobalt (II/III)–based redox electrolyte exceed 12 percent efficiency, Science (80-.). 334 (2011) 629–634.

[4] J.Y. Liao, B.X. Lei, D. Bin Kuang, C.Y. Su, Tri-functional hierarchical TiO_2 spheres consisting of anatase nanorods and nanoparticles for high efficiency dye-sensitized solar cells, Energy Environ. Sci. 4 (2011) 4079–4085.

[5] F. Huang, D. Chen, X.L. Zhang, R.A. Caruso, Y. Cheng, Dual-function scattering layer of submicrometer-sized mesoporous TiO_2 beads for high-efficiency dye-sensitized solar cells, Adv. Funct. Mater. 20 (2010) 1301–1305.

[6] K. Zhu, N.R. Neale, A. Miedaner, A.J. Frank, Enhanced charge-collection efficiencies and light scattering in dye-sensitized solar cells using oriented TiO2 nanotubes arrays, Nano Lett. 7 (2007) 69–74.

[7] D.K. Roh, W.S. Chi, H. Jeon, S.J. Kim, J.H. Kim, High efficiency solid-state dye-sensitized solar cells assembled with hierarchical anatase pine tree-like TiO_2 nanotubes, Adv. Funct. Mater. 24 (2014) 379–386.

[8] H.H. Thi Vu, T.S. Atabaev, J.Y. Ahn, N.N. Dinh, H.K. Kim, Y.H. Hwang, Dye-sensitized solar cells composed of photoactive composite photoelectrodes with enhanced solar energy conversion efficiency, J. Mater. Chem. A. 3 (2015) 11130–11136.

[9] N. Sakai, T. Miyasaka, T.N. Murakami, Efficiency enhancement of ZnO-based dye-sensitized solar cells by low-temperature $TiCl_4$ treatment and dye optimization, J. Phys. Chem. C. 117 (2013) 10949–10956.

[10] A. Sacco, A. Lamberti, R. Gazia, S. Bianco, D. Manfredi, N. Shahzad, F. Cappelluti, S. Ma, E. Tresso, High efficiency dye-sensitized solar cells exploiting sponge-like ZnO nanostructures, Phys. Chem. Chem. Phys. 14 (2012) 16203–16208.

[11] N. Memarian, I. Concina, A. Braga, S.M. Rozati, A. Vomiero, G. Sberveglieri, Hierarchically assembled ZnO nanocrystallites for high-efficiency dye-sensitized solar cells, Angew. Chemie. 123 (2011) 12529–12533.

[12] W.C. Chang, Y.Y. Cheng, W.C. Yu, Y.C. Yao, C.H. Lee, H.H. Ko, Enhancing performance of ZnO dye-sensitized solar cells by incorporation of multiwalled carbon nanotubes, Nanoscale Res. Lett. 7 (2012) 1–7.

[13] Q. Wali, A. Fakharuddin, I. Ahmed, M.H. Ab Rahim, J. Ismail, R. Jose, Multiporous nanofibers of SnO_2 by electrospinning for high efficiency dye-sensitized solar cells, J. Mater. Chem. A. 2

(2014) 17427–17434.

[14] A. Birkel, Y.G. Lee, D. Koll, X. Van Meerbeek, S. Frank, M.J. Choi, Y.S. Kang, K. Char, W. Tremel, Highly efficient and stable dye-sensitized solar cells based on SnO_2 nanocrystals prepared by microwave-assisted synthesis, Energy Environ. Sci. 5 (2012) 5392–5400.

[15] R. Abdul Rani, A.S. Zoolfakar, J. Subbiah, J.Z. Ou, K. Kalantar-Zadeh, Highly ordered anodized Nb2O5 nanochannels for dye-sensitized solar cells, Electrochem. Commun. 40 (2014) 20–23.

[16] Y.H. Jang, X. Xin, M. Byun, Y.J. Jang, Z. Lin, D.H. Kim, Erratum: An unconventional route to high efficiency dye-sensitized solar cells via embedding graphitic thin films into TiO_2 nanoparticle photoanode (Nano Letters (2012) 12:1 (479-486).

[17] B. Li, E. Guo, C. Wang, L. Yin, Novel Au inlaid Zn_2SnO_4/SnO_2 hollow rounded cubes for dye-sensitized solar cells with enhanced photoelectric conversion performance, J. Mater. Chem. A. 4 (2015) 466–477.

[18] M. Muruganandham, M. Swaminathan, Solar photocatalytic degradation of a reactive azo dye in TiO 2-suspension, Sol. Energy Mater. Sol. Cells. 81 (2004) 439–457.

[19] G.A. Epling, C. Lin, Photoassisted bleaching of dyes utilizing TiO_2 and visible light, Chemosphere. 46 (2002) 561–570.

[20] S.S. Shin, D.W. Kim, D. Hwang, J.H. Suk, L.S. Oh, B.S. Han, D.H. Kim, J.S. Kim, D. Kim, J.Y. Kim, Controlled interfacial electron dynamics in highly efficient Zn_2SnO_4-based dye-sensitized solar cells, ChemSusChem. 7 (2014) 501–509.

[21] J. Chen, L. Lu, W. Wang, Zn_2SnO_4 nanowires as photoanode for dye-sensitized solar cells and the improvement on open-circuit voltage, J. Phys. Chem. C. 116 (2012) 10841–10847.

[22] B. Tan, E. Toman, Y. Li, Y. Wu, Zinc Stannate (Zn_2SnO_4) Dye-Sensitized Solar Cells, Journal of the American Chemical Society 129, (2007): 4162-4163.

[23] I. Hod, M. Shalom, Z. Tachan, S. Rühle, A. Zaban, $SrTiO_3$ recombination-inhibiting barrier layer for type II dye-sensitized solar cells, J. Phys. Chem. C. 114 (2010) 10015–10018.

[24] G. Natu, Y. Wu, Photoelectrochemical study of the ilmenite polymorph of $CdSnO_3$ and its photoanodic application in dye-sensitized solar cells, J. Phys. Chem. C. 114 (2010) 6802–6807.

[25] R. Tang, L. Yin, Enhanced photovoltaic performance of dye-sensitized solar cells based on Sr-doped $TiO_2/SrTiO_3$ nanorod array heterostructures, J. Mater. Chem. A. 3 (2015) 17417–17425.

[26] Y. Li, H. Zhang, B. Guo, M. Wei, Enhanced efficiency dye-sensitized $SrSnO_3$ solar cells prepared using chemical bath deposition, Electrochim. Acta. 70 (2012) 313–317.

[27] D.W. Kim, S.S. Shin, S. Lee, I.S. Cho, D.H. Kim, C.W. Lee, H.S. Jung, K.S. Hong, $BaSnO_3$ perovskite nanoparticles for high efficiency dye-sensitized solar cells, ChemSusChem. 6 (2013) 449–454.

[28] L. Zhu, J. Ye, X. Zhang, H. Zheng, G. Liu, X. Pan, S. Dai, Performance enhancement of perovskite solar cells using a La-doped $BaSnO_3$ electron transport layer, J. Mater. Chem. A. 5 (2017) 3675–3682.

[29] S.S. Shin, J.S. Kim, J.H. Suk, K.D. Lee, D.W. Kim, J.H. Park, I.S. Cho, K.S. Hong, J.Y. Kim, Improved quantum efficiency of highly efficient perovskite $BaSnO_3$-based dye-sensitized solar cells, ACS Nano. 7 (2013) 1027–1035.

[30] A. Roy, P.P. Das, P. Selvaraj, S. Sundaram, P.S. Devi, Perforated $BaSnO_3$ Nanorods Exhibiting Enhanced Efficiency in Dye Sensitized Solar Cells, ACS Sustain. Chem. Eng. 6 (2018) 3299–3310.

[31] S. Raghavan, T. Schumann, H. Kim, J.Y. Zhang, T.A. Cain, S. Stemmer, High-mobility $BaSnO_3$ grown by oxide molecular beam epitaxy, Apl Mater. 4 (2016) 16106.

[32] H.J. Kim, U. Kim, H.M. Kim, T.H. Kim, H.S. Mun, B.-G. Jeon, K.T. Hong, W.-J. Lee, C. Ju, K.H. Kim, High mobility in a stable transparent perovskite oxide, Appl. Phys. Express. 5 (2012) 61102.

[33] D.O. Scanlon, Defect engineering of $BaSnO_3$ for high-performance transparent conducting oxide applications, Phys. Rev. B. 87 (2013) 161201.

[34] J. Cerdà, J. Arbiol, G. Dezanneau, R. Díaz, J.R. Morante, Perovskite-type $BaSnO_3$ powders for high temperature gas sensor applications, Sensors Actuators, B Chem. 84 (2002) 21–25.

[35] W. Zhang, F.A. Guo, G. Li, Barium staminate as semiconductor working electrodes for dye-sensitized solar cells, Int. J. Photoenergy. 2010 (2010).

[36] Y. Zhang, H. Zhang, Y. Wang, W.F. Zhang, Efficient visible spectrum sensitization of $BaSnO_3$ nanoparticles with N719, J. Phys. Chem. C. 112 (2008) 8553–8557.

[37] N. Rajamanickam, P. Soundarrajan, V.K. Vendra, J.B. Jasinski, M.K. Sunkara, K. Ramachandran, Efficiency enhancement of cubic perovskite $BaSnO_3$ nanostructures based dye sensitized solar cells, Phys. Chem. Chem. Phys. 18 (2016) 8468–8478.

[38] N. Rajamanickam, P. Soundarrajan, S.M. Senthil Kumar, K. Jayakumar, K. Ramachandran, Boosting photo charge carrier transport properties of perovskite $BaSnO_3$ photoanodes by Sr doping for enhanced DSSCs performance, Electrochim. Acta. 296 (2019) 771–782.

[39] S.S. Shin, E.J. Yeom, W.S. Yang, S. Hur, M.G. Kim, J. Im, J. Seo, J.H. Noh, S. Il Seok, Colloidally prepared La-doped $BaSnO_3$ electrodes for efficient, photostable perovskite solar cells, Science (80-.). 356 (2017) 167–171.

[40] N. Purushothamreddy, M. Kovendhan, R.K. Dileep, G. Veerappan, K.S. Kumar, D.P. Joseph, Synthesis and characterization of nanostructured La-doped $BaSnO_3$ for dye-sensitized solar cell application, Mater. Chem. Phys. 250 (2020) 123137.

[41] G.S. Lotey, N.K. Verma, Synthesis and characterization of $BiFeO_3$ nanowires and their applications in dye-sensitized solar cells, Mater. Sci. Semicond. Process. 21 (2014) 206–211.

[42] R.A. Naphade, M. Tathavadekar, J.P. Jog, S. Agarkar, S. Ogale, Plasmonic light harvesting of dye sensitized solar cells by Au-nanoparticle loaded TiO_2 nanofibers, J. Mater. Chem. A. 2 (2014) 975–984.

[43] P. Pratim Das, A. Roy, S. Das, P.S. Devi, Enhanced stability of Zn_2SnO_4 with N719, N3 and

eosin y dye molecules for DSSC application, Phys. Chem. Chem. Phys. 18 (2016) 1429–1438.

[44] C. Huang, X. Wang, X. Wang, X. Liu, Q. Shi, X. Pan, X. Li, Preparation of $BaSnO_3$ and $Ba_{0.96}La_{0.04}SnO_3$ by reactive core-shell precursor: Formation process, CO sensitivity, electronic and optical properties analysis, RSC Adv. 6 (2016) 25379–25387.

[45] S.S. Shin, J.H. Suk, B.J. Kang, W. Yin, S.J. Lee, J.H. Noh, T.K. Ahn, F. Rotermund, I.S. Cho, S. Il Seok, Energy-level engineering of the electron transporting layer for improving open-circuit voltage in dye and perovskite-based solar cells, Energy Environ. Sci. 12 (2019) 958–964.

[46] W. Zhang, J. Tang, J. Ye, Structural, photocatalytic, and photophysical properties of perovskite MSnO3 (M= Ca, Sr, and Ba) photocatalysts, J. Mater. Res. 22 (2007) 1859–1871.

[47] C. Shan, T. Huang, J. Zhang, M. Han, Y. Li, Z. Hu, J. Chu, Optical and electrical properties of sol-gel derived $Ba_{1-x}La_xSnO_3$ transparent conducting films for potential optoelectronic applications, J. Phys. Chem. C. 118 (2014) 6994–7001.

[48] C.W. Myung, G. Lee, K.S. Kim, La-doped $BaSnO_3$ electron transport layer for perovskite solar cells, J. Mater. Chem. A. 6 (2018) 23071–23077.

[49] J. Akilavasan, K. Wijeratne, A. Gannoruwa, A.R.M. Alamoud, J. Bandara, Significance of $TiCl_4$ post-treatment on the performance of hydrothermally synthesized titania nanotubes-based dye-sensitized solar cells, Appl. Nanosci. 4 (2014) 185–188.

[50] B.C. O'Regan, J.R. Durrant, P.M. Sommeling, N.J. Bakker, Influence of the $TiCl_4$ treatment on nanocrystalline TiO_2 films in dye-sensitized solar cells. 2. Charge density, band edge shifts, and quantification of recombination losses at short circuit, J. Phys. Chem. C. 111 (2007) 14001–14010.

[51] S.S. Shin, W.S. Yang, E.J. Yeom, S.J. Lee, N.J. Jeon, Y.C. Joo, I.J. Park, J.H. Noh, S. Il Seok, Tailoring of Electron-Collecting Oxide Nanoparticulate Layer for Flexible Perovskite Solar Cells, J. Phys. Chem. Lett. 7 (2016) 1845–1851.

[52] K. Mahmood, H.J. Sung, A dye-sensitized solar cell based on a boron-doped ZnO (BZO) film with double light-scattering-layers structured photoanode, J. Mater. Chem. A. 2 (2014) 5408–5417.

[53] E.S. Kwak, W. Lee, N. Park, J. Kim, H. Lee, Compact Inverse-Opal Electrode Using Non-Aggregated TiO_2 Nanoparticles for Dye-Sensitized Solar Cells, Adv. Funct. Mater. 19 (2009) 1093–1099.

[54] C. He, Z. Zheng, H. Tang, L. Zhao, F. Lu, Electrochemical impedance spectroscopy characterization of electron transport and recombination in ZnO nanorod dye-sensitized solar cells, J. Phys. Chem. C. 113 (2009) 10322–10325.

[55] G. Kron, U. Rau, J.H. Werner, Influence of the built-in voltage on the fill factor of dye-sensitized solar cells, J. Phys. Chem. B. 107 (2003) 13258–13261.

[56] L. Han, N. Koide, Y. Chiba, T. Mitate, Modeling of an equivalent circuit for dye-sensitized solar cells, Appl. Phys. Lett. 84 (2004) 2433–2435.

CHAPTER: 5

Synthesis and characterization of the Sb-doped $BaSnO_3$ nanoparticles for use as photoanodes in DSSCs

This chapter describes the results obtained on facile peroxide precipitate-route synthesized Sb doped $BaSnO_3$ compound ($BaSn_xSb_{1-x}O_3$, where x= 0, 0.01, 0.03). The focus is on structural, morphological, optical, and electrical properties of donor element Sb doped $BaSnO_3$ for use as photoanode material to explore its performance in DSSC. The obtained results on the characterization of the nanocrystalline samples and also the DSSC device performance are discussed in sufficient detail in this chapter.

5.1 Introduction

The DSSCs constitute a unique category of 3rd generation photovoltaics with certain distinct advantages over their 1st and 2nd generation counterparts. Their ease of fabrication, cost-effectiveness, robustness, low-light and relatively high temperature performance, versatile design, use of eco-friendly and stable materials, etc. [1–4] are some of the major factors which continue to attract researchers towards developing novel materials and device design strategies to improve their efficiency. Certain limitations of the prominently used TiO_2 metal oxide photoanodes in DSSCs have motivated researchers to explore alternate materials [4–6]. Among the various ternary metal oxides, alkaline earth stannates with standard formula $RSnO_3$ (R = Ba, Sr, Ca, etc.) have promising technological applicability due to their electron affinity, ionization potential, and band-gap which can be conveniently modified by varying the synthesis strategy [7–10]. In particular, $BaSnO_3$ has an ideal perovskite structure and behaves as a wide-bandgap (3.1-3.4 eV depending on the dopant) n-type semiconductor with structural stability up to 1000 °C [11–13]. Moreover, its constituents Ba^{2+}, $Sn^{4+,}$ and O^{2-} have well-matching ionic radii with several dopants and host materials. The smaller Sn^{4+} ions in perovskite $BaSnO_3$ are octahedrally coordinated to the oxygen atoms. In oxides, Sb typically adopts either 3+ ($4d^{10}5s^2\ 5p^0$) or 5+

($4d^{10}5s^{0}5p^{0}$) oxidation state [14]. Oxygen vacancies are formed if Sb^{3+} substitutes at the Sn^{4+} sites, leading to charge compensation. Conversely, compensation due to cation vacancies takes place in the case of Sb^{5+} substitution [14].

Antimony doped stannates in the nanostructured form are hardly reported, especially for energy related applications. The facile peroxide-precipitate route does not require expensive instrumentation and is suitable for tuning the microstructure, particle size, doping concentration, and surface area of nanocrystalline $BaSnO_3$ [15]. The proposed work intends to explore the development and applicability of the less explored nanocrystalline undoped and Sb-doped $BaSnO_3$ perovskites as alternative photoanodes in DSSCs. Since $BaSnO_3$ is a ternary compound, the solubility of the incorporated Sb dopant is limited and high doping concentration leads to the formation of secondary phases [14]. Hence, in the present work, the Sb dopant concentration in $BaSn_{(1-x)}Sb_xO_3$ is limited to x = 0.01 and 0.03. The solute (dopant) ions Sb^{5+} (0.60 Å) and/or Sb^{3+} (0.76 Å) fulfill Hume-Rothery rules for incorporation at the host ionic sites Sn^{4+} (0.69 Å), hence, stoichiometric calculations for substitution of 'Sb' ions at the 'Sn' sites are made[14]. The facile peroxide-precipitate synthesis of Sb-doped $BaSnO_3$ nanoparticles has been little explored which may prove to be fruitful in generating new insights for its applicability as photoanode material in DSSCs.

5.2 Experimental methods

In this chapter, we have followed the facile peroxide precipitate route to synthesize $BaSnO_3$ and Sb doped $BaSnO_3$ compound. To dope antimony (Sb) at the Sn sites, $SbCl_3$ precursor solution is used. Undoped and Sb doped $BaSn_{(1-x)}Sb_xO_3$ (x = 0, 0.01 and 0.03) nanocrystalline samples (Hereafter referred to as BSO, ABSO1, and ABSO3, respectively) were synthesized using the facile peroxide-precipitate route as depicted in Fig. 5.1 which is already described in Chapter 4, section 4.2.1. The Sb doped $BaSnO_3$ samples are collectively referred to as ABSO.

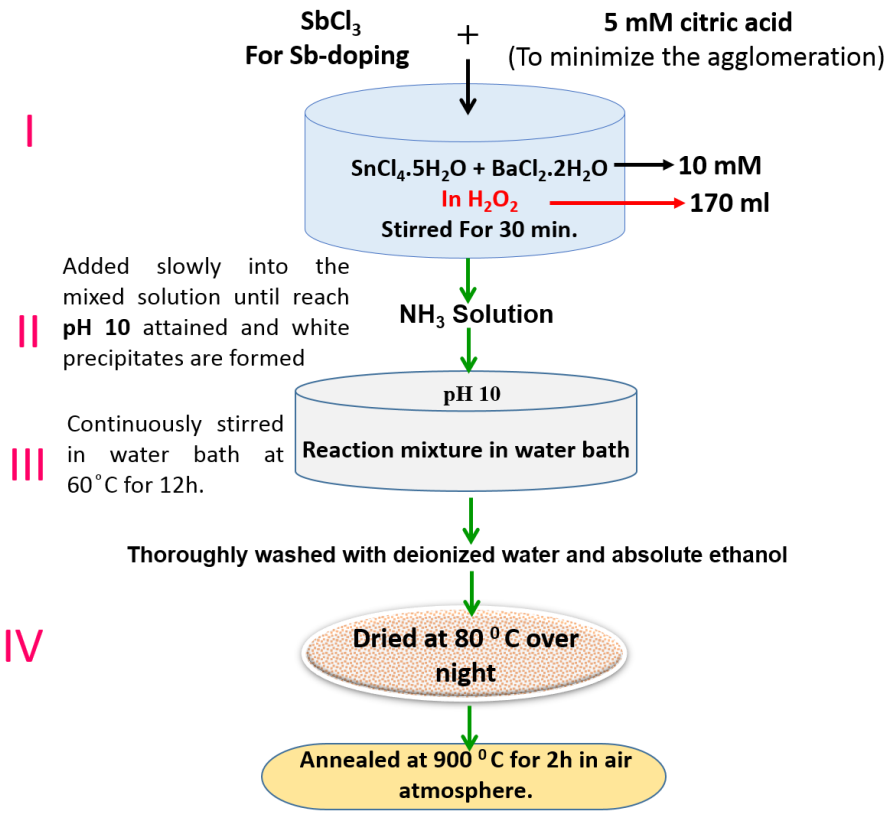

Fig. 5.1. Schematics of facile peroxide synthesis route of pure and Sb doped $BaSnO_3$ nanoparticles.

5.2.1 DSSC fabrication and characterization

The annealed nanocrystalline BSO and ABSO samples were coated over the ultrasonically cleaned FTO substrates using the doctor blade technique. These electrodes were then treated with 40 mM $TiCl_4$ solution at 100 °C for 1h followed by annealing at 500 °C for 30 min. The annealed electrodes were then soaked in 0.3 mM of N719 dye dissolved in absolute ethanol at room temperature for 12h. The electrodes were thoroughly rinsed with a mild stream of ethanol to remove physically adsorbed dye molecules on the surface. The counter electrodes were prepared by coating thin platinum (Pt) layer on the FTO substrate followed by annealing at 450 °C for 30 min in air. Sandwich-type DSSCs were then fabricated using the prepared photoanodes and counter electrodes by sealing them at 130 °C using surlyn spacer over a hot plate. The iodine redox couple (I^-/I_3^-) electrolyte was injected into the sealed device through a

fine hole drilled from the rear side of the counter electrode. The active area of the fabricated device was 0.25 cm^2. The current density-voltage (J-V) characteristics of the photovoltaic devices were evaluated at room temperature in ambient conditions using Keithley 2400 source meter under AM 1.5 G solar irradiation of 100 mW cm^{-2} obtained from a 300 W Oriel solar simulator which was calibrated using a mono-Si reference cell with a KG5 filter. The DSSC devices fabricated by using the paste of the stabilized powders serving as photoanode materials are referred to as D_{BSO}, $D_{ABSO1,}$ and D_{ABSO3} hereafter.

5.3 Results and discussions

5.3.1 X-ray diffraction analysis

The XRD patterns of the stabilized BSO and ABSO nanoparticles are shown in Fig. 5.2(a). Formation of single-phase compound with space group Pm-3m and cubic symmetry is confirmed from Rietveld refinement of the XRD data obtained using FullProf.2 k, Version 7.00 are shown in Fig. 5.2 (b-d). From Table 5.1, a marginal decrease is observed in the lattice constant which implies lattice contraction, possibly due to the substitution of a smaller ionic radius of Sb^{5+} (0.60 Å) compared to that of Sn^{4+} (0.69 Å). The crystallite size is estimated using the Scherrer formula for the highest intensity (110) peak for BSO, ABSO1, and ABSO3 samples, and no significant variation in crystallite size was inferred (Table. 5.1).

5.3.2 Surface morphological studies

Morphological features of the synthesized BSO and ABSO photoanodes with considerable aggregate of fine particles characterized using FE-SEM (Hitachi, S-4300SE) are shown in Fig. 5.3 (a-c). Energy-dispersive X-ray (EDX) analysis confirms the presence of Ba, Sn, O, and Sb elements in the samples in the desired composition with only a nominal deviation as shown in the inset of Fig. 5.3(d-e).

Table 5.1. Refined structural parameters and optical bandgaps of BSO and ABSO samples.

Sample code	Crystallite size (nm)	a = b = c (Å)	Volume (Å^3)	Chi^2	Bandgap (eV)
BSO	11.03	4.1184(2)	69.8530	1.51	3.48
ABSO1	11.59	4.1182(2)	69.8429	1.48	3.44
ABSO3	11.59	4.1176(1)	69.8123	1.74	3.43

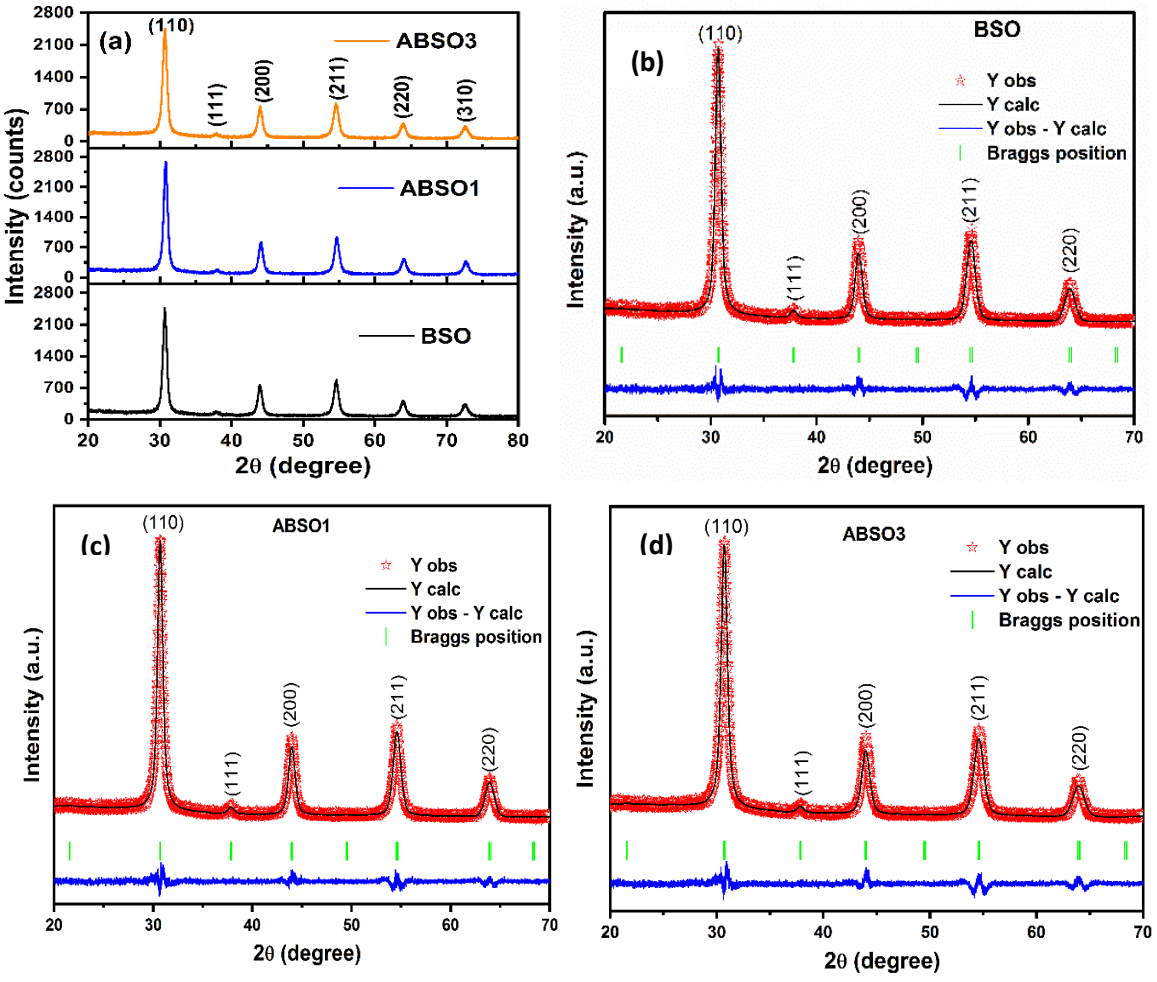

Fig. 5.2. (a) XRD patterns of BSO and ABSO samples. Rietveld refinement of XRD patterns of (b) BSO, (c) ABSO1 and (d) ABSO3 samples.

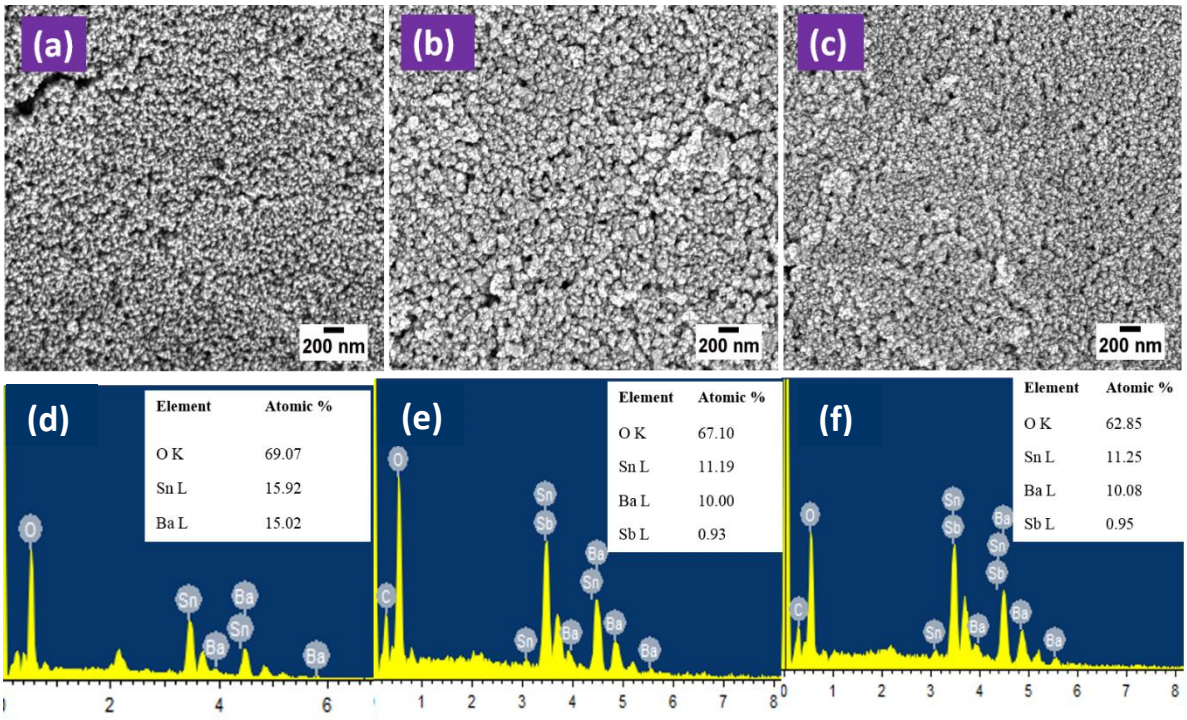

Fig. 5.3. FE-SEM images (a-c) and the EDX spectra (d-f) of undoped BSO, ABSO1 and ABSO3 samples, respectively.

The transmission electron microscopy (TEM) images, HR-TEM, and selected area electron diffraction (SAED) patterns (Model: Talos F200S-G2, Thermofisher) of nanocrystalline BSO and ABSO1 samples are shown in Fig. 5.4(a-d). From Fig. 5.4(a and b), the average crystallite sizes determined for BSO and ABSO1 are 16 nm and 17 nm, respectively. From the HR-TEM images, the d-spacing is determined to be around 0.27 nm and 0.33 nm for BSO and ABSO1 samples, respectively (Fig. 5.4 b & d) corresponding to the (110) and (211) diffraction planes of the cubic perovskite structure. The inset of Fig. 5.4 (b and d) shows a clear signature of polycrystalline nature which is observed from the SAED pattern with diffuse diffraction rings corresponding to (110), (211), and (200) planes of the perovskite BSO structure.

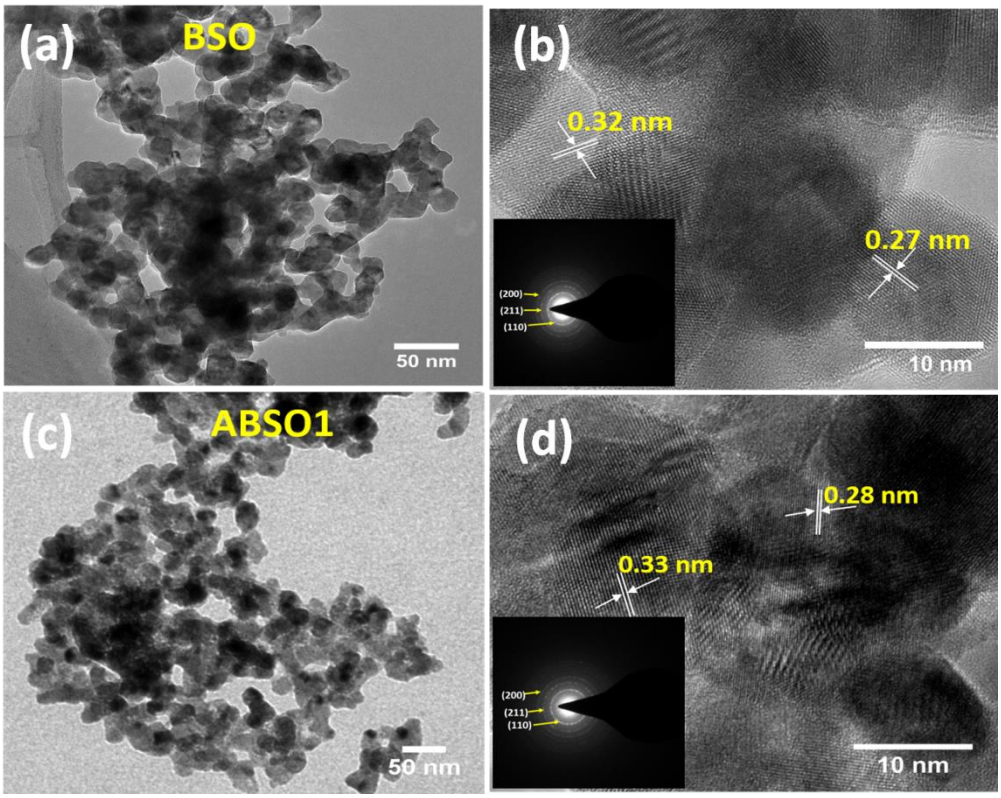

Fig. 5.4. The TEM, HR-TEM pattern images of (a-b) BSO and (c-d) ABSO1 sample. The inset images (b) and (d) show the SAED patterns of BSO and ABSO1 samples.

5.3.3 Optical properties

The diffuse reflectance spectra of the nanocrystalline samples show a linear region corresponding to the band edge absorption in the range of 350 nm to 450 nm. For the BSO sample, a vivid absorption edge around 400 nm is seen and the reflectance percentage after 450 nm is nearly flat in the entire visible region as shown in Fig. 5.5(a). Upon increasing Sb concentration, the percentage of reflectance is significantly declined to imply strong absorbance of the incident radiation in the visible region, and a subtle redshift in bandgap is observed with increasing Sb content (Table 5.1).

Optical band-gap values (Fig. 5.5 b) of the BSO and ABSO samples are estimated from the onset of linear fit of the diffuse reflectance spectra (DRS). A significant decrease in reflectance intensity is observed upon Sb-doping. This indicates effective photon absorption by the doped samples in the visible region of the electromagnetic spectrum [14]. The linear region in the DRS with highest slope and sharp increase in percentage reflectance is commonly attributed to an exponential decrease in absorption coefficient. The band-gap value for undoped BSO sample is obtained to be 3.48 eV and it decreases slightly with Sb-doping (3.44 eV and 3.43 eV for ABSO1 and ABSO3, respectively). The possibility of bandgap tuning with Sb-doping using facile peroxide-precipitate synthesis method indicates its suitability in photovoltaic applications.

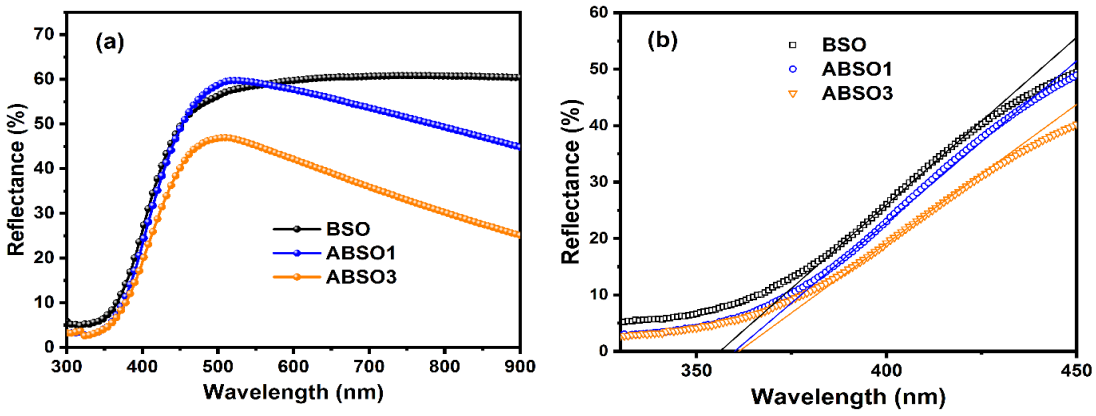

Fig. 5.5. (a) Diffuse reflectance spectra and (b) optical band-gap estimation of nanocrystalline BSO and ABSO samples.

5.3.4 X-ray photoelectron spectroscopy analysis

The X-ray photoelectron spectroscopy (XPS) measurement was performed over a wide range (200-900 eV) to study the oxidation states of the elements present in the BSO and ABSO1 sample to understand the basic charge transport mechanism and also to confirm the presence of Sb in the doped sample. Fig. 5.6(a) is the survey scan spectra of the samples showing the presence of Ba, Sn, O, and Sb elements and it has been identified that the Sb peak has relatively low intensity due to low dopant concentration (x= 0.01) in the samples.

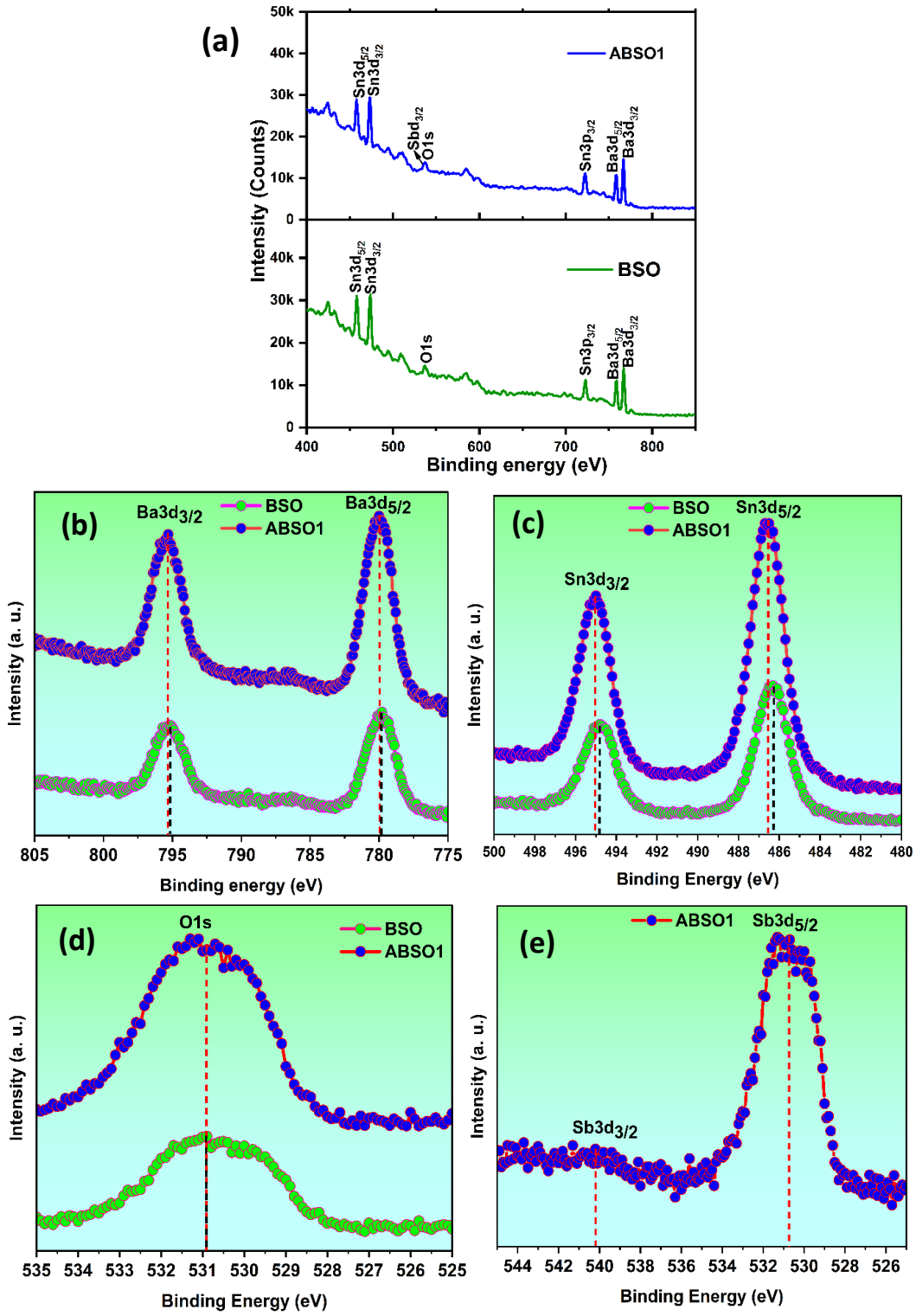

Fig. 5.6. The XPS (a) full survey spectrum and narrow scan spectra of (b) Ba 3d, (c) Sn 3d, (d) O1s and (e) Sb 3d of BSO and ABSO1 samples.

Figure 5.6(b) represents the narrow scan spectra of Ba for BSO and ABSO1 samples. The characteristic doublet peaks of Ba are observed at binding energy values of 780.1 eV and 795.3

eV ascribed to Ba $3d_{5/2}$ and Ba $3d_{3/2}$ for both BSO and ABSO1 samples, respectively. The Sn spectra corresponding to Sn $3d_{5/2}$ and $Sn3d_{3/2}$ binding energy peaks of BSO and ABSO1 samples are shown in Fig. 5.6(c). The Sn doublets at 486.3 eV and 494.8 eV binding energies correspond to $3d_{5/2}$ and $3d_{3/2}$ levels of the BSO sample (Fig. 5.6c). Upon doping Sb at the Sn sites, the doublet peaks corresponding to $Sn3d_{5/2}$ (486.5 eV) and $Sn3d_{3/2}$ (495.1eV) are shifted to a higher binding energy side by 0.2 eV and 0.3 eV, respectively, for the ABSO1 sample (Fig. 5.6c). The Sn binding energy reveals that the Sn ions exist in a 4+ charge state [16]. The bonding states of O1s spectra centered at 530.9 eV (O II) for BSO and ABSO1 samples are shown in Fig. 5.6(d). It is the characteristic O^{2-} ions peak in the BSO metal oxide lattice framework. Figure 5.6(e) shows the narrow scan spectra of $Sb3d_{3/2}$ and $Sb3d_{5/2}$ oxidization states with binding energy at 540.2 eV and 530.7 eV, respectively [17]. The Sb binding energy reveals that Sb exists in the Sb^{5+} charge state. The effectiveness of Sb doping may lead to improved electrical properties of ABSO1 based DSSC. It has been reported that the doping of Sb in the Sn lattice sites may increase the free carrier concentration [18].

5.3.5 Photovoltaic and electrochemical impedance analysis of the fabricated DSSCs

Current density-voltage (J-V) characteristics and the corresponding semi-log plots under AM 1.5 G solar illumination for the DSSCs fabricated using the BSO, ABSO1, and ABSO3 photoanodes are shown in Figs. 5.7(a) and (b). Photovoltaic parameters like short circuit current density (J_{SC}), open-circuit voltage (V_{OC}), fill factor (FF), and power conversion efficiency (η) determined from Fig. 5.7(a) are given in Table 5.2. Device D_{ABSO1} fabricated using ABSO1 as photoanode exhibits high η of 4.06 % and J_{SC} of 9.97 mA/cm^2 which implies significant improvement in the photovoltaic performance upon Sb-doping with x = 0.01 in $BaSn_{(1-x)}Sb_xO_3$. However, with a further increase in Sb-doping for x = 0.03, there is a slight decrement in the D_{ABSO3} parameters (although higher than that of D_{BSO}) which may be due to the self-compensation effect [14]. From the semi-log plot (Fig. 5.7b), it should be noted that

D_{ABSO3} exhibits a slightly higher forward photocurrent compared to other devices, whereas V_{OC} is found to be almost constant. Reverse leakage current in a solar cell is usually independent of light intensity. However, at constant illumination, the variation in reverse leakage current (Fig. 5.7b) can be attributed to an increase in oxygen vacancy defects due to the incorporation of Sb dopant ions in the $BaSnO_3$ lattice [14,19].

Table 5.2. Photovoltaic and electrochemical impedance parameters of the DSSC devices using the BSO and ABSO photoanodes.

Device ID	V_{OC} (V)	J_{SC} ($mAcm^{-2}$)	FF (%)	PCE (%)	R_S (Ω)	R_{CT1} (Ω)	R_{CT2} (Ω)
D_{BSO}	0.73	6.50	67.42	3.23	23.95	11.34	3.25
D_{ABSO1}	0.74	9.97	55.14	4.06	21.74	9.70	2.98
D_{ABSO3}	0.73	7.79	65.36	3.76	19.01	8.08	3.45

The interfacial charge transport and recombination properties of the DSSCs are investigated from electrochemical impedance spectroscopy (EIS) (Solartron SI 1260). Fig. 5.7(c) shows the Nyquist plots and equivalent circuit diagram in the frequency range 0.01 Hz-1 MHz. The two semicircles correspond to charge-transfer resistance (R_{CT1}) at the Pt counter electrode/electrolyte interface with I^-/I_3^- redox reaction, and internal charge transfer resistance (R_{CT2}) at the ABSO/dye/electrolyte interfaces related to electron recombination [20]. Several factors like interfacial and electrode surface roughness, film inhomogeneities, thickness variation, and non-uniform distribution of current density cause the devices to behave as imperfect capacitors in the equivalent circuit [21].

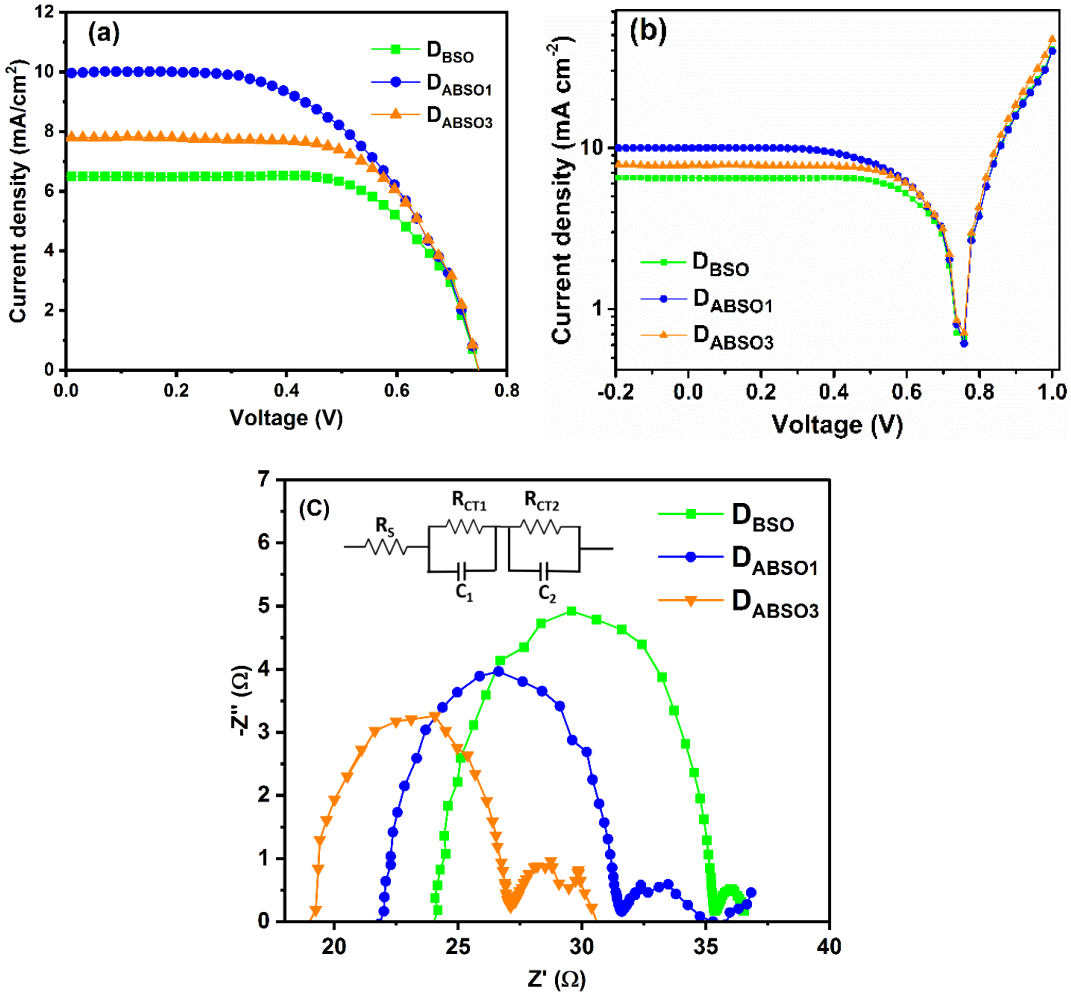

Fig. 5.7. (a) J-V characteristics, (b) Semi-log plots, and (c) Nyquist plots with equivalent circuit of the DSSCs fabricated using BSO and ABSO based photoanodes.

The high frequency intercept with the real axis represents the series resistance (R_s) comprising contact resistance, FTO glass substrate resistance, and bulk resistance of the counter electrode [9]. The values of R_S, R_{CT1} and R_{CT2} (Table 5.2) are obtained from the fit to the equivalent circuit. The value of R_{CT1} is lowest for D_{ABSO3}, whereas D_{ABSO1} exhibits the lowest R_{CT2} value of 2.98 Ω compared to other devices. The reduction in R_{CT2} for the D_{ABSO1} device indicates improved charge transport at the ABSO/dye/electrolyte interfaces compared to that of the D_{BSO} device. It also implies reduced charge recombination, leading to an improved value of J_{SC}, thereby corroborating with the photovoltaic performance.

5.4 Conclusions

A facile peroxide-precipitate route is adapted to successfully synthesize undoped and Sb-doped perovskite $BaSnO_3$ nanoparticles. Formation of single-phase compound with Sb dopant ions incorporated at the Sn sites of $BaSnO_3$ is confirmed from Rietveld refinement of the XRD data and also from TEM measurements. Band-gap tuning with Sb-doping is a promising approach to tailor the properties of $BaSnO_3$ as per application requirements. The DSSCs fabricated using the synthesized undoped and Sb-doped $BaSnO_3$ samples used as photoanodes show reasonably good photovoltaic performance. The device D_{ABSO1} exhibits the highest power conversion efficiency of 4.06 % with a short circuit current density of 9.97 mA/cm^2. The power conversion efficiency can be further improved by optimizing the Sb dopant concentration and also by varying other preparation parameters for comprehensive analysis. These results imply that incorporation of Sb dopant in $BaSnO_3$ yields interesting data that may also be favorable for further exploration of its applicability in several other optoelectronic devices.

References

[1] D. Devadiga, M. Selvakumar, P. Shetty, M.S. Santosh, Recent progress in dye sensitized solar cell materials and photo-supercapacitors: A review, J. Power Sources. 493 (2021) 229698.

[2] M. Grätzel, The advent of mesoscopic injection solar cells, Prog. Photovoltaics Res. Appl. 14 (2006) 429–442.

[3] A. Yella, H.-W. Lee, H.N. Tsao, C. Yi, A.K. Chandiran, M.K. Nazeeruddin, E.W.-G. Diau, C.-Y. Yeh, S.M. Zakeeruddin, M. Grätzel, Porphyrin-sensitized solar cells with cobalt (II/III)–based redox electrolyte exceed 12 percent efficiency, Science 334 (2011) 629–634.

[4] A. Kumar, S.C. Veerla, K.V. Anand, A.A. Kumar, Alkaline Earth Stannate Nanomaterials as an Electron Transport Layer in Dye-Sensitized Solar Cells, Journal: Handbook of Polymer and Ceramic Nanotechnology (2021): 99-120.

[5] N. Sakai, T. Miyasaka, T.N. Murakami, Efficiency enhancement of ZnO-based dye-sensitized solar cells by low-temperature $TiCl_4$ treatment and dye optimization, J. Phys. Chem. C. 117 (2013) 10949–10956.

[6] Q. Wali, A. Fakharuddin, I. Ahmed, M.H. Ab Rahim, J. Ismail, R. Jose, Multiporous nanofibers of SnO_2 by electrospinning for high efficiency dye-sensitized solar cells, J. Mater. Chem. A. 2 (2014) 17427–17434.

[7] S.S. Shin, D.W. Kim, D. Hwang, J.H. Suk, L.S. Oh, B.S. Han, D.H. Kim, J.S. Kim, D. Kim, J.Y. Kim, K.S. Hong, Controlled interfacial electron dynamics in highly efficient Zn_2SnO_4 -based dye-sensitized solar cells, ChemSusChem. 7 (2014) 501–509.

[8] I. Hod, M. Shalom, Z. Tachan, S. Rühle, A. Zaban, $SrTiO_3$ recombination-inhibiting barrier layer for type II dye-sensitized solar cells, J. Phys. Chem. C. 114 (2010) 10015–10018.

[9] G. Natu, Y. Wu, Photoelectrochemical study of the ilmenite polymorph of $CdSnO_3$ and its photoanodic application in dye-sensitized solar cells, J. Phys. Chem. C. 114 (2010) 6802–6807.

[10] Y. Li, H. Zhang, B. Guo, M. Wei, Enhanced efficiency dye-sensitized $SrSnO_3$ solar cells prepared using chemical bath deposition, Electrochim. Acta. 70 (2012) 313–317.

[11] D.W. Kim, S.S. Shin, S. Lee, I.S. Cho, D.H. Kim, C.W. Lee, H.S. Jung, K.S. Hong, $BaSnO_3$ Perovskite nanoparticles for high efficiency dye-sensitized solar cells, ChemSusChem. 6 (2013) 449–454.

[12] S.S. Shin, J.S. Kim, J.H. Suk, K.D. Lee, D.W. Kim, J.H. Park, I.S. Cho, K.S. Hong, J.Y. Kim, Improved quantum efficiency of highly efficient perovskite BaSnO3-based dye-sensitized solar cells, ACS Nano. 7 (2013) 1027–1035.

[13] A. Roy, P.P. Das, P. Selvaraj, S. Sundaram, P.S. Devi, Perforated $BaSnO_3$ Nanorods Exhibiting Enhanced Efficiency in Dye Sensitized Solar Cells, ACS Sustain. Chem. Eng. 6 (2018) 3299–3310.

[14] H. Mizoguchi, P. Chen, P. Boolchand, V. Ksenofontov, C. Felser, P.W. Barnes, P.M. Woodward, Electrical and Optical Properties of Sb-Doped $BaSnO_3$, Chem. Mater. 25 (2013) 3858–3866.

[15] H.J. Kim, U. Kim, H.M. Kim, T.H. Kim, H.S. Mun, B.-G. Jeon, K.T. Hong, W.-J. Lee, C. Ju, K.H. Kim, High mobility in a stable transparent perovskite oxide, Appl. Phys. Express. 5 (2012) 61102.

[16] Y. Li, Q. Xin, L. Du, Y. Qu, H. Li, X. Kong, Q. Wang, A. Song, Extremely sensitive dependence of SnOx film properties on sputtering power, Sci. Rep. 6 (2016) 1–9.

[17] A.R. Babar, S.S. Shinde, A. V Moholkar, C.H. Bhosale, J.H. Kim, K.Y. Rajpure, Sensing properties of sprayed antimony doped tin oxide thin films: Solution molarity, J. Alloys Compd. 509 (2011) 3108–3115.

[18] M. Zheng, J. Ni, F. Liang, M.-C. Wang, X. Zhao, Effect of annealing temperature on the crystalline structure, growth behaviour and properties of SnO2: Sb thin films prepared by radio frequency (RF)-magnetron sputtering, J. Alloys Compd. 663 (2016) 371–378.

[19] H. He, Z. Yang, Y. Xu, A.T. Smith, G. Yang, L. Sun, Perovskite oxides as transparent semiconductors: a review, Nano Converg. 7 (2020) 1–10.

[20] N. Purushothamreddy, M. Kovendhan, R.K. Dileep, G. Veerappan, K.S. Kumar, D.P. Joseph, Synthesis and characterization of nanostructured La-doped BaSnO3 for dye-sensitized solar cell application, Mater. Chem. Phys. 250 (2020) 123137.

[21] J.M. Fernandes, C. Swetha, E. Appalnaidu, K. Navamani, V.J. Rao, M.N. Satyanarayan, G. Umesh, Optoelectronic properties of novel alkyl-substituted Triphenylamine derivatives, Org. Electron. 47 (2017) 24–34.

CHAPTER: 6

Alternative transparent conducting 'Sb' doped SnO_2 thin film electrode for dye-sensitized solar cell

This chapter presents the results of antimony (Sb) doped tin oxide (SnO_2) (ATO) thin film as an alternative transparent conducting electrode (TCE) deposited by cost-effective spray pyrolysis technique. The ATO thin film is a well-known n-type TCO material explored by several research reports but not yet commercialized due to its moderate optical and electrical properties. The 5×5 cm^2 area deposited ATO thin film is explored for its structural, optical, and electrical properties. More importantly, the thermal stability of electrical properties of ATO films is studied to elucidate its applicability as TCE in DSSC. Finally, the deposited ATO film is used as an alternative photoanode in DSSC and its performance is demonstrated.

6.1. Introduction

Transparent conducting oxides (TCOs) constitute a class of most significant components in solar cells [1], display devices [2], smart windows [3], sensors [4,5], electrochromic [3], etc. The optical transparency and electrical conductivity properties of these TCOs are crucial for their use as transparent conducting electrodes in various optoelectronic devices, depending on the range of sheet resistance values. However, it is challenging to stabilize both the optical transparency and electrical conductivity in the same host material, and there exists a trade-off between these two properties. For example, glass is transparent but insulating in nature, whereas metals are conductive but opaque. Nevertheless, by changing the dimension of a material from bulk to nanoscale, and also by incorporating suitable dopants, one can successfully obtain efficient transparent conducting properties in the same host material. In 1907, Karl Baedeker [6] identified the first TCO material by annealing sputtered Cd film in air, where incomplete oxidation of Cd turned it into non-stoichiometric CdO, leading to increase in transparency and

electrical conductivity due to creation of oxygen vacancies. Although the performance was not optimal, subsequent investigations have yielded metal-like behaviour in CdO [6]. However, the extreme toxicity of Cd has been a major obstacle towards its commercialization for widespread use. Later, Corning laboratories identified tin-doped indium oxide (90%)In_2O_3:Sn(10%) (ITO) as a potential TCO material in 1930 [7]. In 1947, Harold McMaster [8] patented a chemically deposited SnO_2 thin film as TCO material with optical transmittance and sheet resistance around 92 % and 200 Ω/□, respectively [9]. The ITO, a binary TCO material, was commercialized by Rupprecht in 1954 [8]. Till date, this material is widely used as transparent conducting electrode in a variety of optoelectronic devices. Recently, due to intense scarcity of indium metal and a surge in market demand for ITO, researchers began to focus on alternative TCO materials which can supplement ITO. Presently, intense research work is being carried out in search of alternative TCO materials with excellent optical and electrical properties on par with that of ITO.

Optical transparency and electrical conductivity of SnO_2 can be increased by doping it with suitable dopants such as In [8], Li [10], F [11], Al [12], Mo [13], Mn [14], Co [15], Ta [16], W [17], Nb [18], and Sb [19]. Among all these dopants, Sb-doped SnO_2 (ATO) is identified as one of the most promising alternative TCO materials. However, its electrical conductivity and optical transparency are still lower compared to that of ITO. Since the deposition method significantly influences the thin film properties, researchers have explored various techniques such as sputtering [20–25], PLD [26], CVD [27,28], hydrolysis [29], wet chemical deposition [30], sol-gel method [31], hydrothermal method [32–34], and spray pyrolysis [35–42] for the deposition of Sb-doped SnO_2 films. Even though there are several reports on ATO thin films, the size of the film deposited using spray pyrolysis is generally limited to a small area. Moreover, there is hardly any report on dye-sensitized solar cells (DSSCs) fabricated using spray-pyrolyzed ATO films as electrodes. In the present study, 5 wt. % Sb-doped SnO_2 thin

film of 5x5 cm^2 area is deposited using optimized spray pyrolysis conditions [43]. The deposited ATO film exhibits reasonably good electrical and optical properties compared to undoped SnO_2 (TO) film, and is demonstrated as an efficient transparent conducting electrode (photoanode)/counter electrode component in DSSCs with reasonably good power conversion efficiency.

6.2. Materials and methods

6.2.1 Materials used

Analytical grade reagents and chemicals such as $SnCl_2.2H_2O$, $SbCl_5$, HCl, and ethylene glycol were used as received. Glass substrates were purchased from Zhuhai Kaivo Optoelectronic Technology Co. Ltd. and cleaned ultrasonically using IPA, ethanol, acetone, and deionized water in a sequence. For DSSC fabrication, standard TiO_2 paste was used as active material. Acetonitrile, Iodine, 4-tert-butyl pyridine, and 1-butyl-3 methylimidazolium iodide purchased from Sigma Aldrich were used without any further purification as redox couple for photoelectrochemical studies. Chloroplatinic acid (5 mM) was used to prepare the counter electrode. Surlyn spacer (SX1170-60, 60 µm thick from Solaronix) was used for sealing the DSSC device. The ATO thin film deposited using spray pyrolysis was used as a photoanode/counter electrode in the fabricated DSSC device. A reference device was also fabricated with standard fluorine-doped tin oxide (FTO, sheet resistance 10 Ω/□) coated glass substrate as photoanode/counter electrode.

6.2.2 Thin film deposition

A 200 ml solution of 0.5 M concentration was prepared by weighing the necessary quantities of precursors. $SnCl_2.2H_2O$ and $SbCl_2.2H_2O$ were weighed and transferred into two separate beakers filled with 16 mL of double-distilled water and were stirred for 30 min each. Few drops of HCl were introduced into the above mixture for better solubility as well as to obtain a transparent solution in each beaker. These two transparent solutions were then mixed

together and 150 mL of ethylene glycol was added and stirred for 3 h to result in a final solution. Undoped SnO_2 solution was also prepared similarly without the addition of dopant precursor. After 3 h of stirring, the final solution was loaded into the spray instrument. Glass substrates of area 5×5 cm^2 were cleaned ultrasonically using standard cleaning process for removal of fine dust, grease or oil traces clinging to the surface. These cleaned glass substrates were then blow-dried with nitrogen gas. High energy plasma cleaner (Harrick Plasma, Model PDC-002) was used to neutralize the ionic charge contaminants on the substrate's surface. Finally, the cleaned glass substrates were loaded into the spray chamber. The substrate temperature was ramped up to 420 °C in 90 min. The distance between the substrate holder and spray gun was kept at 35 cm. The pressure of compressed air was maintained at 30 kg/cm^2, and the spray duration was 0.5 sec with an interval of 30 sec. A double walled glass spray gun with a tapered inner nozzle of diameter 0.3 mm was used to spray the solution, and a total of 650 sprays were performed for both the films using 200 mL of the pure and doped precursor solutions. The pure SnO_2 and Sb-doped SnO_2 thin films are named as TO and ATO, respectively, in this chapter.

6.2.3 Dye-sensitized solar cell fabrication

The DSSC devices were fabricated in standard architecture using the TO and ATO thin films as electrodes. A reference device with a commercially available FTO electrode was also fabricated to compare the performance of the devices. The standard device architectures are, TO/TiO_2/N719 dye/electrolyte/Pt/TO, ATO/TiO_2/N719 dye/electrolyte/Pt/ATO and FTO/TiO_2/N719 dye/electrolyte/Pt/FTO. The transparent conductive substrates were cleaned once again using the previously described procedure, and additionally, they were blow-dried and then pre-treated with UV-O_3.

Commercially available TiO_2 paste was coated onto the TO and ATO conductive substrates as well as on FTO using doctor-blade technique [44], and then sintered at 450 °C for 30 min. After the preparation of the TiO_2 electrode, the TO, ATO, and FTO substrates were treated with 0.04

M of $TiCl_4$ for 30 min at 80 °C. Then, the treated glasses were rinsed with deionized water and calcined at 450 °C for 30 min. After cooling to room temperature, the TiO_2 films were immersed into 0.5 mM N719 dye solution and sensitized for 6 h. To load the electrolyte solution, two fine holes were drilled from the rear side of the counter electrode. The drilled electrodes were coated with 5 mM of chloroplatinic acid using the drop-casting method [45]. The coated films were calcinated at 450 °C for 30 min in air. The photoanode and Pt-coated counter electrode were sandwiched using a Surlyn (55 μm, Greatcellsolar, Australia) polymer spacer as a hot melt sealing foil. The iodide-based liquid electrolyte was injected from the counter electrode side through the drilled holes using a micropipette. After filling the electrolyte, the holes on the counter electrode side were sealed using a Surlyn spacer and a piece of thin coverslip glass.

6.2.4 Characterization

The structural properties were analyzed using Rigaku SmartLab automated multipurpose X-ray diffractometer with Cu Kα radiation of λ = 1.5406 Å. The oxidation states of the deposited thin films were confirmed using X-ray photoelectron spectroscopy (XPS) (Model: ESCA 3400, Make: Kratos/Shimadzu Amicus). Optical properties were studied using a UV-visible spectrometer (Analytik Jena, SPECORD 210 PLUS). Surface morphology and topology of the thin films were characterized from field emission scanning electron microscopy (FESEM) with energy dispersive X-ray spectroscopy (EDX) (Hitachi, S-4300SE), and atomic force microscopy (AFM) measurements using Park Scientific Instrument (Model: Park NX10). Thickness measurements were performed using a stylus profilometer (Model: DektakXT, Bruker). Photoluminescence emission spectra were analyzed using a Horiba Jobin Yvon Flourolog-3-21 spectrofluorometer (450 W xenon arc lamp) with an excitation wavelength of 325 nm at room temperature. Contact angle measurements were performed using DSA25 Drop Shape Analyzer with a temperature-controlled chamber (KRUSS, Germany). Electrical properties were measured using linear four-probe and Hall effect (Ecopia, HMS 3000)

techniques. The *J-V* characteristics of the fabricated DSSCs were measured under one sun illumination at AM 1.5G standards (Class AAA simulator, Oriel Instruments). The photoelectrochemical impedance measurements were performed in the frequency range 100 mHz - 100 kHz using a Solartron SI- 1260 impedance analyzer.

6.3. Results and discussion

6.3.1 Structural and elemental analysis

Fig. 6.1 shows the X-ray diffraction (XRD) patterns of undoped SnO_2 (TO) and Sb-doped SnO_2 (ATO) thin films deposited onto glass substrates at 420 °C. The XRD patterns of TO and ATO films show high crystallinity with peaks corresponding to tetragonal crystal structure. The peaks of TO and ATO thin films are well-matched with JCPDS file: 41-1445. There are no other peaks related to Sb_2O_3, Sb_2O_5, SnO, or SnO_3, which is evidence for the successful incorporation of Sb dopant as a substitutional impurity into the SnO_2 host lattice. The lattice constants of the TO and ATO film are estimated using eq. 6.1. The estimated values are found to be $a = b = 4.738$ Å and $c = 3.185$ Å for TO; and $a = b = 4.741$ Å and $c = 3.185$ Å for ATO. These values are nearly matching to those given in standard JCPDS file No.: 41-1445 ($a = b = 4.738$ Å and $c = 3.187$ Å) of SnO_2. The minor variation in the lattice parameters of ATO film is related to the difference in ionic radii of Sn^{4+} (69 pm) and Sb^{5+} (60 pm). The average crystallite size values of the TO and ATO films are calculated using eq. 2.2 and are found to be 58.25 and 37.48 nm, respectively. The main peaks in SnO_2 JCPDS file No: 41-1445 with higher intensities are (110), (101), and (211). In the spray-deposited TO and ATO films, the (110) peak is observed to be dominant, whereas the (101) and (211) peaks are suppressed. Notably, the (200) peak is observed to possess significant intensity. It is observed from Fig. 6.1 that the growth of TO and ATO films is preferred along the (110) and (200) planes. The texture coefficient TC_{hkl} represents the texture of a particular plane, and its deviation from unity implies preferred growth.

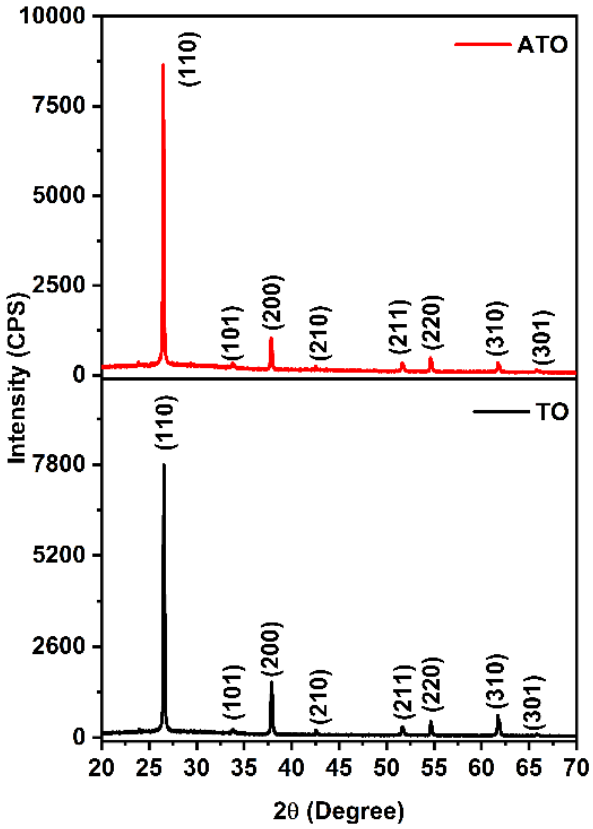

Fig. 6.1 XRD patterns of the spray-deposited TO and ATO thin films.

TC_{hkl} is calculated using eq. 6.2, where I_{hkl} is the measured intensity of X-ray reflection, I_{0hkl} is the standard intensity of the same reflection and N is the total number of reflections observed in the XRD patterns of the films. The estimated TC_{hkl} values corresponding to (110) and (200) planes are found to be 2.69 and 1.54 for the ATO film; and 2.09 and 2.02 for the TO film, respectively. The textured growth results from reorientation effects induced by Sb ions being incorporated into the Sn lattice sites, and also due to subtle variation in spray dynamics.

$$\frac{1}{d^2} = \frac{h^2+k^2}{a^2} + \frac{l^2}{c^2} \tag{6.1}$$

where a,b, and c are lattice parameters, (hkl) are Miller indices and d is the interplanar spacing

$$TC_{hkl} = \frac{I_{hkl}/I_{0hkl}}{1/N \sum_{N=1}^{N} I_{hkl}/I_{0hkl}} \tag{6.2}$$

where TC_{hkl} is texture co-efficient, I_{hkl} is diffraction intensity obtained from the XRD, and I_{ohkl} is the intensity of the diffraction plane from the standard JCPDS file.

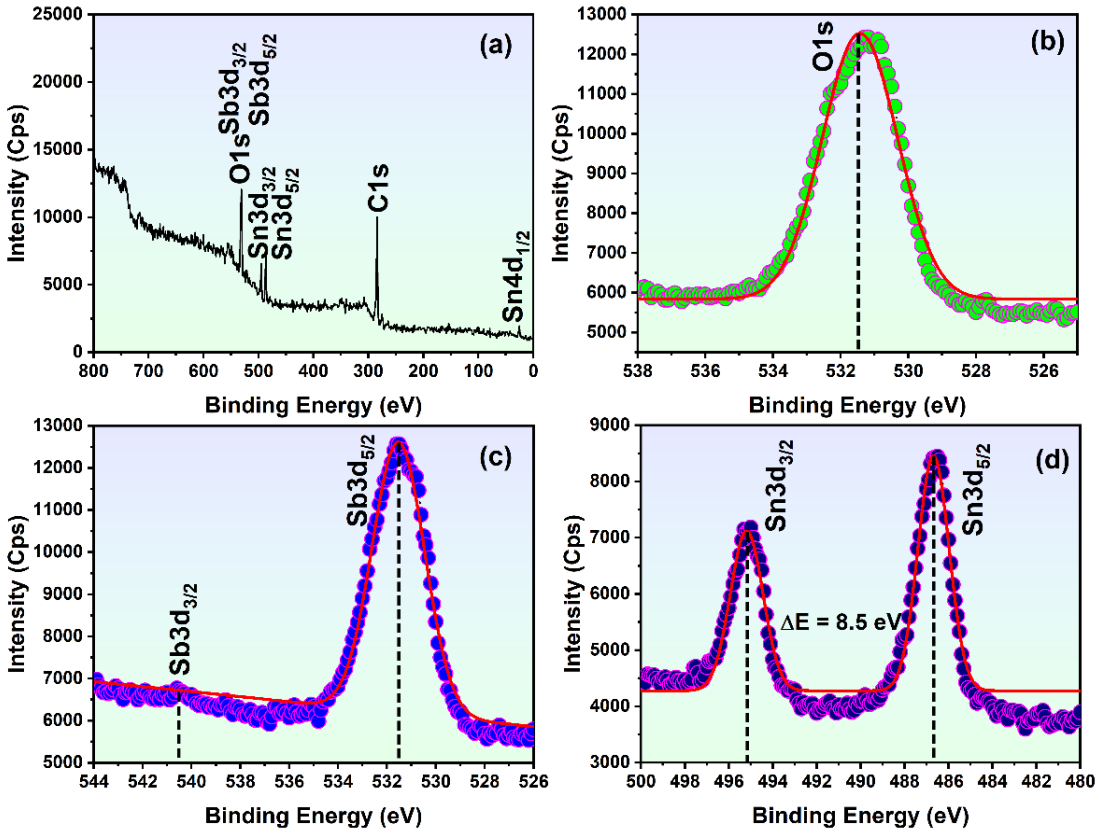

Fig. 6.2 XPS analysis of ATO film: (a) survey scan spectrum, and close scan of peaks related to (b) Sb, (c) Sn and (d) O atoms.

Fig. 6.2 (a) shows the X-ray photoelectron spectroscopy (XPS) survey spectrum of the ATO thin film. The full scan indicates the presence of constituent elements Sn, Sb, and O, in addition to a carbon contamination peak at 285 eV due to exposure to ambient air [46]. In Fig. 6.2 (b), the main characteristic binding energy of oxygen O1s is 530.73 eV which is shifted slightly towards higher energy of 531.5 eV. From Fig. 6.2 (c), it is observed that the binding energy peaks located around 540.5 eV and 531.5 eV belong to Sb $3d_{3/2}$ and Sb $3d_{5/2}$ oxidation states, respectively, confirming the existence of Sb in the +5 charge state. This is also implied from the significant improvement in free carrier concentration with Sb dopant content (explained

later). The peaks at 495.2 eV and 486.7 eV in Fig. 6.2 (d) correspond to Sn $3d_{3/2}$ and Sn $3d_{5/2}$ oxidation states of Sn atoms, respectively, indicating the Sn atoms to be in a +4 charge state. The difference in the binding energy between these two oxidation states is 8.5 eV which is consistent with the values reported in the literature [16,46–48]. The +4 valence state of 'Sn' covalently bonds with the pentavalent Sb donor atom, yielding a free electron to the lattice. The XPS results of the present study match with the data available in the literature [46,47].

6.3.2 Optical properties

Fig. 6.3 (a) and (b) show the absorbance and transmittance spectra of the TO and ATO thin films, respectively. The bandgap estimation of the films from the Tauc plots is shown in Fig. 6.3 (c). Higher absorption of light and lower transmittance (80% at 550 nm) is observed upon Sb doping into the SnO_2 lattice. The reason for the decreased transmittance with Sb doping is mainly due to the grey tinge of Sb existing in the +5 charge state, apart from increased surface roughness, variation in film thickness, and also due to subtle deviation in the growth pattern of the film. The thickness of the ATO film (500 nm) is higher than that of the TO film (300 nm) (Table 6.1). In the case of undoped TO film, there are no dopants involved; but in the case of ATO film, the dopant Sb acting as substitutional point defect leads to the formation of a grey tinge (due to +5 charge state of Sb), resulting in reduced transparency. Doping with Sb also causes a decrease in the optical band gap (E_g) from 3.86 eV to 3.77 eV (Fig. 6.3 c). The decrease in the bandgap is related to an increase in charge carriers, thereby lowering the Fermi level in the doped ATO film. Similar results have been reported in spray-deposited SnO_x, SnO_x:F, and SnO_x:Sb films [41,49].

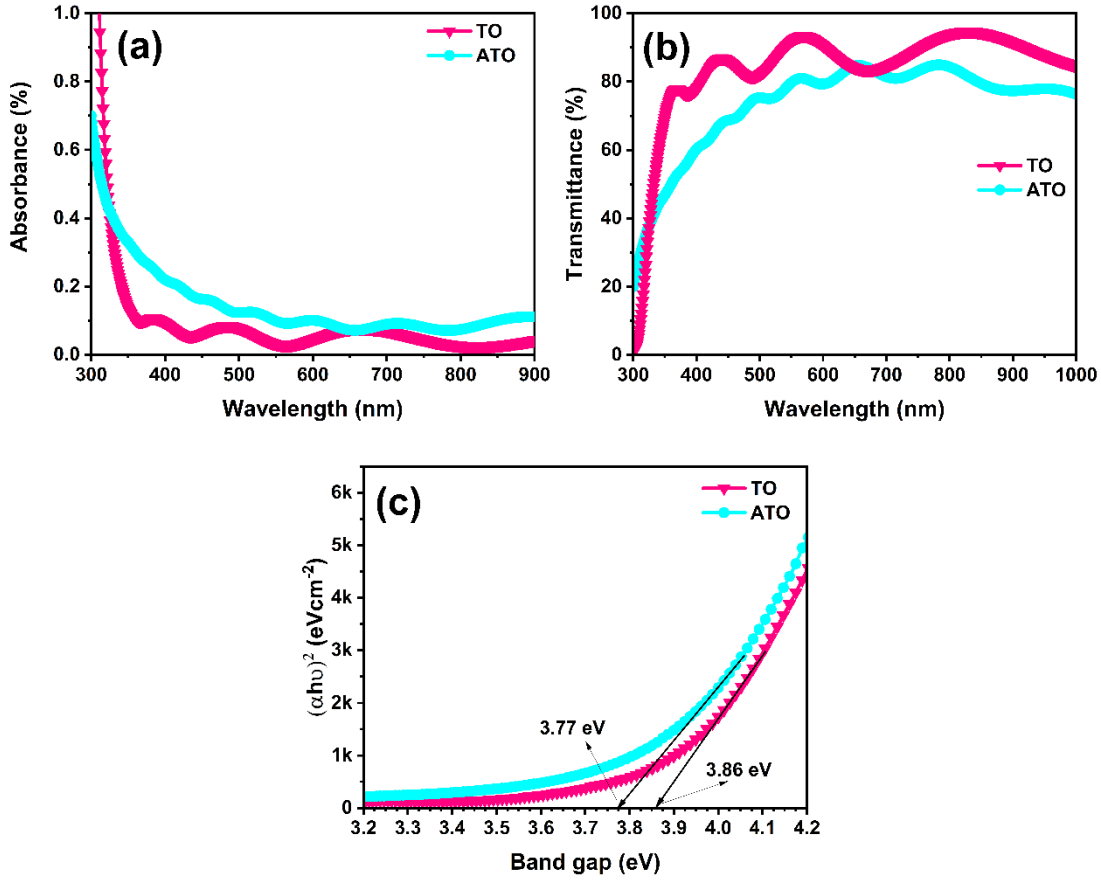

Fig. 6.3. (a) Absorption spectra, (b) Transmittance spectra, and (c) Band gap estimation from the Tauc plots of the spray-deposited TO and ATO thin films.

6.3.3 Surface morphology and compositional analysis

Fig. 6.4 (a) and 6.4 (b) show the field emission scanning electron microscopy (FE-SEM) images of TO and ATO thin films, respectively. The inset of Fig. 6.4 (b) clearly shows tetragonal morphology with nearly uniform-sized particles. Fig. 6.4 (c) shows the energy dispersive X-ray (EDX) analysis and chemical composition of ATO thin film, indicating the presence of constituent elements in the desired percentage with only a nominal variation. This confirms the successful substitution of Sb in the SnO_2 host lattice.

Fig. 6.5 (a) and 6.5 (b) depict the two-dimensional (2D) and three-dimensional (3D) AFM images of the TO thin film, respectively. Fig. 6.5 (c) and (d) are the 2D and 3D images of the ATO thin film, respectively. The surface morphologies of both films appear to be dense,

indicating the films to be of good quality. The RMS surface roughness values of the TO and ATO films are found to be 18 nm and 45 nm, respectively (Table 6.1).

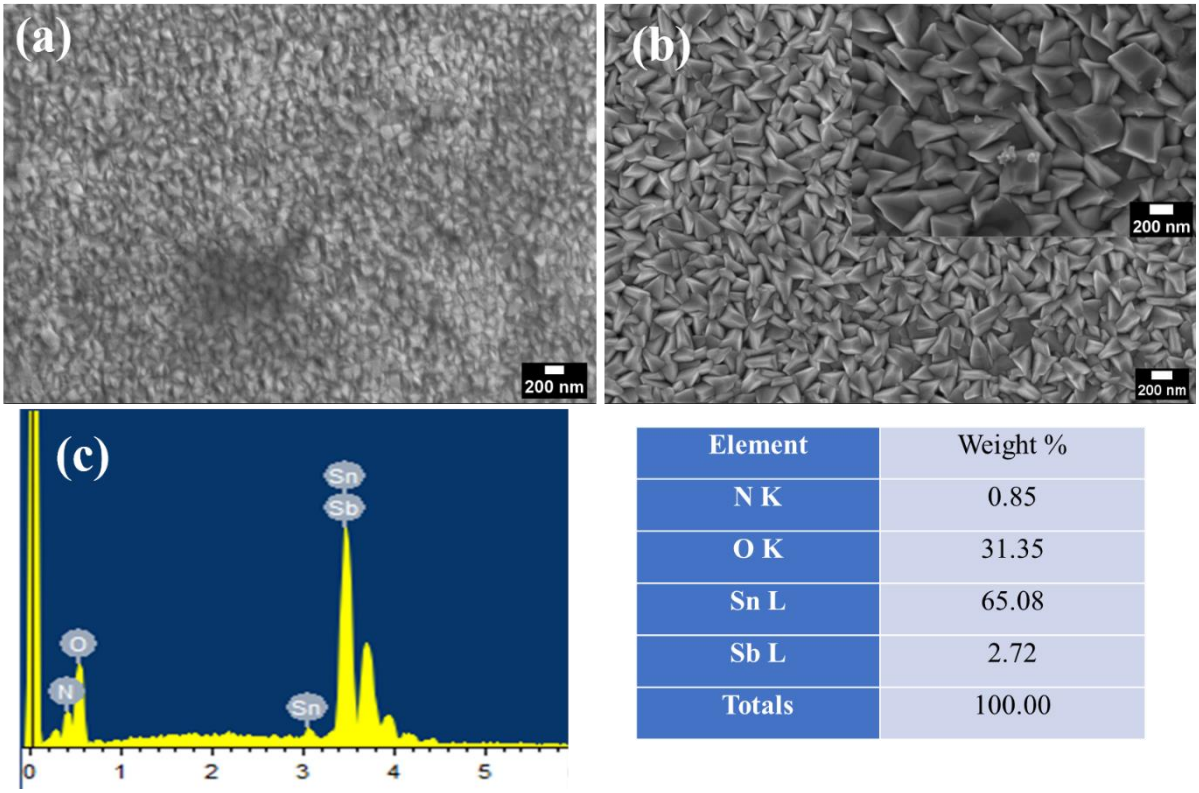

Element	Weight %
N K	0.85
O K	31.35
Sn L	65.08
Sb L	2.72
Totals	100.00

Fig. 6.4 FE-SEM images of (a) TO and (b) ATO films (inset is the high magnification image), and (c) EDX spectrum of ATO film showing the presence of constituent elements.

The increase in surface roughness reveals that the growth of grains is suppressed by the addition of the Sb element, and more grain boundaries might exist upon doping with 'Sb' donor atoms in the SnO_2 lattice [50]. Grain boundaries are known to play a critical role in carrier mobility which would significantly influence the electrical resistance of thin films [51]. The increase in RMS surface roughness with an increase in doping concentration is reported in the literature [52–54]. A rough surface enhances the reflection of incident photons back into the electrode, ensuring a decrease in the loss of photons, thereby improving the light gathering ability [15,55].

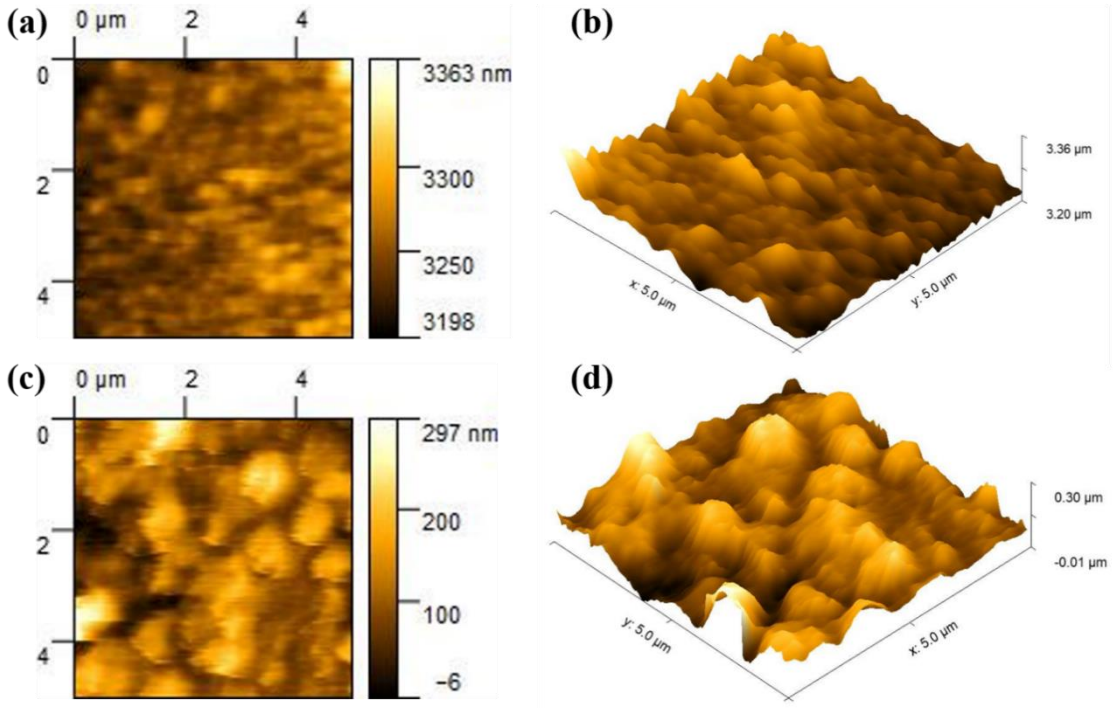

Fig. 6.5. The 2D and 3D AFM images of spray-deposited (a-b) TO and (c-d) ATO thin films.

Table 6.1. Structural and optical parameters of spray-deposited TO and ATO thin films

Sample code	Crystallite size *D* (nm)	Thickness (nm)	Transmittance (*T*) (%)	Bandgap E_g (eV)	Roughness (nm)	Average Rs (Ω/□)
TO	58.25	300	91	3.86	18	255.48
ATO	37.48	500	80	3.77	45	12.18

6.3.4 Photoluminescence studies

Fig. 6.6 shows the photoluminescence (PL) emission spectra of the spray-deposited TO and ATO thin films. The excitation wavelength for both the thin films is 330 nm. From Fig. 6.6, it is observed that the peak corresponding to ultraviolet emission is located around 393 nm, and upon deconvolution of this broad peak, two additional sub-bands are located at 368 nm and 454 nm within the envelope are evident. The peak at 393 nm represents the near-band-edge (NBE) emission of electrons from the bottom of the conduction band to the top of

the valence band [56]. The two other minor emission peaks located at 546 nm and 634 nm also arise due to oxygen vacancy defects present in the films [57–59]. The most common defects in metal oxides are oxygen vacancies (V_O) which act as luminescent centers. V_O^0, V_O^+, and V_O^{2+} are the well-known oxygen vacancy states [60], where Vo^0 is a shallow donor which exists near the conduction band. Most of the common oxygen vacancies are likely to exist in the V_O^+ charge state, and on recombining with a hole, they change to V_O^{2+} state, corresponding to blue and green emission [61].

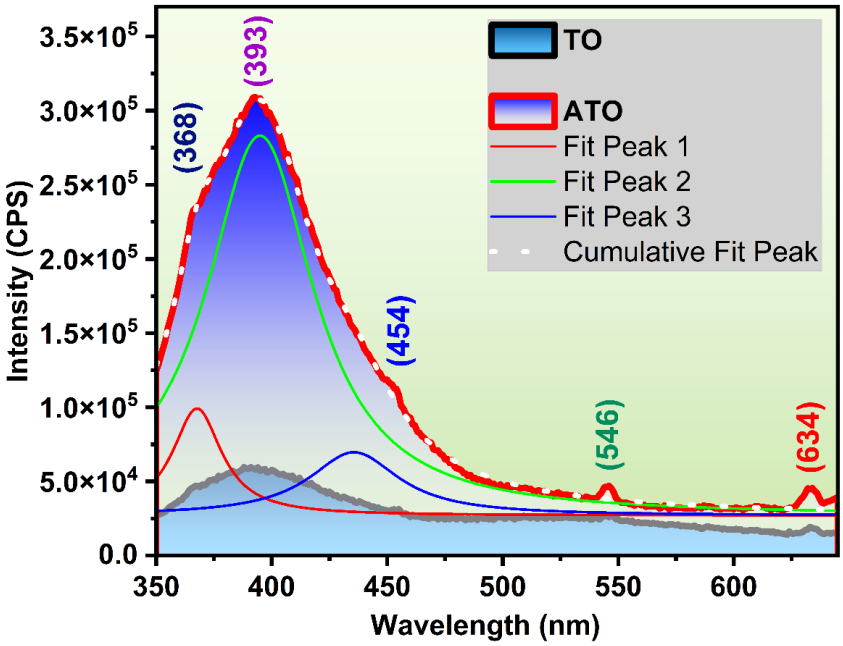

Fig. 6.6. Photoluminescence emission spectra of the spray-deposited TO and ATO thin films.

The substitution of Sb into the interstitial sites of SnO_2 lattice forms defect energy levels near the conduction band, and these defects play a vital role in creating luminescent centers. The oxygen vacancy point defect density can be calculated from Smakula's formula [62],

$$N = 1.29x10^{17} \frac{n}{f(n^2+2)^2} \alpha W_{1/2} \quad (6.3)$$

where n = 2 is the refractive index of SnO_2, F = 1 is the oscillator strength of optical transmission, and $\alpha W_{1/2}$ is the Gaussian area of the PL emission peak. The calculated oxygen vacancy point-defect density of 1.57 x 10^{23} cm^{-3} for the ATO film is one order higher than that

of the undoped TO film, which is 2.7 x 10^{22} cm^{-3}. This increase in oxygen vacancies is induced by Sb-doping.

6.3.5 Contact angle measurement

To investigate the surface wettability of the TO and ATO thin films, the contact angle of a water droplet on their surfaces was measured as shown in Fig. 6.7 (a) and (b), respectively. It is observed that the contact angle of the ATO film (89.6°) decreases in comparison with the undoped TO film (94.0°), indicating improvement in hydrophilicity of the film with Sb-doping. This behavior substantiates the Wenzel equation given as follows[63]

$$cos\theta_W = r_W cos\theta_Y \quad (6.4)$$

where θ_W and θ_Y are Wenzel's contact angle (measured) and Young's contact angle (for ideal surface), respectively. r_W is Wenzel's roughness factor defined as the ratio of the actual area of a rough surface to the geometric projected area.

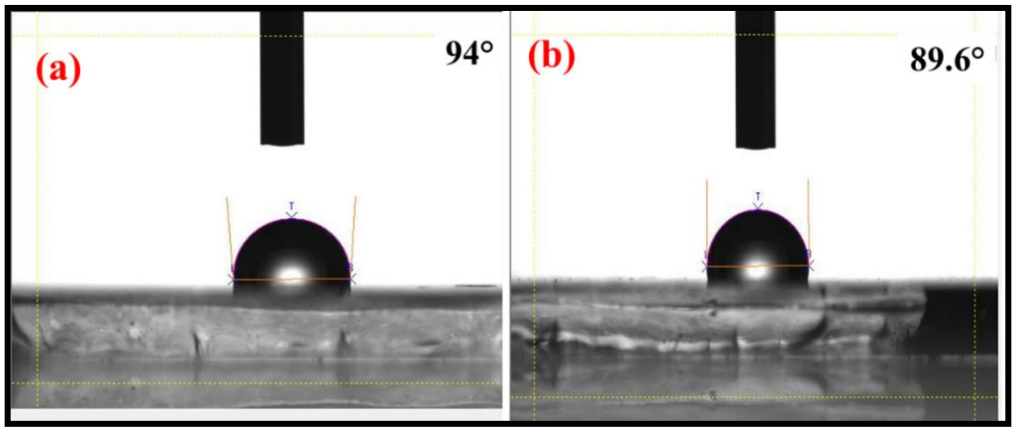

Fig. 6.7. Contact angle measurement of water droplet on the surface of spray-deposited (a) TO and (b) ATO thin films.

As observed in the AFM images in section 6.3.3, the surface roughness of the ATO thin film is higher than that of the undoped TO film. As per the Wenzel equation, the higher surface roughness of the hydrophilic ATO film decreases its contact angle [64].

6.3.6 Electrical transport properties and thermal stability of sheet resistance

The electrical transport properties of the deposited TO and ATO thin films were measured using the Hall effect at room temperature. Both the films are found to possess n-type electrical conductivity. The carrier concentration (n_c), resistivity (ρ) and mobility (μ_e) values are given in Table 6.2. The ATO film shows low resistivity (6.09 x 10^{-4} Ω cm) compared to that of TO film (4.66 x 10^{-3} Ω cm). The dopant Sb has a +5 charge state where four electrons form bonds with oxygen molecules and the remaining electron is donated as a free carrier to the lattice, thereby contributing to the increase in free charge carrier concentration. In the case of undoped SnO_2, there are limited free charge carriers (due to relatively lesser defects) since Sn has a +4 charge state and it will form bonds with two oxygen atoms, leading to very high resistivity compared to that of Sb-doped SnO_2 thin film. The increase in electrical conductivity of the ATO film is mainly due to the increase in free carriers through Sb-doping and the presence of oxygen vacancies, which is evident from the increase in its carrier concentration (6.20 x 10^{20} cm^{-3}) and defect density (1.57 x 10^{23} cm^{-3}). However, the reduction in mobility may be due to inter-carrier collisions, owing to the presence of excess charge carriers and also due to scattering by defects.

Fig. 6.8 (a-b) shows the 3D contour mapping of sheet resistance (R_{Sheet}) of the deposited TO and ATO thin films over a 5x5 cm^2 area. The observed variation in sheet resistance is because of the variation in spray dynamics which depends on several parameters like spray flow rate, the pressure of the gas, concentration of the solution, distance from the spray nozzle to the substrate, and substrate temperature. The pressure of the spray solution varies from the center of the film to its edges due to the use of a single nozzle spray gun. As a result, the central portion of the film presents low sheet resistance (violet color) when compared to that at the edges (red color). From Fig. 6.8 a and b, one can observe that the average R_{Sheet} value (light blue color) of the undoped TO film is very high (255.48 Ω/□), whereas the ATO film shows a significantly

lower average R_S value of 12.18 Ω/□. The reduced sheet resistance is attributed to the increase in charge carrier concentration upon doping with Sb^{5+} into the SnO_2 lattice.

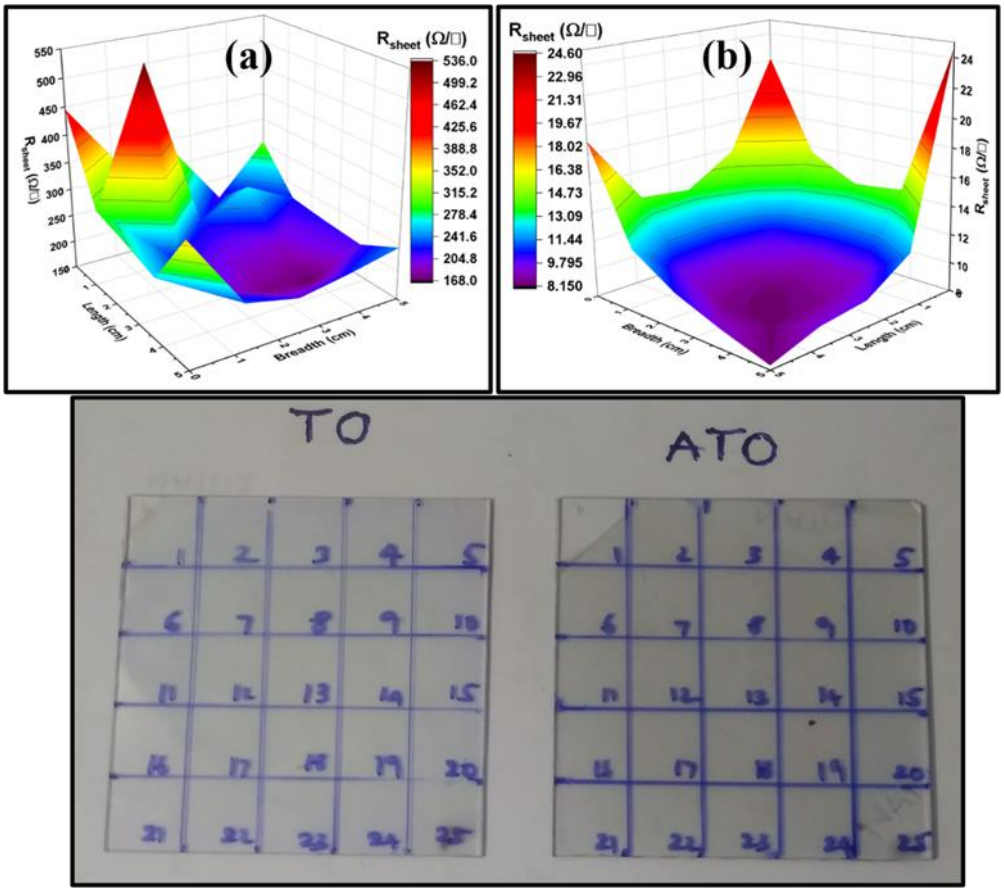

Fig. 6.8. The 3D contour plot of sheet resistance mapping and the photographs of the spray-deposited (a) TO and (b) ATO thin films.

Thermal stability of sheet resistance is a crucial parameter for analyzing the suitability of the TO and ATO thin films in various device applications. Ideally, sheet resistance must be consistent even at high processing temperatures. The thermal stability of sheet resistance of the TO and ATO films is investigated by varying the annealing temperature (150 °C to 500 °C in steps of 50 °C) and the resulting change in R_{Sheet} is measured using a linear four-probe setup.

Fig. 6.9 (a-b) shows the variation in R_{Sheet} values of the TO and ATO films as a function of annealing temperature from 150 °C to 500 °C with a step of 50 °C for 30 min annealing duration. For the TO film, R_{Sheet} is nearly stable (277- 331 Ω/□) up to 350 °C without significant

increase. At 400 °C, R_{Sheet} increases to three times its initial value (i.e., to 877 Ω/□). Above 400 °C, there is a rapid increase in R_{sheet} for 450 °C and 500 °C and reaches a value by an eight-fold increase (2369 Ω/□) compared to its initial value. In the case of ATO film, R_{Sheet} is stable up to 350 °C without much variation (≅ 12 to 14 Ω/□). For 400 °C, the value of R_{Sheet} doubles, and for 500 °C, there is a significant five-fold increase compared to the initial R_{sheet} value.

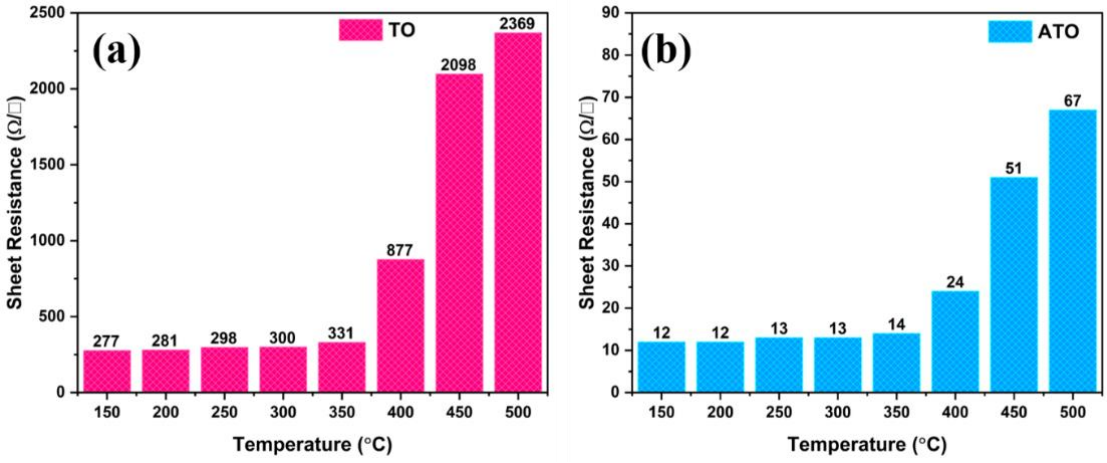

Fig. 6.9. Variation in sheet resistance of (a) TO and (b) ATO thin films as a function of annealing temperature for 30 min duration (Actual sheet resistance value in Ω/□ is indicated against each temperature).

The overall comparison indicates that the ATO film has good resistance stability with temperature than the TO film without drastic changes up to 400 °C. Whereas, in the case of TO film, the R_{Sheet} value increases drastically from 350 °C to 500 °C (eightfold increase), which decreases upon doping with Sb; and the thermal stability of R_{Sheet} is enhanced up to 400 °C, with only a fivefold increase in its initial value. Compared to TO film, the ATO film has a relatively lower increase in R_{Sheet} value which may be due to the following factors: (a) thermally activated free carriers may lead to the attainment of optimal carrier concentration that helps to maintain the stability of sheet resistance up to 400 °C and (b) free charge carriers get scattered by oxygen vacancy defects and grain boundaries [65,66]. This study indicates improvement in the thermal stability and electrical conductivity of the ATO film due to Sb-doping.

The figure of merit (FoM) values relating to the optical transmittance and sheet resistance are estimated from the Haacke formula [67] for the TO and ATO films and the values are given in Table 6.2. The ATO film shows a slight improvement in the FoM value (8.23 x 10^{-3} Ω^{-1}) when compared to that of the TO film (1.52 x 10^{-3} Ω^{-1}), which is mainly due to a significant decrease in sheet resistance.

Table 6.2. Electrical transport parameters of the spray-deposited TO and ATO thin films

Sample code	Carrier concentration n_c (cm^{-3})	Resistivity ρ (Ω cm)	Mobility μ_e ($cmV^{-1}s^{-1}$)	Fig. of merit FoM (Ω^{-1})
TO	5.68 x 10^{19}	4.66 x 10^{-3}	23.54	1.52 x 10^{-3}
ATO	6.20 x 10^{20}	6.09 x 10^{-4}	16.49	8.23 x 10^{-3}

6.3.7 Dye-sensitized solar cells and electrochemical impedance spectroscopy

Dye-sensitized solar cells (DSSCs) were fabricated employing the spray-pyrolyzed TO, ATO electrodes as well as commercially available FTO electrode, and the respective device architectures are (i) ATO (or TO)/TiO_2/N719 dye/electrolyte/Pt/ATO (or TO) and (ii) FTO/TiO_2/N719 dye/electrolyte/Pt/FTO. The DSSC device fabricated using an undoped TO electrode (denoted as D_{TO}) exhibits poor performance (inset of Fig. 6.10 a). Hence, only the *J–V* curves (under AM 1.5 G solar illumination) for the DSSCs fabricated using the ATO and FTO electrodes (D_{ATO} and D_{FTO}, respectively) are compared as shown in Fig. 6.10 (a). Their corresponding photovoltaic parameters such as V_{OC}, J_{SC}, *FF*, and η are given in Table 6.3.

For device D_{ATO}, the V_{OC} is 0.69 V and J_{SC} is 9.16 mA cm^{-2} with η of 4.05%. However, for the standard device D_{FTO}, V_{OC} and J_{SC} show a significant increase to 0.77 V and 12.38 mA cm^{-2}, respectively, with an efficiency of 7.22%. As evident from the previous sections, the optical and electrical parameters of the deposited ATO thin film are slightly lower than that of commercial FTO. The sheet resistance of commercially available FTO is around 10-13 $\Omega/\square$ and

the optical transmittance is around 85 % at 550 nm, whereas the deposited ATO thin film has an average sheet resistance of 12.18 Ω/□ and a transmittance of 80 % at 550 nm. This may be the reason for the observed lower photocurrent density and power conversion efficiency of the device D_{ATO} compared to that of D_{FTO}. The semi-log plots corresponding to the *J-V* characteristics are shown in Fig. 6.10 (b). A substantial reduction in the forward bias photocurrent is observed for device D_{ATO} when compared to D_{FTO}. However, the reduction in the reverse leakage current is not that drastic.

Fig. 6.10 (c) shows the external quantum efficiency (EQE) of D_{ATO} and D_{FTO} devices, where a higher EQE (60%) is observed for D_{FTO} compared to that of D_{ATO} (35%). However, to achieve higher power conversion efficiency for the DSSC device fabricated using ATO electrode, the sheet resistance, optical transmittance, and the surface work function of ATO thin films are to be improved by varying the deposition parameters and/or by altering the composition of dopant element. Though the efficiency of D_{ATO} is lower than that of D_{FTO}, for an alternative electrode, the performance is very promising.

To gain information about the frequency-dependent photoelectrochemical mechanism of the device D_{ATO}, its charge transport properties are investigated using electrochemical impedance spectroscopy (EIS). The depiction of real (Z_{re}) and imaginary (Z_{im}) parts of the complex impedance of devices D_{ATO} and D_{FTO} (for comparison) as a function of frequency is presented in Fig. 6.11 (a) (Nyquist plot). The equivalent circuit is shown in the inset of Fig. 6.11 (a) and the corresponding parameters (shown in Table 6.3) are obtained from the Nyquist plot. The high-frequency intercept on the real axis of the Nyquist plot represents the series resistance (R_{series}) of the respective electrodes, R_{ct1} is the interfacial charge carrier transfer resistance between the photoanode and electrolyte, and R_{ct2} is the interfacial charge carrier transfer resistance between the counter electrode and electrolyte for I^-/I_3^- redox reaction.

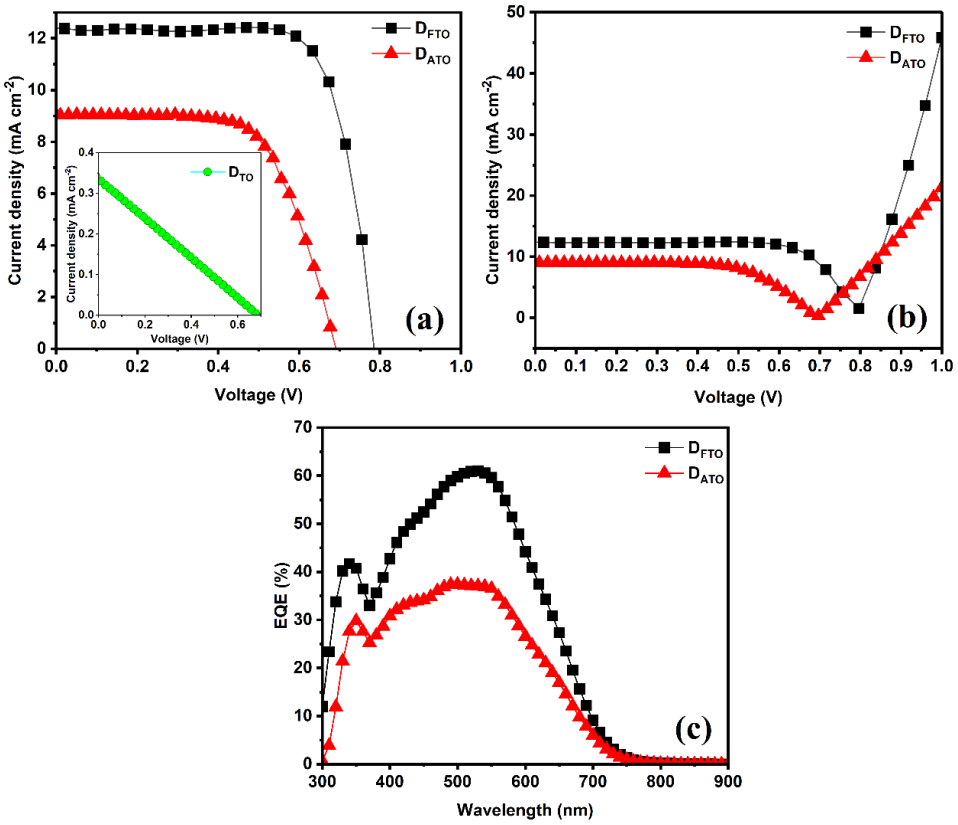

Fig. 6.10 (a) J-V curves (Inset is for TO electrode), (b) Semi-log plots and (c) External quantum efficiency of DSSCs fabricated using ATO and FTO as conductive electrodes.

The series resistance R_{Series} of the device D_{ATO} (60.93 Ω) is higher than that of the reference device D_{FTO} (17.91 Ω) which affects the collection of charge carriers, leading to relatively lower photocurrent density in D_{ATO}. Both the D_{ATO} and D_{FTO} devices exhibit two semicircles as indicated in Fig. 6.11 (a) (inset is the equivalent circuit and enlarged images of the smaller semicircles of D_{FTO} and D_{ATO}). For device D_{FTO}, the semicircle in the low-frequency region (0.1–100 Hz) indicates charge carrier transport resistance (R_{ct1} = 15.11 Ω) at the photoanode-electrolyte interface. In the higher frequency region (100 kHz to 1 MHz), the relatively larger semicircle indicates charge transfer resistance (R_{ct2} = 2.3 Ω) at the electrolyte-counter electrode interface. For the device D_{ATO}, the semicircle in the low frequency region corresponds to high electrical resistance (R_{ct1} = 23.61 Ω) which may justify its slightly lower power conversion

efficiency. The charge transfer resistance (R_{ct2} = 7.17 Ω) at the counter electrode/electrolyte interface (counter electrode/redox I^-/ I_3^- couple) is depicted by a larger semicircle in the higher frequency region, and this may influence the charge carrier collection ability of the counter electrode[68]. The electron lifetime (τ_e) corresponds to the relaxation processes influenced by the electrical conduction mechanism in the devices. The τ_e values determined from the Bode plot (Fig. 6.11 b) are 39.97 μs for device D_{ATO} and 25.22 μs for device D_{FTO}.

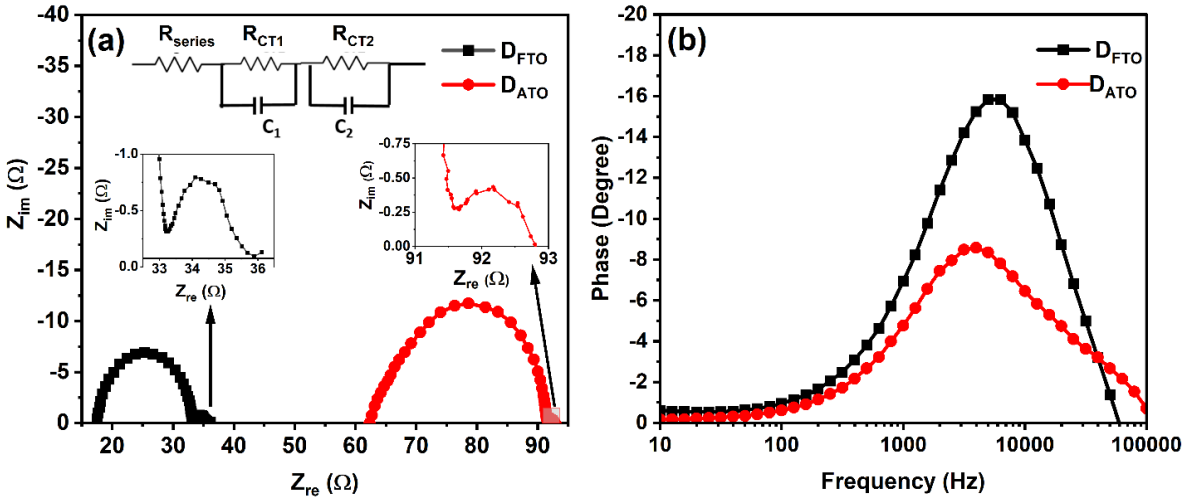

Fig. 6.11. The EIS measurement showing the (a) Nyquist plot (inset is the equivalent circuit and enlarged images of the smaller semicircles of D_{FTO} and D_{ATO}) and (b) Bode plot for DSSCs fabricated using the ATO and FTO conductive substrates.

Table 6.3. The photovoltaic and EIS parameters of DSSC devices based on ATO and FTO conductive electrodes.

Device code	V_{oc} (V)	J_{sc} (mAcm^{-2})	FF (%)	η (%)	R_{series} (Ω)	R_{ct1} (Ω)	R_{ct2} (Ω)	τ_e (μs)
D_{ATO}	0.69	9.16	64.03	4.05	60.93	23.61	7.17	39.97
D_{FTO}	0.777	12.38	74.98	7.22	17.91	15.11	2.30	25.22

6.4. Conclusions

The deposition of 5 wt.% Sb-doped SnO_2 thin film as an alternative transparent conducting electrode was carried out using the facile spray pyrolysis method. The successful doping of Sb into the SnO_2 lattice is confirmed by its unaltered structural properties. The XPS spectra reveal the existence of Sb and Sn in +5 and +4 charge states, respectively. The SEM micrographs show tetragonal morphology with twisted metal sheet-like features. In corroboration with the surface roughness of the ATO film, the contact angle measurements indicate that its surface is hydrophilic in nature. The optical transmittance of the as-deposited ATO film (80 % at 550 nm) is lower than that of the undoped TO film (91 % at 550 nm). However, it possesses low average sheet resistance of 12.18 Ω/□ and a high carrier concentration of 6.20 x 10^{20} cm^{-3} compared to the undoped SnO_2 film. A higher oxygen defect density of 1.57 x 10^{23} cm^{-3} is observed for the ATO film compared to the undoped TO (2.7 x 10^{22} cm^{-3}) film due to Sb-doping. The ATO film exhibits thermal stability of sheet resistance up to 400 °C. In the present study, the deposited ATO thin film shows a high figure of merit of 8.23 x 10^{-3} Ω^{-1} due to the low sheet resistance value compared to that of TO film. The performance of the DSSC device fabricated using the deposited ATO electrode is compared with that of a reference device fabricated using commercially available FTO. Although the FTO-based DSSC shows higher efficiency of 7.22 % compared to the spray-deposited ATO-based DSSC, the efficiency obtained from this device is reasonably good (4.05 %) and has wide scope for improvement. The present study indicates that the Sb-doped SnO_2 electrode is a reliable and promising candidate showing reasonably good properties for its use as an alternative TCO in optoelectronic applications. The performance can be improved by further exploration and comprehensive analysis, either by varying the deposition parameters/dopant concentration and/or by performing certain post annealing treatments in specific non-ambient conditions.

References

[1] S. Chappel, S. Chen, A. Zaban, TiO_2 -Coated Nanoporous SnO_2 Electrodes for Dye-Sensitized Solar Cells, (2002) 3336–3342.

[2] M.Y. Tsai, O. Bierwagen, J.S. Speck, Epitaxial Sb-doped SnO2 and Sn-doped In_2O_3 transparent conducting oxide contacts on GaN-based light emitting diodes, Thin Solid Films. 605 (2016) 186–192.

[3] R. Goei, A.J. Ong, T.J. Hao, L.J. Yi, L.S. Kuang, D. Mandler, S. Magdassi, A.I. Yoong Tok, Novel Nd–Mo co-doped SnO_2/α-WO_3 electrochromic materials (ECs) for enhanced smart window performance, Ceram. Int. 47 (2021) 18433–18442.

[4] M. Batzill, Surface science studies of gas sensing materials: SnO_2, Sensors. 6 (2006) 1345–1366.

[5] D.L. Kamble, N.S. Harale, V.L. Patil, P.S. Patil, L.D. Kadam, Characterization and NO_2 gas sensing properties of spray pyrolyzed SnO_2 thin films, J. Anal. Appl. Pyrolysis. 127 (2017) 38–46.

[6] B. K, Electrical conductivity and thermoelectric power of some heavy metal compounds, Ann. Phys. 22 (1907) 749–766.

[7] G. Bauer, Elektrisches und optisches Verhalten von Halbleitern. XIII Messungen an Cd-, Tl- und Sn-Oxyden, Ann. Phys. 422 (1937) 433–445.

[8] G. Rupprecht, Untersuchungen der elektrischen und lichtelektrischen Leitfähigkeit dünner Indiumoxydschichten, Zeitschrift Für Phys. 139 (1954) 504–517.

[9] H. Mcmaster, Conductive coating for glass and method of application, US Pat. 2,429,420. (1947) 1–4.

[10] D.P. Joseph, P. Renugambal, M. Saravanan, S.P. Raja, C. Venkateswaran, Effect of Li doping on the structural, optical and electrical properties of spray deposited SnO_2 thin films, Thin Solid Films. 517 (2009) 6129–6136.

[11] A. Bhardwaj, B.K. Gupta, A. Raza, A.K. Sharma, O.P. Agnihotri, Fluorine-doped SnO_2 films for solar cell application, Sol. Cells. 5 (1981) 39–49.

[12] M.M. Bagheri-Mohagheghi, M. Shokooh-Saremi, The influence of Al doping on the electrical, optical and structural properties of SnO_2 transparent conducting films deposited by the spray pyrolysis technique, J. Phys. D. Appl. Phys. 37 (2004) 1248–1253.

[13] G. Turgut, E. Sönmez, Synthesis and characterization of Mo doped SnO_2 thin films with spray pyrolysis, Superlattices Microstruct. 69 (2014) 175–186.

[14] A. Espinosa, N. Sánchez, J. Sánchez-Marcos, A. De Andrés, M.C. Muñoz, Origin of the magnetism in undoped and Mn-doped SnO_2 thin films: Sn vs oxygen vacancies, J. Phys. Chem. C. 115 (2011) 24054–24060.

[15] A.M. El Sayed, S. Taha, M. Shaban, G. Said, Tuning the structural, electrical and optical properties of tin oxide thin films via cobalt doping and annealing, Superlattices Microstruct. 95 (2016) 1–13.

[16] R. Ramarajan, N. Purushothamreddy, R.K. Dileep, M. Kovendhan, G. Veerappan, K. Thangaraju, D. Paul Joseph, Large-area spray deposited Ta-doped SnO_2 thin film electrode for DSSC application, Sol. Energy. 211 (2020) 547–559.

[17] S. Nakao, N. Yamada, T. Hitosugi, Y. Hirose, T. Shimada, T. Hasegawa, Fabrication of transparent conductive W-doped SnO_2 thin films on glass substrates using anatase TiO_2 seed layers, Phys. Status Solidi Curr. Top. Solid State Phys. (2011).

[18] R. Ramarajan, M. Kovendhan, K. Thangaraju, D.P. Joseph, Indium-free large area Nb-doped SnO_2 thin film as an alternative transparent conducting electrode, Ceram. Int. (2020) 0–1.

[19] R. Ramarajan, M. Kovendhan, K. Thangaraju, D.P. Joseph, R.R. Babu, Facile deposition and characterization of large area highly conducting and transparent Sb-doped SnO_2 thin film, Appl. Surf. Sci. 487 (2019) 1385–1393.

[20] H.K. Lee, D.H. Joo, M.S. Kim, J.S. Yu, Improved light extraction of InGaN/GaN blue LEDs by GaOOH NRAs using a thin ATO seed layer, Nanoscale Res. Lett. 7 (2012) 1–7.

[21] T. Minami, Transparent Conductive Oxides for Transparent Electrode Applications, 1st ed., Elsevier Inc., 2013.

[22] S.U. Lee, B. Hong, W.S. Choi, Structural, electrical, and optical properties of antimony-doped tin oxide films prepared at room temperature by radio frequency magnetron sputtering for transparent electrodes, J. Vac. Sci. Technol. A Vacuum, Surfaces, Film. 27 (2009) 996–1000.

[23] W. Yang, S. Yu, Y. Zhang, W. Zhang, Properties of Sb-doped SnO_2 transparent conductive thin films deposited by radio-frequency magnetron sputtering, Thin Solid Films. 542 (2013) 285–288.

[24] C. Guillén, J. Herrero, Structural and plasmonic characteristics of sputtered SnO_2:Sb and ZnO:Al thin films as a function of their thickness, J. Mater. Sci. 51 (2016) 7276–7285.

[25] M.O. Guler, O. Cevher, U. Tocoglu, T. Cetinkaya, H. Akbulut, Synthesis and characterization of antimony doped tin oxide nanocomposites for li-ion batteries, Acta Phys. Pol. A. 123 (2013) 383–385.

[26] H. Kim, A. Piqué, Transparent conducting Sb-doped SnO_2 thin films grown by pulsed-laser deposition, Appl. Phys. Lett. 84 (2004) 218–220.

[27] N.S. Murty, S.R. Jawalekar, TrJ ° / Rsh, 108 (1983) 277–283.

[28] K.S. Kim, S.Y. Yoon, W.J. Lee, K. Ho Kim, Surface morphologies and electrical properties of antimony-doped tin oxide films deposited by plasma-enhanced chemical vapor deposition, Surf. Coatings Technol. 138 (2001) 229–236.

[29] K. Tsukuma, T. Akiyama, H. Imai, Hydrolysis Deposition of Thin Films of Antimony-Doped Tin Oxide, J. Am. Ceram. Soc. 84 (2001) 869–871.

[30] L. Luo, D. Bozyigit, V. Wood, M. Niederberger, High-quality transparent electrodes spin-cast from preformed antimony-doped tin oxide nanocrystals for thin film optoelectronics, Chem. Mater. 25 (2013) 4901–4907.

[31] J.P. Correa Baena, A.G. Agrios, Transparent conducting aerogels of antimony-doped tin oxide, ACS Appl. Mater. Interfaces. 6 (2014) 19127–19134.

[32] F. Bai, Y. He, P. He, Y. Tang, Z. Jia, One-step synthesis of monodispersed antimony-doped tin oxide suspension, Mater. Lett. 60 (2006) 3126–3129.

[33] G.H. An, D.Y. Lee, Y.J. Lee, H.J. Ahn, Ultrafast Lithium Storage Using Antimony-Doped Tin Oxide Nanoparticles Sandwiched between Carbon Nanofibers and a Carbon Skin, ACS Appl. Mater. Interfaces. 8 (2016) 30264–30270.

[34] Y. Sanehira, N. Shibayama, Y. Numata, M. Ikegami, T. Miyasaka, Low-Temperature Synthesized Nb-Doped TiO_2 Electron Transport Layer Enabling High-E ffi ciency Perovskite Solar Cells by Band Alignment Tuning, (2020).

[35] M. Esro, S. Georgakopoulos, H. Lu, G. Vourlias, A. Krier, W.I. Milne, W.P. Gillin, G. Adamopoulos, Solution processed SnO_2:Sb transparent conductive oxide as an alternative to indium tin oxide for applications in organic light emitting diodes, J. Mater. Chem. C. 4 (2016) 3563–3570.

[36] A.R. Babar, K.Y. Rajpure, Effect of intermittent time on structural, optoelectronic, luminescence properties of sprayed antimony doped tin oxide thin films, J. Anal. Appl. Pyrolysis. 112 (2015) 214–220.

[37] A. Rahal, A. Benhaoua, C. Bouzidi, B. Benhaoua, B. Gasmi, Effect of antimony doping on the structural, optical and electrical properties of SnO_2 thin films prepared by spray ultrasonic, Superlattices Microstruct. 76 (2014) 105–114.

[38] G. Muruganantham, K. Ravichandran, K. Saravanakumar, P. Philominathan, B. Sakthivel, Effect of doping level on physical properties of antimony doped nanocrystalline tin oxide films fabricated using low cost spray technique, Surf. Eng. 27 (2011) 376–381.

[39] E. Elangovan, S.A. Shivashankar, K. Ramamurthi, Studies on structural and electrical properties of sprayed SnO_2:Sb films, J. Cryst. Growth. 276 (2005) 215–221.

[40] H. Kaneko, K. Miyake, Physical properties of antimony-doped tin oxide thick films, J. Appl. Phys. 53 (1982) 3629–3633.

[41] A.R. Babar, S.S. Shinde, A. V. Moholkar, C.H. Bhosale, J.H. Kim, K.Y. Rajpure, Sensing properties of sprayed antimony doped tin oxide thin films: Solution molarity, J. Alloys Compd. 509 (2011) 3108–3115.

[42] A. Heiras-Trevizo, P. Amézaga-Madrid, L. Corral-Bustamante, W. Antúnez-Flores, P. Pizá Ruiz, M. Miki-Yoshida, Structural, morphological, optical and electrical properties of Sb-doped SnO_2 thin films obtained by aerosol assisted chemical vapor deposition, Thin Solid Films. 638 (2017) 22–27.

[43] R. Ramarajan, M. Kovendhan, K. Thangaraju, D. Paul Joseph, Substrate Temperature Dependent Physical Properties of Spray Deposited Antimony-Doped SnO_2 Thin Films, Thin Solid Films. 704 (2020) 137988.

[44] P. Tang, C. Qiu, J. He, T. Zhang, X. Feng, X. Luo, Effect of the substrate temperature on the properties of spray-deposited SnO_2:F thin films, J. Mater. Sci. Mater. Electron. 25 (2014) 4369–4374.

[45] A. Kaliyaraj Selva Kumar, Y. Zhang, D. Li, R.G. Compton, A mini-review: How reliable is the drop casting technique?, Electrochem. Commun. 121 (2020) 106867.

[46] V.H. Tran, R. Khan, I.H. Lee, S.H. Lee, Low-temperature solution-processed ionic liquid modified SnO_2 as an excellent electron transport layer for inverted organic solar cells, Sol. Energy Mater. Sol. Cells. 179 (2018) 260–269.

[47] C.W. Shih, A. Chin, C.F. Lu, W.F. Su, Remarkably High Hole Mobility Metal-Oxide Thin-Film Transistors, Sci. Rep. 8 (2018) 1–6.

[48] S.S. Pan, G.H. Li, L.B. Wang, Y.D. Shen, Y. Wang, T. Mei, X. Hu, Atomic nitrogen doping and p-type conduction in SnO_2, Appl. Phys. Lett. 95 (2009) 10–13.

[49] E. Shanthi, A. Banerjee, K.L. Chopra, Dopant effects in sprayed tin oxide films, Thin Solid Films. 88 (1982) 93–100.

[50] B. Benrabah, A. Bouaza, A. Kadari, M.A. Maaref, Impedance studies of Sb doped SnO_2 thin film prepared by sol gel process, Superlattices Microstruct. 50 (2011) 591–600.

[51] W. Mao, B. Xiong, Y. Liu, C. He, Correlation between defects and conductivity of Sb-doped tin oxide thin films, Appl. Phys. Lett. 103 (2013) 1–5.

[52] S. B. W., H. N. Narasimha Murthy, M. Krishna, S. C. Sharma, Investigation of Influence of Spin Coating Parameters on the Morphology of ZnO Thin Films by Taguchi Method, Int. J. Thin Film. Sci. Technol. 2 (2013) 143–154.

[53] M. Kumar, B. Singh, P. Yadav, V. Bhatt, M. Kumar, K. Singh, A.C. Abhyankar, A. Kumar, J.H. Yun, Effect of structural defects, surface roughness on sensing properties of Al doped ZnO thin films deposited by chemical spray pyrolysis technique, Ceram. Int. 43 (2017) 3562–3568.

[54] J. Kaur, S.C. Roy, M.C. Bhatnagar, Highly sensitive SnO_2 thin film NO_2 gas sensor operating at low temperature, Sensors Actuators, B Chem. 123 (2007) 1090–1095.

[55] J.T. Wang, X.H. Zhong, J.N. Wang, Significant roughness enhancement of fluorine-doped tin oxide films with low resistivity and high transparency by using HNO_3 addition, RSC Adv. 5 (2015) 52174–52182.

[56] R. Khokhra, B. Bharti, H.-N. Lee, R. Kumar, Visible and UV photo-detection in ZnO nanostructured thin films via simple tuning of solution method, Sci. Reports 2017 71. 7 (2017) 1–14.

[57] T. Rakshit, I. Manna, S.K. Ray, Effect of SnO_2 concentration on the tuning of optical and electrical properties of ZnO-SnO_2 composite thin films, J. Appl. Phys. 117 (2015) 025704.

[58] L.Z. Liu, X.L. Wu, J.Q. Xu, T.H. Li, J.C. Shen, P.K. Chu, Oxygen-vacancy and depth-dependent violet double-peak photoluminescence from ultrathin cuboid SnO_2 nanocrystals, Appl. Phys. Lett. 100 (2012) 121903.

[59] L.Z. Liu, J.Q. Xu, X.L. Wu, T.H. Li, J.C. Shen, P.K. Chu, Optical identification of oxygen vacancy types in SnO_2 nanocrystals, Appl. Phys. Lett. 102 (2013) 031916.

[60] X. Li, R. Deng, Y. Li, B. Yao, Z. Ding, J. Qin, Q. Liang, Effect of Mg doping on optical and electrical properties of SnO_2 thin films: An experiment and first-principles study, Ceram. Int. 42 (2016) 5299–5303.

[61] P.S. Shajira, M.J. Bushiri, B.B. Nair, V.G. Prabhu, Energy band structure investigation of blue and green light emitting Mg doped SnO_2 nanostructures synthesized by combustion method, J. Lumin. 145 (2014) 425–429.

[62] H. Sefardjella, B. Boudjema, A. Kabir, G. Schmerber, Structural and photoluminescence properties of SnO_2 obtained by thermal oxidation of evaporated Sn thin films, Curr. Appl. Phys. 13 (2013) 1971–1974.

[63] R.N. Wenzel, RESISTANCE OF SOLID SURFACES TO WETTING BY WATER, Ind. Eng. Chem. 28 (2002) 988–994.

[64] B.J. Ryan, K.M. Poduska, Roughness effects on contact angle measurements Roughness effects on contact angle measurements, American Journal of Physics 76, (2008): 1074-1077

[65] I.H. Kim, J.H. Ko, D. Kim, K.S. Lee, T.S. Lee, J. h. Jeong, B. Cheong, Y.J. Baik, W.M. Kim, Scattering mechanism of transparent conducting tin oxide films prepared by magnetron sputtering, Thin Solid Films. 515 (2006) 2475–2480.

[66] S. Calnan, A.N. Tiwari, High mobility transparent conducting oxides for thin film solar cells, Thin Solid Films. 518 (2010) 1839–1849.

[67] G. Haacke, New figure of merit for transparent conductors, J. Appl. Phys. 47 (1976) 4086–4089.

[68] M. Grätzel, Dye-sensitized solar cells, J. Photochem. Photobiol. C Photochem. Rev. 4 (2003) 145–153.

CHAPTER: 7

Prickly pear fruit extract as photosensitizer in dye-sensitized solar cell

In this chapter, the focus is on the natural dye extraction from prickly pear fruit to explore as an alternative photosensitizer in DSSCs. The natural photosensitizer is extracted from prickly pear fruits by a facile extraction process. This chapter presents the studies of structural, optical, chemical, and electronic properties of prickly pear fruit extract adhered to the surface of TiO_2 serving as a photoanode. The prickly pear fruit extract is also tested as a photoanode in DSSCs and the performance of the device is discussed in sufficient detail in this chapter.

7.1 Introduction

A dye-sensitized solar cell (DSSC) is a renewable energy device, which can convert solar radiation into usable electrical energy. DSSCs are easy to fabricate, lower in cost, environment-friendly, and compatible for mass production [1]. The DSSC first developed by O'Regan and Gratzel in 1991 achieved 7 % energy conversion efficiency using TiO_2 as a photoanode [2]. The DSSC is made up of a nanocrystalline wide bandgap semiconductor layer coated onto fluorine-doped tin oxide (FTO) as working electrode (WE), ruthenium-based dye as a photosensitizer, iodine (I_3^-/I^-) redox couple as a liquid electrolyte, and platinum (Pt) coated FTO as a counter electrode (CE) [3,4]. Usually, the WE made up of TiO_2 anchored with a ruthenium complex based photosensitizer dye plays a critical role in the generation of photo-excited electrons to inject them into the conduction band of the TiO_2 layer towards better performance of the DSSC. Ruthenium based photosensitizer along with iodine (I_3^-/I^-) liquid electrolyte has successfully achieved the highest conversion efficiency of 11-12 % using nano-porous semiconducting TiO_2 electrodes [5–8]. The common synthetic dyes are ruthenium,

polypyridine metal complexes, phthalocyanine, and porphyrin dyes [9,10]. However, metal-organic complex based dyes are very expensive, difficult to synthesize, complex in design, feign high environmental and health risks due to their toxic nature [11]. As an alternative, researchers nowadays focus on dyes extracted from natural sources as a photosensitizer to convert solar energy into electricity. The natural dyes are eco-friendly, cost-effective, non-toxic, and abundant [12–14]. Natural dye pigments containing anthocyanin, betalains (betacyanin), chlorophyll, flavonoids, and carotenoids have been greatly investigated as photosensitizers in DSSCs [15–21]. These natural photosensitizers are extracted from commonly available fruits, leaves, roots, and flowers which are capable to absorb light photons having wavelengths in the visible region of the solar spectrum [22–24].

Natural dye sources from commonly available fruits, leaves, and roots have been investigated recently for being used as photo-sensitizer in DSSC [14,16,25–33]. Betalains containing natural pigments extracted from red beetroot having absorption maxima in the red-violet color range have been widely used as a photosensitizer in DSSCs and reported to have an efficiency in the range from 0.44% to 0.67% [25,34]. In this chapter, prickly pear fruit extract (Cactus) belonging to the Cactaceae family containing natural betacyanin which appears deep red is extracted for investigation. The cactus plants grow in several tropical regions all over the world, like South Africa, the Mediterranean basin, Middle East, Australia, and India [35]. Prickly pear fruits are relatively less explored compared to other natural sources and are worth exploring since they have carboxylic groups with oxidation potential similar to that of ruthenium polypyridyl complexes [36]. Few reports exist in the literature reporting the extract of prickly pear fruit used as a photosensitizer in DSSC, among them G. Calogero et al., have shown an improved efficiency of 2.06% for Sicilian prickly pear fruits [36]. However, they obtained a slightly low fill factor (0.60) and open-circuit voltage (389 mV). In general, the variation in performance of DSSCs depends on fabrication steps adopted, like the procedure

used for extracting and purifying the extract of cactus fruit, etc. It is also to be noted that the mineral content and the concentration/ratio of the natural dye components present in the cactus fruits highly depend on the geographical location where they are grown.

In this chapter, the natural dye extracted from the common prickly pear fruit belonging to the Cactaceae family, Opuntia genus, and ficus-Indica species grown in the Western Ghats mountain range located in the southern part of Tamilnadu, India is considered for exploration. The prickly pear extract is first characterized for its optical properties using UV-Vis and FTIR to confirm the presence of betacyanin. Later, the prickly pear extract is made to adsorb on the surface of nanocrystalline TiO_2 and characterized for its structural and optical properties using XRD, SEM, XPS, and UV-Vis-DRS. A DSSC fabricated using the prickly pear extract as sensitizer measured for its I-V characteristics and electrochemical impedance is found to present interesting results which are elaborated in the following sections.

7.2 Materials and experimental methods

7.2.1 Materials

Fully ripened prickly pear fruits (Collected from the western Ghats mountain range located in the southern part of Tamilnadu, India) without stain or bumps were taken for extracting the pulp after carefully removing the thorns and seeds. Ethanol (99.9% A.R grade), P25 (TiO_2) powder (Degussa Germany), Ethylcellulose, α- Terpineol (90% analytical grade) were procured from Sigma Aldrich. Fluorine doped tin oxide (FTO, sheet resistance 10 Ω/□) glass substrates are used as conducting electrodes. $TiCl_4$ (TCI chemicals, 99.99%) was used for post-treatment on the surface of the TiO_2 electrode. Acetonitrile, Iodine, 4-tert-butyl pyridine, 1-butyl-3 methylimidazolium iodide purchased from sigma Aldrich were used without any further purification as the redox couple for photo-electrochemical studies. Platinum paste

purchased from Solaronix, Switzerland, were used for making counter electrode. Surlyn spacer (SX1170-60, 60 µm thick from Solaronix) was used for sealing of DSSC device.

7.2.2 Preparation of dye solution

Approximately 50 g of fully ripened prickly pear fruits pulp was taken and added with 50 ml of ethanol, stirred for 2h to extract the red colored solution at room temperature. The red coloured extract was then filtered, centrifuged at 10000 rpm for 15 min at room temperature, and decanted to separate it from a suspension of insoluble solid particles like fibers. This extract was then carefully transferred into air-tight containers and covered with aluminum foil for light protection and stored in the refrigerator at 3 °C for further use.

7.2.3 Preparation of photoanode and fabrication of DSSC device

The electrode preparation and device fabrication were done as reported in the literature [37]. Mesoporous TiO_2 paste was coated onto FTO substrates marking an active area of 0.25 cm^2 and annealed at 500 °C for 30 min. The films were further treated with 40 mM of $TiCl_4$ at 100 °C for 1 h and then sintered at 500 °C for 30 min in air. The $TiCl_4$ treated TiO_2 electrodes were then soaked in the prickly pear dye (prepared in absolute ethanol) at room temperature for 12 h. The dye adsorbed electrodes were thoroughly washed in a mild stream of ethanol to remove the weakly adsorbed prickly pear dye molecules onto the surface of the TiO_2 film. The FTO substrates were drilled with two fine holes to fill the electrolyte solution. The cleaned substrates were coated with a thin layer of platinum paste by doctor blade method and sintered at 500 °C for 30 min to serve as the counter-electrode. The photoanode and counter electrodes were then sandwiched with the help of surlyn polymer. The iodide-based liquid electrolyte was injected into the cell through the hole from the counter electrode side. After filling the electrolyte, the holes were sealed using surlyn and coverslip glass.

7.3 Results and discussion

7.3.1 X-Ray diffraction

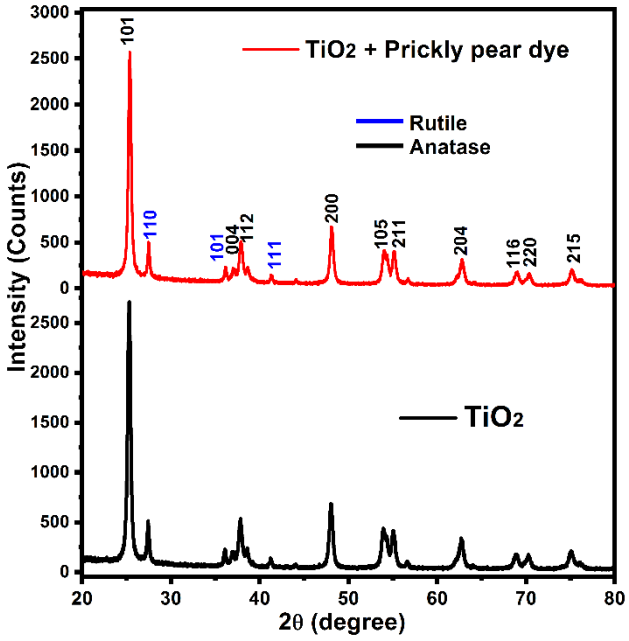

Fig. 7.1. XRD pattern of pure and prickly pear extract adsorbed TiO_2 nanoparticles.

The X-ray diffraction (XRD) spectra of pure TiO_2 and dye adsorbed TiO_2 are shown in Fig. 7.1. The prickly pear extract though centrifuged and filtered, may contain fibers and sugar in it apart from the coloring compound of the dye. The presence of these may induce significant amorphization upon adsorption to the TiO_2 surface; and to ensure this, we have performed the XRD analysis to check for the crystallinity. Fig. 7.1 shows that the major peaks belonging to the anatase phase of TiO_2 (JCPDS No. # 73-1764) are present without significant modification in crystallinity even after adsorption of the natural dye.

7.3.2 Morphological studies of dye adsorbed TiO_2 electrode

The surface morphology of pure and prickly pear extract adsorbed TiO_2 nanoparticles coated onto an FTO substrate is shown in Fig. 7.2 (a and b). The nanoparticles are observed to

be porous in the SEM image for pure TiO_2 (Fig. 7.2a). There are no morphological changes observed after dye adsorption onto the TiO_2 film (Fig. 7.2b), however, it reveals that the smooth dye aggregation onto the surface of TiO_2 nanoparticles make the electrode much more compact compared to the uncoated one.

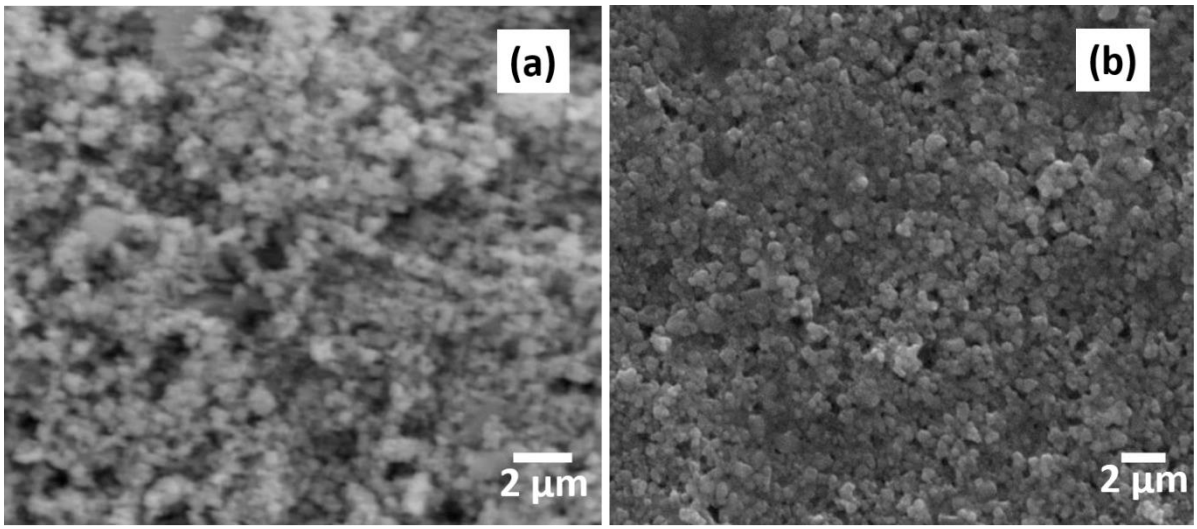

Fig. 7.2. The SEM images of (a) pure and (b) prickly pear fruit extract adsorbed TiO_2 electrodes.

7.3.3 UV-Visible DRS studies

The absorption spectra of prickly pear fruit extract solution shown in Fig. 7.3 exhibit an intense broad absorption band in the visible region of the solar spectrum between 400 nm to 600 nm with a peak at 534 nm. This peak is envisaged to occur due to the presence of betacyanin which acts as a natural photosensitizer in the dye [14]. The prickly pear dye solution is deep red-purple (Inset of Fig. 7.3) due to the electronic transition occurring between π-π^* of betacyanin present in the extract [14]. The basic structure of betacyanin is shown in Fig. 7.4 and this compound has been reported to absorb in the blue to the green region and reflect the red wavelength. The diffuse reflectance spectra (DRS) of pure and prickly pear extract adsorbed TiO_2 are shown in Fig. 7.5. The bandgap of semiconductors in thin-film form is usually estimated from Tauc relation by estimating the absorption coefficient 'α', which is dependent

on film thickness. However, for opaque/coloured powder samples, estimation of thickness and the subsequent calculation of 'α' is cumbersome. In such case, DRS is a suitable method for the estimation of absorption edges of coloured powdered materials. Sufficient quantity of powder sample was used to prevent loss by partial transmission, if any, during the DRS measurement. The bandgap of the powder material is calculated from the onset of the linear increase of the diffuse reflectivity spectrum [38,39]. The sharply increasing percent reflectance constitutes the linear region with the highest slope, indicating an exponential drop in the absorption coefficient. The bandgap can be deduced without estimating the absorption coefficient by extrapolating the linear fit to R=0 [39]. The diffuse reflectance spectrum of pure TiO_2 shows a single linear region corresponding to the band edge absorption in the range of 350 nm to 400 nm. The percent reflectance after 400 nm is nearly flat in the entire visible region. The intercept of the linear fit to R=0 yields the direct bandgap value of pure TiO_2 to be 3.44 eV (Fig. 7.5). Upon adsorbing with the natural dye, the percentage of reflectance is significantly decreased, indicating strong absorbance of the incident radiation in the visible region. Interestingly, the reflectance spectra of prickly pear extract adsorbed TiO_2 show two absorption edges, one corresponding to the band edge of TiO_2 and the other one significantly red-shifted towards 600 nm in the visible region (Fig. 7.5).

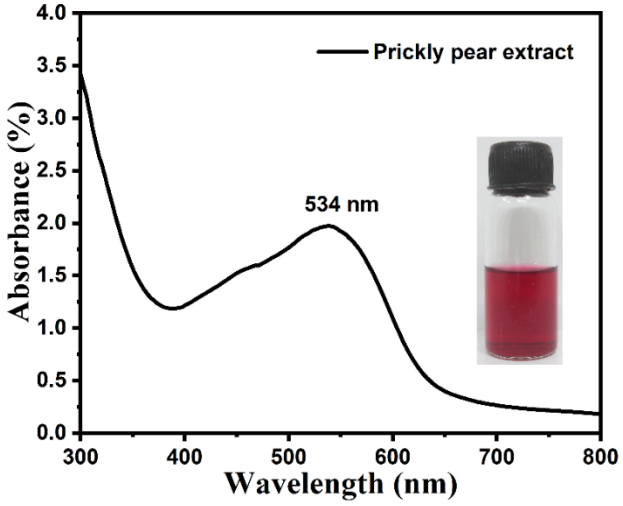

Fig. 7.3. UV-Vis absorption spectra of the prickly pear fruit extract dissolved in ethanol. Inset is the photograph of the extract in ethanol.

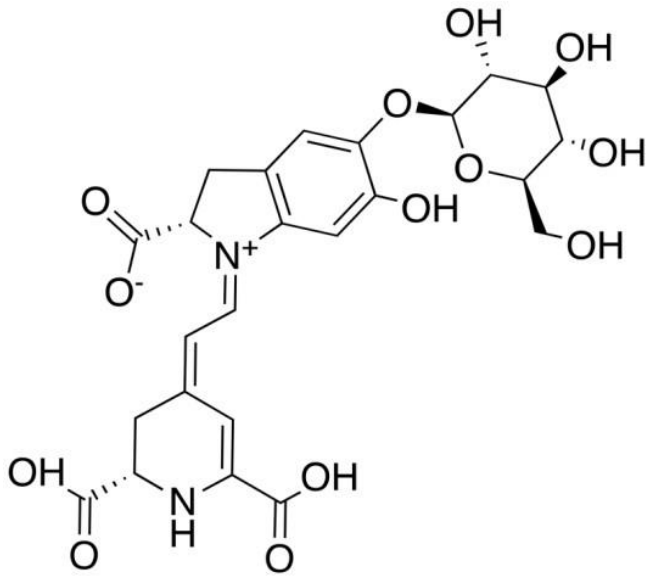

Fig. 7.4. Chemical structure of betacyanin present in the extract of prickly pear fruit.

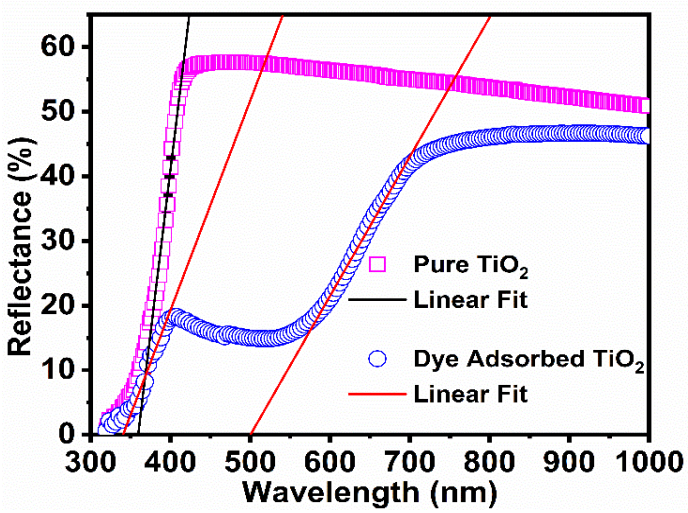

Fig. 7.5. UV-Vis diffuse reflectance spectra of pure and prickly pear fruit extract adsorbed TiO_2 nanoparticles.

The observed redshift is due to the chelation of betacyanin with Ti (IV) ions through the hydroxyl (OH) groups. According to Yoon et al., the chelation of organic ligands with Ti (IV) ions can lead to strong dye-TiO_2 charge transfer (DTCT) bands in the visible region [40,41]. The direct bandgap values of prickly pear extract adsorbed TiO_2 are found to be 3.63 eV and 2.47 eV, respectively in the lower and higher wavelength regions. The appearance of the second reflectance region indicates that the natural dye has been adsorbed effectively onto the surface

of TiO_2. The onset of the second linear region starts around 540 nm which is in the same region as that of the absorption peak of the prickly pear extract solution (Fig. 7.3). This matching of wavelength indicates that the dye adsorbed onto the TiO_2 surface effectively absorbs the incident photons.

7.3.4 Fourier transform infrared analysis

The chemically active functional groups of prickly pear fruit dye extracted using ethanol as a solvent and identified by Fourier transform infra-red (FTIR) spectroscopy are shown in Fig. 7.6. The presence of functional groups in the betacyanin such as hydroxyl, carbonyl, methyl and ethers are shown in the chemical structure (Fig. 7.4). The FTIR spectrum shows the presence of hydroxyl (O-H) and amine (N-H) groups as a strong broadband stretching mode appearing between 3200 cm^{-1} - 3600 cm^{-1}. Also, the presence of broadband stretching mode of hydroxyl group, carboxylic acid, phenolic O-H, and N-H around 3367 cm^{-1} is confirmed.

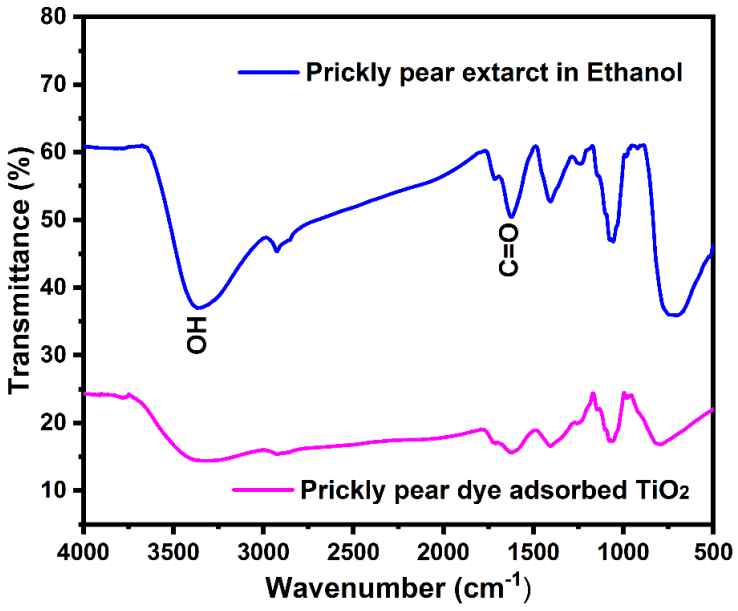

Fig. 7.6. The FTIR spectra of prickly pear fruit extract showing the presence of functional groups and its variation when adsorbed over the surface of TiO_2 nanoparticles.

In the aliphatic CH_2 and CH functional groups, a small peak at 2925 cm^{-1} is associated with the symmetric C-H (alkane) stretching vibrational mode. The small shoulder peak around 1722 cm^{-1} is due to the stretching mode of C=O (carbonyl). The conjugated C=C stretching vibration is also observed at 1625 cm^{-1}. The aromatic C=C stretching vibrational band confirms the peak at 1405 cm^{-1}. The C-N bending vibrational band is found to be present at 1240 cm^{-1}. The functional group of ethers and esters of C-O stretching vibrations is further confirmed at 1057 cm^{-1}. The broad peak observed around 722 cm^{-1} corresponds to the aromatic C-H bending vibration. Upon the natural dye adsorption, the transmittance peak intensity decreases slightly, indicating absorption by the dye. In general, the pure anatase TiO_2 compound has the O-Ti-O bonding around 720 cm^{-1}. The broadened peaks around 1060 cm^{-1} and 790 cm^{-1} indicate the effective anchoring of the dye molecules onto the surface of TiO_2 [42,43].

7.3.5 X-ray photoelectron spectroscopy

The X-ray photoelectron spectroscopy (XPS) measurements were performed to further analyze the chemical composition and binding energies of TiO_2 before and after prickly pear fruit extracted dye adsorption. The narrow scan spectra of Ti 2p levels are well resolved into doublets of Ti $2p_{3/2}$ and Ti $2p_{1/2}$ components corresponding to binding energies 458.41 eV and 464.2 eV, respectively, as shown in Fig. 7.7a. The binding energy values indicate Ti to be present in a 4+ charge state which match with the existing literature [44]. Upon natural dye adsorption, the peak positions are not shifted, instead, the intensity of the peaks decreases significantly, indicating the dye component to intimately adhere over the surface of the TiO_2 nanoparticles. The narrow scan XPS spectra of O 1s state (Fig. 7.7b) with binding energy at 529.6 eV is characteristic of O^{2-} state corresponding to O–Ti–O metal-oxide bonding. A subtle shoulder at the base of O 1s peak is also witnessed at 531.6 eV which is reported to arise from traces of OH adsorbed onto the surface of pure TiO_2 [44]. Upon natural dye adsorption, the

intensity of the O 1s peak decreases considerably and a peak with significant intensity belonging to the OH group is observed at higher binding energy side at 532.4 ± 0.1 eV [45].

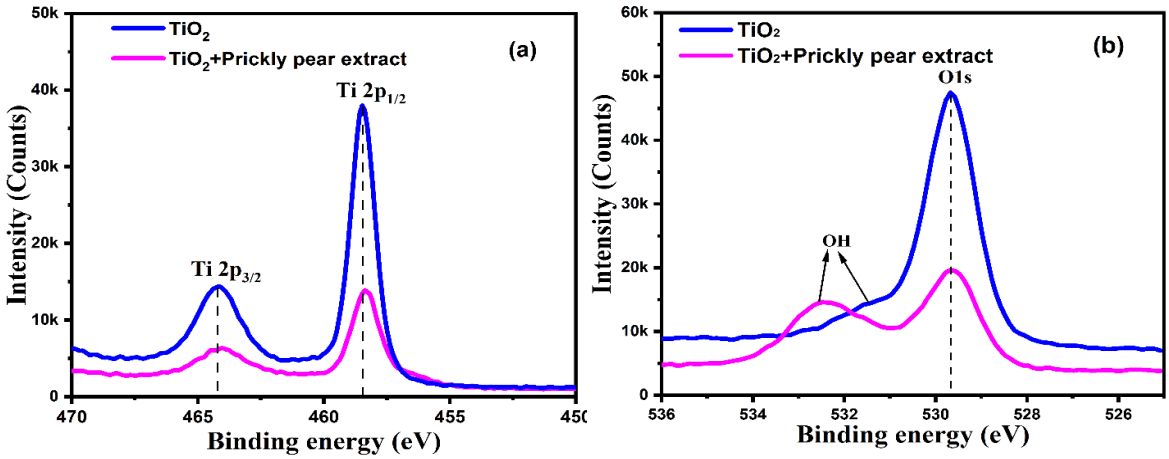

Fig. 7.7. The XPS spectra of (a) Ti 2p levels and (b) O1s levels of pure and prickly pear extract adsorbed TiO_2.

The shift in OH binding energy peak is 0.9 eV which is due to the increased number of hydroxyl (OH) groups from the prickly pear extract anchored onto the surface of TiO_2 as also identified in the FTIR spectra (Fig. 7.6). The OH groups adsorbed onto a metal-oxide surface are envisaged to promote effective trapping of photoelectrons and holes, leading to reduced electron-hole pair recombination rate [46,47]. Therefore, the DRS, FTIR, and XPS data confirm that the natural prickly pear fruit extract dye is attached intimately onto the surface of TiO_2.

7.3.6 Photoelectrical properties of DSSC fabricated using prickly pear fruit extract

Current density-voltage (I-V) characteristics of the DSSC fabricated using a natural prickly pear and N719 dye were measured under standard AM 1.5G conditions (Fig. 7.8). The overall fill factor (FF) and photoconversion efficiency were calculated by using eq. 1.11 and eq. 1.12. The natural dye-sensitized DSSC device performance parameters in comparison with N719 dye are listed in Table 7.1. The photo-conversion efficiency is lower than that of the traditional ruthenium dye (N719).

The DSSC fabricated using wild Sicilian prickly pear fruit (Opuntia Vulgaris) dye extracted in an acidic medium (Dye absorption at 450 nm) is found to show a maximum efficiency of 2.06 % [36], with FF value of 0.60. Recently, R. Ramamoorthy et al. [48], showed that the efficiency of 0.47 % and a FF value of 0.69 for is obtained for the prickly pear fruit extract from the species Opuntia dilleniid (Dye absorption at 517 nm). In the present case, the DSSC fabricated using the extract of Opuntia ficus-Indica (Dye absorption at 534 nm) exhibits an efficiency of 0.56 % and FF of 0.85.

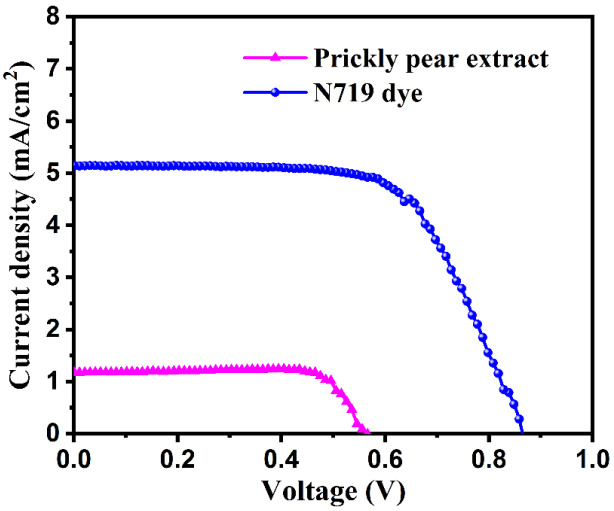

Fig. 7.8. The J-V characteristic curves of DSSC fabricated using prickly pear fruit extract is compared with N719 Dye.

Table 7.1. The J-V characteristic parameters of DSSC fabricated using prickly pear fruit extract in comparison with N719 Dye.

Sample	J_{SC} (mA/cm^2)	V_{OC} (V)	FF	η (%)	R_s (Ω)	R_1 (Ω)	R_2 (Ω)
Prickly pear fruit extract	1.17	0.56	0.85	0.56	21	226	2738
N719	5.1	0.86	0.68	3.05	24	132	7

The obtained V_{oc} and FF values are higher compared to DSSCs fabricated using various species of prickly pear fruits reported in the literature. The lower performance of the cell can be attributed to the high charge transfer resistance at the TiO_2/dye/electrolyte interface. The presence of carbonyl and hydroxyl groups in the prickly pear extract help in better anchoring and effective regeneration of the iodine-based redox couple with the TiO_2 nanoparticles [36]. This intimate adherence and better interaction between the prickly pear dye molecules with the surface of TiO_2 nanoparticles lead to a better charge-transfer performance, thereby improving the fill factor [43]. It has been reported in the literature that the crude extract performs better in the case of anthocyanin, attributing to the presence of co-pigments [12] which is also envisaged in the present case.

7.3.7 Electrochemical impedance studies

Electrochemical impedance studies (EIS) were carried out to analyze the interfacial electron transfer, electron recombination process, and the resistance involved between the internal components of the fabricated DSSC devices. The Nyquist plot along with the equivalent circuit (Fig. 7.9a inset) and Bode plots are shown in Fig. 7.9a and 7.9b. The Nyquist plot of the DSSC device exhibits two semicircles, one corresponding to the high-frequency region and the other semi-circle corresponding to the mid-frequency frequency region. R_1 is the Faraday or charge-transfer resistance that is developed at the interface of redox reaction I_3^-/I^- at the Pt counter electrode/electrolyte interface. The next semicircle at the mid-frequency region is attributed to the internal electron transfer resistance R_2 at the TiO_2/dye/electrolyte interfaces which is related to the charge recombination of the electrons [21,49]. Here, R_s, R_1, and R_2 values are calculated by fitting the equivalent circuit. The R_s representing the total internal series resistance of the DSSC cell is 21 Ω for the natural dye cell, and 24 Ω for the standard N719 cell. The value of R_1 for the standard N719 reference cell is appreciably lower than the one with natural dye. On contrary, the R_2 value of the natural dye-sensitized DSSC is higher (2738 Ω)

than that of the N719 reference (7 Ω) cell. The value of R_2 indicates that the charge recombination is higher at the TiO_2/dye/electrolyte interface for the prickly pear DSSC device which may be the reason for fewer photoelectrons to accumulate in the conduction band of TiO_2, leading to a lower collection of photoexcited electrons, resulting in low V_{oc} and J_{sc}, yielding low efficiency [11]. The FF mainly depends on the internal series resistance R_s of the DSSC cell. The R_s value is low for the DSSC device fabricated from prickly pear extract compared to that of the N719 reference cell (Table 7.1).

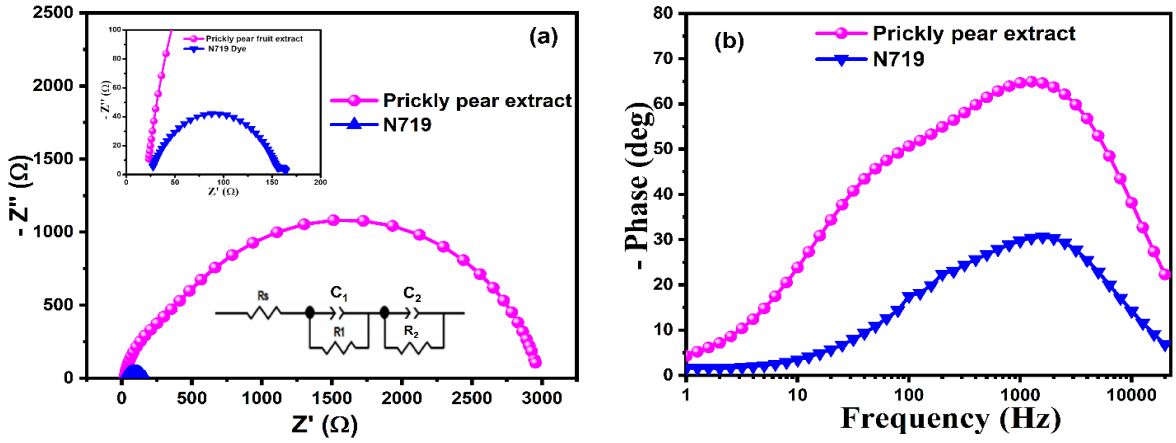

Fig. 7.9. The (a) Nyquist plot of the DSSCs, inset are the enlarged plot and the equivalent circuit diagram and (b) the Bode phase plot of the DSSC devices.

The Bode plots shown in Fig. 7.9b indicate the presence of a broad peak with a discernible shoulder peak. The shoulder peak is prominently seen in the DSSC using natural dye than in the N719 reference cell. The shoulder peak at the low-frequency region corresponds to electron transfer and the peak at the high-frequency region implies the charge recombination process to take place in the DSSC fabricated using natural prickly pear extract.

The electron lifetime (τ_e) is estimated from the following relationship,

$$\tau_e = \frac{1}{2\pi f_{max}} \tag{7.1}$$

where f_{max} is the maximum frequency of the peak obtained in the mid-frequency region [37]. Here, the τ_e of DSSC from prickly pear extract is 0.12 ms which is slightly lower than 0.15 ms for the N719 reference cell. This indicates that the charge recombination is higher in the prickly pear DSSC cell, leading to a decrease in the value of J_{sc}.

7.4. Conclusions

In this chapter, it is experimentally confirmed that the prickly pear fruit extract can be used as a natural, cost effective, and environmentally friendly photosensitizer in dye-sensitized solar cells for energy harvesting. When compared with the conventional N719 dye, the prickly pear fruit extract is highly economical and free from toxicity which gives an added advantage to this natural dye. The presence of betacyanin with a deep red-purple color solution is confirmed from the FTIR and UV-Vis measurements. After the natural dye adsorption, the red-shift of the reflectance edge of TiO_2 to the higher wavelength region is confirmed from the DRS data. The spectroscopic measurements collectively indicate effective anchoring of the dye molecules onto the surface of TiO_2 which is mainly due to the presence of hydroxyl and carbonyl groups in the prickly pear extract. Though the prickly pear dye adsorbed DSSC shows a conversion efficiency lower than DSSCs using other cactus based natural dyes, the values of open-circuit voltage and fill factor are higher. The performance of the prickly pear dye can be improved by optimizing several other parameters like dye isolation and purification, altering the dye loading duration, pre-treatment of the photoanode, etc.

References

[1] Brian O'Regan & Michael Grätzel, A low-cost, high-efficiency solar cell based on dye-sensitized colloidal TiO_2 films, Nature. 353 (1991) 737–740.

[2] M. Grätzel, Photoelectrochemical cells, Nat. 2001 4146861. 414 (2001) 338–344.

[3] H.J. Kim, D.J. Kim, S.N. Karthick, K. V. Hemalatha, C. Justin Raj, S. Ok, Y. Choe, Curcumin dye extracted from Curcuma longa L. used as sensitizers for efficient dye-sensitized solar cells, Int. J. Electrochem. Sci. 8 (2013) 8320–8328.

[4] W.S. Jeong, J.W. Lee, S. Jung, J.H. Yun, N.G. Park, Evaluation of external quantum efficiency of a 12.35% tandem solar cell comprising dye-sensitized and CIGS solar cells, Sol. Energy Mater. Sol. Cells. 95 (2011) 3419–3423.

[5] Sanghoon Kim, Jae Kwan Lee, Sang Ook Kang, Jaejung Ko, J.-H. Yum, Simona Fantacci, Filippo De Angelis, D. Di Censo, and Md. K. Nazeeruddin, Michael Grätzel, Molecular Engineering of Organic Sensitizers for Solar Cell Applications, J. Am. Chem. Soc. 128 (2006) 16701–16707.

[6] M. Grätzel, Dye-sensitized solar cells, J. Photochem. Photobiol. C Photochem. Rev. 4 (2003) 145–153.

[7] H. Choi, C. Baik, S.O. Kang, J. Ko, M.-S. Kang, M.K. Nazeeruddin, M. Grätzel, Highly Efficient and Thermally Stable Organic Sensitizers for Solvent-Free Dye-Sensitized Solar Cells, Angew. Chemie. 120 (2008) 333–336.

[8] T. Bessho, S.M. Zakeeruddin, C.-Y. Yeh, E.W.-G. Diau, M. Grätzel, Highly Efficient Mesoscopic Dye-Sensitized Solar Cells Based on Donor–Acceptor-Substituted Porphyrins, Angew. Chemie Int. Ed. 49 (2010) 6646–6649.

[9] J. Gong, J. Liang, K. Sumathy, Review on dye-sensitized solar cells (DSSCs): Fundamental concepts and novel materials, Renew. Sustain. Energy Rev. 16 (2012) 5848–5860.

[10] K.M. Lee, C.Y. Hsu, W.H. Chiu, M.C. Tsui, Y.L. Tung, S.Y. Tsai, K.C. Ho, Dye-sensitized solar cells with a micro-porous TiO_2 electrode and gel polymer electrolytes prepared by in situ cross-link reaction, Sol. Energy Mater. Sol. Cells. 93 (2009) 2003–2007.

[11] I.C. Maurya, Neetu, A.K. Gupta, P. Srivastava, L. Bahadur, Callindra haematocephata and Peltophorum pterocarpum flowers as natural sensitizers for TiO_2 thin film based dye-sensitized solar cells, Opt. Mater. (Amst). 60 (2016) 270–276.

[12] C.Y. Chien, B.D. Hsu, Optimization of the dye-sensitized solar cell with anthocyanin as photosensitizer, Sol. Energy. 98 (2013) 203–211.

[13] R. Hemmatzadeh, A. Mohammadi, Improving optical absorptivity of natural dyes for fabrication of efficient dye-sensitized solar cells, J. Theor. Appl. Phys. 7 (2013) 1–7.

[14] G. Calogero, G. Di Marco, S. Cazzanti, S. Caramori, R. Argazzi, A. Di Carlo, C.A. Bignozzi, Efficient Dye-Sensitized Solar Cells Using Red Turnip and Purple Wild Sicilian Prickly Pear Fruits, Int. J. Mol. Sci. 11 (2010) 254–267.

[15] H. Hug, M. Bader, P. Mair, T. Glatzel, Biophotovoltaics: Natural pigments in dye-sensitized solar cells, Appl. Energy. 115 (2014) 216–225.

[16] Q. Dai, J. Rabani, Photosensitization of nanocrystalline TiO_2 films by anthocyanin dyes, J. Photochem. Photobiol. A Chem. 148 (2002) 17–24.

[17] S. Hao, J. Wu, Y. Huang, J. Lin, Natural dyes as photosensitizers for dye-sensitized solar cell, Sol. Energy. 80 (2006) 209–214.

[18] K. Wongcharee, V. Meeyoo, S. Chavadej, Dye-sensitized solar cell using natural dyes extracted from rosella and blue pea flowers, Sol. Energy Mater. Sol. Cells. 91 (2007) 566–571.

[19] S. Ananth, P. Vivek, T. Arumanayagam, P. Murugakoothan, Natural dye extract of lawsonia inermis seed as photo sensitizer for titanium dioxide based dye sensitized solar cells, Spectrochim. Acta Part A Mol. Biomol. Spectrosc. 128 (2014) 420–426.

[20] L.K. Singh, T. Karlo, A. Pandey, Performance of fruit extract of Melastoma malabathricum L. as sensitizer in DSSCs, Spectrochim. Acta Part A Mol. Biomol. Spectrosc. 118 (2014) 938–943.

[21] A. Lim, N.T.R.N. Kumara, A.L. Tan, A.H. Mirza, R.L.N. Chandrakanthi, M.I. Petra, L.C. Ming, G.K.R. Senadeera, P. Ekanayake, Potential natural sensitizers extracted from the skin of Canarium odontophyllum fruits for dye-sensitized solar cells, Spectrochim. Acta Part A Mol. Biomol. Spectrosc. 138 (2015) 596–602.

[22] N.A. Ludin, A.M. Al-Alwani Mahmoud, A. Bakar Mohamad, A.A.H. Kadhum, K. Sopian, N.S. Abdul Karim, Review on the development of natural dye photosensitizer for dye-sensitized solar cells, Renew. Sustain. Energy Rev. 31 (2014) 386–396.

[23] P. Luo, H. Niu, G. Zheng, X. Bai, M. Zhang, W. Wang, From salmon pink to blue natural sensitizers for solar cells: Canna indica L., Salvia splendens, cowberry and Solanum nigrum L., Spectrochim. Acta Part A Mol. Biomol. Spectrosc. 74 (2009) 936–942.

[24] E.M. Jin, K.-H. Park, B. Jin, J.-J. Yun, H.-B. Gu, Photosensitization of nanoporous TiO_2 films with natural dye, Phys. Scr. 2010 (2010) 014006.

[25] D. Zhang, S.M. Lanier, J.A. Downing, J.L. Avent, J. Lum, J.L. McHale, Betalain pigments for dye-sensitized solar cells, J. Photochem. Photobiol. A Chem. 195 (2008) 72–80.

[26] A. Kay, M. Graetzel, Artificial photosynthesis. 1. Photosensitization of titania solar cells with chlorophyll derivatives and related natural porphyrins, J. Phys. Chem. 97 (2002) 6272–6277.

[27] G. Calogero, G. Di Marco, Red Sicilian orange and purple eggplant fruits as natural sensitizers for dye-sensitized solar cells, Sol. Energy Mater. Sol. Cells. 92 (2008) 1341–1346.

[28] K. Tennakone, G.R.R.A. Kumara, I.R.M. Kottegoda, K.G.U. Wijayantha, The photostability of dye-sensitized solid state photovoltaic cells: factors determining the stability of the pigment in a nanoporous n-/cyanidin/p-CuI cell, Semicond. Sci. Technol. 12 (1997) 128.

[29] G.P. Smestad, M. Grätzel, Demonstrating Electron Transfer and Nanotechnology: A Natural Dye-Sensitized Nanocrystalline Energy Converter, J. Chem. Educ. 75 (1998) 752–756.

[30] Qing Dai, Joseph Rabani, Photosensitization of nanocrystalline TiO_2 films by pomegranate

pigments with unusually high efficiency in aqueous medium, Chem. Commun. 0 (2001) 2142–2143.

[31] Qing Dai, Joseph Rabani, Unusually efficient photosensitization of nanocrystalline TiO_2 films by pomegranate pigments in aqueous medium, New J. Chem. 26 (2002) 421–426.

[32] Nerine J. Cherepy, Greg P. Smestad, and Michael Grätzel, Jin Z. Zhang, Ultrafast Electron Injection: Implications for a Photoelectrochemical Cell Utilizing an Anthocyanin Dye-Sensitized TiO_2 Nanocrystalline Electrode, J. Phys. Chem. B. 101 (1997) 9342–9351.

[33] A.S. Polo, N.Y. Murakami Iha, Blue sensitizers for solar cells: Natural dyes from Calafate and Jaboticaba, Sol. Energy Mater. Sol. Cells. 90 (2006) 1936–1944.

[34] Z. D, Y. N, Y. T, M. H, Natural Dye Sensitized Solar Cells., Trans. Mater. Res. Soc. Japan. 27 (2002) 811–814.

[35] U. Osuna-Martínez, J. Reyes-Esparza, L. Rodríguez-Fragoso, Cactus (Opuntia ficus-indica): A Review on its Antioxidants Properties and Potential Pharmacological Use in Chronic Diseases, Nat Prod Chem Res. 2 (2014) 153.

[36] G. Calogero, J.H. Yum, A. Sinopoli, G. Di Marco, M. Grätzel, M.K. Nazeeruddin, Anthocyanins and betalains as light-harvesting pigments for dye-sensitized solar cells, Sol. Energy. 86 (2012) 1563–1575.

[37] G. Veerappan, D.-W. Jung, J. Kwon, J.M. Choi, N. Heo, G.-R. Yi, J.H. Park, Multi-Functionality of Macroporous TiO_2 Spheres in Dye-Sensitized and Hybrid Heterojunction Solar Cells, Langmuir. 30 (2014) 3010–3018.

[38] P.D. Fochs, The Measurement of the Energy Gap of Semiconductors from their Diffuse Reflection Spectra, Proc. Phys. Soc. Sect. B. 69 (1956) 70.

[39] D.P. Joseph, C. Venkateswaran, Bandgap Engineering in ZnO By Doping with 3d Transition Metal Ions, J. At. Mol. Opt. Phys. 2011 (2011).

[40] S.A. Agarkar, R.R. Kulkarni, V. V. Dhas, A.A. Chinchansure, P. Hazra, S.P. Joshi, S.B. Ogale, Isobutrin from Butea Monosperma (Flame of the Forest): A Promising New Natural Sensitizer Belonging to Chalcone Class, ACS Appl. Mater. Interfaces. 3 (2011) 2440–2444.

[41] Eunju Lee Tae, Seung Hwan Lee, Jae Kwan Lee, Su San Yoo, and Eun Ju Kang, K.B. Yoon, A Strategy To Increase the Efficiency of the Dye-Sensitized TiO_2 Solar Cells Operated by Photoexcitation of Dye-to-TiO_2 Charge-Transfer Bands, J. Phys. Chem. B. 109 (2005) 22513–22522.

[42] S. Bagheri, K. Shameli, S.B. Abd Hamid, Synthesis and characterization of anatase titanium dioxide nanoparticles using egg white solution via Sol-Gel method, J. Chem. (2013).

[43] R. Ramanarayanan, P. Nijisha, C. V. Niveditha, S. Sindhu, Natural dyes from red amaranth leaves as light-harvesting pigments for dye-sensitized solar cells, Mater. Res. Bull. 90 (2017) 156–161.

[44] E. Han, K. Vijayarangamuthu, J. sang Youn, Y.K. Park, S.C. Jung, K.J. Jeon, Degussa P25 TiO_2

modified with H_2O_2 under microwave treatment to enhance photocatalytic properties, Catal. Today. 303 (2018) 305–312.

[45] I.K.J.-H.S.-G. Jang, Enhancement of Dye Adsorption on TiO_2 Surface through Hydroxylation Process for Dye-sensitized Solar Cells, Bull. Korean Chem. Soc. 34 (2013) 2883–2888.

[46] Q.H. Wu, A. Thissen, W. Jaegermann, M. Liu, Photoelectron spectroscopy study of oxygen vacancy on vanadium oxides surface, Appl. Surf. Sci. 236 (2004) 473–478.

[47] J. Jun, M. Dhayal, J.H. Shin, J.C. Kim, N. Getoff, Surface properties and photoactivity of TiO_2 treated with electron beam, Radiat. Phys. Chem. 75 (2006) 583–589.

[48] R. Ramamoorthy, N. Radha, G. Maheswari, S. Anandan, S. Manoharan, R. Victor Williams, Betalain and anthocyanin dye-sensitized solar cells, J. Appl. Electrochem. 2016 469. 46 (2016) 929–941.

[49] J. Wu, Z. Tang, Y. Huang, M. Huang, H. Yu, J. Lin, A dye-sensitized solar cell based on platinum nanotube counter electrode with efficiency of 9.05%, J. Power Sources. 257 (2014) 84–89.

CHAPTER: 8

Summary, conclusions, and perspectives for future work

This chapter summarizes and concludes on the results obtained on alternative doped (La, Sb) $BaSnO_3$ photoanode materials, Sb doped SnO_2 transparent conducting electrode, and prickly pear fruit natural dye extract photosensitizer that are discussed in detail in the individual chapters from 3 to 7. Firstly, the summary of all the core chapters by comparing the key results are given in the form of a table. Secondly, conclusions drawn from the key findings are presented in brief. Finally, the chapter is concluded with perspectives for future work.

8.1 Summary of the research work

In view of the long-term research on DSSCs to develop high performance and stable cells using abundant, environment friendly, cost-effective materials and facile techniques, the ternary perovskite $BaSnO_3$ (doped with La and Sb) photoanodes, Sb doped SnO_2 transparent conducting electrode and natural prickly pear fruit dye extract photosensitizer investigated and discussed in the core chapters of this thesis are compared as shown in Table 8.1.

The synthesized optimal samples were appropriately post treated and characterized for their structural, surface/morphological, optical, and electrical properties by using various analytical techniques. The DSSC devices fabricated using the optimal samples as components were tested for their potential as an alternative materials. La-doping at the Ba sites of $BaSnO_3$ by the hydrothermal method is found to play a significant role in inducing a mixed nanorod-nanoparticle morphology for 0.03 La-doped $BaSnO_3$ sample.

Table 8.1 Comparison of the optimal alternative La, Sb doped $BaSnO_3$ photoanodes, Sb doped SnO_2 transparent conducting electrode, and prickly pear fruit extract photosensitizer based DSSC

Synthesis Method	Sample ID	Role of the sample	Alternative component in DSSC device architecture	V_{OC} (V)	J_{SC} (mA/cm^2)	FF (%)	η (%)	Remarks
Hydrothermal	H-LBSO3	ETL	FTO/***H-LBSO3***+N719/FTO	0.62	3.05	65.02	1.23	Yielded bigger particles with lesser dye adsorption
Facile peroxide-route	LBSO3	ETL	FTO/***LBSO3***+N719/FTO	0.72	14.37	57.58	5.96	Yielded mixed morphology with enhanced dye adsorption
	ABSO1	ETL	FTO/***ABSO1***+N719/FTO	0.74	9.97	55.14	4.06	Yielded smaller particles with reasonably good PCE
Spray pyrolysis	ATO	TCE	***ATO***/TiO_2+N719 Dye/***ATO***	0.69	9.16	64.03	4.05	Sheet resistance decreased drastically and showed reasonably good efficiency and better figure of merit
Natural dye extraction process	Prickly pear fruit extract	Dye	FTO/TiO_2+***Pricklypeardye***/FTO	0.56	1.17	85.13	0.56	Natural dye adsorption enhanced absorption in the visible range
Commercial	Standard DSSC	Commercial TiO_2 as ETL and FTO as TCE	FTO/TiO_2/N719/Elec/Pt CE/FTO	0.77	12.38	74.98	7.22	DSSC fabricated with standard materials in our lab

Among the hydrothermal synthesized La-doped $BaSnO_3$ photoanodes, 0.03% La doped photoanode exhibits a better conversion efficiency of 1.23% compared to DSSC with pure $BaSnO_3$. This low value of efficiency is due to the bigger particle size induced by the hydrothermal method of preparation. To overcome this issue, the facile peroxide route was adopted to synthesize 0.03% La doped $BaSnO_3$ sample which also shows mixed morphological features with nanocuboids/nanoparticles. This sample when used as photoanodes is observed to yield higher efficiency due to enhanced dye loading upon double surface treatment with $TiCl_4$. Among all the fabricated photanodes, the LBSO3 photoanode based device exhibited highest conversion efficiency of 5.96% compared to other devices. A typical pre and post $TiCl_4$ treatment of the photoanode is found to further enhance the conversion efficiency and is attributed to the increased electron lifetime and charge transferability as confirmed from the EIS analysis. From the stability test, the photovoltaic performance is found to be remarkably stable for the nanostructured LBSO photoanode devices retaining ~ 80 % of their initial PCE on the 16^{th} day of the test. The Sb-doped SnO_2 thin film is optimized by a cost-effective chemical spray pyrolysis method and is used as an alternative transparent conducting electrode instead of FTO in a DSSC. The Sb doped SnO_2 film shows high electrical conductivity and good thermal stability of the sheet resistance up to 400 °C compared to pure SnO_2 film. The transparent conducting Sb doped SnO_2 film tested in a DSSC shows a reasonably high power conversion efficiency compared to that using undoped SnO_2 film. The natural dye extracted from prickly pear fruit used as an alternative photosensitizer in DSSC shows an efficiency of 0.56% and the absorption of light is found to increase in the visible region upon dye adsorption.

8.2 Conclusions

Following are the conclusions drawn from the experimental results discussed in the core chapters of this thesis:

- ☑ Facile peroxide-route is beneficial to obtain fine grain sized nanomaterials compared to the hydrothermal method.

- ☑ $Ba_{(1-x)}La_xSnO_3$ with x = 0.03 leads to mixed nanocuboid/nanoparticle morphology exhibiting high dye adsorption compared to undoped $BaSnO_3$ within mere 60 minutes.

- ☑ Pre- and post $TiCl_4$ treatment of photoanode enhances the PCE to 5.96% for LBSO3 cells, due to increased electron lifetime and better charge transferability.

- ☑ Nanostructured $Ba_{(1-x)}La_xSnO_3$ (x = 0, 0.01, 0.03 and 0.05) photoanodes based DSSCs retain ~ 80 % of their initial PCE up to 16^{th} day of the stability test, implying their potential for stable power conversion efficiency.

- ☑ Sb doped at the 'Sn' sites of $BaSn_{(1-x)}Sb_xO_3$ with x = 0.01 shows a promising PCE of 4.01% which is reasonably high for a material under initial stages of exploration as an alternative electron transport layer in DSSCs.

- ☑ Spray pyrolyzed Sb-doped SnO_2 films shows a power conversion efficiency of 4.05% which is promising for a material under initial stages of exploration as an alternative transparent conducting electrode in DSSCs.

- ☑ The natural dye extracted from prickly pear fruits used as a photosensitizer in DSSC exhibits a power conversion efficiency of 0.56%. This low value of efficiency may be enhanced by adopting a co-sensitizing strategy and by altering other device fabrication parameters.

8.3 Perspectives for future work

With the rapid advancement in the 3rd generation solar cells, it is fruitful to extend the research on DSSCs by embracing the advent of newer materials, modified synthesis, and advanced characterization techniques. Because of these aspects, the following are some of the perspectives for future investigations which can be executed by extending the work presented in this thesis.

- Efforts shall be made to assemble DSSCs by only using the optimized alternative components to explore and stabilize their performance.
- The facile peroxide route has to be further modified to induce porosity in the nanostructured La-doped $BaSnO_3$ samples to use as a mesoporous layer in perovskite solar cells (PSCs) which is currently a hot topic of investigation.
- The Sb doped SnO_2 transparent conductive electrode has to be fine-tuned for enhancing its figure of merit and also the thermal stability of sheet resistance by adopting other types of deposition techniques/substrates/post treatment strategy.
- The actual dye component from the prickly pear fruit extract has to be purified and separated using HPLC techniques to enhance the performance of the natural dye and to elucidate its working mechanism.

****

List of publications and conference proceedings

Journals Published

1. **Nandarapu Purushothamreddy**, Reshma Dileep K, V. Ganapathy, M. Kovendhan, D. Paul Joseph "Prickly Pear Fruit Extract as Photosensitizer for Dye sensitized solar cell Applications", *Spectrochimica Acta Part A: Molecular and Biomolecular Spectroscopy, 2019, 117686. https://doi.org/10.1016/j.saa.2019.117686*
2. **Nandarapu Purushothamreddy**, M. Kovendhan Reshma K. Dileep, Ganapathy Veerappan and D. Paul Joseph. "Synthesis and characterization of nanostructured La doped $BaSnO_3$ for dye sensitized solar cells applications", *Material Chemistry and Physics (2020): 123137. https://doi.org/10.1016/j.matchemphys.2020.123137*
3. **Nandarapu Purushotham Reddy**, Rampivalasa Santhosh, Jean Maria Fernandes, Reddivari Muniramaiah, Murali Banavoth, D. Paul Joseph "Nanocrystalline Sb-doped-$BaSnO_3$ perovskite electron transport layer for dye-sensitized solar cells", *Materials Letters* (2021): 131629. https://doi.org/10.1016/j.matlet.2021.131629
4. **Nandarapu Purushotham Reddy**, Rampivalasa Santhosh, Suresh Thogiti, Murali Banavoth, D. Paul Joseph, "Nanostructured La-doped $BaSnO_3$ perovskite oxide as photoconversion efficiency enhancer for DSSC", ***J. Mater. Chem. C***, 2022,**10**, 1403-1413. https://doi.org/10.1039/D1TC04584A
5. **Nandarapu Purushotham Reddy**, Reddivari Muniramaiah, Rompivalasa Santhosh, Jean Maria Fernandes, Gouranga Maharana, M. Kovendhan, D. Paul Joseph, and Banavoth Murali, "Spray-pyrolyzed Sb-doped SnO_2 as highly stable and efficient alternative transparent conducting electrode for dye-sensitized solar cells". (**Major Revison**, ***J. Mater. Chem. C, 2022***)

Papers in conference proceedings

1. **Nandarapu Purushothamreddy**, Rompivalsa Santhosh, Ravi Ketavath, Banavoth Murali, D. Paul Joseph, "Optimization of nanocrystalline Sb doped $BaSnO_3$ for dye-sensitized solar cell applications". ***AIP Conference Proceedings, (2020),*** *2265, 1, 030650.*
2. Mahantesh Khetri, R. Ramarajan, **N. Purushotham Reddy**, M. Kovendhan, K. V. Ashish Srivatsav, Bonta Srinivasa Rao, K. Thangaraju, D. Paul Joseph "Stabilization of 5 wt % 'Sb' doped SnO_2 thin film by post oxidation of thermally evaporated metallic layer", AIP Conference Proceedings, (2019), 2115, 1, 030278.

****